NORTHWESTERN UNIVERSITY

Shape Anisotropy and Electrostatics in Self-assembly of Colloidal Particles

A DISSERTATION

SUBMITTED TO THE GRADUATE SCHOOL

IN PARTIAL FULFILLMENT OF THE REQUIREMENTS

for the degree

DOCTOR OF PHILOSOPHY

Field of Applied Physics

By

Ziwei Wang

EVANSTON, ILLINOIS

September 2020

ABSTRACT

Shape Anisotropy and Electrostatics in Self-assembly of Colloidal Particles

Ziwei Wang

Self-assembly of colloidal particles at the nano- and microscale has been a powerful tool for producing structures with emergent properties in applications ranging from electro-mechanical systems to photonics and biomedical devices. Great success has been achieved in experiments, where a variety of exotic phases have been discovered and even reconfigurable and self-healing structures have been created by utilizing external fields. The self-assembly process results from a delicate balance between different physical interactions, thermal fluctuations, and external fields. Thus, understanding, predicting, and controlling the self-assembled structure and its dynamic process has been a challenging and central problem in materials design and engineering. In this dissertation, I employ various simulation techniques to study the self-assembly of a range of colloidal systems and specifically explore how shape anisotropy and electrostatic polarization effects play a role in the process.

Chapter 2 presents a study on the crystallization process of triangular nanoprisms into a hierarchical hexagonal lattice. Large-scale Monte Carlo simulations reveal the microscopic details of the assembled superlattice which is composed of columns of randomly stacked prisms. I demonstrate that positional ordering of the superlattice indeed emerges from

orientational disorder, from which the design rule is proposed that different phases can be realized by varying the ionic strength and cell height.

Chapter 3 focuses on crystal growth kinetics at the nanoscale, where a prevalent layer-by-layer growth mode is discovered for a diversity of nanoparticles. Coarse-grained modeling and molecular dynamic simulations are applied to map the energy landscape involving key diffusive barriers of the nanoparticle system, which explains the thermodynamic and kinetic driving forces of the observed growth mode. By further coupling analysis of experimental imaging and kinetic Monte Carlo simulations, we show that building block size governs the crystal growth process by simultaneously controlling the ratio of surface diffusion rate to incoming flux and the interaction range.

From Chapter 4, we turn our attention to explore how electrostatic polarization effects play a role in self-assembly and how it can be utilized to realize structures with controlled properties. Chapter 4 presents a general review of dielectric effects in mesoscale simulations, which provides comparison of different methods for handling polarization and highlights key physical phenomena attributed to dielectric effects at the nano- and microscale.

In Chapter 5, I investigate the structural and dynamical properties of a confined dipole hard-sphere fluid near a polarizable interface. The Image Charge Method is incorporated into the Ewald summation to deal with the polarization in simulations. I demonstrate that while the global polarization only weakly depends on the substrate permittivity, the dipolar orientation in the contact layer is strongly affected by the dielectric mismatch, as is the anisotropy of the rotational dynamics.

Inspired by the above observation, Chapter 6 focuses on a two-dimensional dipolar film supported by a dielectric substrate. Simulations show that the dielectric mismatch across

the substrate can be utilized to achieve modulated patterns in the dipolar material. Notably, a rich phase diagram arises, where stripped and circular morphologies emerge with geometric properties that can be controlled through variation of particle shape and substrate permittivity.

Chapter 7 presents a detailed comparison between the recently proposed hybrid method and the iterative boundary element method on solving the systems containing spherical dielectric interfaces. By examining the challenging case of close-packed crystal structures, we demonstrate that the hybrid method is superior to the iterative boundary element method in terms of efficiency. The effects of various parameters on efficiency, convergence, and accuracy are also explored for both methods.

By applying the hybrid method in simulations, I study the self-assembly of binary suspensions of oppositely charged polarizable colloids presented in Chapter 8. A variety of anisotropic superstructures are observed, resulting from the many-body dielectric effects which impart effective directionality to interactions. Notably, both local connectivity and fractal dimension can be well controlled by varying particle size ratio and relative permittivity.

Lastly, I conclude this dissertation with a brief summary of the main findings and future outlook for each chapter in Chapter 9.

Acknowledgments

First and foremost, I would like to thank my advisor, Prof. Erik Luijten, for his continued mentorship and enduring support throughout the years. It has been very rewarding and pleasant to work with Erik. Thanks to him, I have gained the opportunity to work on many interesting topics and collaborate with excellent research groups. As an advisor, he has always been generous with encouragement and supportive with every decision I made. I have learned a lot of valuable lessons from him, from critical thinking, attention to details, to writing and presentation, which I will benefit from for many years to come. I would also like to express my sincere gratitude to the members of my committee, Prof. Monica Olvera de la Cruz and Prof. Michelle M. Driscoll, for taking the time to review this dissertation and offering valuable advice at my thesis prospectus.

This research would not have been possible without my passionate and hard-working collaborators, Prof. Qian Chen, Prof. Zhenli Xu, Prof. Shidong Jiang, Prof. Chad A. Mirkin, Prof. Samuel I. Stupp, Dr. Zihao Ou, Dr. Binbin Luo, Ahyoung Kim, Dr. Zecheng Gan, Dr. Lam-Kiu Fong, Dr. Tine Curk and Eric Bruckner. My special thanks to Prof. Qian Chen, Dr. Zihao Ou and Dr. Binbin Luo. We have been working together on understanding the nanoscale crystallization since I joined the group. We spent so many long afternoons via skype on brainstorming, discussing ideas and writing, which greatly elevated the quality and impact of my work. I truly appreciate this collaboration opportunity and wish you all the best in future career.

I want to thank my wonderful labmates Bernard Beckerman, Huanxin Wu, Ming Han, Zonghui Wei, Amir Maghsoodi, Tine Curk, Hanne Antila, Ian Madden, Hang Yuan, Weihua Lei, Garrett Watson, Max Meirow and Savanna Dautle, who have always been helpful and supportive. Special thanks to Ming Han and Zonghui Wei for offering me so much advice within and outside the research and bringing a lot of joy and laughter to my PhD journey. I would also like to thank my dear friends at Northwestern who have accompanied me over the past five years. I feel so fortunate to have met you and build the long-lasting friendships.

Lastly, I want to express my deepest gratitude to my parents and my husband Xinyuan You. Thank you for always being there, comforting my upsets, celebrating my success, and giving me strength to chase my dreams. Your love and support is the reason I am here.

Table of Contents

List of Tables

List of Figures

CHAPTER 1

Introduction

Self-assembly of colloidal particle with sizes of 10 nm to 10 μm is ubiquitous in nature[1], where particles spontaneously organize into complex patterns or ordered structures. Such processes enable parallelized reproduction and structure formation across length scales that are often difficult to realize by conventional means. Notably, great success has been achieved at the nano- and microscale, where a variety of exotic phases have been discovered, such as quasi-[2], hierarchical[3], and clathrate crystals[4], and even reconfigurable[5,6] and self-healing[7] structures have been created by utilizing external fields. These assembled materials usually have emergent properties for applications ranging from photonics, electronics to sensing technologies[8]. Thus, understanding, predicting, and controlling the self-assembled structure and its dynamic process has become a central problem in materials design and engineering.

Self-assembly of particles results from a balance between different mechanisms, such as various interparticle interactions (e.g., van der Waals, electrostatic, magnetic and molecular interactions)[9], entropy (particularly shape entropy)[10], and external fields (e.g., flow field and electromagnetic field)[11]. This competition becomes exceedingly delicate as the particle size reaches nanoscale, where various interactions (many of which scale with the volume of particle) are of comparable magnitudes close to the thermal energy $k_{\mathrm{B}}T$[9]. Despite the crucial role played in applications such as metamaterials and photocatalysis, understanding and predicting the assembled structure and its associated kinetics has been highly nontrivial

at the nanoscale. On the one hand, the increased importance of discreteness and fluctuations[12], resulting from the fact that the building blocks, solvent and ligand molecules have comparable length scales, precludes the use of mean-field theory and thus poses significant barriers to theoretical calculations. On the other hand, experimental challenges arise from the difficulty of directly imaging real-time, real-space nanoscale dynamics in solution at the needed spatial resolution[13–15], where conventional electron microscopy requires dry and thus static samples[4,16], while ensemble scattering (e.g., small-angle neutron or X-ray scattering) methods do not resolve structure or dynamics at the level of individual particles[17,18]. Therefore, particle-based computer simulation has become a powerful tool to study this problem, in which the great spatial and temporal resolution offer the opportunity to investigate the microscopic details and thus gain mechanistic understanding of the thermodynamics and kinetics of the self-assembly process.

In this dissertation, I employ various simulation techniques to study the self-assembly of a range of systems at nano- and microscale, including anisotropic nanoparticles, two-dimensional dipolar film, and polarizable colloids. Each system is properly coarse-grained at the length scale of interest, and Monte Carlo or molecular dynamics simulations are used to extract the underlying physics as well as explore the phase space to guide the rational design of materials. Specifically, I focus on how shape anisotropy and electrostatic polarization effects play a role in the self-assembly process and how they can be utilized to achieve tunable structures. Accordingly, the content of this thesis is divided into two parts: Crystallization at the Nanoscale (Part 1, focusing on shape-anisotropic nanoparticles) and Dielectric Effects in Self-assembly (Part 2, focusing on systems with polarizable interfaces).

Shape is considered as one of the most important features of the building blocks, which could give rise to a variety of ordered structures[19,20]. To isolate and resolve the role of shape

entropy in self-assembly, a series of simulations of non-spherical colloidal particles have been performed which only take account hard-core interactions[21]. However, besides the effects on entropy, non-spherical shape also induces the anisotropy of intrinsic (e.g., van der Waals and electrostatic) interactions, potentially affecting the assembly behaviors. While the omission of this shape-induced enthalpic effects might be tolerable for micron-size colloids whose interactions are usually short ranged compared with particle size, it can become problematic for nanoparticles which often possess long-range interactions[22]. Therefore, a far more detailed modeling than the hard excluded-volume potentials is required, which at the same time needs to be computationally efficient to allow large-scale simulations. This remains challenging, as the pairwise interaction between anisotropic particles depends not only on their relative position but also on their orientations. In Part 1 (Chapter 2 to 3), I address this technical challenge by deriving analytical functional forms of pairwise potential from the detailed coarse-grained models of nanoparticles. The content of this part is closely interwoven with experimental collaborations. Chapter 2 studies the crystallization process of triangular nanoprisms into a hierarchical hexagonal lattice composed of columns of randomly stacked prisms. Large-scale Monte Carlo simulations demonstrate that positional ordering of the superlattice actually emerges from orientational disorder resulting from highly anisotropic interactions. The design rule is further proposed that different phases can be realized by varying the ionic strength and cell height. Additionally, by utilizing liquid-phase transmission electron microscopy (TEM), we resolve the full transition of dispersed nanoprisms to the superlattice at the single-particle level and reveal a nonclassical nucleation pathway involving a dense, amorphous intermediate. In Chapter 3, we turn our attention to crystal growth kinetics and discover a prevalent layer-by-layer growth mode resembling atomic crystallization for a diversity of nanoparticles. Coupling statistical analysis of experimental

TEM videos with molecular dynamics and kinetic Monte Carlo simulations, we elucidate that building block size governs the crystal growth process in two distinct ways, by simultaneously controlling the ratio of surface diffusion rate to incoming flux and the interaction range. These two parameters in turn determine the thermodynamic and kinetic driving forces for different growth behaviors. Notably, our framework explains the prevalence of corrugated crystal surfaces composed of micron-sized colloids[23-25] in contrast to the faceted nanoparticle superlattices with smooth surfaces[26,27].

As one of the most ubiquitous interactions, electrostatic forces have shown their great power in mediating and directing self-assembly of colloidal particles[22,28], including colloidal aggregation[29,30], clustering[31], and formation of nanostructured materials[32-34]. However, a mechanism that, owing to its complicated many-body nature, has often been neglected or oversimplified in both experiment and computation, is the electrostatic polarization effects arising from the dielectric mismatch at material interfaces (e.g., dielectric contrast between particles and solvent). This omission is noteworthy, given the demonstrated effects of polarization on protein folding[35], plasmonics[36], and ion transport[37]. In Part 2 (Chapter 4 to 8), by applying different computational methods to deal with the polarization effects, I investigate systems with dielectric interfaces of different geometries and further demonstrate how electrostatic polarization can be utilized to achieve assembled structures with tunable properties. A general review of dielectric effects in mesoscale simulation is presented in Chapter 4, which provides comparison of different methods for handling polarization in simulation and highlights key physical phenomena attributed to polarization effects at the nano- and microscale. Following this, I first focus on systems with dielectric interface of slab geometry, which can be efficiently solved by incorporating the Image Charge Method into the Ewald summation. In Chapter 5, I study the structural and dynamical properties of a

confined dipole hard-sphere fluid, representing e.g., magnetic colloids or charged janus particles, near a dielectric interface. Simulation results reveal that while the global polarization only has a weak dependency on substrate permittivity, the dipolar orientation in the contact layer is significantly affected, as is the anisotropy of the rotational dynamics. Inspired by this observation, in Chapter 6, I further demonstrate how dielectric mismatch across the substrate can be utilized to achieve modulated patterns in a two-dimensional dipolar film. Notably, a rich phase diagram arises, where striped and circular morphologies emerge with geometric properties that can be controlled through variation of particle shape and substrate permittivity.

Besides the slab geometry, system with spherical dielectric interfaces, e.g., an ensemble of charged dielectric spheres, has attracted even more attention, as it is able to represent a wide range of biological and synthetic systems such as colloidal suspensions and proteins. Such system can be solved by multiple approaches, including the Image Charge Method[38–40], the Method of Moments[41–45], the Boundary Element Method[46–50], and the perturbative many-body expansion method[51,52]. Specifically, Chapter 7 presents a detailed comparison between a recently proposed hybrid method[53], which combines the Method of Moments, the Image Charge Method, and the Fast Multipole Method, and the iterative Boundary Element Method[50]. By exploring the effect of various parameters on efficiency, convergence, and accuracy, we demonstrate that for densely packed configurations of relatively small number of dielectric spheres, the hybrid method computes the electrostatic energy with a deviation of less than 0.01% at a rate that is more than two orders of magnitude faster than the Boundary Element Method can achieve for deviations of 3%. Therefore, I apply this efficient hybrid method in large-scale simulations to study the self-assembly of binary suspensions of oppositely charged polarizable colloids, as presented in Chapter 8. Notably, I

show that the dielectric many-body effects impart effective directionality to the interactions and thus permit robust self-assembly into a variety of anisotropic superstructures. Both local coordination number and fractal dimension can be accurately controlled through variation of particle size ratio and relative permittivity. The mechanism I identified here offers a potential avenue to designing materials with controllable structural properties.

Part 1

Crystallization at the Nanoscale

CHAPTER 2

Kinetic Pathways of Crystallization at the Nanoscale

This chapter presents a combined experimental–computational study on the nanoscale crystallization. To present a complete story, I have included experimental results that were obtained by Zihao Ou. The content of this chapter is based on the following publication:

- Z. Ou[1], Z. Wang[1], B. Luo, E. Luijten, and Q. Chen, "Kinetic pathways of crystallization at the nanoscale," Nat. Mater. **19**, 450–455 (2020).

2.1. Abstract

Nucleation and growth are universally important in systems from the atomic to the micrometre scale as they dictate structural and functional attributes of crystals. However, at the nanoscale, the pathways toward crystallisation have been largely unexplored owing to the challenge of resolving the motion of individual building blocks in a liquid medium. Here we address this gap by directly imaging the full transition of dispersed nanoparticles to a superlattice at the single-particle level. We utilise liquid-phase transmission electron microscopy at low dose rates to control nanoparticle interactions without affecting their motions. Combining particle tracking with Monte Carlo simulations, we reveal that positional ordering of the superlattice emerges from orientational disorder. Otherwise elusive parameters including line tension and phase coordinates are measured, charting the nonclassical

---

[1]These authors contributed equally to the work

nucleation pathway involving a dense, amorphous intermediate. We demonstrate the versatility of our approach via crystallisation of different nanoparticles, pointing the way to more general applications.

2.2. Introduction

The physical properties of crystals, such as structure, shape, defects, domain size and polymorphism, display a wide variability, strongly correlated with the crystallisation pathways underlying their formation[54–56], with ramifications for mineralization[57], pharmaceuticals[58], optics[59] and electronics[60]. For example, carbonate-silica minerals can be engineered into diversely shaped device elements (e.g. vase, stem, coral) by dynamically sculpting the curved nuclei that arise in accretive crystallisation[61]. Protein crystallisation can be accelerated by orders of magnitude via critical density fluctuations, allowing the creation of high-quality lattices for structural analysis and drug formulation[62]. DNA-coated micron-sized colloids can be grown into cubic diamond lattices with an omnidirectional photonic bandgap by starting from preformed seeds with tetrahedral symmetry[63]. The central role of crystallisation for building blocks spanning this range of length scales makes understanding and engineering the underlying pathways of fundamental interest and crucially relevant for applications.

Due to the stochastic nature of nucleation and growth, an effective route to mechanistic understanding is to directly capture the translational and rotational motion of individual building blocks as they interact and crystallise. On the micron scale, this approach has revealed a series of crystallisation pathways beyond classical nucleation theory, such as prenucleation cluster formation[64], multi-step nucleation[65] and diffusion-limited solidification[66], via time-lapse optical microscopy. For nanoscale entities, a richer variety of phases has been

observed, such as quasi-[2], hierarchical[3] and clathrate crystals[4]. Their pathways can be more complicated, owing to the increased importance of discreteness and fluctuations resulting from the fact that the building blocks, solvent and ligand molecules have comparable length scales[12]. However, direct imaging of dynamics at the nanoscale has been challenging, because TEM with the needed spatial resolution[67] was not compatible with the liquid media in which crystallites nucleate and grow.

2.3. Results and Discussion

2.3.1. Hierarchical self-assembly of nanoprisms

Here we exploit recent advances in low-dose liquid-phase transmission electron microscopy (TEM), a technique rapidly gaining importance in materials research[56,69–72], to achieve the in-situ imaging of nanoscale entities ordering into crystals, distinct from the non-periodic nanoparticle aggregates observed in recent liquid-phase TEM studies[71,73]. We employ a sandwich geometry of two SiN_x chips accommodating and sealing, against the high vacuum of TEM, a liquid suspension containing many interacting nano entities (Fig. 2.1a). We focus on a system of triangular gold nanoprisms as representative nonspherical, anisotropic nanoscale building blocks. The nanoparticle interactions are highly directional due to the large aspect ratio (100.5 ± 9.5 nm side length, 7.5 nm thickness). Moreover, the prisms are coated with negatively charged thiolated ligands to render them well-dispersed by electrostatic repulsion in the initial suspension (Fig. 2.1a).

We observe a surprising transition from dispersed prisms to a hexagonal lattice, which is constructed hierarchically in three dimensions (3D) from standing columns of stacked, misaligned prisms (solid arrowed path in Fig. 2.1ac). The hierarchical construction proceeds as follows. Through radiolysis of water, the imaging beam monotonically increases the ionic
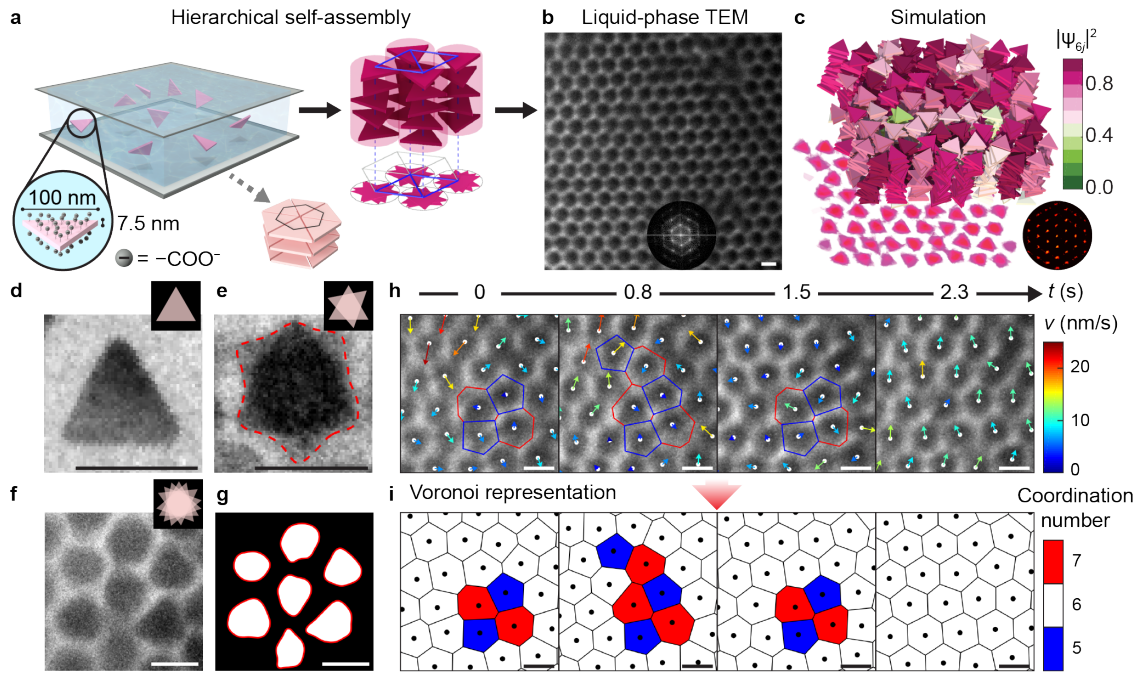
Figure 2.1. Gold triangular nanoprisms crystallise hierarchically in 3D to an unexpected hexagonal lattice. (a–c) Illustration of the hierarchical crystallisation process. a, An aqueous suspension of nanoprisms sealed and sandwiched between two SiN_x chips. Instead of packing into a space-filling honeycomb lattice (dotted arrow), the nanoprisms stack face-to-face into columns (magenta), which subsequently bundle into a hexagonal lattice (solid arrow). b, Liquid-phase TEM image showing the highly ordered hexagonal lattice. Inset shows the Fourier transform of the image. c, MC simulations confirm the hexagonal lattice as the thermodynamically stable structure, as illustrated via a colour map denoting the squared modulus of the bond orientational order parameter[68] per column j, $|\psi_{6j}|^2$, two-dimensional (2D) projection and diffraction pattern. (d–g) Liquid-phase TEM snapshots showing the stacking of misaligned prisms (top view): an individual prism sitting on the SiN_x chip (d), two prisms stacking with misalignment (e, polygonal projection contoured in dotted red line) and more prisms stacking into columns (f–g, nearly circular projections contoured in solid red lines in the binary image). (h–i) Time lapse liquid-phase TEM images (h) and corresponding Voronoi representations (i) of the lattice, showing the annealing of imperfectly coordinated sites. Colour of each cell denotes the coordination number. Arrows in the top panel are coloured by the magnitude of the instantaneous velocity of individual columns v calculated from successive TEM images. Scale bars for all images: 100 nm.

strength in the illuminated region within seconds, facilitating counterion screening of the electrostatic repulsions[72,73]. The dispersed prisms in this region thus experience a stronger

net attraction than elsewhere, initiating stacking on the flat SiN_x chip into vertically standing columns. The prisms in a column are not in perfect registry but misaligned in angular orientation (cf. circular projection in Fig. 2.1d–g). These columns then interact to form the final structure that appears as a hexagonal lattice of evenly spaced dark, circular disks under TEM (Fig. 2.1b). The equilibrium lattice constant measured from the TEM images matches that for hexagonally packed columns with touching edges. Voronoi cell analysis of the movies shows that the columns vibrate rapidly, eventually annealing all imperfectly bonded 5- and 7-fold clusters into hexagonal sublattice units (Fig. 2.1h–i). At the low electron dose rates used here (3.7–8.9 $e^- Å^{-2} \cdot s^{-1}$), the ligands on the prism surface remain intact and nanoparticle interactions are not affected other than through variation of the ionic strength[73]. Quantification of the relationship between dose rate and ionic strength make it possible to trigger and capture the complete crystallisation starting from dispersed prisms.

We note that this hexagonal lattice differs from the space-filling honeycomb lattice predicted by prior computer simulations (dotted arrowed path, Fig. 2.1a)[74], because the nanoparticles in our experiments are not hard-core geometric shapes, but interact via a combination of van der Waals and electrostatic interactions. The hierarchical lattice also transcends the simple one-dimensional columns formed from face-to-face prism stacking[75] or other loosely packed chain-like aggregates observed in liquid-phase TEM[71,73], where substrate adhesion prevented nanoparticle motions in 3D. Repeatedly switching the electron beam off and on leads to reversible crystallisation and disassembly of the hexagonal lattice, confirming the role of local ionic strength variation.

Explicit calculation shows that the misaligned stacking of prisms into columns originates from an intricate balance between pairwise interaction energy and rotational entropy. The comparable size of the building blocks and the interaction range necessitates far more detailed

modelling than the hard excluded-volume potentials[74] typically employed for anisotropic colloids, so we compute the inter-prism pairwise interaction $E_{\text{tot}} = E_{\text{vdW}} + E_{\text{el}}$ (with E_{vdW} the van der Waals attraction and E_{el} the electrostatic repulsion) via numerical summation over 250,000 discretised elements per prism (see Section 2.5.1 for details). The net interaction E_{tot} is highly directional and strongly attractive, explaining why the prisms predominantly stack in parallel and coaxially, with minimal tilting of their basal planes at a vertical separation d. To understand the energetics of prism misalignment, we plot the computed pairwise interactions in polar maps along relative orientation $\Delta\theta$, the spin-angle difference between neighbouring prisms (Fig. 2.2a). At the effective experimental ionic strength, E_{el} favours anti-alignment of adjacent prisms, while the alignment-favouring E_{vdW} dominates slightly, resulting in a minimum in interaction energy E_{tot} at $\Delta\theta = 0$ and vertical separation d_{min} (Fig. 2.2b). Yet, E_{el} suppresses variation of E_{tot} near $\Delta\theta = 0$, so that rotational entropy negates the energetic penalty for small misalignments (penalty less than $k_{\text{B}}T$ for $|\Delta\theta| < \pi/10$; Fig. 2.2c), consistent with the experimental observations (Fig. 2.1 d–g).

The misalignment of prisms within each column has consequences that propagate to the large-scale crystal structure, giving rise to radially isotropic interactions between columns that promote their hexagonal packing. From the explicit pairwise interaction E_{tot} we obtain an effective functional form (Section 2.5.2 and 2.5.3) that allows efficient large-scale Monte Carlo (MC) simulations (see Section 2.5.4 for details). On the individual column level, the misalignment between adjacent prisms propagates as the prism number M in a column increases (see Section 2.5.5.4). For a typical M of 23, we find that the orientational correlation function along the column axis decreases exponentially to less than 10% for the fourth neighbour, reflecting high orientational randomness (Fig. 2.2d,e). As a result, the inter-column interactions at different relative column orientations collapse onto a master curve (Fig. 2.2f).
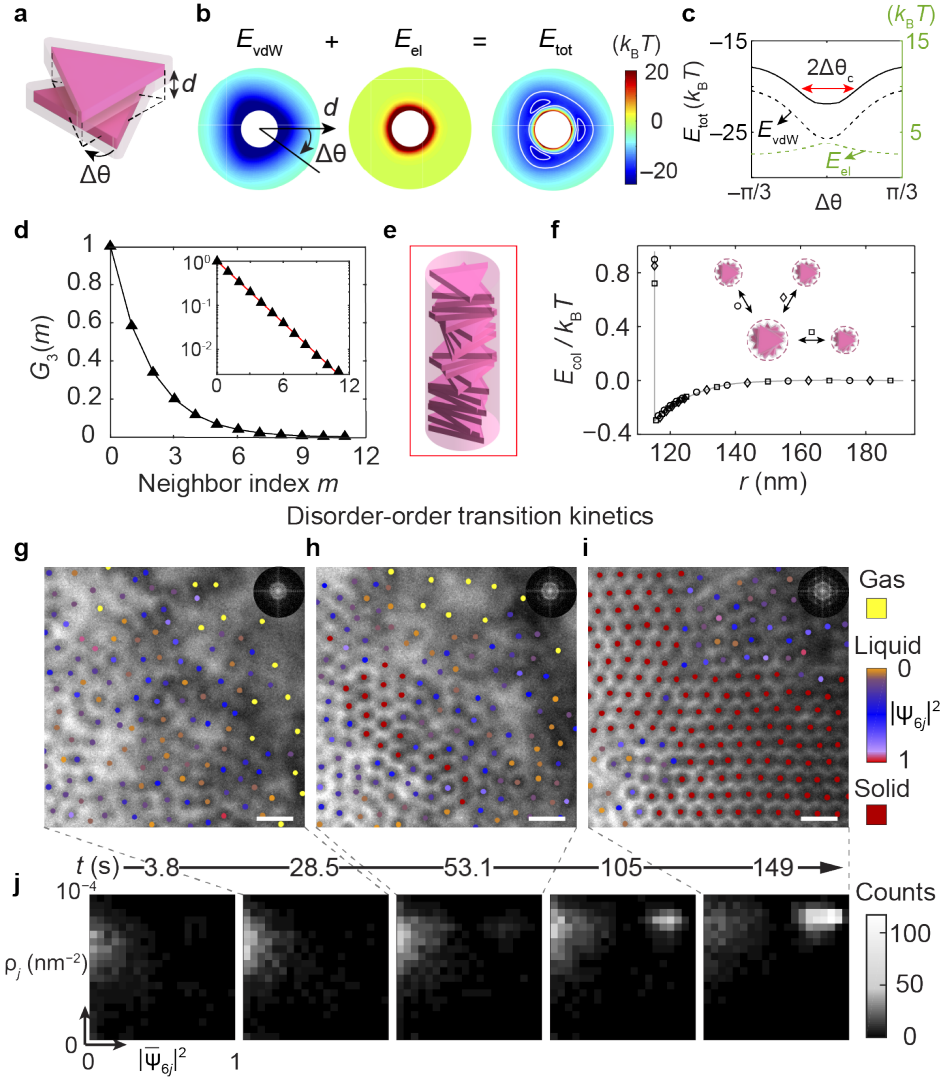
Figure 2.2. Energetics and in-situ observation of the crystallisation process. (a–c) Pairwise interaction between two stacked prisms at the effective experimental ionic strength of 0.5 M. a, Definitions of vertical separation d and spin-angle difference $\Delta\theta$. b, Coloured polar maps showing van der Waals attraction E_{vdW}, electrostatic repulsion E_{el} and total interaction energy $E_{\mathrm{tot}} = E_{\mathrm{vdW}} + E_{\mathrm{el}}$ as a function of d and $\Delta\theta$. c, Pairwise energies vs. $\Delta\theta$ at $d = d_{\mathrm{min}}$, the prism separation at the global energy minimum. $[\Delta\theta_{\mathrm{c}}, \Delta\theta_{\mathrm{c}}]$ marks the spin-angle range with energy penalty less than $k_{\mathrm{B}}T$. (d) Orientational pair correlation function between prisms in a single column computed from simulations. Inset: $G_3(m)$ on a semi-logarithmic scale, with a fitted decay length of 1.86 prisms, indicating low orientational correlation beyond the second neighbour. (e) Representative snapshot of a column. (f) Inter-column interaction E_{col} is independent of relative orientation (marked by different symbols). (g–i) Time-lapse TEM images show the real-time crystallisation process, with gas columns coloured yellow, liquid columns coloured according to $|\psi_{6j}|^2$ and solid columns coloured red. Insets: Fourier transforms highlighting increasing crystalline order. (j) Corresponding order-density ($|\bar{\psi}_{6j}|^2$, ρ_j) histograms showing the counts of columns exhibiting specific $|\bar{\psi}_{6j}|^2$ and ρ_j values. The liquid domain (low $|\bar{\psi}_{6j}|^2$) gradually expands and transitions to the solid domain (high $|\bar{\psi}_{6j}|^2$) at approximatedly constant ρ_j. Scale bars: 200 nm.

The potential well of this curve is shallow $(-0.3k_{\mathrm{B}}T)$, making columns interact as nearly hard circular cylinders. Thermodynamically, such cylinders are expected to crystallise at sufficiently high volume fraction[76], consistent with our experiments and MC simulations (Fig. 2.1b,c). Note that inter-column interactions in turn affect the intra-column alignment (see Section 4.2 for details); this is fully taken into account in the large-scale simulations.

2.3.2. Nonclassical nucleation pathways

Since the agreement of the multiscale computation and the TEM observations underpins the thermodynamic origin of the observed hierarchical crystallisation, we develop and apply single-particle tracking codes to the TEM movies, obtaining a series of otherwise elusive parameters quantifying the crystallisation pathway. Accurate statistics are achieved by locating more than 110,000 columns in independent movies. To specify the crystalline nuclei, we measure the sixfold symmetry of bonds for each column j using the modulus squared bond-orientational order parameter[68] $|\psi_{6j}|^2$. The establishment of crystalline order is accompanied by density fluctuations, which we illustrate by directly measuring the evolution of the local density ρ_j, the inverse Voronoi cell area[65], as local order develops. Jointly, these two instantaneous local parameters describe the structural state of a column at any given time. The time-lapse TEM images (Fig. 2.2g–i) show that initially the columns are in a dilute phase, translating rapidly– the analogue of a "gas" state with low $|\psi_{6j}|^2$ and low ρ_j ($\rho_j < 0.50\rho_0$, where ρ_0 is the density of a dense-packed hexagonal lattice). Subsequently, a region of columns with low $|\psi_{6j}|^2$ but higher ρ_j appears and transiently coexists with the gas, analogous to a dense, amorphous "liquid" state. This liquid region expands steadily until stable hexagonal crystallites nucleate from within, the "solid" state (characterised by a solid bond number, the number of crystalline nearest neighbours of column j, $\xi_j >= 4$).
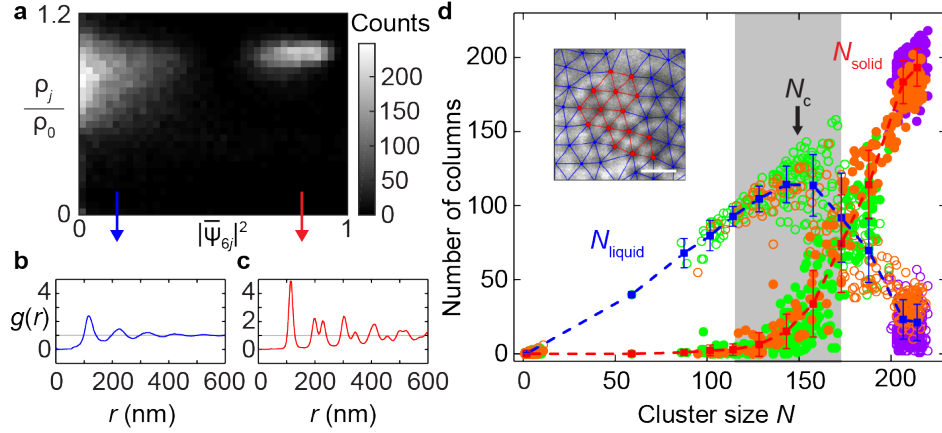
Figure 2.3. Multi-step crystallisation of a nanoparticle superlattice via a dense, amorphous liquid state as the intermediate. (a) Direct visualisation of the crystallisation pathway in the order-density $(|\bar{\psi}_{6j}|^2, \rho_j)$ histogram collected during the full crystallisation process. The populated region on the left represents the liquid columns with low structural order, whereas the bright region on the right represents the ordered solid. (b–c) Radial distribution functions corresponding to the two regions highlight their structural differences. (d) Number of liquid columns N_{liquid} (open) and solid columns N_{solid} (filled) in a cluster of N columns. Data from three independent experiments (differentiated by colour) are described by master curves for liquid columns (blue, mean $\pm$ s.d. from three independent experiments) and solid columns (red, mean $\pm$ s.d. from three independent experiments). Grey shaded region highlights where the liquid-solid transition occurs, illustrated by the TEM image (inset, scale bar: 200 nm) showing an emerging solid nucleus (red) surrounded by a liquid (blue) network. The master curve reveals a characteristic cluster size N_{c} beyond which a stable solid cluster emerges and continues to grow.

The liquid columns envelop the nuclei as they grow into large crystalline domains, which represent the intermediate during the crystallisation. Note that this observed liquid phase is indeed a metastable intermediate characteristic of a two-step crystallisation process, rather than a transient state. These insights into the prenucleation intermediate and its dynamic transformation into nuclei are enabled by observing time-dependent nanoscale motions and rearrangements at the single-particle level, which is not possible via common in-situ techniques, such as small-angle X-ray scattering, that only resolve ensemble-level parameters (e.g., lattice spacing, symmetry group, domain size)[75,77].

To quantify the crystallisation pathway, we illustrate the liquid to solid conversion in the plane of local order versus local density. We employ the coarse-grained order parameter[65] $|\bar{\psi}_{6j}|^2 = |\left(\sum_{k=0}^{Z^*} \psi_{6k}\right)/(Z^*+1)|^2$ to further distinguish the liquid and solid states, where the sum runs over column j and its Z^* nearest neighbours that belong to the same state. The time evolution of the $(|\bar{\psi}_{6j}|^2, \rho_j)$ histogram shows that the liquid domain expands along the $|\bar{\psi}_{6j}|^2$ axis, maintaining a high and roughly constant local density but significantly increasing the local order to reach the solid domain (Fig. 2.2j). The $(|\bar{\psi}_{6j}|^2, \rho_j)$ histogram accumulated over the full crystallisation process (Fig. 2.3a) clearly distinguishes the intermediate (left peak, liquid) and final lattice (right peak, solid), with corresponding radial distribution functions (Fig. 2.3b,c) resembling those of liquid and solid states of atomic matter. Interestingly, this nonclassical nucleation pathway involving formation of a dense amorphous intermediate was also found to assist crystallisation from a dilute state in proteins[62,78] and Lennard-Jones systems[79], but hitherto could not be observed on the nanoscale.

The observed pathway is quantitively consistent in independent experiments. For ease of comparison, we track the populations of liquid and solid columns in growing clusters, defined[65] as sets of contiguously bonded columns. Initially, the number of liquid columns N_{liquid} grows to a characteristic size N_{c} (Fig. 2.3d), consistent among multiple crystallisation events, and then decreases steadily while the number of solid columns N_{solid} grows at a higher rate until the cluster has fully solidified. This two-step process agrees with a phenomenological two-barrier free energy[79], where the intermediate liquid state acts as a "wetting" layer that lowers the interfacial tension, so that ordering happens within (Fig. 3.4d, inset). Moreover, the short-range character of the inter-column interaction (Fig. 2.2f, with interaction range smaller than 25% of the column diameter) may be responsible for the existence of the liquid intermediate, consistent with previous theoretical work[62,79].

Taking this concept a step further quantitatively, we use statistical-mechanical principles[80] to determine the line tension from the cluster distribution for the gas-liquid interface from TEM movies. The result, $1.0 \pm 0.1\ k_\mathrm{B}T$ per column diameter, is in remarkable agreement with the computed inter-column attraction of magnitude $0.9\ k_\mathrm{B}T$ (three column pairs of $0.3\ k_\mathrm{B}T$ each).

2.3.3. Exploration of the phase space and other nanoparticle systems

Lastly, full-scale MC simulations spanning the parameter space reveal how positional ordering is inextricably linked with orientational disorder (See Section 4.2 for details). To illustrate this "order from disorder", we characterise the orientational order of prisms within a column via the triatic order parameter[81] $S_\theta = \max_{\theta_0} \left(\frac{1}{M} \sum_{i=1}^{M} \cos\left[3(\theta_i - \theta_0)\right] \right)$, where θ_i denotes the in-plane spin angle of prism i in the column (Fig. 2.4a, see Section 2.5.5.2 for free energy calculation). We focus on 2D packing fractions $\phi_{2D} = N_{\mathrm{col}} A_\Delta / (L_x L_y)$ (N_{col} the total number of columns and A_Δ the area of a prism face) between 0.362 and 0.433, the regime where multiple phases can be realised. When columns are orientationally ordered (e.g., $\langle S_\theta \rangle = 0.84$), the inter-column interaction exhibits a radial anisotropy and a deep attractive well for side-to-side columnar attachment ($-23 k_\mathrm{B}T$, Fig. 2.4b,c). The MC simulations reveal slowly evolving clusters of columns that are laterally connected. In contrast, on the same time scale, misaligned columns (e.g., $\langle S_\theta \rangle = 0.37$) fully crystallise into a perfect lattice (Fig. 2.4d,e). Systematically varying both cell height L_z and ionic strength I (Fig. 2.4f) at each 2D packing fraction ϕ_{2D}, we find a hexagonal lattice if $\langle S_\theta \rangle < 0.4$. The global hexagonal order parameter is a function solely of $\langle S_\theta \rangle$ for the entire ϕ_{2D} range, with data for a wide range of I and L_z collapsing onto a single master curve (Fig. 2.4g, see Section 2.5.4.5 for different ϕ_{2D}).
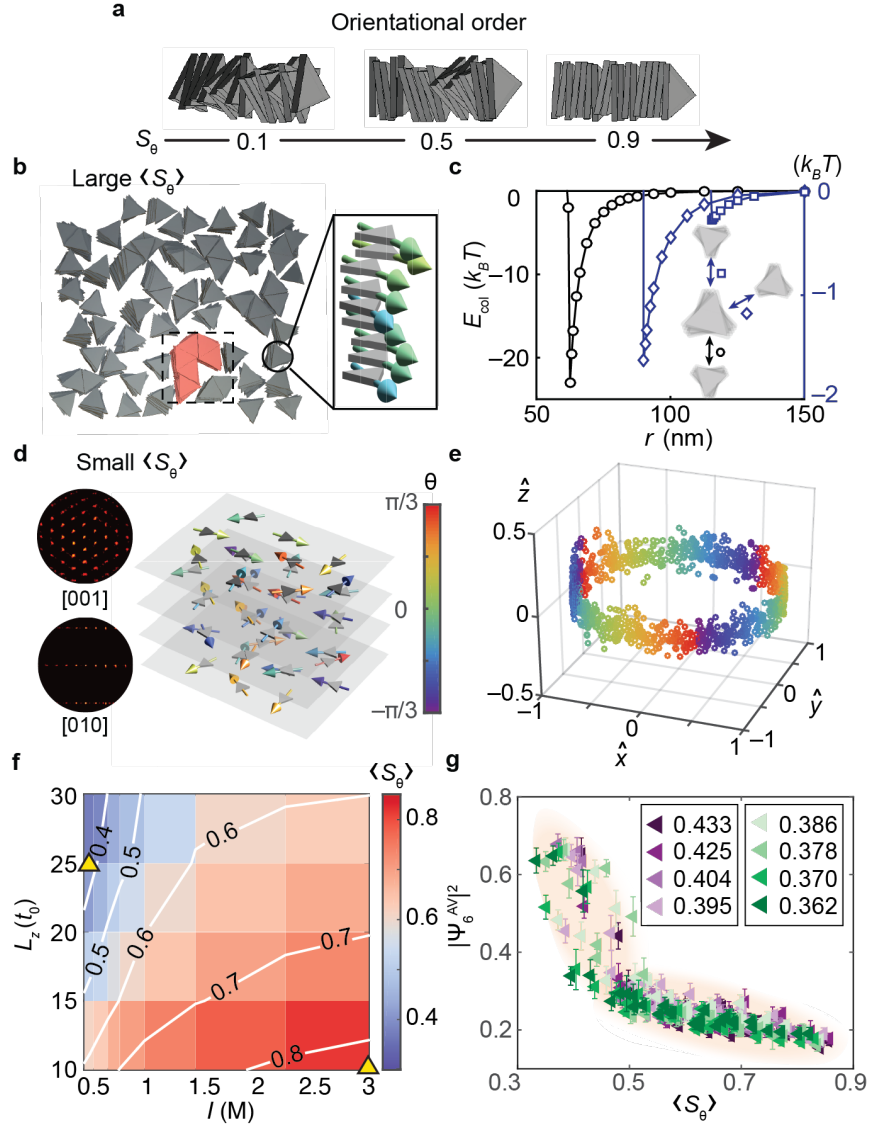
Figure 2.4. Positional ordering originates from orientational disorder. (a) Orientational order S_θ of a column. (b–c) Columns of highly aligned prisms aggregate into slowly evolving clusters (b), driven by strong and highly anisotropic inter-column interactions E_{col} (c), shown as a function of centre-to-centre distance r for three relative orientations: side-by-side (left axis, black), side-to-tip (right axis, blue rhombi) and tip-to-tip (right axis, blue squares). (d) Orientationally highly disordered columns form a plastic crystal. Prism orientations are highlighted by arrows coloured according to their in-plane spin angle θ $(-\pi/3 < \theta < \pi/3)$. Diffraction patterns confirm the positional columnar order. (e) Orientational trajectory of an arbitrary prism reflects orientational randomness in (d). (f) Column-averaged orientational order $\langle S_\theta \rangle$ as a function of ionic strength I and cell height L_z (in units of prism thickness t_0) at 2D packing fraction $\phi_{2D} = 0.386$. Yellow triangles mark the conditions for the highly ordered and disordered columns that give rise to the structures in panels (b) and (d), respectively. (g) Global hexagonal order, described by $|\Psi_6^{\text{AV}}|^2$ (mean $\pm$ standard error from 100 independent samples), develops over the 2D packing fraction range $0.362 < \phi_{2D} < 0.433$. Within this entire concentration range, data for widely different ionic strengths and cell heights collapse onto a master curve described by the global columnar order $\langle S_\theta \rangle$.
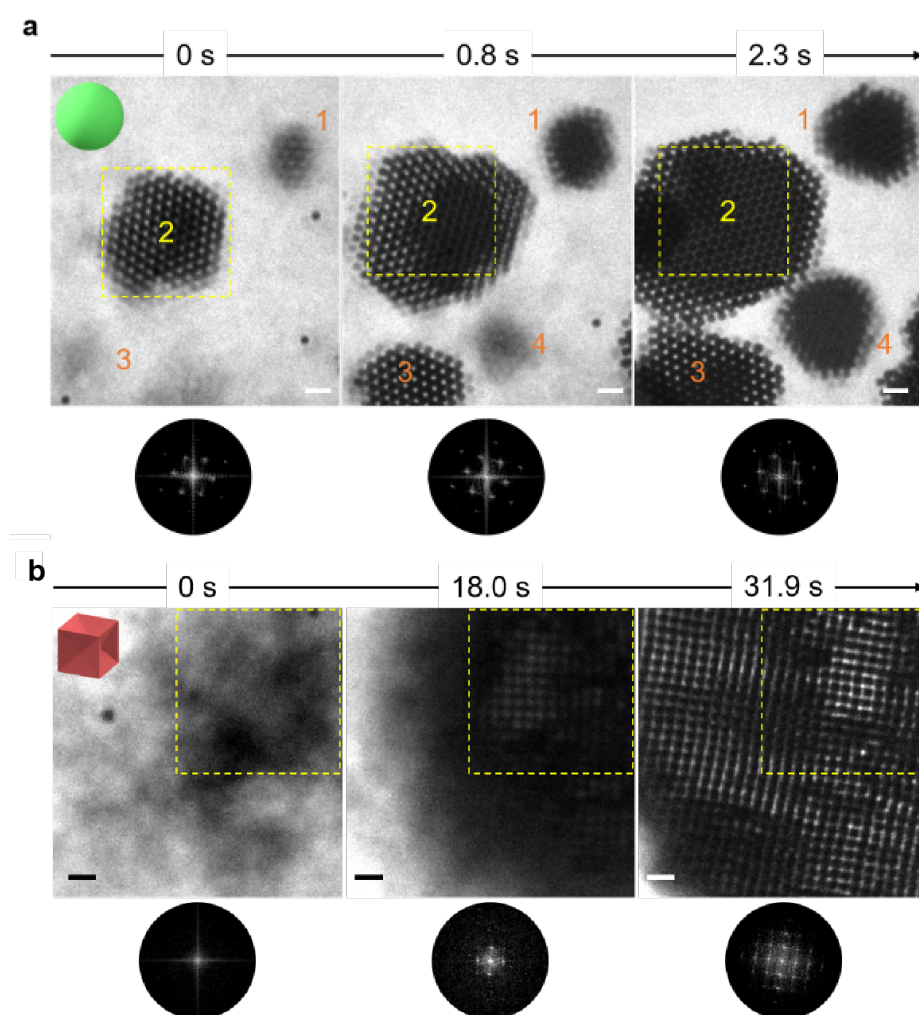
Figure 2.5. Superlattice formation of gold nanospheres and concave nanocubes. Time-lapse liquid-phase TEM images showing the real-time crystallisation process of nanospheres (a, at dose rate $11.9e^-\text{Å}^{-2}\text{s}^{-1}$) and concave nanocubes (b, at dose rate $27.1e^-\text{Å}^{-2}\text{s}^{-1}$) into 3D superlattices. Fourier transforms provided are corresponding to the boxed regions. Scale bars: 200 nm.

This plastic mesophase, with simultaneous orientational randomness and positional ordering, is akin to structures common in molecular solids[82], yet arises here without the conventional conditions of high axial symmetry and long-range repulsion[83]. The physical parameters measured for this model system of nanoprisms, involving both high shape anisotropy and hierarchy, can provide experimental guidance to future refinements of theories

for the pathways of nucleation and growth. To illustrate the versatility of our approach we extend it to gold nanoparticles of different shapes, namely nanospheres (Fig. 2.5a) and concave nanocubes (Fig. 2.5b). Capped with the same charged thiols as the nanoprisms, these nanoparticles are triggered to crystallise into high-quality 3D lattices following a similar mechanism (Fig. 2.5), validating the robustness of our low-dose liquid-phase TEM platform to probe nanoscale crystallisation.

2.4. Conclusions

As the approach is extended to other interacting nano-entities, more parameters can be derived from the imaged coordinates. Fluctuating local features (symmetry of nuclei, topological defects, strain map, etc.) and global characteristics computable only from sufficient single-particle statistics (such as nucleation rate, phonon modes, nanoparticle interaction) are all of crucial importance for understanding the nanoscopic pathways of phase transitions. Our workflow, combining nanoscale resolution of particle motion and shape with a statistical-mechanical framework, can translate knowledge of fundamental interactions, fluctuations and motion on the nanoscale into free-energy landscapes and design rules that will make it possible to optimise dynamic switching of artificial[16] and biological[84] nanoscopic entities between different functional states.

2.5. Methods and Supplementary Information

2.5.1. Coarse-grained model for pairwise interaction calculation

To describe the pairwise interaction between two triangular prisms at all possible relative positions and orientations, we construct a coarse-grained (CG) model in which each prism coated with charged ligands is discretised as a mesh of beads, placed on stacked hexagonal

layers with both intralayer spacing and hexagonal lattice spacing $\Delta_b = 0.5$ nm. We represent the triangular prism shape and surface ligands using $N_1 = 252,540$ beads of type 1 (dark pink beads in Fig. 2.6a) to model the gold atoms and $N_2 = 54,402$ type-2 beads (light pink beads in Fig. 2.6a) to model the coating of charged ligands. The type-1 beads form a 15-layer triangular prism with thickness 7.5 nm. The type-2 beads form a triangular prism-shaped monolayer representing the ligands. The resulting prism has a side length of 100 nm and a thickness of 12.5 nm (7.5 nm prism thickness plus 5.0 nm for two monolayers of ligands), matching the dimensions measured in experiment.

The type-1 beads have a van der Waals interaction $u_{vdW}(r_{b-b})$, and the type-2 beads interact via a screened Coulomb potential $u_{el}(r_{b-b})$ using Debye–Hückel approximation, where r_{b-b} denotes the distance between pairs of interacting beads. The van der Waals interactions between ligands and between ligands and gold atoms are negligible owing to the very small Hamaker constants for hydrocarbon/hydrocarbon and gold/hydrocarbon across water[85]. The interactions $u_{vdW}(r_{b-b})$ and $u_{el}(r_{b-b})$ are given by

$$u_{vdW}(r_{b-b}) = -\frac{H\Delta_b^6}{\pi^2 r_{b-b}^6} \ , \tag{2.1}$$

$$u_{el}(r_{b-b}) = \frac{Z_b^2 e^2}{4\pi\epsilon_0\epsilon_r r_{b-b}} e^{-\kappa r_{b-b}} = \frac{Z_b^2 l_B}{r_{b-b}} e^{-\kappa r_{b-b}} k_B T \ , \tag{2.2}$$

where $H = 28.9 k_B T$ is the Hamaker constant for gold in water, ϵ_0 the vacuum permittivity, ϵ_r the relative permittivity of water, κ^{-1} the Debye length which depends on the salt concentration via $\kappa^{-1} \approx 0.304/\sqrt{I(M)}$ nm for water at room temperature, $l_B = 0.7$ nm the Bjerrum length of water at 25°C and $Z_b = \sigma\Delta_b^2/e = 0.075$ the effective charge (with $e = 1.6 \times 10^{-19}$C the unit charge) of each type-2 bead, derived from the surface charge density $\sigma = -0.048$C/m^2 as measured in experiment. Note that the charge per bead is smaller
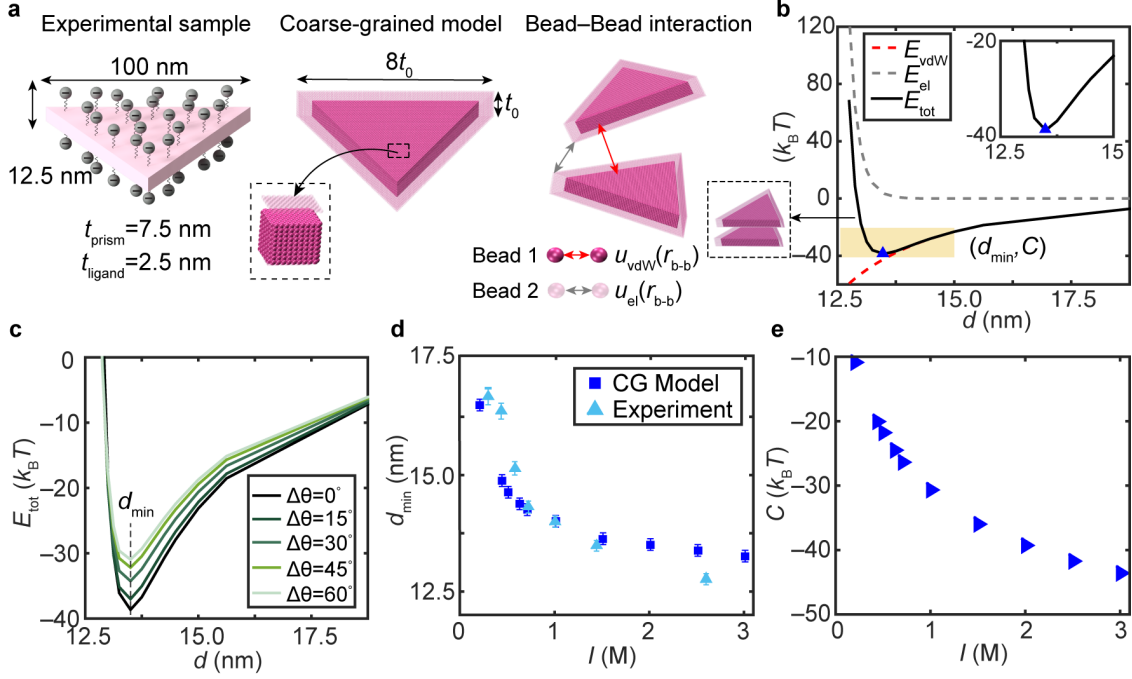
Figure 2.6. CG model for prism–prism pairwise interactions and model validation. (a) Schematic depiction of the CG model consisting of 252,540 type-1 beads (dark pink beads) to model the gold triangular prism and 54,402 type-2 beads (light pink beads) forming the ligand monolayer shell to model the charged ligands. Type-1 bead have a van der Waals interaction $u_{\mathrm{vdW}}(r_{\mathrm{bb}})$ (Eq. 2.1) and type-2 beads have a screened Coulomb interaction $u_{\mathrm{el}}(r_{\mathrm{bb}})$ (Eq. 2.2). The pairwise interaction between two prisms is computed as a summation over all beadbead interactions. The total thickness of the CG prism including two monolayers of ligands is denoted as t_0. (b) Van der Waals interaction E_{vdW} (Eq. 2.3, dashed red line), electrostatic interaction E_{el} (Eq. 2.4, dashed grey line) and the total pairwise energy E_{tot} (solid black line) between two coaxial parallel and aligned ($\Delta\theta = 0$) prisms (as shown in the lower left schematic) versus the prism–prism separation d at ionic strength $I = 2.0$ M, computed in the CG model. The minimum total interaction energy C (at corresponding separation $d_{\min}$) is marked with a blue triangle. The inset shows a magnified view of the shaded part of the $E_{\mathrm{tot}} - d$ curve to highlight the deep and narrow potential well. The definitions of d and $\Delta\theta$ are shown in Fig. 2.2a. (c) Total pairwise interaction energy E_{tot} for two coaxial parallel prisms as a function of vertical separation d at different values of relative spin angle $\Delta\theta$. The minimum-energy separation $d_{\min}$ is independent of $\Delta\theta$. (d) Minimum-energy separation $d_{\min}$ versus ionic strength I computed in the CG model (dark blue squares) and prism spacings measured in our previous experiments (light blue triangles), validating the CG model. (e) Minimum energy C between two coaxial parallel prisms as a function of ionic strength I computed in the CG model.

than the unit charge because we treat the surface charge density as smeared out uniformly over the surface. We assume that the charge density of the ligands on the edges of the prism is the same as on its face.

In our CG model, for computational efficiency we assume that the electrostatic and van der Waals interactions are additive and pairwise. This is not exactly correct, especially at the nanoscale and below, where the size of the building blocks, solvent and ligand molecules are comparable[12]. However, these non-additivity effects appear to be minor in our case, as shown in Section 2.5.4.6, which summarizes the consistency between simulations/modelling and experiments at different levels. Moreover, we assume that the Debye–Hückel approximation still holds in the ionic strength range of interest. Note that Debye–Hückel theory is only valid in the dilute regime but fails at moderate or high salt concentrations due to the neglect of ion–ion correlations, hydration forces and steric effects. Remarkably, recent experiments[86] have shown that the Debye length is a nonmonotonic function of salt concentration, so that the interaction between charged surfaces in concentrated electrolytes decays exponentially but with a decay length longer than the Debye length. This renders the electrostatic repulsion stronger and longer-ranged than predicted by Debye–Hückel theory. On the other hand, recent simulation work[87] indicates that charged spherical nanoparticles with either low or high surface charge densities experience strong long-range depletion attractions at high monovalent salt concentrations, with ion clusters serving as the depletants. Owing to these competing effects, it is not clear to what extent in our case the interactions will deviate from the Debye–Hückel approximation (Eq. 2.2) at high ionic strengths. Empirically, we note that the prism spacings predicted by our CG model exhibit a fair match with experimental measurements over a wide range of ionic strengths (Fig. 2.6d). In Section 2.5.4.6, we provide

a more complete list of comparisons between our modelling/simulations and the experiments at different levels, showing good consistency and thus validating our assumptions here.

Based on the interactions $u_{\mathrm{vdW}}(r_{\mathrm{b-b}})$ between type-1 beads and $u_{\mathrm{el}}(r_{\mathrm{b-b}})$ between type-2 beads, the total pairwise interaction E_{tot} between two arbitrarily oriented and positioned prisms in our CG model is then computed by summing over pairwise interactions between beads on the two prisms. The discretisation spacing Δ_{b} is chosen small enough to ensure convergence of this summation. Thus, we define the total pairwise van der Waals interaction E_{vdW} between two prisms as

$$E_{\mathrm{vdW}} = \sum_{i=1}^{N_1} \sum_{j=1}^{N_1} u_{\mathrm{vdW}}(|\mathbf{r}_i - \mathbf{r}_j|) = -\sum_{i=1}^{N_1} \sum_{j=1}^{N_1} \frac{H\Delta_{\mathrm{b}}^6}{\pi^2 |\mathbf{r}_i - \mathbf{r}_j|^6} \;, \qquad (2.3)$$

where the sums over i and j run over all type-1 beads in the first and the second prism, respectively. Here $\mathbf{r}_i$ and $\mathbf{r}_j$ denote the position vectors of the beads being considered, and N_1 is the number of type-1 beads in a prism. Likewise, the pairwise electrostatic interaction E_{el} between two prisms is

$$E_{\mathrm{el}} = \sum_{i=1}^{N_2} \sum_{j=1}^{N_2} u_{\mathrm{el}}(|\mathbf{r}_i - \mathbf{r}_j|) = -\sum_{i=1}^{N_1} \sum_{j=1}^{N_1} \frac{Z_{\mathrm{b}}^2 l_{\mathrm{B}}}{|\mathbf{r}_i - \mathbf{r}_j|} e^{-\kappa|\mathbf{r}_i - \mathbf{r}_j|} k_{\mathrm{B}}T \;, \qquad (2.4)$$

where the sums over i and j run over all type-2 beads on the ligand shell of the first and the second prism, respectively, and N_2 is the number of type-2 beads in a prism.

Next, we examine how $E_{\mathrm{tot}} = E_{\mathrm{vdW}} + E_{\mathrm{el}}$ depends on the relative position and orientation of two prisms. Starting from the simplest case, where two prisms are coaxial, parallel and fully aligned ($\Delta\theta = 0$) with a vertical separation d, we compute E_{vdW}, E_{el}, and E_{tot} as a function of d at ionic strengths varying from 0.2 M to 3.0 M, using the CG model. The definitions of d and $\Delta\theta$ for the parallel and coaxial case are illustrated in Fig. 2.2a. As a

typical example, Fig. 2.6b shows the interaction energy as a function of d at $I = 2.0$ M. The potential minimum is very deep and narrow (Fig. 2.6b, inset). We denote the corresponding separation and (minimum) energy of a pair of prisms as $d_{\min}$ and C, respectively (identified by the blue triangle in Fig. 2.6b). We will refer to C as the coupling constant. Besides this simple fully aligned case ($\Delta\theta = 0$), we compute $E_{\text{tot}} - d$ at different $\Delta\theta$ values at $I = 2.0$ M. As shown in Fig. 2.6c, the equilibrium separation at which E_{tot} is minimal remains constant, independent of $\Delta\theta$, whereas the energy minimum becomes less deep when $\Delta\theta$ increases (up to $60°$). Thus, the global energy minimum of a pair of parallel and coaxial prisms corresponds to $d = d_{\min}$ and $\Delta\theta = 0$. The strong coupling and the small value of $d_{\min}$ ($1.08t_0$ at $I = 2.0$ M, where $t_0 = 12.5$ nm denotes the total thickness of the prism defined in Fig. 2.6a) indicates that only minimal tilting of the prism basal planes is permitted and that the parallel two-prism configuration is a representative arrangement to study the energetics of stacked prisms inside a column. The dependence of $d_{\min}$ on ionic strength I is illustrated in Fig. 2.6d, where the values for $d_{\min}$ predicted by the CG model are shown to be in good agreement with experimental values, validating our model. Likewise, we compute the coupling constant C versus ionic strength I (Fig. 2.6e). As higher salt concentration screens the electrostatic repulsion more effectively, the coupling constant increases in magnitude. The coupling constant will be used as a key parameter to connect the pairwise interaction with ionic strength in our analytical modelling below.

2.5.2. Analytical model for inter-particle interaction employed in Monte Carlo simulations

The CG model is accurate but computationally very costly. Therefore, we derive an analytical model for use in the Monte Carlo simulations, by approximating the pairwise interaction

energy obtained from the CG model along different degrees of freedom by analytical functions that are inexpensive to evaluate. Beyond the coaxial case considered in Section 2.5.1, we now focus on the case where the two prisms are only required to be parallel but not necessarily coaxial. Therefore, their relative position and orientation can be fully described by four parameters: the vertical separation d, the spin-angle difference $\Delta\theta$, the magnitude of the horizontal displacement $\mathbf{x}$ and the angle α (see schematic in Fig. 2.7a). The vertical separation d is defined as the distance from the centre of one prism (prism2) to the basal plane of the other prism (prism1 or central prism). The horizontal displacement vector $\mathbf{x}$ points from the centre of prism1 to the projected centre of prism2 on the basal plane of prism1. The magnitude of $\mathbf{x}$ is denoted by x and its direction is measured by the angle α ($\in [-\pi/3, \pi/3]$ owing to the threefold symmetry) between $\mathbf{x}$ and the orientation vector (defined as the vector from the prism centre through an arbitrary vertex of its triangular basal plane, shown by the red arrows in Fig. 2.7a) of prism1. The spin-angle difference $\Delta\theta$ ($\in [-\pi/3, \pi/3]$) is defined as the angle between the orientation vector of prism1 (red arrows) and the projection of the orientation vector of prism2 on the basal plane of prism1 (green arrow). For two parallel prisms, the assignment of prism1 and prism2 does not make a difference for the values of d, $\Delta\theta$, α or x. However, the order does make a difference when the basal planes of two prisms are not parallel, where we will have unequal $d_{i \to j}$ and $d_{j \to i}$; $x_{i \to j}$ and $x_{j \to i}$; $\Delta\theta_{i \to j}$ and $\Delta\theta_{j \to i}$; and $\alpha_{i \to j}$ and $\alpha_{j \to i}$, depending on which prism's basal plane is used for the measurement (see Section 2.5.2.4 for details).

Due to the strong screening of the electrostatic repulsion in the range of ionic strengths considered here (0.2 to 3.0 M), the total interaction energy E_{tot} between two parallel prisms computed from the CG model consists of a short-range repulsive contribution and a relatively long-ranged attractive contribution (see Fig. 2.6b for an example). The left panel of
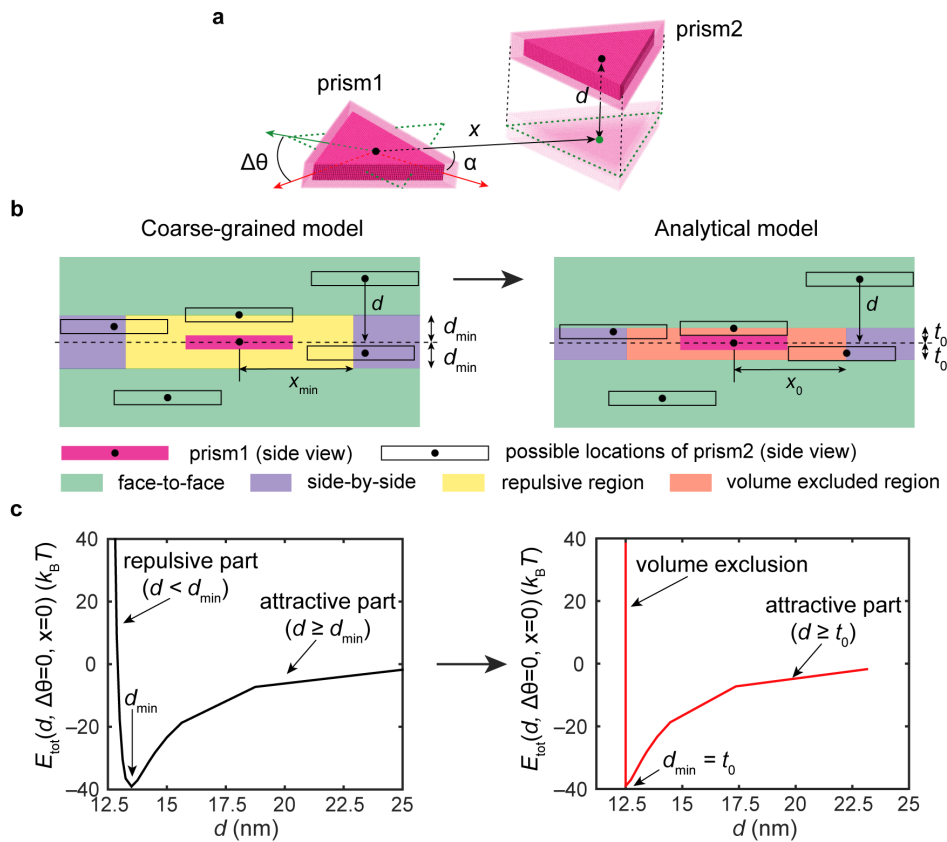
Figure 2.7. Connection between the CG model and the analytical model; classification of configurations. (a) Schematic showing the definition of the four degrees of freedom for a pair of parallel prisms (prism1, which is the central prism, and prism2) employed in the analytical model: the vertical separation d, spin-angle difference $\Delta\theta$, horizontal displacement magnitude x and direction angle α. The black dots stand for the geometric centres of prism1 and prism2, while the green dot denotes the projected centre of prism2 on the basal plane of prism1. (b) Side-view schematic showing different interaction regions (repulsive, face-to-face attractive, side-by-side attractive and excluded-volume regions) around the central prism (prism1) in the CG model (left) and the analytical model (right). Due to its short-range character, we choose to replace the repulsive part of the prism–prism interaction in the CG model (yellow region) by the excluded-volume repulsion of the prisms in the analytical model (orange region), whereas the attractive part of the interaction (green plus purple regions in left panel) in the CG model is fitted by analytical functions in the analytical model. The configuration of two parallel prisms (prism1 and prism2) is classified as face-to-face (side-by-side) if the centre of prism2 is located in the green (purple) region. (c) Total interaction energy E_{tot} between two parallel, coaxial ($x = 0$) and fully aligned ($\Delta\theta = 0$) prisms versus their vertical separation d at $I = 2.0$ M in the CG model (left) and the analytical model (right). Note that the minimum-energy separation d_{min} in the analytical model becomes exactly t_0 regardless of the ionic strength.

Fig. 2.7b shows a schematic illustration of which term dominates in different regions around a central prism (prism1), according to the CG model. To simplify the analytical modelling, we approximate the repulsive part of E_tot by merely the volume exclusion of the prisms in the analytical model (cf. right panels of Fig. 2.7b,c), whereas the remaining attractive part of E_tot at larger distances, which is more complicated, is approximated by analytical functions of $d, x, \Delta\theta$ and α derived from the fitting procedures detailed below. A direct consequence of this simplification is that unlike the repulsive region in the CG model (whose boundary shrinks or expands with ionic strength), the boundary of the excluded-volume region (orange in Fig. 2.7b) in the analytical model is fixed by the geometry of the prism, e.g., the minimum-energy separation d_min in the analytical model becomes simply the total thickness of the prism t_0 regardless of ionic strength (Fig. 2.7c, right panel). As shown in Fig. 2.7b, inside the attractive region the configuration of the two parallel prisms can be classified as either face-to-face (green region) or side-by-side (purple region); we will derive functional forms of the pairwise interaction energy (attractive part) for these two types of configurations below, see Sections 2.5.2.1 and 2.5.2.2.

Throughout this section, all lengths are expressed in dimensionless units, measured in terms of the total prism thickness $t_0 = 12.5$ nm, and denoted by an asterisk.

2.5.2.1. Face-to-face configurations.

A. Dependence of interaction energy on spin-angle difference $\Delta\theta$ (at $d^* = d^*_\text{min}, x^* = 0$)

The pairwise interaction energy $E_\text{tot}(d^* = d^*_\text{min}, \Delta\theta, x^* = 0)$ between two coaxial parallel prisms at the minimum-energy separation vs. the spin-angle difference $\Delta\theta$ is computed using the CG model at various ionic strengths ranging from 0.2 to 3.0 M. We find that the curve
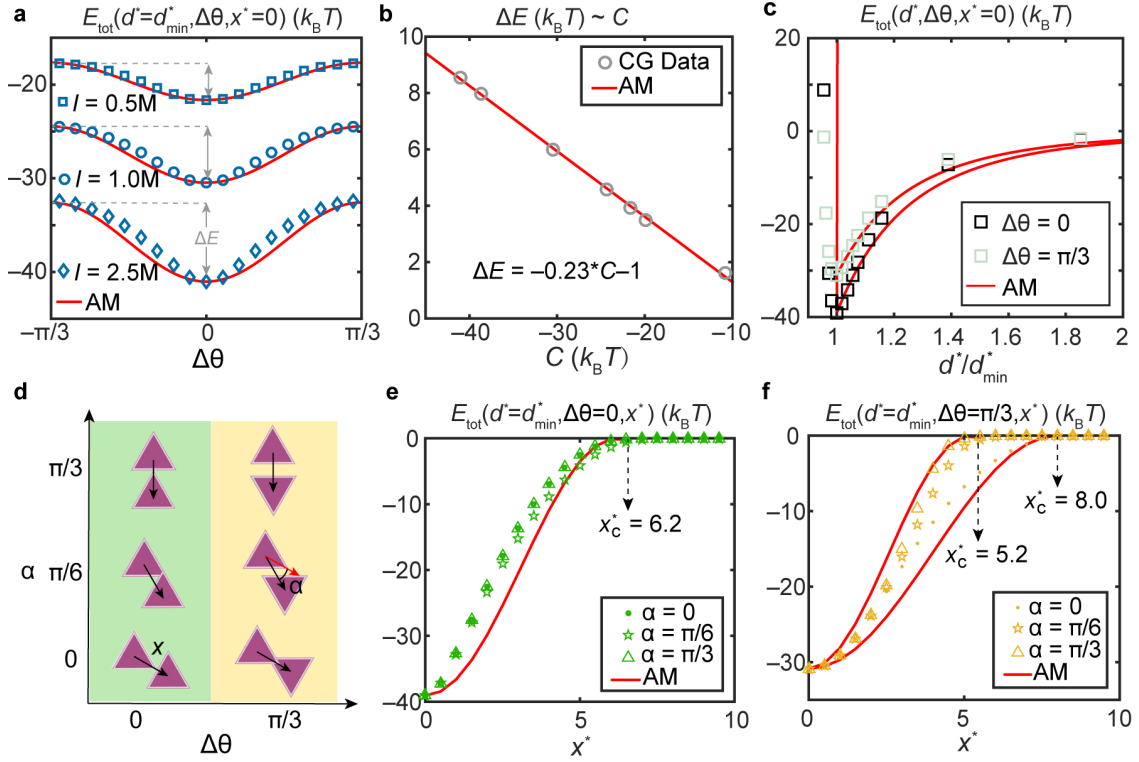
Figure 2.8. Attractive part of pairwise interaction energy E_{tot} in the analytical model for a pair of parallel prisms in face-to-face configuration. (a) Pairwise interaction energy E_{tot} between two coaxial ($x = 0$) parallel prisms at the minimum-energy separation $d^* = d^*_{\min}$ as a function of the spin-angle difference $\Delta\theta$ at three different ionic strengths ($I = 0.5, 1.0, 2.5$ M). Blue symbols are the data computed using the CG model, fitted by the analytical model (AM) $E_{\text{tot}}(d^* = d^*_{\min}, \Delta\theta, x^* = 0) = C + \Delta E \left(1 - \cos(3\Delta\theta)\right)/2$ (solid red lines). The energy difference ΔE between the anti-aligned ($\Delta\theta = \pi/3$) and aligned ($\Delta\theta = 0$) cases is labelled in the plot. (b) ΔE versus coupling constant C determined from the CG model (grey circles) and fitted by a linear function in the analytical model (solid red line). (c) Pairwise interaction energy E_{tot} between two coaxial parallel prisms as a function of $d^*/d^*_{\min}$ for $\Delta\theta = 0$ (black squares) and $\Delta\theta = \pi/3$ (light green squares). The data from the CG model (squares) are well fitted by the analytical model $E_{\text{tot}}(d^*, \Delta\theta, x^* = 0) = E_{\text{tot}}(d^* = d^*_{\min}, \Delta\theta, x^* = 0) \cdot (d^*_{\min}/d^*)^4$ for $d^* \geq d^*_{\min}$, accounting for the attractive part, combined with excluded-volume repulsion $E_{\text{tot}}(d^* < d^*_{\min}) = +\infty$ (solid red lines). (d) Schematic showing the six typical combinations of $(\alpha, \Delta\theta)$ considered for fitting the dependence of E_{tot} on horizontal displacement x^*, with either $\Delta\theta = 0$ (green column, fits shown in panel e) or $\Delta\theta = \pi/3$ (yellow column, fits shown in panel f). (e, f) E_{tot} between two parallel prisms at the minimum-energy separation $d^* = d^*_{\min}$ as a function of x^* for $\alpha = 0$ (dot), $\alpha = \pi/6$ (star) and $\alpha = \pi/3$ (triangle) at (e) $\Delta\theta = 0$ and (f) $\Delta\theta = \pi/3$, at ionic strength $I = 2.0$ M. The data computed using the CG model (symbols) are well fitted by $E_{\text{tot}}(d^*, \Delta\theta, x^*) = E_{\text{tot}}(d^*, \Delta\theta, x^* = 0) \left(1 + \cos(\pi x^*/x^*_c)\right)/2$ for $x^* < x^*_c$ used in the analytical model (solid red lines), where x^*_c (which depends on $\Delta\theta$ and α) is the cutoff distance beyond which $E_{\text{tot}}(d^*, \Delta\theta, x^* > x^*_c) = 0$.

for $E_{\text{tot}}(d^* = d^*_{\min}, \Delta\theta, x^* = 0)$ versus $\Delta\theta$ can be fitted very well with a cosine function,

$$E_{\text{tot}}(d^* = d^*_{\min}, \Delta\theta, x^* = 0) = C + \frac{\Delta E}{2} \left(1 - \cos(3\Delta\theta)\right) , \tag{2.5}$$

where $\Delta E = E_{\text{tot}}(d^* = d^*_{\min}, \Delta\theta = \pi/3, x^* = 0) - E_{\text{tot}}(d^* = d^*_{\min}, \Delta\theta = 0, x^* = 0)$ is the difference in total interaction energy between the anti-aligned and aligned cases, and C is the interaction energy minimum between two coaxial and parallel prisms $E_{\text{tot}}(d^* = d^*_{\min}, \Delta\theta = 0, x^* = 0)$, as defined in Section 2.5.1, which only depends on the ionic strength I (see Fig. 2.6e). As shown in Fig. 2.8a, the effective form Eq. 2.5 works well for typical ionic strengths in the range probed, $I = 0.5$, 1.0 and 2.5 M. The interaction energy difference ΔE (labelled in Fig. 2.8a) is directly related to the coupling constant C (or ionic strength I) as shown in Fig. 2.8b, following a linear dependence $\Delta E = -0.23 \cdot C - 1$. Thus, in the analytical model we write the pairwise energy as a function of $\Delta\theta$ as

$$E_{\text{tot}}(d^* = d^*_{\min}, \Delta\theta, x^* = 0) = C - \frac{0.23 \cdot C + 1}{2} \left(1 - \cos(3\Delta\theta)\right) . \tag{2.6}$$

B. Dependence of interaction energy on vertical separation d^* (at $x^* = 0$)

The magnitude of the pairwise interaction E_{tot} (the attractive part) between two coaxial parallel prisms decreases as the separation d^* increases (Fig. 2.6b and Fig. 2.8c). This decay can be fitted by $E_{\text{tot}}(d^* > d^*_{\min}, \Delta\theta, x^* = 0) = E_{\text{tot}}(d^* = d^*_{\min}, \Delta\theta, x^* = 0) \cdot (d^*_{\min}/d^*)^4$ at different ionic strengths and $\Delta\theta$ values. As an example, we plot the full range of $E_{\text{tot}}(d^*, \Delta\theta, x^* = 0)$ versus $d^*/d^*_{\min}$ at ionic strength $I = 2.0$ M for two extreme $\Delta\theta$ values: $\Delta\theta = 0$ and $\Delta\theta = \pi/3$ in Fig. 2.8c, where the squares are the data computed from the

CG model and the red solid lines represent the analytical model below,

$$E_{\text{tot}}(d^* \geq d^*_{\text{min}}, \Delta\theta, x^* = 0) = E_{\text{tot}}(d^* = d^*_{\text{min}}, \Delta\theta, x^* = 0) \cdot \left(\frac{d^*_{\text{min}}}{d^*}\right)^4$$
$$= \frac{C}{d^{*4}} - \frac{0.23C + 1}{2d^{*4}}(1 - \cos(3\Delta\theta)) \ . \tag{2.7}$$

The last equality follows since $d^*_{\text{min}} = 1$ in the analytical model due to the approximation of the repulsive part of the pairwise energy by the excluded-volume interaction.

C. Dependence of interaction energy on horizontal displacement x^*

Now we turn to the off-centre case where the second prism has a horizontal displacement with respect to the first prism with magnitude x^* and direction characterised by the angle α $(-\pi/3 \leq \alpha \leq \pi/3)$, as defined in Fig. 2.7a. To determine the dependence of the attractive part of the pairwise interaction energy E_{tot} on x^* at different values of $\Delta\theta$ and α, we consider six typical cases listed in Fig. 2.8d, where the two prisms are perfectly aligned $(\Delta\theta = 0)$ or anti-aligned $(\Delta\theta = \pi/3)$ and the displacement angle α is chosen to be $0, \pi/6$ or $\pi/3$. We observe that the qualitative dependence of E_{tot} on x^* remains similar at different ionic strengths and vertical separations d^*. As an illustration, we plot the interaction energy between two prisms at the minimum-energy separation $d^* = d^*_{\text{min}}$ as a function of x^* for the above 6 cases at ionic strength $I = 2.0$ M in Fig. 2.8e $(\Delta\theta = 0$ with $\alpha = 0, \pi/6, \pi/3)$ and Fig. 2.8f $(\Delta\theta = \pi/3$ with $\alpha = 0, \pi/6, \pi/3)$ obtained from the CG model. For all curves, the dependence on x^* can be described by a cosine function,

$$E_{\text{tot}}(d^* \geq d^*_{\text{min}}, \Delta\theta, x^*, \alpha) = \frac{1}{2}E_{\text{tot}}(d^* \geq d^*_{\text{min}}, \Delta\theta, x^* = 0)\left(1 + \cos\frac{\pi x^*}{x^*_{\text{c}}(\Delta\theta, \alpha)}\right) \ , \tag{2.8}$$

where $E_{\text{tot}}(d^* \geq d^*_{\min}, \Delta\theta, x^* = 0)$ is defined in Eq. 2.7. The cutoff distance x^*_c in the above expression determines the off-centre distance beyond which the interaction energy is negligible, i.e., $E_{\text{tot}}(d^* = d^*_{\min}, \Delta\theta, x^* \geq x^*_c) = 0$. As shown in Fig. 2.8e,f, x^*_c is insensitive to α at $\Delta\theta = 0$, but increases with decreasing α at $\Delta\theta = \pi/3$. We qualitatively capture this trend by setting $x^*_c = 6.2$ independently of α when $\Delta\theta \leq \pi/6$, whereas for the more misaligned case $\Delta\theta > \pi/6$ we set $x^*_c = 8.0$ for $\alpha \leq \pi/18$, $x^*_c = 6.5$ for $\pi/18 < \alpha < \pi/6$ and $x^*_c = 5.2$ for $\pi/6 \leq \alpha \leq \pi/3$. Combining Eqs. 2.5– 2.8, the general analytical form for the attractive part of the pairwise energy, $E_{\text{tot}}(d^* \geq d^*_{\min}, \Delta\theta, x^*, \alpha)$, between two parallel prisms arranged in a face-to-face fashion can be summarised as

$$E_{\text{tot}}(d^* \geq d^*_{\min}, \Delta\theta, x^*, \alpha) = \frac{2C - (0.23 \cdot C + 1)\left(1 - \cos(3\Delta\theta)\right)}{4d^{*4}} \left(1 + \cos\frac{\pi x^*}{x^*_c(\Delta\theta, \alpha))}\right) .$$

(2.9)

This equation covers all the different cases discussed in Section 2.5.2.1. Combination of Eq. 2.9 with the excluded-volume repulsion $E_{\text{tot}}(d^* < d^*_{\min}, \Delta\theta, x^*, \alpha) = +\infty$, yields the full pairwise interaction energy for face-to-face configurations.

2.5.2.2. Side-by-side configurations.

We now consider the configurations where the centre of one prism is located in the side-by-side region (purple region in Fig. 2.7b) of the other prism, see inset of Fig. 2.9a. Starting from the simplest case where the two prisms are placed on the same plane with zero vertical separation $(d^* = 0)$ and oriented such that $\Delta\theta = \alpha = \pi/3$, we compute their pairwise interaction energy $E_{\text{tot}}(d^* = 0, \Delta\theta = \alpha = \pi/3, x^*)$ versus x^* using the CG model at ionic strengths ranging from 0.2 to 3.0 M. We find that the data at different ionic strengths exhibit a common trend. As shown in Fig. 2.9a, the curve $E_{\text{tot}}(d^* = 0, \Delta\theta = \alpha = \pi/3, x^*)$ versus

x^* at $I = 2.0$ M has a well-defined minimum side-by-side total interaction energy C_{side} and horizontal displacement x^*_{min}. Since E_{tot} shows a rapidly increasing repulsion as x^* decreases below x^*_{min}, we use the excluded-volume interaction of the prisms to model their repulsion, similar to the analytical model for the face-to-face configurations (Section 2.5.2.1). Therefore, the minimum-energy horizontal displacement x^*_{min} in the analytical model is the centre-to-centre distance between two fully attached side-by-side prims, x^*_0 (defined in Fig. 2.9a, inset). In this arrangement, C_{side} (i.e., $E_{\text{tot}}(d^* = 0, \Delta\theta = \alpha = \pi/3, x^* = x^*_{\text{min}})$), is directly related to the coupling constant C (the global interaction energy minimum for face-to-face configurations, cf. Section 2.5.2.1), as shown in Fig. 2.9b, which illustrates the linear fit $C_{\text{side}} = 0.15 \cdot C + 0.75$. Our general model for the attractive part of the interaction energy, $E_{\text{tot}}(x^* \geq x^*_{\text{min}})$, is described in detail below in Part A and B.

As a matter of simplification, we note that $|\Delta\theta| \approx |\alpha| \approx \pi/3$ holds for all side-by-side configurations (purple region in Fig. 2.7b) and therefore we approximate the interaction energy $E_{\text{tot}}(d^*, \Delta\theta, x^*, \alpha)$ between two side-by-side prisms by $E_{\text{tot}}(d^*, \Delta\theta = \alpha = \pi/3, x^*)$. The justification for this assumption is that the pairwise attraction for the side-by-side configurations is only substantial when the two edges are close enough (see Fig. 2.9a), where $|\Delta\theta|$ and $|\alpha|$ cannot deviate significantly from $\pi/3$ for two non-overlapping prisms. For example, if we choose the cutoff for the horizontal distance $x^*_c = 5.2$ (as introduced below), we have $|\Delta\theta| > 50°$ and $|\alpha| > 35°$, and our approximation introduces an error within $k_{\text{B}}T$.

A. Dependence of interaction energy on horizontal displacement x^* (at $d^* = 0$)

To examine the dependence of the pairwise interaction energy between two side-by-side prisms on the horizontal displacement x^*, we first consider zero vertical separation, $E_{\text{tot}}(d^* = 0, \Delta\theta = \alpha = \pi/3, x^*)$. The trend of the curves for $E_{\text{tot}}(d^* = 0, \Delta\theta = \alpha = \pi/3, x^*)$ versus x^* is qualitatively similar for all ionic strengths examined, and we choose $I = 2.0$ M for
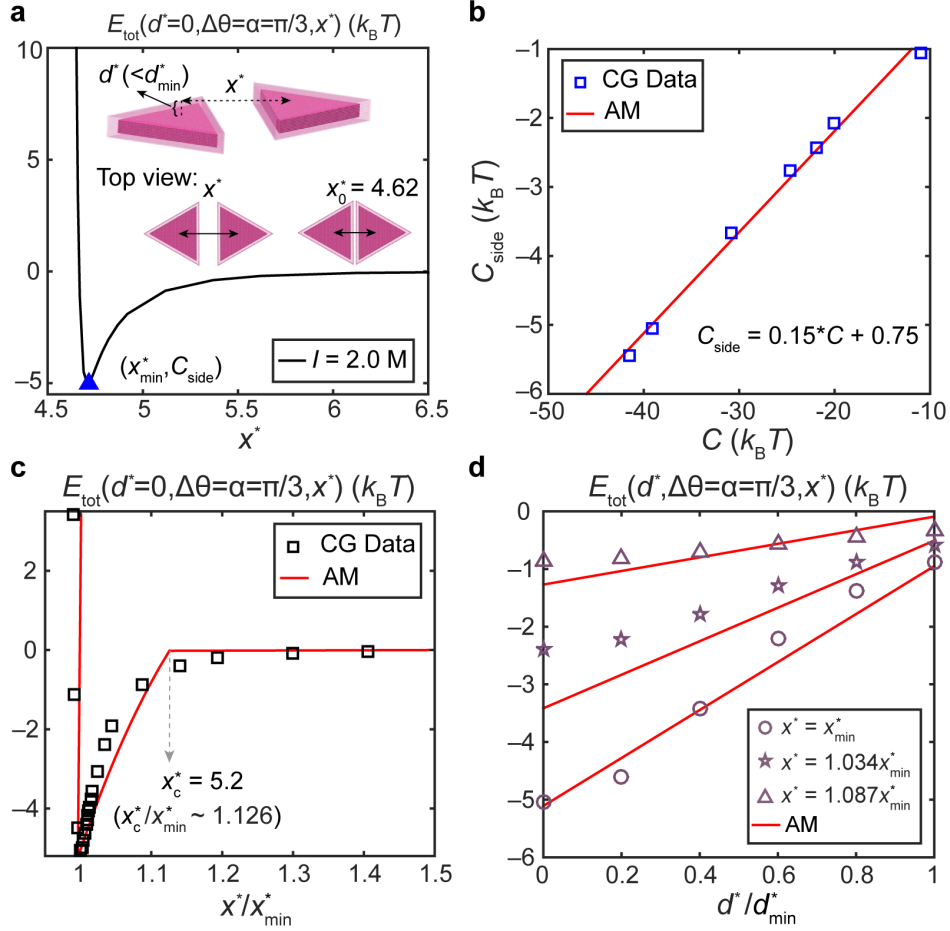
Figure 2.9. Attractive part of pairwise interaction energy E_{tot} in the analytical model for a pair of parallel prisms in side-by-side configuration. (a) Pairwise interaction energy E_{tot} between two parallel prisms arranged in side-by-side fashion ($\Delta\theta = \alpha = \pi/3$) with zero vertical separation ($d^* = 0$), as a function of horizontal displacement magnitude x^* computed using the CG model at ionic strength $I = 2.0$ M. The equilibrium distance $x^*_{\min}$ and side-by-side interaction energy minimum C_{side} are identified in the plot. Inset: Schematic of a typical side-by-side configuration of two parallel prisms and definition of x^*_0 denoting the centre-to-centre distance between two fully attached side-by-side prisms. (b) Relationship between the side-by-side energy minimum C_{side} and the coupling constant C measured from the CG model (blue squares), described by a linear fit that we employ in the analytical model (solid red line). (c) Pairwise energy E_{tot} between two side-by-side ($\Delta\theta = \alpha = \pi/3$) parallel prisms with zero vertical separation ($d^* = 0$) as a function of the reduced horizontal displacement $x^*/x^*_{\min}$ at $I = 2.0$ M. Black squares are the data from the CG model and the red line is the fit function Eq. 2.11 combined with the excluded-volume repulsion $E_{\text{tot}}(d^* = 0, \Delta\theta = \alpha = \pi/3, x^* < x^*_{\min}) = +\infty$. (d) Pairwise energy between two side-by-side ($\Delta\theta = \alpha = \pi/3$) parallel prisms as a function of the reduced vertical separation $d^*/d^*_{\min}$ at three different values of x^* ($x^*_{\min}$: circle; $1.034x^*_{\min}$: star; $1.087x^*_{\min}$: triangle) at $I = 2.0$ M. Symbols represent the CG model, fitted by the linear function of d^*, Eq. 2.13 (solid red lines).

illustration purposes. Fig. 2.9c shows E_{tot} versus reduced distance x^*/x^*_{min} ($x^*_{\text{min}} = x^*_0$ in the analytical model, as discussed above) for this case, where the squares represent the data from the CG model. The short-range repulsive part of E_{tot} at $x^* < x^*_{\text{min}}$ is well described by the excluded-volume repulsion (vertical red line at $x^* = x^*_{\text{min}}$). We approximate the attractive part of the total energy at $x^* \geq x^*_{\text{min}}$ via $E_{\text{tot}}(d^* = 0, \Delta\theta = \alpha = \pi/3, x^*) = Y/x^{*4} + Z$, with Y and Z to be determined from the boundary conditions at $x^* = x^*_{\text{min}}$ and at the cutoff $x^* = x^*_c$,

$$
\begin{cases}
E_{\text{tot}}(d^* = 0, \Delta\theta = \alpha = \pi/3, x^* = x^*_{\text{min}}) = Y/x^{*}_{\text{min}}{}^4 + Z \\
\qquad\qquad\qquad\qquad\qquad = C_{\text{side}} = 0.15 \cdot C + 0.75 \\
E_{\text{tot}}(d^* = 0, \Delta\theta = \alpha = \pi/3, x^* = x^*_c) = Y/x^{*4}_c + Z = 0 \qquad (x^*_c = 5.2)
\end{cases}
. \quad (2.10)
$$

For simplicity, the cutoff distance is chosen as $x^*_c = 5.2$ for all ionic strengths (the same as the face-to-face case when $\Delta\theta = \alpha = \pi/3$, see Section 2.5.2.1 Part C). Equation 2.10 yields $Y = C_{\text{side}} x^{*}_{\text{min}}{}^4 x^{*4}_c/(x^{*4}_c - x^{*}_{\text{min}}{}^4)$ and $Z = -C_{\text{side}} x^{*}_{\text{min}}{}^4/(x^{*4}_c - x^{*}_{\text{min}}{}^4)$. Thus, in the analytical model the attractive part of the pairwise interaction energy for the side-by-side configuration ($\Delta\theta = \alpha = \pi/3$) at $d^* = 0$ as a function of x^* is

$$
\begin{aligned}
E_{\text{tot}}(d^* = 0, \Delta\theta = \alpha = \pi/3, x^* \geq x^*_{\text{min}}) &= \frac{x^{*}_{\text{min}}{}^4}{x^{*4}_c - x^{*}_{\text{min}}{}^4} \left(\frac{x^{*4}_c}{x^{*4}} - 1\right)(0.15 \cdot C + 0.75) \\
&= \frac{x^{*4}_0}{x^{*4}_c - x^{*4}_0} \left(\frac{x^{*4}_c}{x^{*4}} - 1\right)(0.15 \cdot C + 0.75)
\end{aligned}, \quad (2.11)
$$

where $x^*_c = 5.2$. Fig. 2.9c shows this expression (solid red curve), with $x^*_{\text{min}} = x^*_0$.

B. Dependence of interaction energy on vertical separation d^*

The pairwise interaction energy E_{tot} for side-by-side configuration vs. the vertical separation d^* is plotted in Fig. 2.9d for different values of the horizontal distance x^* at $I = 2.0$ M.

Since the CG data (symbols) exhibit a fairly linear dependence on d^*, we approximate it as

$$E_{\text{tot}}(d^*, \Delta\theta = \alpha = \pi/3, x^*) = d^* E_{\text{tot}}(d^* = 1, \Delta\theta = \alpha = \pi/3, x^*)$$

$$+ (1 - d^*) E_{\text{tot}}(d^* = 0, \Delta\theta = \alpha = \pi/3, x^*) , \tag{2.12}$$

where $E_{\text{tot}}(d^* = 1, \Delta\theta = \alpha = \pi/3, x^*)$ follows from Eq. 2.9 in the face-to-face case and $E_{\text{tot}}(d^* = 0, \Delta\theta = \alpha = \pi/3, x^*)$ from Eq. 2.11. The curves for this analytical model are plotted in Fig. 2.9d (solid red curves), showing an overall good agreement.

Thus, we obtain the general form of the attractive part of the pairwise total energy between two side-by-side parallel prisms ($\Delta\theta = \alpha = \pi/3$) with vertical separation d^* (< 1) and horizontal distance x^* ($\geq x^*_{\min}$),

$$E_{\text{tot}}(d^*, \Delta\theta = \alpha = \pi/3, x^* \geq x^*_{\min}) = d^* \frac{C - (0.23 \cdot C + 1)}{2} \left(1 + \cos\frac{\pi x^*}{x^*_{\text{c}}} \right)$$

$$+ (1 - d^*) \frac{x^{*4}_0}{x^{*4}_{\text{c}} - x^{*4}_0} \left(\frac{x^{*4}_{\text{c}}}{x^{*4}} - 1 \right) (0.15 \cdot C + 0.75) , \tag{2.13}$$

where $x^*_{\text{c}} = 5.2$ and the only control parameter is the coupling constant C (or the ionic strength I).

2.5.2.3. Summary of the analytical functional forms for the pairwise interaction energy between two parallel prisms.

Based on the pairwise interactions for face-to-face (Section 2.5.2.1) and side-by-side (Section 2.5.2.2) configurations, the pairwise total energy between two *parallel* prisms with vertical separation d^*, horizontal centre-to-centre distance x^*, spin-angle difference $\Delta\theta$ and horizontal relative direction α can be fully described by the volume exclusion of the prisms

plus the analytical function $E_{\text{tot}}(d^*, \Delta\theta, \alpha, x^*)$,

$$
\begin{cases}
\approx E_{\text{tot}}(d^*, \Delta\theta = \alpha = \pi/3, x^*) \\[4pt]
\quad = \dfrac{d^*[C - (0.23 \cdot C + 1)]}{2}\left(1 + \cos\dfrac{\pi x^*}{x_{\text{c}}^*(\pi/3, \pi/3)}\right) \\[10pt]
\quad + (1 - d^*)\dfrac{x_0^{*4}\left(x_{\text{c}}^*(\pi/3, \pi/3)^4 - x^{*4}\right)}{\left(x_{\text{c}}^*(\pi/3, \pi/3)^4 - x_0^{*4}\right)x^{*4}}(0.15 \cdot C + 0.75) & (x^* \le x_{\text{c}}^*, 0 \le d^* < 1) \\[12pt]
= \dfrac{2 \cdot C - (0.23 \cdot C + 1)(1 - \cos(3\Delta\theta))}{4d^{*4}}\left(1 + \cos\dfrac{\pi x^*}{x_{\text{c}}^*(\alpha, \Delta\theta)}\right) & (x^* \le x_{\text{c}}^*, 1 \le d^* \le d_{\text{c}}^*) \\[12pt]
= 0 & (x^* > x_{\text{c}}^* \text{ or } d^* > d_{\text{c}}^*)
\end{cases}
$$

$$(2.14)$$

where the coupling constant C (which is also the global energy minimum for face-to-face configurations) is the only control parameter, directly related to the ionic strength I. The cutoff distance x_{c}^* is assigned based on the rule introduced in Section 2.5.2.1 (Part C). For computational efficiency, the cutoff for the vertical separation is set to the fairly small value $d_{\text{c}}^* = 3.0$ (i.e., $E_{\text{tot}}(d^* > d_{\text{c}}^*, \Delta\theta, x^*, \alpha) = 0$). This is justified by the d^{*-4} decay of E_{tot} versus d^* and guarantees a relative error of less than 1.2%.

2.5.2.4. Generalisation of the analytical model to nonparallel pairs and the approximations being made.

The analytical forms presented in Section 2.5.2.3 apply to prisms that are nearly parallel. For nonparallel prism pairs, there are additional degrees of freedom to be taken into account. However, due to the short-range character of the interactions (e.g., the cutoff distance for the vertical separation $d_{\text{c}}^* = 3.0$), two prisms within the same column must be very close and almost parallel to have a nonzero pairwise interaction. In addition, the attraction between prisms and the substrate (see Section 2.5.3) promotes the vertical growth of columns on the substrate, so that most prisms are nearly parallel with each other and with the substrate.
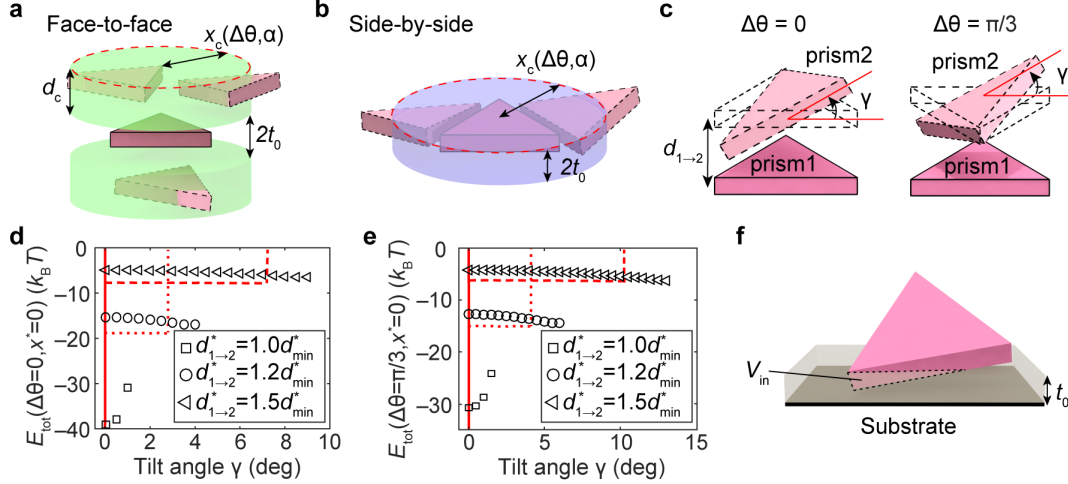
Figure 2.10. Schematic summarising the interaction zone of two interacting prisms and the dependence of interaction energy on tilt angle γ. (a–b) Schematics showing the interaction zone of face-to-face (a) and side-by-side (b) configurations, outside which the pairwise interaction is zero in our analytical model. Here the central prism (prism1, with solid border) interacts with all almost parallel (as defined in the text) prisms (prism2, with dashed border) whose centres are located inside the (a) green or (b) purple regions. d_c denotes the cutoff distance for the vertical separation, which we set to $d_c = 3t_0$ for computational efficiency (see Section 2.5.2.3 for details). Note that the cutoff for the horizontal displacement x_c varies with the angles $\Delta\theta$ and α (see Section 2.5.2.1 Part C for details) and is plotted here as a constant just for visual clarity. (c) Configurations used to examine the effect of tilt angle γ in panels d and e: $\Delta\theta = 0$ (left) and $\Delta\theta = \pi/3$ (right). (d–e) Dependence of pairwise interaction energy E_{tot} on tilt angle γ between two coaxial prisms with spin-angle difference (d) $\Delta\theta = 0$ and (e) $\Delta\theta = \pi/3$ at $I = 2.0$ M. Black symbols are calculated from the CG model and red lines represent the analytical model Eq. 2.15. Three different vertical separations with respect to prism1 are investigated, $d^*_{1\to2} = d^*_{\min}$ (open square, solid line), $d^*_{1\to2} = 1.2d^*_{\min}$ (open circle, dotted line) and $d^*_{1\to2} = 1.5d^*_{\min}$ (open triangle, dashed line). (f) Schematics of the prismsubstrate interaction, showing the overlap volume V_{in} between a prism and the substrate interaction zone.

Therefore, we impose in our analytical model that two prisms have nonzero interaction energy only if $|\hat{\mathbf{n}}_A \cdot \hat{\mathbf{n}}_B| > 0.95$, where $\hat{\mathbf{n}}_A$ and $\hat{\mathbf{n}}_B$ are the normal vectors of the two prisms, respectively. This requirement in the analytical model promotes nematic order of the system and artificially lowers the probability of certain rare nonequilibrium configurations, e.g., face-to-edge arrangements, but does not affect equilibrium configurations. For near-parallel prisms,

the interaction zone around a central prism in the analytical model is shown in Fig. 2.10a,b for face-to-face and side-by-side configurations, respectively. The combined interaction zone (green and purple regions) around the central prism appears as an approximately cylindrical shape due to the simplification (in the schematic only) that x_c^* is a constant. Since x_c^* varies with $\Delta\theta$ and α, the actual contour is considerably more complicated. As mentioned at the beginning of Section 2.5.2 and shown in Fig. 2.7a, a pair of non-parallel prisms (i and j) has unequal interaction parameters when i and j are exchanged, i.e., the pairs $d_{i\to j}^*$ and $d_{j\to i}^*$; $\Delta\theta_{i\to j}$ and $\Delta\theta_{j\to i}$; $\alpha_{i\to j}$ and $\alpha_{i\to j}$; and $x_{i\to j}^*$ and $x_{j\to i}^*$ are not identical. To eliminate this geometric asymmetry, we employ their average as the true pairwise interaction energy,

$$E_{\text{tot}}^{ij} = \frac{1}{2}\left[E_{\text{tot}}(d_{i\to j}^*, x_{i\to j}^*, \Delta\theta_{i\to j}, \alpha_{i\to j}) + E_{\text{tot}}(d_{j\to i}^*, x_{j\to i}^*, \Delta\theta_{j\to i}, \alpha_{j\to i})\right] , \tag{2.15}$$

where $E_{\text{tot}}(d_{i\to j}^*, x_{i\to j}^*, \Delta\theta_{i\to j}, \alpha_{i\to j})$ and $E_{\text{tot}}(d_{j\to i}^*, x_{j\to i}^*, \Delta\theta_{j\to i}, \alpha_{j\to i})$ are defined in Eq. 2.14.

Lastly, we examine the validity of restricting pairwise attractions to near-parallel prisms. The requirement $|\hat{\mathbf{n}}_A \cdot \hat{\mathbf{n}}_B| > 0.95$ corresponds to tilt angles $\gamma < 18.2°$. For two coaxial cases, $\Delta\theta = 0$ and $\Delta\theta = \pi/3$ (Fig. 2.10c), we compute the pair potential from the CG model as a function of tilt angle at different separations $d_{1\to 2}^*$ (Fig. 2.10d,e). The data from the CG model (symbols) agree fairly well with the analytical model Eq. 2.15 (red lines). Note that at each value for $d_{1\to 2}^*$, beyond a certain tilt angle γ the interaction energy increases sharply due to the strong electrostatic repulsion (CG model) or the excluded-volume interactions (analytical model). In particular, at $d_{1\to 2}^* = d_{\min}^* = 1$ no tilting is permitted in the analytical model.

2.5.3. Prism–substrate interaction employed in Monte Carlo simulations

As reported earlier[88] and also observed in the present work, there is a short-range attraction between the substrate and the prisms. Since prisms attracted to the surface are greatly confined in their motion, the substrateprism attraction plays an important role in templating the assembly of the final hierarchical lattice and promoting the vertical growth of stacks of prism (see Fig. 2.1d–g).

We model this prismsubstrate interaction via an attractive square-well potential with range t_0 from the substrate (Fig. 2.10f). Thus, the interaction energy E_{PS} is proportional to the overlap volume between the prism and the interaction zone (V_{in} in Fig. 2.10f), $E_{PS} = E_0 V_{in}/V_\Delta$, where $E_0 < 0$ is a constant and $V_\Delta = 16\sqrt{3}t_0^3$ is the total volume of the prism including the coated ligands (i.e., the volume of the prism in the analytical model). Setting the magnitude of E_0 too large will result in prisms first fully covering the entire substrate before forming columns, whereas a too small value will not lead to vertical columns, in contradiction to the experimental observations. Thus, we choose $E_0 = C/2$, where C is the minimum of the prism–prism interaction.

2.5.4. Large-scale Monte Carlo simulations of hierarchical assembly

2.5.4.1. Simulation methods.

Monte Carlo (MC) simulations are conducted of systems of M_{tot} triangular prisms in a rectangular simulation box in the canonical ensemble. The system is periodic in x and y directions, but finite along the z-axis to make it consistent with the experimental setup. The aspect ratio of the box is chosen to be $L_x : L_y = 2 : \sqrt{3}$, which ensures that the target crystal structure (hexagonal lattice) will not be forbidden by the periodic boundary conditions in

the $x - y$ plane[89]. All prisms have pairwise interactions described by the analytical model in Section 2.5.2, Eqs. 2.14 to 2.15. For the excluded-volume interactions, overlapping prisms are detected via the Möller–Trumbore raytriangle interaction algorithm[90].

Each simulation runs for 10^7 MC cycles for equilibration and then another 10^7 MC cycles for production, where a cycle consists of M_{tot} MC moves. In each MC move, a prism is randomly picked for a translation, rotation or spin with respective probabilities 0.4, 0.3 and 0.3. In a rotation, the normal vector of the prism face is rotated to a trial orientation generated by adding a randomly oriented vector with magnitude α_{r} to the original normal vector. Thus, α_{r} controls the maximum range of the rotational motion. A spin refers to rotation of the prism around its normal vector within the range $[-\alpha_{\text{s}}, \alpha_{\text{s}}]$. During the equilibration process, α_{r} and α_{s}, as well as the maximum displacement of the translational move α_{t}, are adjusted after every cycle to maintain an acceptance rate of 20%.

The initial configuration of the system consists of $N_{\text{col}} = 64$ columns organised on a 2D square lattice in order to accelerate the assembly of individual prisms into columns. There are M prisms inside each column, where M is determined by L_z to achieve an average spacing L_z/M of $1.1t_0$. We use $M_{\text{tot}} = N_{\text{col}} \cdot M$ to denote the total number of prisms. Note that the columns are free to disassemble or rearrange themselves during the equilibration cycles. To ensure that the equilibrium structure does not depend on the initial configuration, we also perform simulations starting from more random initial configurations, where the system is composed of M layers within which prisms are randomly distributed and oriented within $x - y$ plane. After a longer equilibration time, such systems arrive at the same final structure as those started from a square-lattice initial configuration.

Since the packing density along the z-axis is controlled by the confinement and does not influence the 2D structural order, we use the 2D packing fraction to describe the concentration of the columns. ϕ_{2D} is defined as the 2D packing faction $\phi_{2D} = N_{\text{col}} \cdot A_\Delta / (L_x L_y)$, where A_Δ is the area of the face of a prism and $N_{\text{col}} = 64$ in all simulations (ϕ_{2D} is varied from 0.29 to 0.5 which is realised by varying L_x). At each ϕ_{2D}, we vary both the height of the simulation box L_z from $10t_0$ to $25t_0$ (with M and M_{tot} being automatically determined) and the ionic strength I from 0.44 to 3.0 M (by varying C in the model). The parameters used in the large-scale simulations are listed in Table 2.1, in which there are three independent variables: ionic strength I, height of the simulation box L_z and the 2D packing fraction ϕ_{2D}.

Table 2.1. Parameters used in the large-scale Monte Carlo simulations.

Parameter 1	I (M)	0.44	0.52	0.65	0.76	0.98	1.44	2.25	3.00
	$C(k_{\text{B}}T)$	-20	-22	-25	-27	-30	-35	-40	-43
Parameter 2	$L_z(t_0)$	10		15		20		25	
	M	9		14		18		23	
	M_{tot}	576		896		1152		1472	
Parameter 3	$L_x(t_0)$	64.4	66.4	68.2	68.8	69.4	71.2	72.0	72.8
		73.6	74.4	75.2	76.0	79.2	84.0		
	ϕ_{2D}	0.494	0.465	0.440	0.433	0.425	0.404	0.395	0.386
		0.378	0.370	0.362	0.355	0.327	0.290		

2.5.4.2. Characterisation of orientational order of a single column.

To quantify the in-plane (i.e., $x-y$) orientational order of the M prisms within a column, we define the orientational order parameter $S_\theta = \max_{\theta_0} \frac{1}{M} \sum_{i=1}^{M} \cos[3(\theta_i - \theta_0)]$, where θ_i denotes the in-plane spin angle (i.e., the angle between the projection of the orientation vector of the prism on the $x-y$ plane and the x axis) of prism i and $\hat{\mathbf{n}} = (\cos\theta_0, \sin\theta_0)$ is the global director for triatic phases. S_θ follows the conventional definition of the triatic order parameter of 2D liquid-crystalline phases due to the three-fold symmetry of triangular prisms. In particular, $S_2 = \max_{\theta_0} \frac{1}{M} \sum_{i=1}^{M} \cos[2(\theta_i - \theta_0)]$ and $S_4 = \max_{\theta_0} \frac{1}{M} \sum_{i=1}^{M} \cos[4(\theta_i - \theta_0)]$ measure

the degree of nematic and tetratic ordering of 2D systems[81]. S_θ ranges from 0, corresponding to an orientationally disordered (randomly misaligned) state, to 1, corresponding to a fully ordered (perfectly aligned) state. The calculation of S_θ can be easily converted to an eigenvalue problem by rewriting it as

$$
\begin{aligned}
S_\theta &= \max_{\theta_0} \frac{1}{M} \sum_{i=1}^{M} \left(2\cos^2\left[\frac{3}{2}(\theta_i - \theta_0)\right] - 1 \right) \\
&= \max_{\theta_0} \frac{1}{M} \sum_{i=1}^{M} \left[2\left(\cos^2\frac{3\theta_i}{2}\cos^2\frac{3\theta_0}{2} + \sin^2\frac{3\theta_i}{2}\sin^2\frac{3\theta_0}{2} + 2\cos\frac{3\theta_i}{2}\cos\frac{3\theta_0}{2}\sin\frac{3\theta_i}{2}\sin\frac{3\theta_0}{2} \right) - 1 \right]. \\
&= \max_{\theta_0} \frac{1}{M} \sum_{i=1}^{M} \left(\cos\frac{3\theta_0}{2}, \sin\frac{3\theta_0}{2} \right) \begin{pmatrix} \cos 3\theta_i & \sin 3\theta_i \\ \sin 3\theta_i & -\cos 3\theta_i \end{pmatrix} \begin{pmatrix} \cos\frac{3\theta_0}{2} \\ \sin\frac{3\theta_0}{2} \end{pmatrix}
\end{aligned}
$$

$$(2.16)$$

If $\hat{\mathbf{n}}'$ denotes the vector $\left(\cos\frac{3\theta_0}{2}, \sin\frac{3\theta_0}{2}\right)$ and $Q = \frac{1}{M}\sum_{i=1}^{M}\left(\begin{smallmatrix} \cos 3\theta_i & \sin 3\theta_i \\ \sin 3\theta_i & -\cos 3\theta_i \end{smallmatrix}\right)$ is the ordering matrix, we obtain the simplified expression $S_\theta = \max_{\hat{\mathbf{n}}'}\left\{\hat{\mathbf{n}}' \cdot Q \cdot \hat{\mathbf{n}}'^T\right\}$. Thus, S_θ is just the largest eigenvalue of the ordering matrix Q, and the director $\hat{\mathbf{n}} = (\cos\theta_0, \sin\theta_0)$ can be obtained from $\left(\cos\frac{3\theta_0}{2}, \sin\frac{3\theta_0}{2}\right) = \hat{\mathbf{n}}_0$, where $\hat{\mathbf{n}}_0$ is the normalised eigenvector corresponding to S_θ. The average columnar orientational order of the system of multiple columns is denoted by $\langle S_\theta \rangle$, where the angular brackets indicate an average over all columns.

The orientational structure of a column can also be quantified by the orientational correlation function $G_3(m) = \langle\cos\left[3(\theta_i - \theta_{i+m})\right]\rangle_i$, quantifying the average orientational correlation between prism i and its $m^t h$-nearest neighbour within the same column. Fitting $G_3(m)$ with e^{-m/l_c} yields the decay length l_c.

2.5.4.3. Characterisation of crystal structure in simulations.

To describe the 2D hexagonal order of the columns we first detect and locate each column. Prisms are considered to belong to the same column if their centre-to-centre distance in the $x - y$ plane lies within a certain cutoff. We find that a cutoff of $50/\sqrt{3}$ nm maximises the accuracy. The center position of the column in the $x - y$ plane is calculated by averaging the $x - y$ centre position of each constituent prism. The local hexagonal order of the columns is quantified by the squared modulus of the six-fold bond-orientation order parameter $|\psi_{6j}|^2$. The cutoff distance used to determine the bonded neighbours is the position of the first minimum after the first peak of the radial distribution function $g(r)$ of the columns. The global bond-orientation order parameter Ψ_6^{AV} is given by

$$\Psi_6^{\text{AV}} = \langle \frac{1}{N_{\text{col}}} \sum_{j=1}^{N_{\text{col}}} \psi_{6j} \rangle \, , \tag{2.17}$$

where the angular brackets indicate the time average. The square of the absolute value of the bond-orientation order parameter $|\Psi_6^{\text{AV}}|^2$ is used to characterise the 2D global structural order of the system[89].

The 3D translational order of the prisms is characterised by the diffraction patterns in Fig. 2.1c and Fig. 2.4d, which were generated by computing the structure factor,

$$S(\mathbf{q}) = \frac{1}{M_{\text{tot}}} \langle \sum_{j=1}^{M_{\text{tot}}} \sum_{k=1}^{M_{\text{tot}}} e^{-i\mathbf{q} \cdot (\mathbf{R}_j - \mathbf{R}_k)} \rangle \, , \tag{2.18}$$

where $\mathbf{R}_j$ is the position vector of the center of prism j and the angular brackets denote the temporal average.

The translational order of the prisms along the z axis is characterised by (i) the structure factor $S(q_z) = \langle \sum_{j=1}^{M_{\text{tot}}} \sum_{k=1}^{M_{\text{tot}}} e^{-iq_z(z_j - z_k)} \rangle / M_{\text{tot}}$, where z_j denotes the z coordinate of the centre of prism j, and (ii) the volume fraction profile along the z axis. The latter is defined
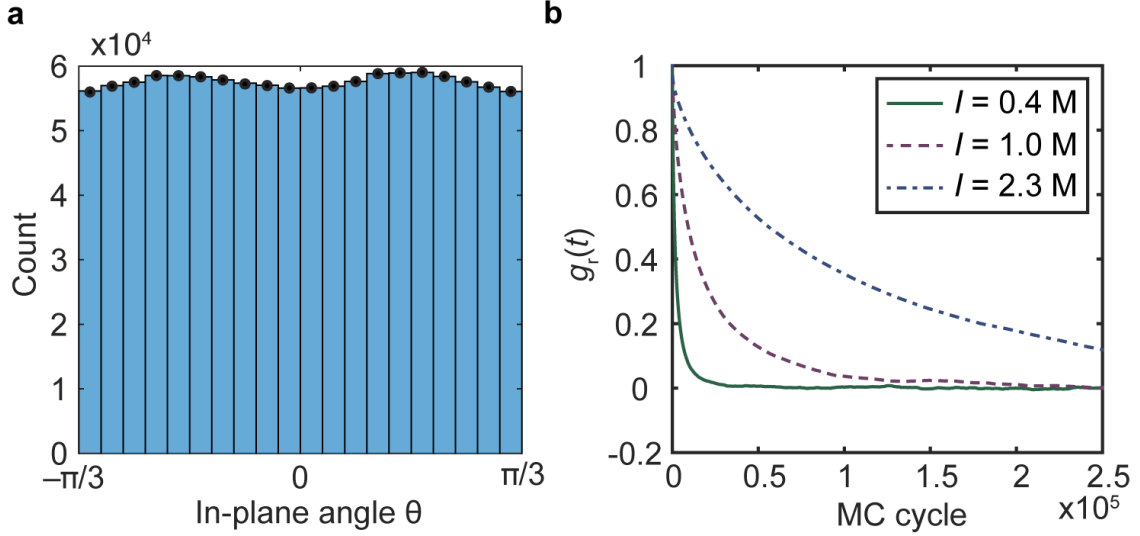
Figure 2.11. In-plane angle distribution and rotational dynamics of the system after reaching equilibrium. (a) Histogram of the in-plane angle θ of each prism measured over the production runs (1000 samples of 1152 prisms). (b) Orientational autocorrelation function $g_r(t)$ at different ionic strengths.

as the ratio between the volume fraction of prisms whose centres lie in a horizontal slab of volume $L_x L_y \Delta z$ between z and $z + \Delta z$ and the overall volume fraction. This ratio can be written as $\phi(z)/\phi = \langle M(z)V_\Delta/(L_x L_y \Delta z)\rangle/\phi = \langle M(z)L_z/(M_{\text{tot}}\Delta z)\rangle$, where $M(z)$ represents the number of prisms whose centres are located between z and $z + \Delta z$ and V_Δ is the volume per prism. We choose $\Delta z = 0.2t_0$.

2.5.4.4. Analysis of single-prism rotational motion from the large-scale simulations.

As shown in Section 2.3.3 (Fig. 2.4d,e), the final assembled lattice is orientationally disordered. Figure 2.11a shows a histogram of the in-plane angle θ of all prisms in the equilibrated hierarchical lattice, consistent with our observation of orientational randomness. The minor variation (peaks) in the histogram originate from the spatial symmetry of the hexagonal lattice, which makes certain orientations $(\pm\pi/6)$ slightly more favourable

in a rectangular simulation cell with periodic boundary conditions. The temporal decay of orientational order can be derived from the orientational autocorrelation function $g_{\mathrm{r}}(t) = \langle \frac{1}{M_{\mathrm{tot}}} \sum_{i=1}^{M_{\mathrm{tot}}} \hat{\mathbf{u}}_i(t_0) \cdot \hat{\mathbf{u}}_i(t_0 + t) \rangle_{t_0}$, where $\hat{\mathbf{u}}_i(t)$ is the unit vector that defines the in-plane orientation of prism i at the instance t and the angular brackets denote the ensemble average. Figure 2.11b illustrates that $g_{\mathrm{r}}(t)$ decays more slowly at higher ionic strength, due to the strong orientational correlation between prisms within the same column.

2.5.4.5. Dependence of 2D hexagonal order on 2D packing fraction.

Within the range of packing fractions examined ($0.362 \leq \phi_{\mathrm{2D}} \leq 0.433$), the correlation between the global hexagonal order parameter $|\Psi_6^{\mathrm{AV}}|^2$ and the average columnar orientational order $\langle S_\theta \rangle$ is described by a master curve (Fig. 2.4g). In Fig. 2.12a,b we illustrate that 2D packing fractions outside this range will suppress the hexagonal order, regardless of $\langle S_\theta \rangle$. In both regimes, $|\Psi_6^{\mathrm{AV}}|^2$ is consistently smaller than 0.5, even at small $\langle S_\theta \rangle$. At lower packing fractions, no crystallisation takes place, whereas higher packing fractions can only be attained for columns consisting of aligned prisms, which then can only crystallise into a honeycomb lattice (if ϕ_{2D} is sufficiently high). The effects of packing fraction on the columnar orientational order $\langle S_\theta \rangle$ are discussed in Section 2.5.5.5 below.

2.5.4.6. Consistency between modelling/simulations and experiments.

The MC simulations presented are consistent with the liquid-phase TEM experiments on the following levels. First, the pairwise interaction modelled in the simulation correctly predicts the equilibrium inter-prism spacing in the columns measured in experiments at different ionic strengths (Fig. 2.6d). Second, on the column level, the prism misalignment in columns given as the equilibrium structure by MC matches the TEM images (Fig. 2.1e). Third, the computed inter-column interaction strength in the simulations matches the line
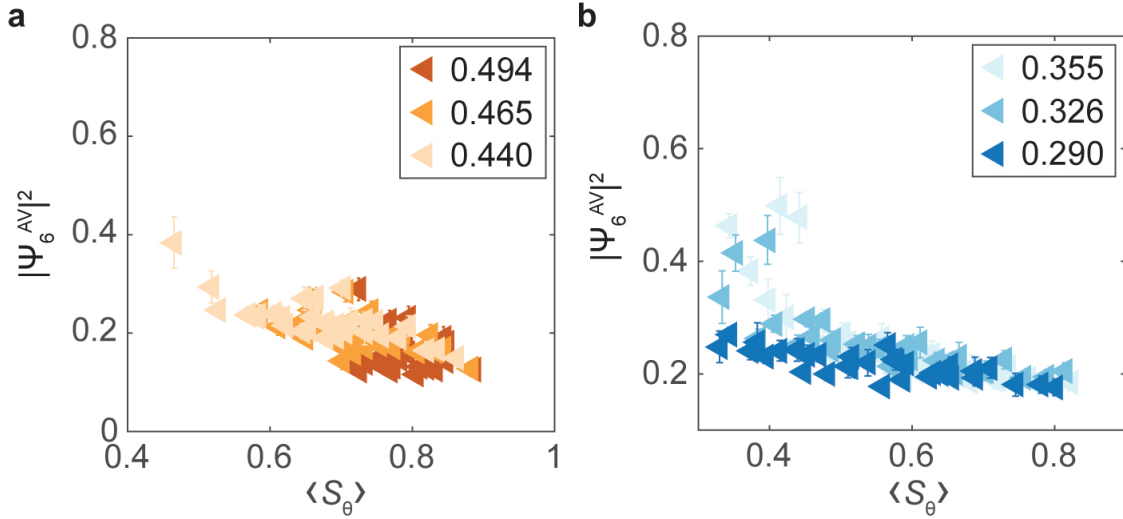
Figure 2.12. Dependence of global 2D hexagonal order on column packing fraction. Correlation between the average global hexagonal order characterised by $|\Psi_6^{\mathrm{AV}}|^2$ and the average columnar orientational order $\langle S_\theta \rangle$ at (a) high and (b) low 2D packing fraction $\phi_{2\mathrm{D}}$.

tension obtained from the cluster analysis in the experiments. Last, the equilibrium (hexagonal) crystal phase observed in the large-scale simulations matches our experimental imaging (Fig. 2.1b,c).

2.5.5. Single-column Monte Carlo simulations of column orientational order

2.5.5.1. Simulation methods.

To understand the energetics driving column formation, we examine the dependence of the orientational structure of a single column on the ionic strength I and the number of constituent prisms M. Thus, we perform single-column simulations, where the centre positions of the prisms are fixed and only spin motion around the z axis is allowed, i.e., $\alpha_{\mathrm{t}} = \alpha_{\mathrm{r}} = 0$ and $\alpha_{\mathrm{s}} = 1$. For simplicity, we simulate the most common case where the prisms are coaxial, equally spaced and parallel to the $x - y$ plane. For consistency with the large-scale simulations, we vary the confinement L_z along the z direction from $10t_0$ to

$25t_0$, choosing M to set the spacing L_z/M to $1.1t_0$. We set L_x and L_y large enough to avoid interactions between periodic images.

2.5.5.2. Helmholtz free-energy calculation in single-column simulations.

We calculate the Helmholtz free energy F, scaled entropy TS and interaction energy E of a single column as a function of the orientational order parameter S_θ. The free energy $F(S_\theta)$ is obtained from the distribution $P(S_\theta)$ of S_θ, since $P(S_\theta) \propto e^{-F(S_\theta)/k_B T}$, i.e., $F(S_\theta) = -k_B T \ln(P(S_\theta)) + \text{const}$. The additive constant is only related to the choice of the reference state. Computation of the interaction energy $E(S_\theta)$ then yields the entropic contribution $TS(S_\theta) = E(S_\theta) - F(S_\theta)$. Although this does not provide the absolute entropy, it permits calculation of free-energy barriers.

We apply this approach to two cases: a short column at high ionic strength (Fig. 2.13a) and a tall column at low ionic strength (Fig. 2.13b). Due to competition between the entropy favouring low S_θ and the interaction energy which is minimised when the prisms are perfectly aligned, the free-energy minimum is located at very different values of S_θ for these two cases, confirming that the orientational order of the column is controlled by both ionic strength and the number constituent prisms.

Owing to the small size of either column, the free-energy well is rather shallow and broad, resulting in large fluctuations in S_θ. Moreover, it is important to note that the orientational order of the columns in the large-scale (many-column) system is also affected by the intercolumn interaction and column packing fraction ϕ_{2D} (see Section 2.5.5.5 for a comparison of single-column and large-scale simulations). In particular, for the large-scale system at the same condition as in Fig. 2.13a, the columns are more aligned and fluctuate less (cf. Fig. 2.4b) than in the single-column simulations due to strong lateral attractions between columns.
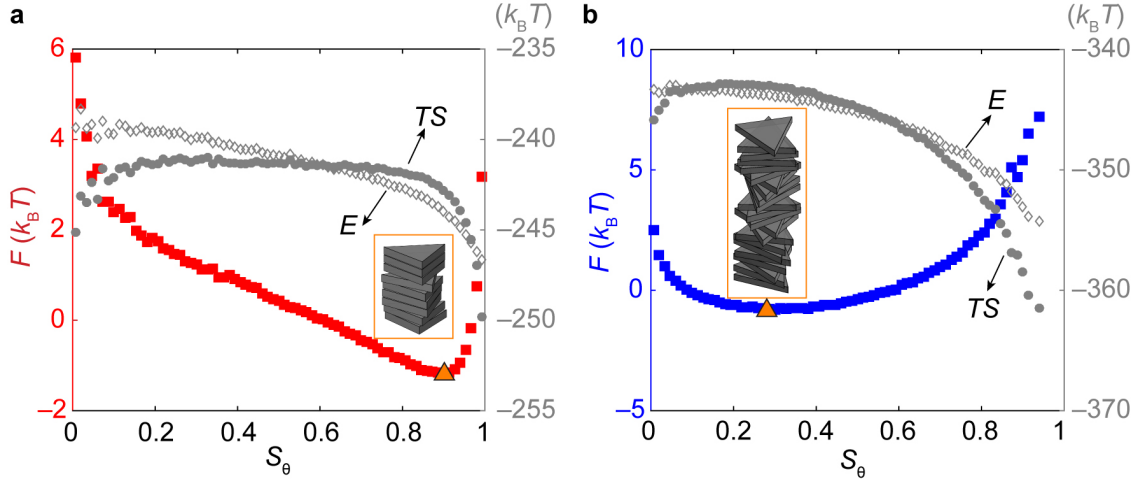
Figure 2.13. Free-energy curve of a single column at the two different conditions discussed in Fig. 2.4b–f. Free energy F (left axis), entropic contribution TS (right axis), and total interaction energy E (right axis) computed from single-column simulations as a function of the column orientational order parameter S_θ at (a) $M = 9, L_z^* = 10$, and $I = 3.0$ M, and (b) $M = 23, L_z^* = 25$, and $I = 0.5$ M. (Insets) Snapshots of typical configurations at the thermodynamic equilibrium state (orange triangle).

A noteworthy point is that the maximum of the entropy curve in Fig. 2.13 is not located at $S_\theta = 0$, the orientationally isotropic state. The reason is that the eigenvalues of the ordering matrix Q (cf. Eq. 2.16) are dependent on the number of constituting prisms M. As reported previously[91], for an orientationally isotropic system, the largest eigenvalue of Q, which we define as S_θ, decays to zero as $1/\sqrt{M}$. Therefore, for the small systems considered here with number of prisms between 9 and 23, the computed S_θ is nonzero even for a perfectly isotropic column, leading to the entropy maximum at a nonzero value. Therefore, S_θ can give a better estimation of the orientational order when the column is in a more ordered phase or the number of prisms is large.

2.5.5.3. Dependence of columnar orientational order on ionic strength.

The ionic strength I determines the pairwise interaction profile versus $\Delta\theta$ between two coaxial parallel prisms (Fig. 2.14a), and thus affects the relative rotational range quantified
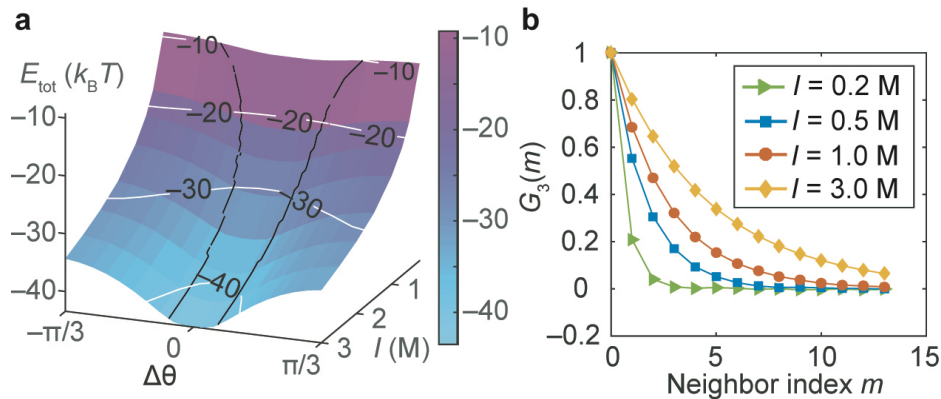
Figure 2.14. Dependence of orientational structure on ionic strength. (a) Total pairwise energy E_{tot} between two parallel and coaxial prisms with minimum-energy separation $d_{\min}$, computed in the CG model and plotted versus $(\Delta\theta, I)$. Black lines mark the $[-\Delta\theta_c, \Delta\theta_c]$ interval upon variation of ionic strength I. (b) Orientational correlation function $G_3(m)$ of an individual column with $M = 27$ and $L_z^* = 30$ at four different ionic strengths.

by $\Delta\theta_c$ (defined in Fig. 2.2c). At low ionic strength, the two prisms have more relative rotational freedom (larger $\Delta\theta_c$). This dependence on ionic strength propagates along the column once prisms are stacked into a column, and thus affects the orientational order of the column. Figure 2.14b confirms that the orientational correlation function $G_3(m)$ of an individual column decays faster at lower ionic strength, indicating a more disordered column as a result of larger $\Delta\theta_c$.

2.5.5.4. Dependence of column orientational order on the number of constituent prisms.

From single column simulations, a random-walk model has been presented to illustrate the dependence of the orientational order on the number of prisms inside the column as shown in Fig. 2.15.

2.5.5.5. Connection between large-scale simulations and single-column simulations.
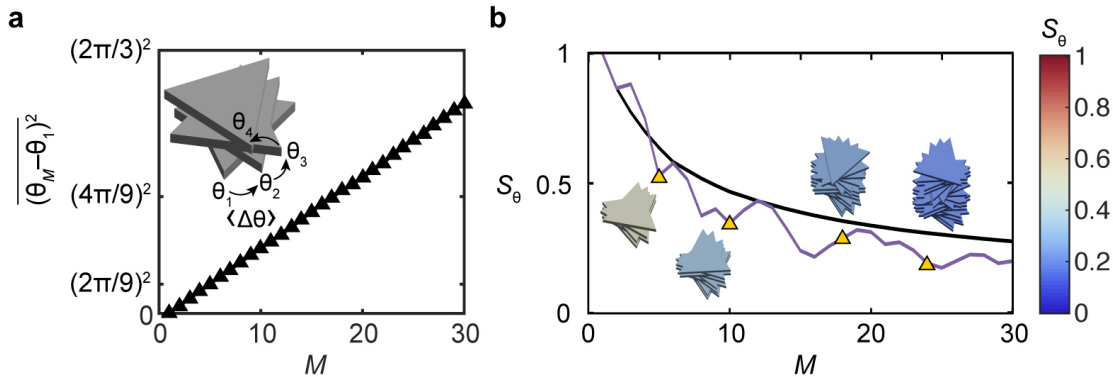
Figure 2.15. Random-walk model illustrating the dependence of orientational order on the number of prisms inside the column M. (a) (Inset) Schematic of the 1D random-walk model in which successive rotations proceed clockwise or counterclockwise with equal probability. The step size is the pairwise relative orientation $\langle \Delta\theta \rangle$, and the number of steps is the number of prisms M within the column. (Main) Mean squared angular displacement relative to the first prism, $\overline{(\theta_M - \theta_1)^2}$, as a function of M calculated from 1,000,000 random paths, confirming the expected linear relationship. (b) Columnar orientational order S_θ versus number of constituent prisms M for a representative random walk path (purple line) and the average over 1000,000 random paths (black line). (Inset) Snapshots showing the configurations of the column at $M = 5$, 10, 18 and 24 for the representative path (marked by the yellow triangles). The colour of the four snapshots reflects their orientational order S_θ (cf. colour bar).

For single-column simulations, the columnar orientational order S_θ depends on ionic strength I and cell height L_z. Figure 2.16a summarises the trends found in Sections 2.5.5.3 and 2.5.5.4, namely that orientational order is promoted by high ionic strength and by small cell height. However, in systems where columns interact with each other, the columnar orientational order is also affected by this interaction and thus also by the column packing fraction ϕ_{2D}. Figure 2.4f shows a 2D map of the column-averaged orientational order $\langle S_\theta \rangle$ obtained in large-scale simulations at a representative packing fraction $\phi_{2D} = 0.386$. This map is qualitatively consistent with the single-column results of Fig. 2.16a, except for a shift toward larger values.

Figure 2.16b quantifies this correlation via a scatter plot of $\langle S_\theta \rangle$ at various I, L_z and ϕ_{2D} (as listed in Table 2.1) determined in large-scale simulations versus the order parameter S_θ obtained from single-column simulations. For low packing fractions, the data points closely follow $\langle S_\theta \rangle = S_\theta$ (red line), i.e., the single column simulations provide a good estimation of the columnar orientational order in the large-scale system. $\langle S_\theta \rangle$ is systematically larger than S_θ at large S_θ, due to the additional intercolumn attraction, which is particularly strong at high ionic strength. At higher packing fractions ϕ_{2D}, the shift of $\langle S_\theta \rangle$ toward larger value becomes more apparent due to the decrease of free space for each column, along with the increased intercolumn attraction. In particular, when ϕ_{2D} is large enough (> 0.440), $\langle S_\theta \rangle$ never reaches low values, no matter how small S_θ is, owing to crowding. Within our ϕ_{2D} range of interest ($0.362 \leq \phi_{2D} \leq 0.433$), the single-column order parameter S_θ serves as a good estimator for $\langle S_\theta \rangle$ in the multi-column systems.
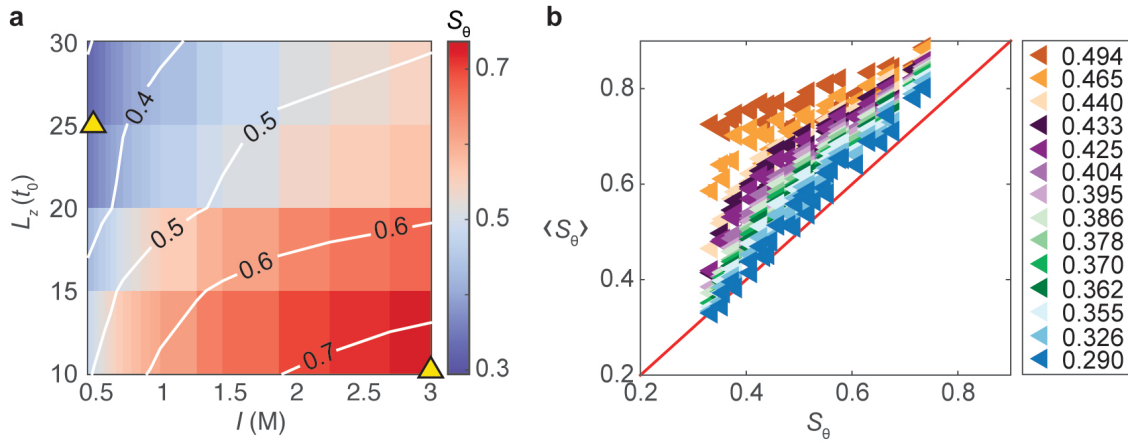
Figure 2.16. Effects of 2D packing fraction and intercolumn interaction on columnar orientational order. (a) Orientational order parameter S_θ from single-column simulations as a function of ionic strength I and cell height L_z (in units of prism thickness t_0). Yellow triangles mark the two conditions used in Fig. 2.4b,d. (b) Scatter plot of average columnar orientational order $\langle S_\theta \rangle$ measured from large-scale simulations versus predicted S_θ in single-column simulations at the same ionic strength and cell height. Symbol colours specify the 2D packing fractions ϕ_{2D} used in the large-scale simulations and each data point corresponds to an (I, L_z) condition listed in Table 2.1.

CHAPTER 3

Universal Layer-By-Layer Growth Mode in Nanoparticle Superlattices

This chapter presents a combined experimental–computational study on the nanoscale crystal growth kinetics. To present a complete story, I have included experimental results that were obtained by Binbin Luo. The content of this chapter is based on the following publication:

- B. Luo[1], Z. Wang[1], Z. Ou, E. Luijten, and Q. Chen, "Universal layer-by-layer growth mode in nanoparticle superlattices," (To be published).

3.1. Abstract

Kinetic growth modes of crystals, which dictate fundamentally the morphology and properties of crystalline materials, have been phenomenologically shown as different for atoms and micron-sized colloids and exhibit an intriguing dependence on the size of building blocks. Using liquid-phase transmission electron microscopy (TEM), we experimentally capture a universal growth mode in the underexplored intermediate nanoscale, where nanoparticles of various symmetries and surface curvatures (cubes, concave polyhedral, spheres) follow an atom-mimetic layer-by-layer growth to generate smooth surface facets. Coupling single particle tracking and simulation, we elucidate the crucial role of the generic particle size in shaping the kinetics and energy landscape (e.g., surface diffusion rate, energy barriers)

---

[1]These authors contributed equally to the work

involved in selecting growth modes. Our work unifying understandings of crystal growth across scales can be applied to enriching crystal morphology engineering

3.2. Introduction

Crystal growth occurs through attachment of new building blocks, such as atoms, ions, molecules, and nanoparticles, to surfaces from a suspended medium[92–96]. This kinetic process dictates major design parameters (e.g., crystal symmetry, morphology, and surface structure) and thereby applications ranging from semiconductors to nanostructures for optical devices[93,97]. For example, the extent of supersaturation has been shown to determine the polymorphs of lysozyme crystals[98], while the ion flux during the growth of semiconductor devices shapes the distribution of grain boundaries and defects, which interfere with transport of charge carriers[95]. Phenomenologically, one robust observation is the intriguing yet puzzling dependence of crystal growth modes on the size of the building blocks[94,99]. On the atomic scale, crystal growth theories were established decades ago and successfully applied to explain and guide experimental crystal growth[92,93,96]. Layer-by-layer growth is often the preferred mode of atomic crystallization, permitting, e.g., production of flat films of semiconductors or alloys[92,93,100]. In contrast, crystalline photonic coatings of micron-sized colloids often adopt corrugated surfaces[23–25], with surface roughness matching predictions from capillary-wave theory. Lack of information on crystal growth behavior at the intermediate nanoscale complicates classification of growth modes for the full range of building block sizes and hinders an explanation of the apparent lack in universality.

Until now, crystal growth modes of nanoscopic building blocks have remained largely unexplored in both experiments[101] and simulations[12], even though the resulting crystal properties play a critical role in applications such as metamaterials and photocatalysis in the case

of nanoparticle superlattices[16]. Experimental challenges arise from the difficulty of directly imaging real-time, real-space dynamics in solution at the needed spatial resolution[13,101], where conventional electron microscopy requires dry and thus static samples[2,16,26,102], while ensemble scattering (e.g., small-angle neutron or X-ray scattering) methods do not resolve structure or dynamics at the level of individual particles[26,103]. For modeling and simulation, crystal growth kinetics also pose challenges unique to the nanoscale[12]. As the building blocks become comparable in size to solvent and ligand molecules, accurate modeling of the interactions and incorporation of fluctuation effects are essential. At the same time, growth processes occur over much larger time and length scales, and involve far more particles, than nucleation. Equally important, the fundamental lack of experimental data on essential kinetic parameters leads to a dearth of reliable input parameters for simulations and precludes their validationa situation manifestly different from atomic crystallization, where materials-specific parametrizations have been established experimentally.

Here we report the first imaging of crystal growth modes at the nanoscale and present a framework applicable to nanoscopic building blocks of different shapes, where key parameters are measured that until now were inaccessible, such as surface diffusion rate and the associated energetic barriers. The experimental imaging is made possible by low-dose liquid-phase transmission electron microscopy (TEM)[101], which combines nanometer resolution and compatibility with a suspension. We focus on model systems of nanoparticles crystallizing into three-dimensional (3D) superlattices, where tracking of individual nanoparticles reveals the superlattice growth process in full detail, including nanoparticle adsorption/desorption, surface diffusion, propagation and merging of steps, and individual nanoparticle displacements in the crystalline structures. Unexpectedly, we discover a prevalent layer-by-layer growth mode resembling atomic crystallization[92] for a diversity of nanoparticle shapes, where a new

surface layer grows only after the preceding layer is complete. Coupling statistical analysis of experimental TEM videos with molecular dynamics (MD) and kinetic Monte Carlo (KMC) simulations, we elucidate that building block size governs the crystal growth process in two distinct ways, by simultaneously controlling the ratio of surface diffusion rate to incoming flux and the interaction range. These two parameters in turn determine the thermodynamic and kinetic driving forces for different growth behaviors, providing mechanistic understanding for crystal morphology engineering at the nanoscale. Notably, our framework explains the consistent observation of corrugated crystal surfaces composed of micron-sized colloids[24,25], whose relatively shorter-ranged interactions suppress the thermodynamic preference for a smooth surface, and whose slower diffusion rate increases trapping at surface sites that represent local energy minima.

3.3. Results and Discussion

Liquid-phase TEM (Fig. 3.1) directly captures the layer-by-layer growth of a simple cubic superlattice from a suspension of concave gold nanocubes. The concave nanocubes, which have an edge length $L = 62.0 \pm 4.6$ nm and a concaving angle[104] $\alpha = 16°$ (Fig. 3.1A), initially remain dispersed in deionized water owing to the electrostatic repulsion between negatively charged thiols uniformly covering their surface. This suspension of highly concentrated nanocubes is sealed between two SiN_x chips following our previously reported protocols[101] to permit liquid-phase TEM imaging. We use low electron beam dose rates (4–27 $e^- \cdot Å^{-2} \cdot s^{-1}$) to ensure that the thiol ligands and nanoparticles remain intact under electron beam illumination and the interparticle interactions are not fundamentally altered. When we increase the phosphate buffer concentration (PBS, pH = 8; range of ionic strength I: 15–110 mM), the van der Waals attraction between the nanocubes overwhelms the screened electrostatic

and (entropic) steric repulsion of the ligands (Fig. 3.1A), thereby triggering nucleation and growth of superlattices. We observe that the nucleation occurs via face-to-face attachment of the nanocubes, but in this work focus on the growth stage, the expansion of single crystallinity following nucleation, which produces large-scale 3D simple cubic superlattices. Due to confinement by the cell along the direction of the electron beam ($\sim$ 3–4 times of nanoparticle size), the superlattices predominantly develop along the lateral directions. The radial distribution function and bond network of the superlattice show high ordering spanning a lateral dimension larger than 2 μm, comprising more than 1000 concave nanocubes in the superlattice. Due to thermal fluctuations, the concave nanocubes exhibit local vibrations and self-correction of mis-coordinated sites as they relax on the lattice sites.

During the growth process, incoming concave nanocubes preferentially attach to the kink sites on a growing crystalline layer to form a flat surface (schematic in Fig. 3.1B); diffusion is sufficiently rapid to prevail over the formation of corrugated terraces ($I = 25$mM). This growth behavior is clearly visible in the time-lapse liquid-phase TEM images (Fig. 3.1, C–D) and surface profiles of the superlattice overlaid over time (Fig. 3.1E). Further tracking of the superlattice surface shows a staged increase in the number of lateral layers (Fig. 3.1F), a key signature of the layer-by-layer growth mode. The orientation map[25] of the nanoparticles in the superlattice shows a high degree of orientational order, confirming the face-to-face alignment of neighboring concave nanocubes (Fig. 3.1D). The binding energy from this alignment serves as the thermodynamic driving force for an incoming building block to position in the most coordinated kink site[92] rather than on a terrace or step site (Fig. 3.1B). To quantify this binding energy, explicitly accounting for the effects of ligand charge and entropy, we perform MD simulations and thermodynamic integration of a detailed coarse-grained model with about 4.6×10^6 gold atoms as the gold core and about 1.6×10^3 grafted ligand chains (see
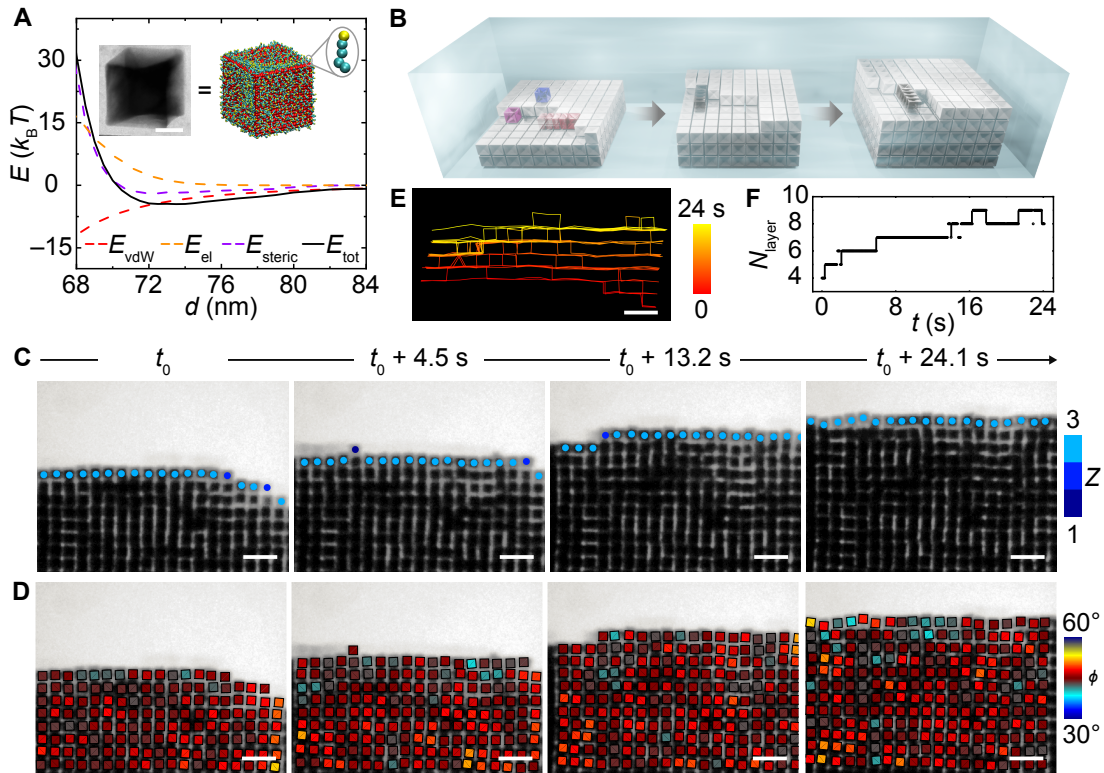
Figure 3.1. Layer-by-layer growth of nanoparticle superlattices from gold concave nanocubes. (A) Contributions to the interaction energy of two concave nanocubes (left inset: TEM image) approaching face-to-face at $I = 25$ mM as a function of center-to-center distance d, as computed from molecular dynamics simulation (right inset: schematic). The pairwise binding energy (with magnitude $\epsilon = 4.5 k_{\mathrm{B}} T$) is estimated as the minimum of E_{tot} versus d. (B) Schematic of terrace (blue), step (purple), and kink (pink) sites on the surface of a simple cubic lattice assembled of concave nanocubes, following layer-by-layer growth. (CD) Time-lapse liquid-phase TEM images showing layer-by-layer growth of superlattice from concave nanocubes at $I = 25$ mM. Whereas the crystal is three-dimensional, the images show projections on the plane perpendicular to the beam. Coordination number of surface particles (C) and orientation of each concave nanocube (D) in the projected view are shown. The gray scale colormap was manually adjusted to highlight individual nanoparticles. Dose rate 27.1 $e^- \mathring{\mathrm{A}}^{-2} \cdot \mathrm{s}^{-1}$. (E) Interface profile of the superlattice. (F) Staged growth of the number of (partial) layers N_{layer} over time t. Scale bars: 30 nm in (A); 200 nm in (CE).

Section 3.5.1 and 3.5.2). Per face-to-face contact (i.e., single coordination), we find an attractive minimum $-4.5 k_{\mathrm{B}} T$ (with its magnitude defined as binding strength ϵ) for $I = 25$mM,

estimated as the minimum in the total energy E_{tot} along the center-to-center distance d (Fig. 3.1A). Estimating the transition from a rough to a smooth surface at $\epsilon \approx 1.77 k_{\text{B}}T$ using Kossel's model[92], we conclude that the attraction between concave nanocubes should be sufficient to favor positioning in the kink sites. However, beyond the existence of a sufficiently strong thermodynamic driving force, a necessary condition for layer-by-layer growth is sufficiently rapid diffusion of the surface-attached building blocks. During crystal growth, incoming particles that are not directly deposited onto kink sites can land on step or terrace sites which are local energy minima with lower coordination[92,93,100]. Diffusion to kink sites then follows through thermally agitated hopping over the in-plane energy barrier ΔE^{in} or the Ehrlich–Schwoebel (step-edge) barrier ΔE^{ES}[105,106] (Fig. 3.2A–B).

Traditionally, the ratio of the (in-plane) surface diffusion rate D to the incoming flux F of building blocks is viewed as the dominant parameter governing growth kinetics, as it measures the extent of surface sites explored by a deposited particle before it joins an existing island or meets another particle to nucleate a new island[93]. Small D/F produces kinetically roughened growth, whereas large D/F can result in layer-by-layer growth. This proves to be a key point in the differentiation of crystal growth for atoms, nanoparticles, and colloids. Although similar deposition rates F can be achieved for building blocks of different sizes, the situation is different for the diffusion rate D. We estimate D via an Arrhenius relationship, $D = D_0 \exp(-\Delta E^{\text{in}}/k_{\text{B}}T)$. The intrinsic diffusion rate D_0 follows the StokesEinstein relationship and depends inversely on building block size. The in-plane barrier ΔE^{in} is more subtle, as it is part of the energy landscape of the crystal surface, which depends on both particle shape and the reduced (i.e., normalized by particle size) interaction range Δ. It is helpful to assess the role of the latter via a generic analytical model (See Section 3.5.3) in which hard spheres of size σ have a pairwise attraction $-\epsilon(\sigma/r)^n$ with
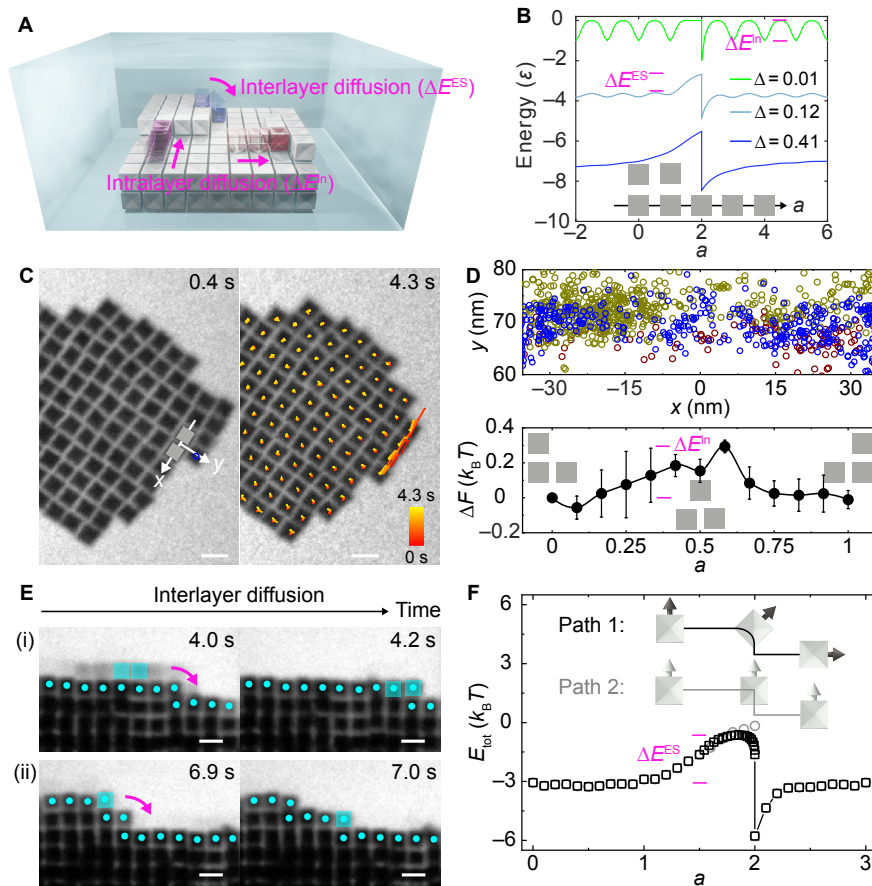
Figure 3.2. Surface diffusion and the corresponding energy landscape. (A) Schematic showing in-plane and interlayer diffusion processes. (B) Energy landscapes experienced by a particle moving across a step edge for different interaction ranges Δ. For ease of comparison, the curves with $\Delta = 0.12$ and 0.41 are displaced vertically by -2.5ϵ and -1.5ϵ, respectively. (C) Time-lapse liquid-phase TEM images showing in-plane diffusion, with trajectories overlaid (right). Dose rate: 17.9 $e^- \text{Å}^{-2} \cdot \text{s}^{-1}$. (D) Top: Scatter plot of surface particle positions x relative to the center of the nearest nanocube pair underneath. Coordinate system defined in (C). Each color represents a data set from an independent TEM movie. Bottom: Relative free energy ΔF as a function of reduced coordinate a (with reference state chosen at the perfect aligned case with $a = 0$) at the superlattice surface measured from experiments. Error bars are standard errors from three independent movies. (E) Time-lapse liquid-phase TEM images of two representative interlayer diffusion events, with diffusing particles labeled as cyan squares. The gray scale colormap was adjusted to highlight the individual nanoparticles. (F) Energy landscape experienced by a concave nanocube diffusing between layers along two possible paths as depicted. Energies are computed from simulations at $I = 25$ mM. Scale bars: 100 nm.

power-law decay n controlling the attraction range. We define the reduced interaction range Δ as $(2^{1/n}1)$, such that the pairwise energy is stronger than $-\epsilon/2$ for separations in the range $[\sigma, \sigma(1 + \Delta)]$. For very short-ranged interactions ($\Delta = 0.01$, $n = 50$), representative of, e.g., micron-sized colloids, we observe a strongly oscillatory energy landscape (Fig. 3.2B, green) with large ΔE^{in} against in-plane hopping, which gradually flattens with increasing interaction range (cf. $\Delta = 0.12$ and $n = 6$, typical for atoms, light blue), ultimately reducing to a smooth profile with negligible ΔE^{in} ($\Delta = 0.41$ and $n = 2$, dark blue). The physical origin of this trend is the increasing importance of interactions beyond nearest neighbors with increasing Δ [99]. For nanoparticles, Δ is shape-dependent and, for van der Waals interactions, approximately lies in the range 0.1 to 0.4 [85], leading to very small ΔE^{in} in general. Combining the size dependence of D_0 and ΔE^{in}, we recognize that atoms and nanoparticles possess a sufficiently large diffusion rate D and thus–for most practical flux rates–a sufficiently large D/F to permit layer-by-layer growth.

While these analytical considerations clarify the generic effects of building block size on surface diffusion, they do not capture the dependence of the energy landscape on the arrangement of particles or their anisotropy. We are able to directly access this crucial information by combining particle diffusion trajectories obtained via liquid-phase TEM and energy calculations from MD simulations, explicitly determining the energy landscape for the nanocube system and the surface diffusion rate. By mapping more than 1,000 coordinates of surface particles relative to the lattice underneath (Fig. 3.2C, $I = 110$ mM) and assuming a Boltzmann distribution, we obtain the energy profile along the lattice surface as a function of lattice coordinate a (Fig. 3.2D, with $a = 0$ or 1 for perfectly aligned and $a = 0.5$ for fully misaligned configurations). Figure 3.2D shows broad energy minima corresponding to perfect face-to-face alignment separated by an in-plane diffusion barrier ΔE^{in} of only $0.3k_{\text{B}}T$.

This agrees fairly well with the MD result of $0.1k_{\mathrm{B}}T$, given the underlying approximations in the simulation model. This low barrier is also consistent with the rapid surface diffusion of nanoparticles, which we measure from their mean square displacement. We find a diffusion rate $D = 161.3\ d_{\mathrm{equil}}^2/\mathrm{s}$ (d_{equil} as the equilibrium lattice spacing), four orders of magnitude larger than the typical surface diffusion rate of micron-sized colloids ($\sim 0.01\ d_{\mathrm{equil}}^2/\mathrm{s}$)[94,107].

Another determinant for crystal growth, potentially as important as surface diffusion is interlayer diffusion, in which particles climb over a step edge from a terrace to merge with the layer underneath[93,108]. This process is primarily controlled by the Ehrlich–Schwoebel barrier ΔE^{ES} (Fig. 3.2A). While surface diffusion D determines the uniformity parallel to the surface, interlayer exchange determines the uniformity perpendicular to it. In liquid-phase TEM we directly observe the frequent occurrence of interlayer diffusion, with nanoparticles diffusing either individually or collectively on a time scale of 0.1–0.2 s (Fig. 3.2E). The simulations yield the associated Ehrlich–Schwoebel barrier $\Delta E^{\mathrm{ES}} = 2.4k_{\mathrm{B}}T$ (Fig. 3.2F). Interestingly, this is markedly lower than for atomic systems, where $\Delta E^{\mathrm{ES}} = 0.2$–$0.5$ eV, i.e., 8–$20k_{\mathrm{B}}T$ at room temperature. Indeed, for such systems layer-by-layer growth is only observed at elevated temperatures upward of 700K[108] (where ΔE^{ES} is reduced to $3.4k_{\mathrm{B}}T$). Conversely, although micron-sized colloids typically display a small (enthalpic) Ehrlich–Schwoebel barrier due to the short range of their interactions (cf. green curve in Fig. 3.2B), they experience a high diffusive (entropic) step-edge barrier[94], which suppresses interlayer exchange and thus serves as another inhibitor for the layer-by-layer growth.

To examine the generality of our observations and understanding of nanoscale crystal growth, we extend our investigation to systems of flat (i.e., non-concave) nanocubes and systems of nanospheres. Despite the differences in symmetry and surface curvature, we observe layer-by-layer growth for all of these (Fig. 3.3). This not only corroborates the kinetic
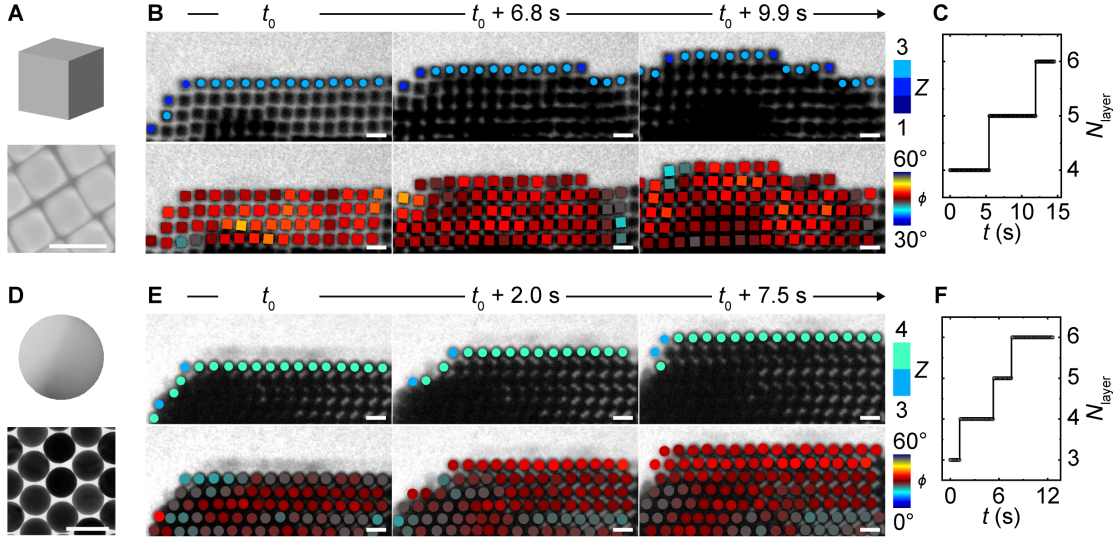
Figure 3.3. Generalization of layer-by-layer growth of nanoparticles with different shapes. (A) Schematic and SEM image of gold nanocubes with flat faces. (B) Top: Time-lapse liquid-phase TEM images showing the layer-by-layer growth of superlattice from nanocubes. Particles in the advancing surface layer are labeled with dots color-coded by their coordination numbers. Dose rate 15.5 $e^-\text{Å}^{-2} \cdot \text{s}^{-1}$. Bottom: Voronoi cell partition and orientation maps of the nanocubes. Each Voronoi cell is colored according to the orientation ϕ_j of each nanocubes. (C) Staged growth of the number of layers N_{layer} over time t in (B). (D) Schematic and TEM image of gold nanospheres. (E) Top: Time-lapse liquid-phase TEM images showing the layer-by-layer growth of superlattice from nanospheres. Particles in the advancing surface layer are labeled with dots color-coded by their coordination numbers. Dose rate 17.6 $e^-\text{Å}^{-2} \cdot \text{s}^{-1}$. Bottom: Voronoi cell partition and orientation maps of the nanospheres. Each Voronoi cell is colored according to the orientation ϕ_j of each nanospheres. (F) Staged growth of the number of layers N_{layer} over time t in (E). Scale bars: 100 nm.

arguments outlined above, but also illustrates that the prevalence of faceted nanoparticle superlattices with smooth surfaces[26,109] is due to layer-by-layer growth.

The universality of crystal growth for different nanoparticle shapes confirms the role of particle size in selecting the preferred growth mode. To obtain a unified picture and disentangle the effect of the intrinsic diffusion rate D_0 and the interaction range Δ on both thermodynamic and kinetic driving forces, we perform kinetic Monte Carlo simulations of
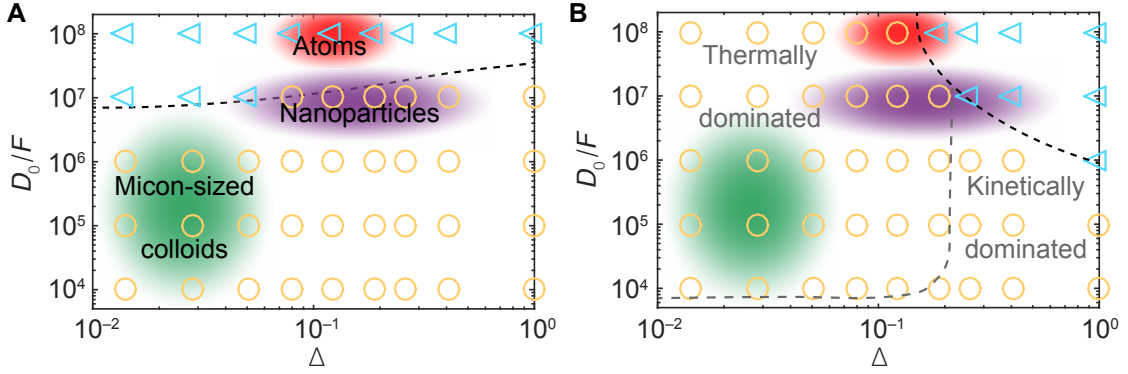
Figure 3.4. Kinetic Monte Carlo simulations distinguish crystal growth modes for atoms, nanoparticles, and colloids. (A–B) Crystal growth modes (blue triangles: layer-by-layer growth; yellow circles: roughened growth) parametrized by interaction range Δ and the ratio between intrinsic diffusivity and flux rate D_0/F at temperature $k_{\mathrm{B}}T = 0.15\epsilon$ (A) and $k_{\mathrm{B}}T = 0.25\epsilon$ (B). The regions where atoms, nanoparticles, and micron-sized colloids reside are shaded in red, purple, and green, respectively. The shadings are semi-quantitative due to the large experimental variability in flux F, and primarily should be interpreted to indicate the relative position of colloidal, nanoparticle, and atomic crystal growth.

systems covering a wide range of D_0 and Δ (see Section 3.5.3). At low temperature ($k_{\mathrm{B}}T = 0.15\epsilon$, below the thermodynamic roughening temperature for all Δ considered), layer-by-layer growth can only be hindered by kinetic effects. Indeed, Fig. 3.4A shows a sharp boundary as a function of D_0/F, only weakly dependent on Δ. This reaffirms that low D_0/F typical of micron-sized colloids, yields roughened growth, whereas large D_0/F typical for nanoparticles or atoms (2–4 orders of magnitude larger) leads to layer-by-layer growth, consistent with our experiments and previous literature. When we increase the temperature ($k_{\mathrm{B}}T = 0.25\epsilon$), the interaction range becomes critical as well. For small Δ(e.g., $\Delta < 0.05$, typical for micron-sized colloids), rough crystal surfaces appear for all D_0/F, owing to thermally excited holes and islands that prevent particles from diffusing across the growing surface (Fig. 3.4B). Conversely, at the larger relative interaction ranges typical for atoms and nanoparticles, kinetic effects dominate again, and layer-by-layer growth reappears for large D_0/F. Thus,
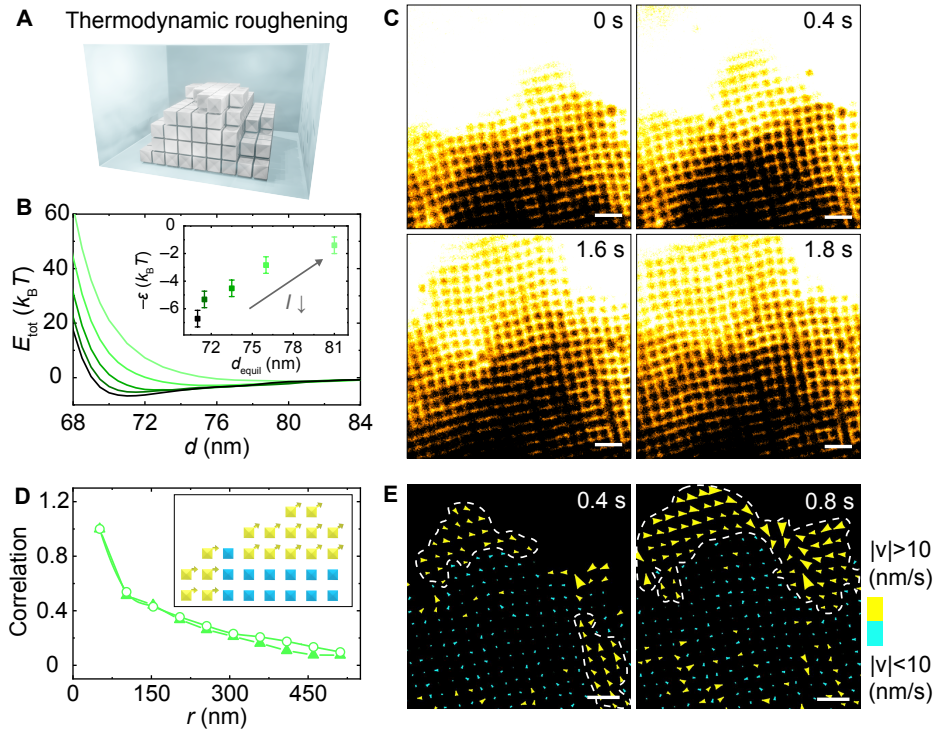
Figure 3.5. Thermodynamic roughening transition in the growth of the superlattice. (A) Schematic showing a thermodynamically roughened surface of a simple cubic lattice. (B) Total pairwise energy versus particle center-to-center distance computed from simulations at different ionic strengths I (from dark to light green: 110 mM, 50 mM, 25 mM, 15 mM, and 10 mM). Inset: Pairwise binding energy $-\epsilon$ versus the predicted lattice constant d_{equil}. (C) Time-lapsed liquid-phase TEM images of a nanoparticle superlattice growing with a roughened surface at $I = 15$ mM. Dose rate 14.9 $e^- \cdot \text{Å}^{-2} \cdot \text{s}^{-1}$. TEM images are colored according to the image intensity to highlight different lattice layers. (D) Correlation in the magnitude (solid triangles) and orientation (open circles) in the velocity field of the lattices. (E) Velocity fields of lattices with roughened surface. Scale bars: 200 nm.

their relatively large intrinsic diffusion rate and wide spectrum of interaction ranges makes nanoparticles likely to display layer-by-layer growth, whereas for micron-sized colloids the opposite is true.

To demonstrate the utility of the insights obtained, we control the surface morphologies that arise in nanoparticle crystallization by manipulating the binding energy ϵ (Fig. 3.5A). We increase the electrostatic repulsion by lowering the ionic strength from 25 mM to 15 mM,

which the MD simulations predict to lower ϵ from $4.5k_\mathrm{B}T$ to $2.8k_\mathrm{B}T$ (Fig. 3.5B). Experimentally, this leads to roughened growth of the superlattice (Fig. 3.5C), with the roughness (defined as the standard deviation of the surface profile) increasing from $\sim 0.9d_\mathrm{equil}$ (layer-by-layer growth) to $\sim 3.6d_\mathrm{equil}$. This observation is reminiscent of the roughening transition that in atomic metal and alloy films[92] can be triggered by elevation of temperature. Tracking the motion of individual particles, we show that the velocity field of concave nanocubes displays extended domains with large, coherent translational motion (Fig. 3.5, D–E).

3.4. Conclusions

Direct real-time and real-space access has not only allowed us to observe and understand the crystal growth mode of nanoparticles, but also completed the gap in length scales between atoms and micron-sized colloids. The "atom-mimetic" behavior of nanoparticles, along with the single-particle resolution of liquid-phase TEM, establishes these systems as a superior alternative to micron-sized colloids for visualizing atom-like kinetics and phase behavior. In combination with the variety of shapes and interactions with which nanoparticles can be endowed, this opens a wealth of possibilities for establishing design rules and quantitative predictions of surface morphology in nanoparticle superlattices or other forms of nanoscale self-assemblies.

3.5. Methods and Supplementary Information

3.5.1. Coarse-grained model for the gold concave nanocubes

To compute the pairwise interaction of two concave nanocubes, we constructed a coarse-grained (CG) model (see Fig. 3.1A) in which each gold concave nanocube core is discretized as a mesh of beads (red), placed on a three-dimensional (3D) simple cubic lattice with a

lattice spacing of $\sigma_{\text{gold}} = 0.332$ nm (diameter of a gold atom). The concaveness ($\alpha = 16°$) of the concave nanocube was considered in the meshing. Each charged ligand coated on the gold surface was characterized by the beadspring model with 5 beads of size $\sigma_{\text{lig}} = 1.25$ nm connected by harmonic springs. The number and size of the beads were determined using the ideal chain model by considering the Kuhn lengths (≈ 1.25 nm) of the polymer segments[110]. The head bead (green) of the ligand chain is rigidly attached on the gold surface and the tail bead (yellow) carries a unit negative charge (e). The charge density ρ_s was set to be $-0.075e/\text{nm}^2$, as measured in our experiment.

The beads making up the gold core have a bead–bead van der Waals interaction $u_{\text{vdW}}(r_{\text{b}-\text{b}})$, and the tail beads of the ligands interact via a screened Coulomb potential $u_{\text{el}}(r_{\text{b}-\text{b}})$ which we modeled following Debye–Hückel approximation, where $r_{\text{b}-\text{b}}$ denotes the distance between the pairs of interacting beads. The van der Waals interactions between ligands and between ligands and gold atoms are negligible owing to the very small Hamaker constants for hydrocarbon/hydrocarbon and gold/hydrocarbon across water[85]. The interactions $u_{\text{vdW}}(r_{\text{b}-\text{b}})$ and $u_{\text{el}}(r_{\text{b}-\text{b}})$ are given by

$$u_{\text{vdW}}(r_{\text{b}-\text{b}}) = -\frac{H\sigma_{\text{gold}}^6}{\pi^2 r_{\text{b}-\text{b}}^6} , \tag{3.1}$$

$$u_{\text{el}}(r_{\text{b}-\text{b}}) = \frac{e^2}{4\pi\epsilon_0\epsilon_{\text{r}} r_{\text{b}-\text{b}}} e^{-\kappa r_{\text{b}-\text{b}}} = \frac{l_{\text{B}}}{r_{\text{b}-\text{b}}} e^{-\kappa r_{\text{b}-\text{b}}} k_{\text{B}}T , \tag{3.2}$$

where $H = 28.9 k_{\text{B}}T$ is the Hamaker constant for gold/gold in water, ϵ_0 the vacuum permittivity, ϵ_{r} the relative permittivity of water, κ^{-1} the Debye length following $\kappa^{-1} = 0.304/\sqrt{I(\text{M})}$ nm (with ionic strength I in unit of M) for aqueous solutions at room temperature, $l_{\text{B}} = 0.7$ nm the Bjerrum length of water at 25°C. Note that cutoff value of 70 nm beadbead distance was chosen in the van der Waals interaction computation for computation efficiency and the

truncation error was tested to be less than $0.2k_BT$ for interparticle interaction energy (Table 3.1). A shift-truncated Lennard-Jones potential $u_{\mathrm{LJ}}(r_{\mathrm{b-b}})$ was applied to all the beads to model the excluded-volume interactions:

$$
u_{\mathrm{LJ}}(r_{\mathrm{b-b}}) = \begin{cases} 4k_BT\left[(\dfrac{\sigma}{r_{\mathrm{b-b}}})^{12} - (\dfrac{\sigma}{r_{\mathrm{b-b}}})^6\right] + k_BT, & (r_{\mathrm{b-b}} \leq 2^{1/6}\sigma) \\ 0, & (r_{\mathrm{b-b}} > 2^{1/6}\sigma) \end{cases}, \qquad (3.3)
$$

where $\sigma = \sigma_{\mathrm{gold}}, \sigma_{\mathrm{lig}}, (\sigma_{\mathrm{gold}} + \sigma_{\mathrm{lig}})/2$ for gold–gold, ligand–ligand, gold–ligand bead pairs, respectively. The bonds between neighboring beads along a ligand chain were modeled with a harmonic potential $u_{\mathrm{bond}}(r_{\mathrm{b-b}}) = K(r_{\mathrm{b-b}} - \sigma_{\mathrm{lig}})^2$, where $K = 25k_BT/\mathrm{nm}^2$ is the spring constant and σ_{lig} sets the native spring length. All model parameters are summarized in Table 3.2.

Table 3.1. Interparticle van der Waals interaction energies (in unit of k_BT) at different interparticle center-to-center distance d computed using different bead–bead cutoff distances.

	$d = 68.0$ nm	$d = 70.0$ nm	$d = 71.0$ nm	$d = 74.0$ nm
Cutoff $= 35$ nm	-10.01	-5.47	-4.14	-1.88
Cutoff $= 70$ nm (chosen)	-11.97	-7.24	-5.82	-3.28
Cutoff $= 80$ nm	-12.05	-7.32	-5.90	-3.36
Cutoff $= 100$ nm	-12.10	-7.37	-5.95	-3.41

It is noteworthy that both the geometrical details (e.g., concaveness) of the concave nanocube and the discreteness of ligand molecules (e.g., steric effects) can significantly affect the magnitude and range of the effective interparticle interaction at this nanoscale (see more discussion in Section 3.5.2). Therefore, including these features in the modeling is crucial in order to provide quantitative predictions of the energy landscape and the lattice spacing of the superlattices. For the same reason, the hard-core models[21] which have been widely used in simulating anisotropic nanoparticles are not feasible here.

Table 3.2. The parameters used in the coarse-grained model.

Symbol	Description	Value
σ_{gold}	Diameter of gold atoms	0.332 nm
H	Hamaker constant (gold-gold across water)	$28.9 k_{\mathrm{B}}T$
L	Concave nanocube edge length	62.0 nm
α	Concave nanocube concaveness	$16°$
σ_{lig}	Diameter of a bead in the bead-spring model for ligands	1.25 nm
	Number of beads per ligand	5
K	Spring constant in the bead-spring model for ligands	$25 k_{\mathrm{B}}T/\mathrm{nm}^2$
l_{B}	Bjerrum length	0.7 nm
ρ_s	Charge density of nanocube	$-0.075 e/\mathrm{nm}^2$
T	Temperature	298 K

3.5.2. Molecular dynamics simulations of the gold concave nanocubes

Molecular dynamics simulations were conducted for the concave nanocubes coated with ligands in the NVT ensemble. All simulations were performed at 298 K using a Langevin thermostat at different ionic strengths from 15 mM to 110 mM, within which the Debye–Hückel approximation is valid. All systems were simulated with a 0.01-fs time step for 2.5 ns during equilibration and a 0.05-fs time step for 500 ns during production. Ten independent runs were conducted for each condition to obtain ensemble averages.

To calculate the total pairwise interaction energy E_{tot} of two concave nanocubes, one important component of E_{tot} we considered is the entropic steric repulsion E_{steric} between the ligands, which occurs as the ligands of two approaching concave nanocubes start to overlap. To measure E_{tot} as a function of the interparticle center-to-center distance d (when the two concave nanocubes perfectly aligned face-to-face), we ran multiple simulations with the two concave nanocubes positioned at different values of d. In each simulation, both the position and orientation of two concave nanocube cores are fixed, while the ligand chains

are free to move and relax. We measured the ensemble-averaged total force between the concave nanocubes at each given d. Total energy profile $E_{\text{tot}}(d)$ was then computed through integration of the force profile. Since the ensemble-averaged potential energy $E_{\text{vdW}} + E_{\text{el}}$ as a function of d is straightforward to extract from the simulations, E_{steric} was obtained from $E_{\text{steric}} = E_{\text{tot}} - E_{\text{vdW}} - E_{\text{el}}$ for discussions in Fig. 3.1A and Fig. 3.6. Note that E_{steric} consists of two parts: the ensemble-averaged excluded-volume interaction energy and the entropic contribution from ligand molecules ($-TS_{\text{lig}}$, S_{lig}: ligand entropy; T: temperature). After obtaining the profile of E_{tot} versus d, the equilibrium interparticle center-to-center distance (dequil) was identified as the distance d at the minimum of E_{tot}, which is our prediction for the lattice spacing. The energy of adsorption per face-to-face contact ($-\epsilon$) is approximated by the minimum of E_{tot} by assuming the interactions with second nearest neighbors are negligible.

A similar approach was adopted to measure the energy landscape experienced by a tracer concave nanocube on top of the superlattice during the interlayer exchange (Fig. 3.2F). At $I = 25$ mM (i.e., the layer-by-layer growth condition), the predicted lattice spacing dequil is 73.5 nm (determined in simulations as noted above, matching well with 73.7 nm measured in experiments) and the ligands on the neighboring concave nanocubes are barely touching ($d_{\text{equil}} > L + 2l_{\text{max}} = 73.25$ nm with $l_{\text{max}} = 5.625$ nm as the length of a fully extended ligand molecule). Therefore, E_{steric} can be ignored and E_{tot} reduces to the ensemble-averaged $E_{\text{vdW}} + E_{\text{el}}$, which was computed between the tracer concave nanocube and the concave nanocubes underneath in the superlattice. Similar to our simulations of two concave nanocubes, the position and orientation of all the concave nanocubes are fixed, while the ligand chains are free to relax. We ran simulations with the tracer concave nanocube sitting at different horizontal lattice coordinates a (where a is the horizontal displacement of the tracer
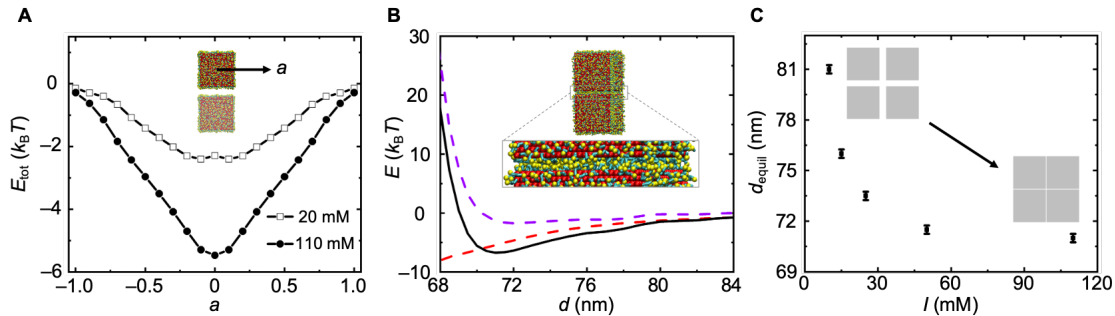
Figure 3.6. Molecular dynamics simulations of the pairwise interaction energy of gold concave nanocubes. (A) Total pairwise interaction energy E_{tot} between two concave nanocubes as a function of the relative horizontal offset a (see the inset schematic) at the respective lattice spacing d_{equil} at ionic strengths of 20 and 110 mM. The energy minima locate around $a = 0$, indicating that the face-to-face configuration with no offsets is energetically preferred. (B) Energy components of two concave nanocubes approaching face-to-face at $I = 110$ mM versus interparticle center-to-center distance d, as computed from molecular dynamics simulations. Purple line: E_{steric}; Red line: $E_{vdW} + E_{el}$; Black line: E_{tot}. The inset snapshot from our simulation shows the overlap between ligands of two concave nanocubes as they approach, resulting in the steric repulsion. (C) Predicted lattice spacing (d_{equil}) as a function of ionic strength (I) computed from simulations, showing that d_{equil} decreases with increased ionic strengths (see the inset schematics).

concave nanocube normalized by d_{equil}, see inset of Fig. 3.2B), while keeping the configuration of the underlying lattice unchanged. We selected two typical paths of the tracer concave nanocube (inset of Fig. 3.2F) to provide a reasonable estimation of the Ehrlich–Schwoebel barrier. Path 1 involves a 90° rotation of the tracer concave nanocube at the step edge. Conversely, path 2 involves no rotation where the tracer concave nanocube vertically drops along the step, resulting in a slightly larger Ehrlich–Schwoebel barrier. Note that we assume the vertical center-to-center distance between the tracer concave nanocube and the concave nanocube layer underneath is 73.5 nm irrespective of a, since the energy landscape near a flat lattice surface is insensitive with a (cf. in-plane energy landscape part of Fig. 3.2F).

Molecular dynamics simulation elucidates that the face-to-face alignment of the concave nanocubes is energetically favored and that the lattice spacing (d_{equil}) can be well-predicted.

As shown in Fig. 3.6A, the face-to-face alignment of zero offset ($a = 0$) is energetically favored over a wide range of ionic strengths, consistent with the experiments. At $I = 15$–50 mM, d_{equil} measured from simulations is mostly contributed by the balance between E_{el} and E_{vdW}, following expectations of DLVO theory[111] (Fig. 3.1A). For higher ionic strengths such as $I = 110$ mM, E_{el} is weakened by counter-ion screening and E_{steric} overwhelms E_{el} to counteract E_{vdW} (Fig. 3.6B), resulting in a minimum of E_{tot} at $d_{\text{equil}} = 71.0$ nm. This value of d_{equil} matches with the lattice spacing (70.8 ± 0.8 nm) measured from the liquid-phase TEM images of the superlattices at $I = 110$ mM. This agreement confirms the increasing importance of the discreteness (e.g., entropic effects of ligands) at the nanoscale and necessity of including it in the modeling[12]. The lattice spacing predicted by our simulations (d_{equil}) was plotted as a function of I (Fig. 3.6C), from which we derived the effective ionic strength in our liquid-phase TEM experiments based on the experimentally measured values of d_{equil} (Table 3.3).

Table 3.3. Lattice spacing d_{equil} measured from liquid-phase TEM and the corresponding effective ionic strengths by matching the experimentally measured d_{equil} with simulation results.

Conditions	d_{equil} measured from experiments (nm)	Effective ionic strength from calculations (mM)
Layer-by-layer growth (Fig. 3.1)	73.7 ± 1.2	25 ± 5
Intralayer diffusion (Fig. 3.2C)	70.8 ± 0.8	$80 - 110$
Roughened growth (Fig. 3.5C,E)	75.6 ± 0.9	15 ± 5

3.5.3. Kinetic Monte Carlo simulations and analytical models for generating phase diagrams

3.5.3.1. Simulation model. To explore how interaction range Δ affects the transition between different growth modes (layer-by-layer growth or roughened growth), we conducted

on-lattice kinetic Monte Carlo simulations on a two-dimensional square lattice (box size $L = 100$ lattice sites) using SPPARKS[112]. Incoming particles are deposited vertically at a flux rate F (in unit of monolayers/second). We employed the Clarke-Vvedensky bond-counting ansatz[113] and assume an Arrhenius-like rate. The hopping rate between lattice sites i and j is thus defined as

$$r_{i,j} = D_0 \text{exp} \left(-\frac{\Delta E^{\text{in}} + n_i E^{\text{b}} + s_{i,j} \Delta E^{\text{ES}}}{k_{\text{B}} T} \right),$$ (3.4)

where D_0 is the intrinsic diffusivity (or attempt frequency), ΔE^{in} denotes the in-plane barrier for diffusion of a free particle, n_i is the number of lateral nearest neighbors of site i, E^{b} is the bond strength of each lateral neighbor, ΔE^{ES} is the step–edge (or Ehrlich–Schwoebel) barrier, and $s_{i,j} = 1$ if the diffusion path leads across a step edge and 0 otherwise.

3.5.3.2. Analytical model. To simulate the system with different reduced interaction ranges Δ, we need to obtain the corresponding values of ΔE^{in}, E^{b} and ΔE^{ES} resulting from the energy landscape for each Δ. Thus, we built up a simple analytical model where the pairwise interaction between particles follows the functional form

$$E(n,r) = \begin{cases} -\dfrac{\epsilon}{(r/\sigma)^n} & (r \geq \sigma) \\ +\infty & (r < \sigma) \end{cases},$$ (3.5)

with a tunable attraction part plus a hard repulsion, where σ denotes the particle size and our length unit, ϵ is the magnitude of energy minimum at contact and our energy unit, and n determines the attraction range. Here the interaction range Δ is defined as $\Delta = (2^{1/n} - 1)$, such that the pairwise energy is lower than $-\epsilon/2$ within the distance $[\sigma, (\Delta+1)\sigma]$. The energy landscape can be mapped out by moving a tracer particle on top of a partially filled lattice
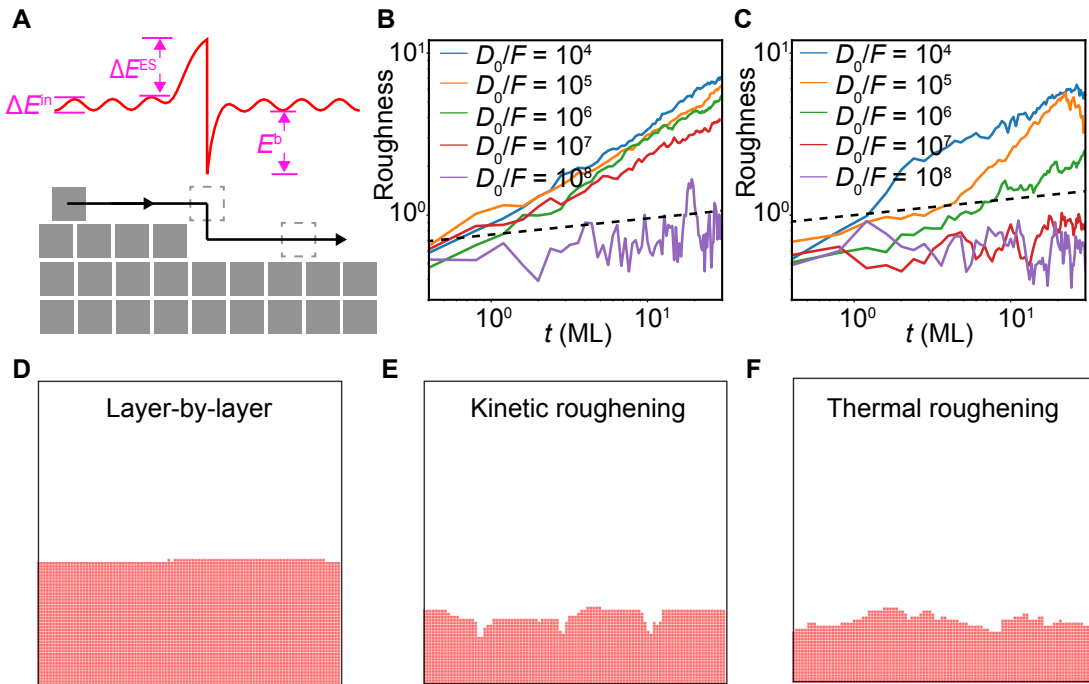
Figure 3.7. Kinetic Monte Carlo simulations of different growth modes. (A) Schematics of the energy landscape a particle experiences along the path (denoted by black line with arrows) with key energetic parameters (ΔE^{in}, ΔE^{b}, and ΔE^{ES}) defined on the graph. (B–C) Surface roughness as a function of time (t, in unit of the time to form one monolayer) at different D_0/F for (B) $n = 6$, $\Delta = 0.12$ and (C) $n = 50$, $\Delta = 0.01$. The black dashed line shows the scaling of $\sim t^{0.1}$. The temperature is at $k_{\text{B}}T = 0.15\epsilon$. (D–F) Simulation snapshots showing the surface profiles at (D) $n = 1$ ($\Delta = 1.00$), $D_0/F = 10^7$, (E) $n = 1$ ($\Delta = 1.00$), $D_0/F = 10^5$, and (F) $n = 14$ ($\Delta = 0.05$), $D_0/F = 10^5$. The temperature is at $k_{\text{B}}T = 0.25\epsilon$.

(Fig. 3.7A) and recording the energy value from direct summation. Key energetic parameters ΔE^{in}, E^{b} and ΔE^{ES}, which are input parameters for kinetic Monte Carlo simulations, can thus be extracted from the potential landscape (Fig. 3.7A). To simulate micron-sized colloids with a very small interaction range (e.g., $\Delta \leq 0.05$), an additional entropic step–edge barrier was also included in ΔE^{ES}. Here this entropic barrier is of the magnitude of $\ln(2) \cdot k_{\text{B}}T$ as the step–edge diffusion path is twice longer than the in-plane path[94].

3.5.3.3. Simulation of phase diagrams. Simulations were conducted at different temperatures (phase diagrams at $k_{\mathrm{B}}T = 0.25\epsilon$ and 0.15ϵ as presented in Fig. 3.2B). At each temperature, we scanned different flux rates F (with respect to a fixed D_0) and interaction ranges Δ (by varying n). For each Δ, the energetic parameters (ΔE^{in}, E^{b} and ΔE^{ES}) are uniquely determined by the analytical model as introduced in Section 3.5.3.2, which are listed in Table 3.4.

To identify different growth modes (layer-by-layer growth or roughened growth), we plot the surface roughness (i.e., standard deviation of the surface height) as a function of time t (in unit of the time to form one monolayer) in the log–log scale (Fig. 3.7, B and C). The curves with a slope smaller than 0.1 (i.e., they have $\beta < 0.1$ for t^{β}) are identified as layer-by-layer growth; while those with a slope larger than 0.1 are classified to be roughened growth. Note that for the case of random deposition without surface diffusion, the surface roughness grows as $\sim t^{0.5}$ [108]. Simulation snapshots of typical surface profiles for layer-by-layer growth, kinetic roughening, and thermal roughening are shown in Fig. 3.7, D–F. The simulated "phase diagrams" are summarized in Fig. 3.4.

Table 3.4. The input parameters at each interaction range Δ (or n) used in kinetic Monte Carlo simulations.

n	1	2	3	4	6	9	14	25	50
Δ	1.00	0.41	0.26	0.19	0.12	0.08	0.05	0.03	0.01
$\Delta E^{\mathrm{in}}/\epsilon$	0.01	0.02	0.05	0.08	0.18	0.35	0.60	0.88	0.99
$\Delta E^{\mathrm{ES}}/\epsilon$	0.92	0.98	0.95	0.92	0.82	0.65	$0.40 + \frac{\ln 2 \cdot k_{\mathrm{B}}T}{\epsilon}$	$0.12 + \frac{\ln 2 \cdot k_{\mathrm{B}}T}{\epsilon}$	$0.01 + \frac{\ln 2 \cdot k_{\mathrm{B}}T}{\epsilon}$
$\Delta E^{\mathrm{b}}/\epsilon$	2.12	1.45	1.19	1.08	1.02	1.00	1.00	1.00	1.00

Part 2

Dielectric Effects in Self-assembly

CHAPTER 4

A Review of Dielectric Effects in Mesoscale Simulation

The content of this chapter is based on the following publication:

- Max Meirow, Ziwei Wang, and Erik Luijten, "Dielectric effects in mesoscale simulation," To be published (2020).

4.1. Introduction

Electrostatic interactions play a fundamental role in determining the spatial organization and dynamic behavior of soft matter systems[114–116]. Examples of their significance abound in the natural sciences, ranging from the assembly of nanoparticle[117] and colloidal crystals[30] to protein folding and binding[118]. Thorough yet efficient treatment of charged systems in molecular dynamics and Monte Carlo simulation is now routine due to a variety of algorithms which greatly accelerate the long-ranged calculation[119–123]. However, such simulations will often treat the dielectric constant as a spatially uniform constant throughout the system, therefore neglecting effects which arise from the electrostatic polarization at dielectric interfaces.

In soft matter systems, common values of the dielectric constant range from $\epsilon_r \approx 2$ for many polymers to $\epsilon_r \approx 80$ for water at room temperature[111]. A spatially uniform dielectric constant screens the free charges of the system by a degree proportional to ϵ_r, but in systems with a piecewise uniform permittivity, dielectric mismatch at the interfaces induces a polarization or bound charge. Notably, the polarization charge modulates a variety of physical

phenomena, including colloidal self-assembly[50], ion transport[37], the structure and stability of emulsions[124,125], and the charging process in supercapacitors[126]. Thus, incorporation of dielectric effects in simulation is physically motivated in a range of systems, if often neglected because of the complexity of the polarization computation.

Accurate evaluation of these many-body dielectric effects is numerically demanding and analytically intractable except for simple geometries such as spheres, planes, and infinite cylinders. In response, a variety of numerical methods have been developed which solve for the electrostatic potential with the inclusion of the polarization charge. The polarization can be coarsely modeled as an electric dipole, ignoring higher-order contributions. A system consisting of many inducible dipoles can be solved self-consistently, approximating polarization effects in dielectric materials[127,128]. Boundary element methods solve for the surface bound charge on a discretized two-dimensional interface, permitting arbitrary geometries[50]. Relevant vectorial or scalar field variables such as polarization or polarization charge density can be used in a variational formulations of the electrostatic potential[129–131]. Finally, for geometrically simple dielectric objects, image charges facilitate solution of the Poisson equation for the electrostatic potential[40]. The relative merits and limitations of these techniques will be evaluated in this work.

Herein, we highlight soft condensed matter systems within the mesoscopic length scale, i.e., matter exhibiting a characteristic length of hundreds of nanometers to a few micrometers. For example, our scope includes colloidal suspensions and coarse-grained biological macromolecules. Studies which treat electronic polarization at the atomistic level, such as simulations using polarizable molecular mechanics force fields or potentials for "soft" ions and atoms, are reviewed thoroughly elsewhere[132–137]. Earlier reviews evaluating the treatment of polarization effects in theory and simulation have highlighted a single method or

physical system (e.g., a single charged particle in an external electric field)[138–142]. In this review, we aim instead to offer a comprehensive survey and comparison of the methods used to investigate dielectric effects in coarse-grained molecular dynamics (MD) and Monte Carlo (MC) simulations. In Section 4.2, we will review the methods most often employed for handling polarization in simulation: dipolar methods, boundary element methods, variational methods, and image charge methods. As means of illustration, we will highlight key physical phenomena attributable to polarization effects which have been observed in such studies in Section 4.3. We will conclude by surveying the remaining challenges which limit contemporary computation and indicate future directions of research.

4.2. Numerical Methods

Methods for determining electrostatic polarization at dielectric interfaces are essentially seeking direct numerical solutions to the Poisson's equation which converge efficiently. In this section, we will review four different categories of methods and provide a table summarizing the efficiency, applications, and available implementations for each method in the end. Before proceeding to each category, we first provide a brief mathematical formulation of the problem.

As a matter of illustration, we consider an ensemble of N dielectric spheres, in which sphere i ($i = 1, \ldots, N$) is centered at $\mathbf{o}_i$, has a radius a_i and a dielectric constant ε_i, and carries a central charge Q_i. The spheres do not overlap and are embedded in a continuum background solvent with dielectric constant ε_{s}. The internal dielectric constants ε_i are generally different from ε_{s}, resulting in polarization contributions to the electrostatic potential that need to be resolved.

We start by seeking the expression for the electrostatic energy. First, for any given free charge density $\rho_{\mathrm{f}}(\mathbf{r})$ that generates a potential field $\Phi(\mathbf{r})$ and is embedded in a dielectric

medium, the electrostatic energy U can be written as[143]

$$U = \frac{1}{2} \int \rho_f(\mathbf{r})\Phi(\mathbf{r})d\mathbf{r} \ . \tag{4.1}$$

In the model we consider, the free charge density originates from the N point charges at the centers of the dielectric spheres, i.e.,

$$\rho_f(\mathbf{r}) = \sum_{i=1}^{N} Q_i \delta(\mathbf{r} - \mathbf{o}_i) \ , \tag{4.2}$$

where $\delta(\cdot)$ is the Dirac delta function. Moreover, the electrostatic potential $\Phi(\mathbf{r})$ satisfies the Poisson equation,

$$-\nabla \cdot [\varepsilon(\mathbf{r})\nabla\Phi(\mathbf{r})] = \rho_f(\mathbf{r}) \ , \tag{4.3}$$

where

$$\varepsilon(\mathbf{r}) = \begin{cases} \varepsilon_i & \text{if } \mathbf{r} \text{ inside sphere } i, \\ \\ \varepsilon_s & \text{if } \mathbf{r} \text{ in the exterior region,} \end{cases} \tag{4.4}$$

and on each spherical interface S_i $(i = 1, \ldots, N)$ the electric potential $\Phi(\mathbf{r})$ has to satisfy the standard dielectric interface conditions,

$$\Phi(\mathbf{r}^-) = \Phi(\mathbf{r}^+) \ , \qquad\qquad \mathbf{r} \in S_i \ , \tag{4.5}$$

$$\varepsilon_i \frac{\partial \Phi(\mathbf{r})}{\partial \mathbf{n}}\bigg|_{\mathbf{r}=\mathbf{r}^-} = \varepsilon_s \frac{\partial \Phi(\mathbf{r})}{\partial \mathbf{n}}\bigg|_{\mathbf{r}=\mathbf{r}^+} \ , \qquad\qquad \mathbf{r} \in \mathcal{S}_i \ , \tag{4.6}$$

where $\mathbf{r}^-$ and $\mathbf{r}^+$ refer to the limits approaching the interface from the inside and outside, respectively, and $\mathbf{n}$ is the surface outward unit normal vector at $\mathbf{r}$. In addition, we impose the vanishing far-field boundary condition, i.e., $\Phi(\mathbf{r}) \to 0$ as $|\mathbf{r}| \to \infty$. Once $\Phi(\mathbf{r})$ has

been obtained, the electrostatic energy can be calculated and the electrostatic forces can be obtained through differentiation.

It is worth noting that an alternative way to solve for the electrostatic potential $\Phi(\mathbf{r})$ is via the bound charge density $\rho_b(\mathbf{r})$, which satisfies

$$\rho_b(\mathbf{r}) = -\nabla \cdot \mathbf{P}(\mathbf{r}) . \tag{4.7}$$

Assuming a linear polarization field $\mathbf{P}(\mathbf{r}) = [\varepsilon(\mathbf{r}) - 1]\mathbf{E}(\mathbf{r})$ and substituting the electric field $\mathbf{E}(\mathbf{r}) = -\nabla\Phi(\mathbf{r})$, one obtains

$$\rho_b(\mathbf{r}) = \nabla \cdot \{[\varepsilon(\mathbf{r}) - 1]\nabla\Phi(\mathbf{r})\} . \tag{4.8}$$

Combining this expression with Eq. (4.3), one obtains the well-known result[144]

$$-\nabla^2\Phi(\mathbf{r}) = \rho_f(\mathbf{r}) + \rho_b(\mathbf{r}) . \tag{4.9}$$

This is a Poisson equation with constant coefficient, so that the solution $\Phi(\mathbf{r})$ can be simply represented as the standard Coulomb potential due to both the free and the bound charge density,

$$\Phi(\mathbf{r}) = \int \frac{\rho_f(\mathbf{r}') + \rho_b(\mathbf{r}')}{4\pi|\mathbf{r} - \mathbf{r}'|} d\mathbf{r}' . \tag{4.10}$$

Substitution of Eq. (4.10) into Eq. (4.1) allows the electrostatic energy to be expressed as

$$U = \frac{1}{8\pi} \iint \rho_f(\mathbf{r}) \frac{[\rho_f(\mathbf{r}') + \rho_b(\mathbf{r}')]}{|\mathbf{r} - \mathbf{r}'|} d\mathbf{r}' d\mathbf{r} . \tag{4.11}$$

The singularity at $\mathbf{r}' = \mathbf{r}$ due to the direct Coulomb interaction of point free charges should be discarded to render the integral finite. The remaining problem in Eq. (4.11) is that the

bound charge density $\rho_{\text{b}}(\mathbf{r})$ is still unknown. For systems with arbitrarily shaped dielectric bodies, the boundary element methods (see Section 4.2.2) and variational methods (see Section 4.2.3) can be employed to numerically obtain $\rho_{\text{b}}(\mathbf{r})$. For the current system of dielectric spheres, the hybrid method framework (an image-charge based method) makes it possible to effectively represent the bound charge density $\rho_{\text{b}}(\mathbf{r})$ as a combination of multipole moments and image charges (see Section 4.2.4).

4.2.1. Approximate Dipolar Methods

Fundamentally, dipolar methods are based on the description of polarization as an electric dipole moment per unit volume[143,145]. Dipolar approximations of polarization effects may be classified by whether they employ constant or mutually-dependent dipoles, and whether a single dipole or multiple dipoles are used to represent a mesoscale dielectric object[127,128]. The term approximation is used here as multipolar contributions to the electrostatic potential and interaction energies are neglected in this family of methods. Such an approximation is most sound when the particles are separated by a distance considerably greater than their diameter, and begins to break down the nearer the particles approach one another.

Constant, or permanent, dipole models, though computationally inexpensive, are not suitable for capturing complex, many-body dielectric effects and physical phenomena associated with polarization[146,147]. In a constant dipole model, the dielectric "objects" in a simulation possess a dipole moment which is linearly proportional only to the applied external electric field. The magnitude of the induced moment depends on the polarizability of the particles. The calculation of the electrostatic interaction between particles of a constant dipole moment is a routine textbook exercise.

For anisotropic colloids, including spherocylinders, ellipsoids, dumbbells, and rods, a related two-charge model may be more appropriate[6,148–151]. In the two-charge model of polarization, two point charges which possess equal magnitude but opposite sign are placed along the long axis of the colloid and are separated by a tunable distance d[149]. The separation distance is chosen so that the potential of the two point charges equals the potential of a permanent dipole. The advantage of the two-charge model over a constant dipole model is that interaction energy between pairs of adjacent particles is simply the sum of their Coulombic interactions[127].

As the density of particles in the system increases, the constant dipole method and two-charge models are not an acceptable approximation because many-body effects are neglected. The dipole moment of a given particle depends not only on the effect of the external electric field but also on the local electric field generated by the induced dipoles of neighboring particles. Accordingly, a better approximation of the interaction energy of polarizable particles must employ a self-consistent calculation. In the literature, this is sometimes referred to as the "mutual dipole model."[128]

Self-consistent dipolar methods were pioneered in the 1960s, in a method referred to as the coupled dipole method (CDM)[152,153]. This method employs the atomistic Lorentz model, in which each atom is represented by a nucleus and a lone electron harmonically bound together. Many such atoms may exist in a cluster, and the ground state potential energy, including their complete, many-body interactions, can be calculated from the sum of the eigenfrequencies of a set of harmonic oscillators. Initially, the coupled dipole method was used to calculate the static polarizabilities of clusters of atoms featuring different geometries[154,155]; a similar derivation is found in Ref. 156, which does not include the formalism of Lorentz atoms. Another extension of the CDM includes image dipoles in the case of a dielectric rod near a

planar surface[157]. For an in-depth discussion of image charges used in simulation of dielectric materials, see Section 4.2.4.

Later, this same self-consistent method was used to calculate the electrostatic interaction energies between colloids of various shapes induced by an applied electric field[127]. In this work, they compared two self-consistent methods, one in which the particles were represented by a single point dipole and another in which the three-dimensional dielectric object is discretized into "chunks," each of which possesses an inducible dipole moment. As the number of point dipoles in the latter method increases, so does the accuracy of the resulting energy. Given the expensive matrix operations which must be calculated in this method, only pairs of interacting particles were considered (though the formalism can handle many-body effects) and implementation in MD or MC simulations involving many particles would be unwieldy. Other examples of self-consistent dipoles used to model polarization may be found in Refs. 128 and 148.

4.2.2. Boundary Element Methods

Boundary element methods (BEM) are often employed when the solution of the partial differential equations (the Poisson equation for our problem) are expressed using boundary integral equations. Considering the system consisting of sharp dielectric interfaces, the boundary integral problem reduces to solving for the induced charge density on the surface patches where the dielectric permittivity has a discontinuity. Levitt[46] first applied such a technique to systems with cylindrical symmetry, and Zauhar et al.[47,158] further extended the method to arbitrary geometries. The reader may refer to review articles[159,160] if interested in the historical developments in the field.

The advantages of the BEM are manifold: there is no constraint on the geometry, the number of unknown (N) is reduced by an order of magnitude compared with methods involving volume discretization (e.g., finite element method or finite difference method), and boundary conditions at infinity (open region problems) can be exactly treated. One notable disadvantage is that although the number of unknowns N is reduced, discretizing the boundary integral equations produces dense linear systems whose memory costs scale as $\mathcal{O}(N^2)$ and solution costs scale as $\mathcal{O}(N^3)$ in the direct solution approach. Moreover, singular boundary integrals affect the accuracy and stability of the solution.

Different approaches have been proposed to accelerate the BEM in order to enable large-scale dynamical simulations[48–50,129,130,161,162]. Here Refs. 129 and 130 are also classified as variational methods and will be covered at length in Section 4.2.3. Bharadwaj et al.[161] developed an adaptive method of successive over relaxation (SOR) to solve the linear matrix equation and applied FMM to calculate the Coulombic interaction between surface elements by linear time cost. Boda et al.[48] proposed an induced charge computation (ICC) method which computes the polarization charges based on the variational formulation of Allen et al.[129]. The minimization of the functional yields a matrix equation $A\mathbf{h} = \mathbf{c}$ where the vector $\mathbf{h}$ contains induced charges for each surface element. Note that this matrix formulation is the same as the one previously introduced by Hoshi et al.[163] through different ways of derivation and is used as basis for later work[49,50]. Since the matrix A only depends on the geometry of the dielectric medium, it needs to be inverted only once at the beginning of the simulation for the systems containing only static dielectric interfaces. Thus, the ICC method scales as $\mathcal{O}(N_{\mathrm{e}}^2)$ in its basic implementation, where N_{e} is the number of surface elements.

However, considering the systems consisting of dynamical dielectric interfaces, it requires $\mathcal{O}(N_{\mathrm{e}}^3)$ operations to solve the matrix equation at each time step. To tackle this problem,

Barros et al.[50] presented a collection of techniques to accelerate simulation of dynamical dielectric objects. Specifically, they solve the matrix equation using the Generalized Minimal Residue method (GMRES), where each GMRES iteration is evaluated using a fast Ewald solver with cost that scales linearly or near-linearly to N_e. The GMRES is found to converge in very few iterations, as the matrix A is positive definite and the residual error decreases exponentially with the number of iterations. The memory allocation required by this GMRES-accelerated method is on the order of N_e, as it needs to store the residual vector and vectors spanning the Krylov subspace at each iteration. Given its competitive efficiency and the flexibility of the BEM on geometry of interfaces, large-scale MD simulations have been done to explore dielectric effects in different systems, such as the self-assembly process of polarizable particles[164] and electric double layer near a dielectric anisotropic particle[165,166] or a structured polarizable interface[167]. Alternatively, Tyagi et al.[49] proposed another efficient iterative algorithm for periodic systems, named the ICC* method, where the * represents any choice of the solver for the electrostatic field (e.g., FMM, Particle-Particle Particle-Mesh, Ewald summation etc.). By reformulating the matrix equation into the form of $\mathbf{h} = B\mathbf{h}$, they applied the SOR approach, similarly with Bharadwaj et al., to solve for the induced charges. In practice, the ICC* method does not require large memory space (linearly to N_e), and its bottleneck is the number of calculations of electric field until convergence.

More recently, an $\mathcal{O}(N_e)$ and scalable parallel approach was developed for BEMs by Jiang et al.[162]. The boundary integrals are accelerated using a kernel-independent FMM which utilizes Chebyshev interpolation and low-rank approximation. The approach does not require storage of the matrix and thus scales as $\mathcal{O}(N_e)$ for memory cost. Notably, the magnetostatic problem can be solved here in the framework of a hybrid finite element (FEM)–BEM, as the volume mesh is required to account for the non-zero volume pole density

$\nabla \cdot \mathbf{M}(\mathbf{r})$, where $\mathbf{M}(\mathbf{r})$ is the magnetization density of the magnetized body at $\mathbf{r}$. The details of the implementation as well as its distribution are presented in Ref. 162. Moreover, the GMRES-accelerated BEM, the ICC* method, and the direct optimization of the functional by Jadhao et al. (cf. Section 4.2.3) are implemented and available for download,[168] where their performance are also compared in different systems.

4.2.3. Variational Methods

Variational methods provide approximate solutions to many physical problems including those involving electronic polarization. Fundamentally, this approach is based on the principle that there exists a unique electrostatic potential function which describes a system at its minimum electrostatic potential energy[143,145]. The potential function must satisfy the Poisson or Laplace equations with the relevant boundary conditions (Dirichlet or Neumann) for the system at equilibrium. An archetypal variational approach to electrostatic problems follows these steps: (1) Construct a trial function of the electrostatic potential or another electrostatic quantity which depends on a number of variable parameters; (2) Select a functional (often the electrostatic energy) of the trial function; (3) Iteratively refine the variational parameters of the trial function to identify the maximum or minimum of the functional. Since at least the 1950s[169], a number of variational methods which treat electronic polarization have been explored[124,129–131,143,169–183]. Of these, only a select few have been implemented in MC or MD simulations[129–131,179,180].

The first variational methods for the solution of the electrostatic potential employed the polarization $\mathbf{P}(\mathbf{r})$ as a field variable. This class of variational formulation was proposed in 1956[169]. The overall polarization was expressed as the vector sum of two independent polarization components: one which is proportional to the local electric field strength and one

which is field-independent. This definition was employed in a functional of the electrostatic free energy which contains several vector functions of various electric fields and polarizations. The functional introduced in Ref. 169 is frequently invoked alongside another free energy functional of the polarization, originally derived in a study of thermal fluctuations in dielectric, magnetic media[178].

The variational methods introduced in Refs. 169 and 178 were not immediately implemented in simulation. Nonetheless, they laid a groundwork for future variational formulations employed in MC and MD schemes. The functional developed by Marcus has been re-expressed in terms of the vectorial polarization and displacement and used to simulate the dielectric response of polarizable media via a cluster Monte Carlo algorithm.[181] Notably, the method proposed in Ref. 181 was also employed in the modeling of nonlinear dielectric response, with comparable computational efficiency with respect to purely linear media. Another variational method which treats nonlinear dielectric functions has been derived–though not implemented in simulation–which is also capable of handling spatial variation in the permittivity[184].

In MD simulations, a method based on the variational formulations of Marcus and Felderhof was used to calculate the forces associated with the electrostatic free energy.[179] Motivated by the application of biomolecules in a dielectric continuum, the functional is minimized according to Car-Parinello-like scheme[185] in which the polarization fields are evolved at the same time as particle coordinates. Numerical solution is facilitated by pseudospectral expansion of the polarization field using a plane wave basis set. Consequently, the fast Fourier transform may be applied, resulting in an algorithm with a computational complexity directly proportional to the number of particles in the simulation.

A few variants of functionals which employ the polarization charge density $\rho_{\mathrm{b}}(\mathbf{r})$ have been proposed. In Ref. 129, a variational method which closely follows the derivation outlined in Ref. 143 is described. Here, the extremum of the functional is a local minimum which equals to the negative of the total electrostatic energy. While this method is suitable for an arbitrary configuration of free charges, the major drawback of this functional is its lack of intuitive physical meaning. The functional of Ref. 129 is not an energy functional, meaning that values of the functional away from its minimum do not correspond to the system's electrostatic potential energy. Accordingly, this method is not suitable for dynamical optimization techniques such as Car-Parinello-like molecular dynamics. Instead, at each time step, the polarization surface charge density must first be optimized before calculating the forces acting on the charges and updating their positions.

Energy functionals offer attractive advantages for implementation in simulation. In Ref. 131, an energy functional with the polarization charge density as the exclusive field variable is derived. To ensure that the functional yields the total electrostatic energy, a constraint such that the polarization charge density equals a specific functional of the spatially-varying polarization charge density is imposed. This so-called "true" energy functional differs from previous, related functionals in the form of the Lagrange multiplier which enforces that constraint[130]. The earliest example of this functional handles a single dielectric interface, while follow-up work has extended the method to simultaneously treat multiple dielectric interfaces[124].

The true energy functional of Ref. 131 may be numerically minimized via a simulated annealing procedure and implemented in molecular dynamics simulations. Minimization of the functional occurs concurrently with the update of particle coordinates, in contrast to

Ref. 129. Accordingly, the variational approach outlined here is described as Car-Parinello-like. This is somewhat misleading as quantum effects are of course neglected in classical, particle-based, mesoscale simulations.

The method highlighted in Refs. 130,131 is closely related to an earlier variational formulation[177]. Both sources develop a functional of the total electrostatic energy suitable for dynamical optimization with the polarization charge density as the variational parameter. They diverge in that the functional form of Ref. 177 requires that all free charges reside in a single, uniform dielectric continuum adjacent to a charge-free region with a different relative permittivity. On the other hand, the variational formulation in Refs. 130,131 is suitable for any configuration of free charges without the former's contingency.

4.2.4. Image Charge Methods

The image charge method (ICM) is generally only available for simple geometries, such as planar, spherical, or cylindrical interfaces. For a slab geometry, the ICM can be efficiently incorporated into the Ewald summation[186–188] and numerous simulations have been conducted to study different dielectric modulated phenomena, including polymer adsorption[189], ionic structure[190], ion mobility[37,191], and pattern formation[192] near a polarizable flat interface.

Recently, more attention has been paid to systems consisting of multiple dielectric spheres, which is able to represent a wide range of biological and synthetic systems such as colloidal suspensions and proteins[193–196]. For a single dielectric sphere, it is well known that the Green's function can be efficiently computed by an image-line construction, namely a point charge plus a line charge density distributed from the sphere center to the Kelvin point. This was first discovered by Neumann[40] and rediscovered several times in different areas[197]. The extension of the ICM to the treatment of multiple spheres can be achieved through different

formalism. Xu et al. has extended the discrete image approximation of the Neumann's image principle to multi-sphere case by recursive reflections of image charges among different dielectric interfaces[198,199]. The ICM is accurate when spheres are close, as the singular quadrature problem for the image line charge integral has been well approximated. However, it has been shown that as the number of spheres N grows, the computational cost of ICM increases as a power law ($\sim \mathcal{O}(N^3)$) due to the repeated image reflection between spheres[200]. The other image-charge based method is the multiple-scattering formalism, developed by Qin et al., which solves for the potential iteratively by considering chains of interfacial polarization with increasing complexity[52,201]. Here the total energy of the system is written as a series expansion including one-body, two-body, and higher-order energies which involve more surface scatterings. Therefore, every term in the series can bear a physical interpretation. The formalism has been extended to the polarizable dipolar systems as well[202]. However, similar with the recursive reflection formalism, the computational cost grows rapidly with number of particles and scales as $\mathcal{O}(N^m)$ if the expansion is truncated at the level of m-body interactions. The method and its application are well summarized in a recent review[142].

In order to deal with the low efficiency of the ICM when the number of spheres is large, an efficient and spectrally accurate hybrid method was recently developed, which combines the ICM with the Method of Moments (MoM)[53]. The MoM can be further accelerated via the FMM to achieve scaling that is linear with the number of spheres N. The basic idea of this hybrid method is as follows. If the dielectric spheres are well separated, the MoM is coupled with the FMM and an iterative solver to take advantage of the spherical geometry and achieve optimal complexity. If the spheres are close to each other, images are generated only for nearly touching pairs of spheres and the ICM is applied. The computational cost

for both the MoM and the ICM parts is linear to N[203]. This method has been recently incorporated in a MD simulation and demonstrates simultaneously linear scaling behavior and high accuracy[203]. A systematical comparison between the hybrid method and the GMRES-accelerated BEM was conducted in terms of accuracy and efficiency at different parameter settings (see Chapter 7). Particularly, for densely packed configurations of relatively small numbers of dielectric spheres, the hybrid method computes the electrostatic energy with a deviation of less than 0.01% at a rate that is more than two orders of magnitude faster than the BEM can achieve with deviations of 3%.

For nonspherical geometries, system containing cylindrical interfaces has attracted much attention as a model system to study biological ion channels[196,204–206]. In Ref. 205, an optimization method was used to find the image representation for cylinder by fitting the exact expression in terms of cylindrical harmonics. In Ref. 206, the ICM was developed for a source charge inside a finite length cylinder due to the electric polarization of the surrounding inhomogeneous continuum. Moreover, the two-level ICM was recently utilized a method to evaluate Green's function in irregular domains[207].

4.2.5. A Brief Comparison Between Different Methods

In order to provide a brief overview of different methods of solving the polarization problem, we construct a table below (Table 4.1) including the time/memory cost, feasibility, and open-source availability of each method. It can be seen that while the BEM (as well as the variational methods) is advantageous in dealing with interfaces of irregular geometries, the ICM, especially the hybrid method by Gan et al., remains more efficient and accurate for close-packed multi-sphere systems, which would require a significant amount of surface elements if using the BEM.

Table 4.1. A table summarizing the advantages, disadvantages as well as the efficiency of different methods to solve the polarization problem. Note that VM is short for variational method, and the symbols N_e, r_e, N, and m below denote the number and the size of surface elements, the number of polarizable spheres, and the level at which the image reflections are truncated, respectively.

	Advantages	Disadvantages	Different Implementations	Time	Memory	Open Source Distribution
BEM & VM	Apply to arbitrary geometries	Singularity when interfaces are close leads to large error $(\sim \mathcal{O}(r_e))$	ICC* by Tyagi et al.	$\mathcal{O}(N_e)$ at best	$\mathcal{O}(N_e)$	bitbucket.org/ndtrung/lammps or ESPResSo software[139]
			GMRES–BEM by Barros			bitbucket.org/ndtrung/lammps
			Kernel–BEM by Jiang et al.			ime-code.uchicago.edu
			Functional by Jadhao et al.		$\mathcal{O}(N_e^2)$	bitbucket.org/ndtrung/lammps
ICM	Accurate for close interfaces	Apply to only simple geometries	Recursive reflection by Xu et al.	$\mathcal{O}(N^m)$	$\mathcal{O}(N^m)$	Not found
			Multiple-scattering by Qin et al.			Not found
			Hybrid method by Gan et al.	$\mathcal{O}(N)$	$\mathcal{O}(N)$	Not found

4.3. Representative Applications

There are numerous physical and chemical problems in which electronic polarization plays a prominent role. In this section, we select several illustrative applications of the methods described previously. These examples demonstrate the diversity of systems accessible to computational study and indicate the importance of including dielectric effects in mesoscale simulations.

4.3.1. Assembly

Electronic polarization contributes to assembly at the mesoscale, by which we broadly mean the spatial organization and ordering of constituent components of the system[50,128,192,208,209]. In the presence of an applied external field, polarizable particles will align and reach a thermodynamically favorable equilibrium configuration[128]. This result for particles with inducible dipole moments is physically intuitive. Such assembly of particles may not be

considered true "self"-assembly, since their collective ordering depends on an external driving force, namely an AC or DC field.

In the absence of an applied field, dielectric effects have been shown to play a role in the true self-assembly of colloids[164], pattern formation involving metamaterial substrates[192], and the ordering of ion-containing droplets in oil/water emulsions[124]. In Ref. 164, as the temperature of a binary mixture of charged colloidal particles is reduced, the particles spontaneously assemble into different structures (strings, sheets, and NaCl crystal) depending on the degree of dielectric mismatch between small and large particles (Fig. 4.1). A later study also claims to display dynamic self-assembly driven by the dielectric mismatch of interacting particles, though the simulation methods used therein are relatively crude in comparison to Ref. 50 and no claim regarding accuracy is made[208]. In a quasi-two-dimensional scenario, systems of dipolar spheres atop a substrate will exhibit different spatial patterns as the dielectric mismatch (between particle and substrate) or particle geometry is tuned, yielding complex phase diagrams[192]. Finally, the aggregation of droplets in an oil/water emulsion was demonstrated to depend on their surface polarization, which contributes an attractive inter-droplet force[124].

4.3.2. Transport

Dielectric effects have been demonstrated to modulate transport processes, ranging from the macromolecular scale down to the motion of individual ions in solution[37,191,210,211]. The translocation of biological macromolecules through solid state nanopores is relevant to applications such as real-time DNA sequencing technologies.[212] The dielectric mismatch between the solvent and nanopore gives rise to a repulsive force within the pore channel which impedes the transport of a highly-charged DNA molecule[211]. The impact of pore polarization on the
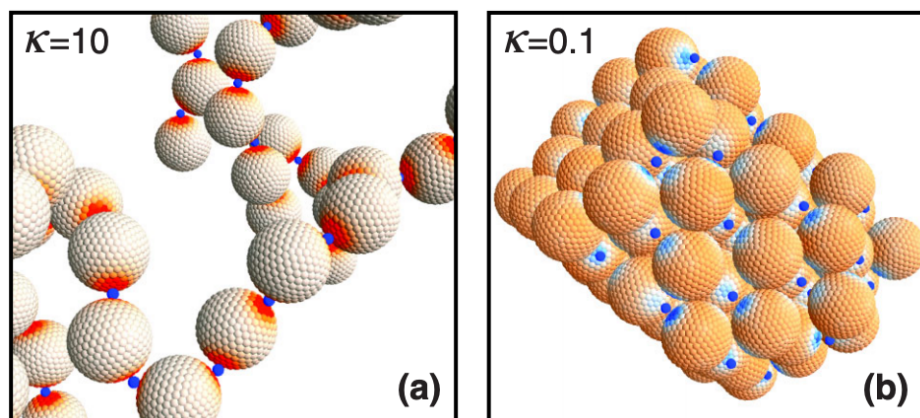
Figure 4.1. Structures formed by dynamical polarizable colloids in MD simulation. The large colloids are positively charged, the small colloids are negatively charged, and the induced surface charges are represented by red (positive) and blue (negative) color gradients. In the left panel, the string-like structures emerge as a result of dielectric many-body effects when κ, the reduced dielectric constant of large colloids, is large. Adapted from Ref. 164.

translocation of DNA was recently investigated by MD simulation as shown in Fig. 4.2[210,211]. After discretizing the surface charge density on the pore, the authors of Refs. 210,211 compute the dielectric boundary force by means of the ICC* algorithm[49]. The computed free energy profiles for the translocation of both single-stranded and double-stranded DNA (ssDNA and dsDNA, respectively) shows an increase in the translocation barrier height of ssDNA relative to dsDNA. The authors attribute this discrepancy to the greater flexibility of the ssDNA chain which increases its proximity to the induced charges on the wall of the pore channel. The dielectric boundary force is shown to be affected by salt concentration, with the energetic barrier height inversely related to salt concentration due to screening effects.

The mobility of ions near a surface is qualitatively different than their mobility in the bulk. In Ref. 37, the authors rationalize this discrepancy in ionic behaviour by examining
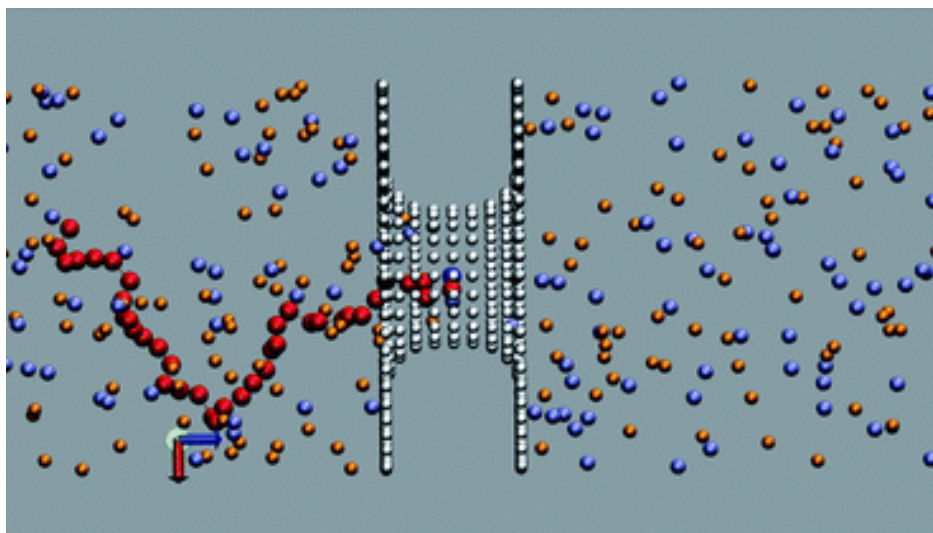
Figure 4.2. Translocation of a flexible ssDNA polymer (red beads) through a solid-state nanopore with explicit monovalent counterions (orange and blue) present. For the ICC* algorithm, the nanopore has been discretized as shown by the white beads. Adapted from Ref. 211.

the contribution of surface polarization. They show that the mobility of ions near a dielectric interface may be modulated by varying the dielectric mismatch between the solvent and the surface. The model system employed in Ref. 37 consists of explicit ions in a dielectric continuum representing the solvent; the planar geometry of the model makes the method of images the most efficient choice for computing surface polarization effects. Surprisingly, they observe that ion mobility increases near surfaces with a high relative permittivity and decreases near surfaces with a lower permittivity. This phenomenon is attributed to distortions in the shape of the counterion atmosphere surrounding the ion of interest, which result from interactions with the induced surface charges. A similar effect on ion mobility is observed in a system consisting of coarse-grained polyelectrolyte brushes grafted to a dielectric surface[191].

4.3.3. Electric Double Layer Structure

The electric double layer (EDL) refers to the diffuse atmosphere of counterions which are attracted to co-ions of opposite charge on the surface of a dielectric material immersed in a liquid[111]. For a polarizable material, the counterions will induce an additional charge on the surface of the dielectric, which in turn influences the density profiles of the ions in the EDL.

One applied example of the importance of elucidating the EDL structure is found in the charging of supercapacitors. The efficient storage of electrical energy is a central challenge in the development of technologies for renewable energy. Supercapacitors, occasionally referred to as double-layer capacitors, outperform conventional batteries in some aspects of energy storage. Namely, they have rapid charge-discharge cycles and can undergo millions of such cycles before the device is retired[126]. Supercapacitors contain an ionic liquid, accumulating and conducting charge via its interaction with porous electrodes. Recently, simulation studies have attempted to reveal new insights into the parameters such as electrode composition and charging cycle protocol which control supercapacitor performance, in particular energy density[126,213–215]. In the case of constant potential, surface structure and finite pore length of the nanoporous channels significantly influences adsorption of ions and their resulting density profiles near the electrode[213,214].

4.4. Conclusion

Dielectric effects may play an important, if often neglected, role in coarse-grained, mesoscale simulation. Over the past several decades, a number of attempts to accurately and efficiently treat polarization in MD and MC simulation have been reported. In this Review, we have

offered a survey of these methods, highlighting approximate dipolar, boundary element, variational, and image charge methods. These techniques have been applied to study various physical phenomena such as ion transport, self-assembly, and charging behavior.

Looking forward, promising directions of future research include:

- developing efficient algorithms for handling non-linear dielectrics where the polarization has a non-linear dependency on the electric fields;

- incorporating anisotropic dielectric objects which possess a tensor-like dielectric constant than a scalar;

- extending current methods to efficiently include a continuously varying permittivity (unlike the systems with piecewise uniform permittivity considered here). Note that this problem currently can be dealt with by the Maxwell equation method (implemented in ESPResSo)[180,216–219] or finite element method, but such techniques are very computationally costly.

CHAPTER 5

Structural and Dynamical Properties of Dipolar Fluids Near a Dielectric Interface

The content of this chapter is based on the following publication:

- Z. Wang and E. Luijten, "Structural and dynamical properties of dipolar fluids near a dielectric interface," To be published (2019)

5.1. Abstract

Dipolar fluids belong to the most fundamental classes of model liquids, providing insight into the structural and thermodynamics properties of a wide range of polar liquids. Spatial confinement can have a profound influence of such properties, inducing anisotropy as well as steric constraints. Owing to the electrostatic interactions in dipolar fluids, an additional effect arising in the presence of interfaces is the dielectric mismatch between medium and substrate. Until now, this effect has largely been ignored in computational studies. Here, we extend the dipolar Ewald summation to incorporate induced polarization for arbitrary permittivity mismatch between medium and substrate, and systematically study the ferroelectric transition and local structural properties of a confined dipole hard-sphere fluid. We demonstrate that while the global polarization only has a weak dependence on substrate permittivity, the dipolar orientation in the contact layer is significantly affected, as is the anisotropy of the rotational dynamics.

5.2. Introduction

The dipolar interaction, one of the most fundamental anisotropic potentials, plays an essential role in many physical systems of technological interest, including ferrofluids[220–222], electrorheological fluids[223], and polar fluids[224,225]. The simplest models described by dipolar interactions are the dipolar hard-sphere (DHS) and soft-sphere fluids, where a permanent point dipole is affixed to the center of each sphere. A variety of fundamental problems related to dipolar systems, including structural properties[226–228], phase behavior[229–232], and dynamics[233,234] have been studied via this model.

Many applications of dipolar systems involve spatial confinement, e.g., polar solvents within narrow pores and thin films of magnetic colloids or ferrofluids[235–239]. Numerous simulations have been conducted of dipolar systems under confinement[236,240–248], and demonstrated that various properties are significantly affected by the spatial confinement. Examples include wall-induced anisotropy and slow-down of dynamics[240,242,246], the inhomogeneity of density profile[241,242], and dielectric response[242,245,247], the enhancement of orientational order[243], and the emergence of layered structures under external field[248]. However, a parameter that, owing to its complicated many-body nature, is typically ignored is the dielectric mismatch between the substrate and the medium in which the dipolar spheres are suspended. This means that one effectively assumes that the substrate is simply characterized by a dielectric constant (ϵ_s) equal to the permittivity of the confined medium (ϵ_m). This omission is noteworthy, given that (i) dielectric contrast across the interface is unavoidable in nearly all real applications and (ii) the polarization charge resulting from the dielectric mismatch results in additional forces that can alter the structural properties and dynamical behavior of the dipolar system. Moreover, it has already been demonstrated that substrate permittivity

can affect the properties of a wide range of electromagnetic systems, from plasmonics[36] to ion mobilities in electrolytes[37] and polyelectrolyte brushes[191].

A notable exception in the existing literature, incorporating dielectric boundary effects on a dipolar fluid, concerns the extreme case of confinement between two conducting plates $(\epsilon_s = +\infty)$[187]. This is a special situation that can be approximated by a periodic system, simplifying the mathematical treatment. Somewhat surprisingly, no qualitative differences were observed in this system compared with the situation without dielectric effects. Here, we demonstrate that this finding resulted from the particular choice adopted for the repulsive fluid–substrate potential[187], which prevented the dipolar particles from approaching the interface very closely. This in turn suppressed polarization effects, which depend on the dipole–wall separation. In the present work, we employ hard sphere–wall interactions that do not suffer from this limitation. Moreover, to the best of our knowledge, no prior studies exist that explore the opposite case of a low-permittivity interface, $\epsilon_s < \epsilon_m$, where the polarization is qualitatively different.

To address these open questions, we perform Monte Carlo (MC) simulations of a DHS fluid confined between two hard walls, one of which has a permittivity mismatch with the medium. We investigate the global isotropic–ferroelectric transition and local structural properties as a function of dielectric mismatch and in different density regimes. To elucidate the origin of the orientational preferences observed for various boundary conditions we compute the ground-state energy of typical configurations. Interestingly, we find that the orientational dynamics depend on the interfacial dielectric mismatch as well. We are able to obtain these results by incorporating image-dipole effects into the dipolar Ewald summation. This approach is applicable to interfaces with arbitrary mismatch in permittivity.

This paper is organized as follows. We introduce the model in Sec. 5.3.1 and derive the Ewald summation for the total energy of the system, taking into account both the slab geometry and polarization effects, in Sec. 5.3.2. The simulation method and definition of important parameters are provided in Sec. 5.3.3. In Sec. 5.4, we discuss the numerical results for the structure and dynamics of the system as a function of dielectric mismatch. Specifically, we show the influence of the dielectric interface on the global isotropic–ferroelectric transition (Sec. 5.4.1) and local orientational order (Sec. 5.4.2). Following that, in Sec. 5.4.3 we explain the origin of different orientational preferences induced by the dielectric mismatch based upon the electrostatic energy of typical one-particle and two-particle configurations. As Sec. 5.4.1 and 5.4.2 suggest an apparent discrepancy between the influence of substrate permittivity on the global polarization and local orientational structure, we correlate these two properties in Sec. 5.4.4. Lastly, we present results for the rotational dynamics in Sec. 5.4.5, followed by a brief summary and discussion in Sec. 5.5.

5.3. Model and Simulation Methods

5.3.1. Model system

We consider a system of N dipolar hard spheres with positions $\mathbf{r}_i$ ($1 \leq i \leq N$) and embedded point dipole moments $\boldsymbol{\mu}_i$ placed at their centers. All dipole moments have the same magnitude $\mu = |\boldsymbol{\mu}_i|$. The potential between a pair of particles i and j with separation vector $\mathbf{r}_{ij} = \mathbf{r}_i - \mathbf{r}_j$ is

$$u_{ij} = u_{\mathrm{HS}}(r_{ij}) + \frac{1}{\epsilon_{\mathrm{m}}} \left\{ \frac{\boldsymbol{\mu}_i \cdot \boldsymbol{\mu}_j}{r_{ij}^3} - 3\frac{(\boldsymbol{\mu}_i \cdot \mathbf{r}_{ij})(\boldsymbol{\mu}_j \cdot \mathbf{r}_{ij})}{r_{ij}^5} \right\} , \qquad (5.1)$$

where $r_{ij} = |\mathbf{r}_{ij}|$ and u_{HS} is the hard-sphere potential,

$$u_{\text{HS}}(r_{ij}) = \begin{cases} +\infty & \text{if } r_{ij} \leq \sigma \\ 0 & \text{if } r_{ij} > \sigma \end{cases}, \tag{5.2}$$

with σ the diameter of the spheres. The DHS fluid is confined by two parallel walls located

at $z = 0$ and $z = L_z$, respectively, and periodically replicated in the x and y directions with

dimensions L_x and L_y. The walls serve as hard boundaries to the particles,

$$u_{\text{wall}}(z_i) = \begin{cases} +\infty & \text{if } z_i < \sigma/2 \text{ or } z_i > L_z - \sigma/2 \\ 0 & \text{if } \sigma/2 \leq z_i \leq L_z - \sigma/2 \end{cases}, \tag{5.3}$$

for a particle with z-coordinate z_i. We assume the upper wall has the same dielectric constant

as the confined medium (ϵ_{m}), while the lower slab has arbitrary permittivity ϵ_{s}. Owing to

the piecewise uniform permittivity, the dielectric mismatch at the lower interface ($z = 0$)

results in surface polarization. Analogous to polarization *charge*, this induced dipole moment

must be computed self-consistently, which requires a numerical solver (e.g., the analog of the

Induced Dielectric Solver of Refs. 50,249) for complex geometries[166,167]. But thanks to simple

geometry, the planar interface can be treated mathematically by means of image dipoles[143]

(Fig. 5.1). A central point of our study is that these image dipoles have interactions with the

real dipoles that are either attractive (for a high-permittivity surface, Fig. 5.1a) or repulsive

(for a low-permittivity surface, Fig. 5.1b).
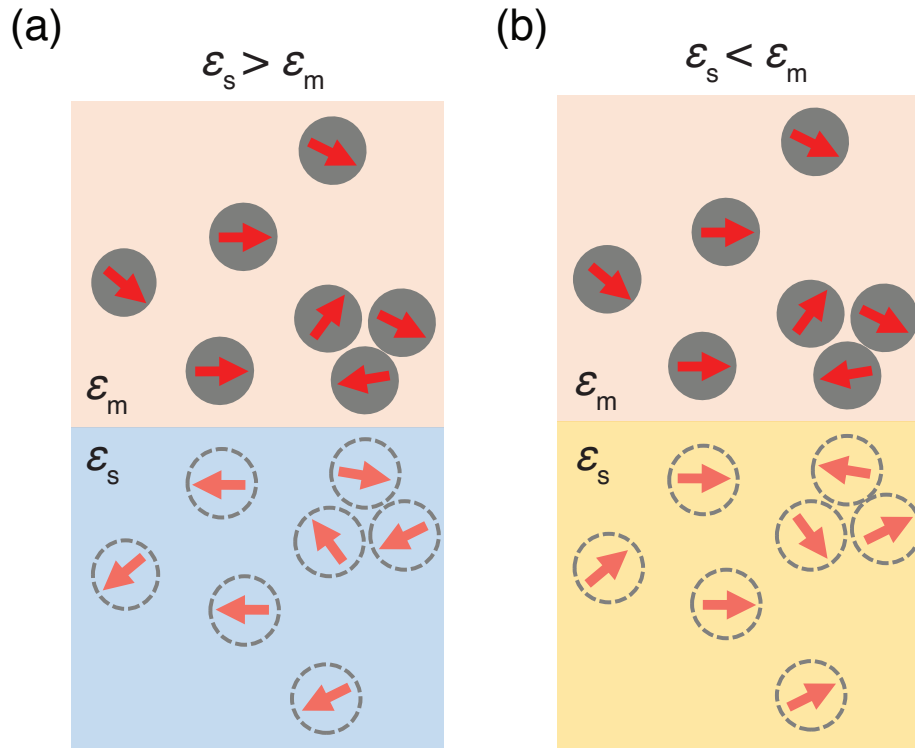
Figure 5.1. Schematic of a system consisting of N dipoles near a dielectric interface. The medium (top half of panels) has permittivity ϵ_m and the substrate (lower half of panels) has permittivity ϵ_s. Mathematically, the role of surface polarization can be treated by means of image dipoles, depicted in the lower half of the panels. For a high-permittivity substrate (a), the interactions between real dipoles and their images are attractive, whereas for a low-permittivity substrate (b) the interactions are repulsive. The arrows in the image dipoles only indicate the directions of the dipole moments, not their magnitude (which depends on the dielectric mismatch). The dipoles are confined to the region near the dielectric interface by a second surface near the top, but this surface has the same permittivity as the medium.

5.3.2. Energy of the dipolar system

To study this dipolar system via MC simulations, we need to compute the electrostatic energy of individual configurations,

$$U_{\text{dip}} = -\frac{1}{2} \sum_{i=1}^{N} \boldsymbol{\mu}_i \cdot \mathbf{E}(\mathbf{r}_i) \ . \tag{5.4}$$

To obtain the electric field $\mathbf{E}$, we start by considering an individual dipole with dipole moment $\boldsymbol{\mu}_j = (\mu_{j,x}, \mu_{j,y}, \mu_{j,z})$, located at position $\mathbf{r}_j = (x_j, y_j, z_j)$, where $\sigma/2 \leq z_j \leq L_z - \sigma/2$. The dielectric mismatch at the $z = 0$ interface results in an image dipole at $\mathbf{r}'_j = (x_j, y_j, -z_j) = \mathbf{r}_j - 2z_j\hat{\mathbf{z}}$ with dipole moment $\boldsymbol{\mu}'_j = \gamma(\mu_{j,x}, \mu_{j,y}, -\mu_{j,z})$. The dielffectric mismatch $\gamma = (\epsilon_{\mathrm{m}} - \epsilon_{\mathrm{s}})/(\epsilon_{\mathrm{m}} + \epsilon_{\mathrm{s}})$ characterizes the relative magnitude and direction of the image dipole, and $\hat{\mathbf{z}}$ represents the unit vector $(0, 0, 1)$. Thus, the electric field at position $\mathbf{r}_i$, created by all dipoles j (excluding dipole i), their image dipoles (including the image of i), and the periodic replicas of all real and image dipoles is

$$
\begin{aligned}
\mathbf{E}(\mathbf{r}_i) = \frac{1}{\epsilon_{\mathrm{m}}} \\
\times \sum_{\mathbf{n}}^{\infty} \left\{ \sum_{j=1}^{N}{}' \left(\frac{3(\mathbf{r}_{ij} + \mathbf{r}_{\mathrm{rep}}) \left(\boldsymbol{\mu}_j \cdot (\mathbf{r}_{ij} + \mathbf{r}_{\mathrm{rep}}) \right)}{|\mathbf{r}_{ij} + \mathbf{r}_{\mathrm{rep}}|^5} - \frac{\boldsymbol{\mu}_j}{|\mathbf{r}_{ij} + \mathbf{r}_{\mathrm{rep}}|^3} \right) \right. \\
\left. + \sum_{j=1}^{N} \left(\frac{3(\mathbf{r}'_{ij} + \mathbf{r}_{\mathrm{rep}}) \left(\boldsymbol{\mu}'_j \cdot (\mathbf{r}'_{ij} + \mathbf{r}_{\mathrm{rep}}) \right)}{|\mathbf{r}'_{ij} + \mathbf{r}_{\mathrm{rep}}|^5} - \frac{\boldsymbol{\mu}'_j}{|\mathbf{r}'_{ij} + \mathbf{r}_{\mathrm{rep}}|^3} \right) \right\} ,
\end{aligned}
\tag{5.5}
$$

where $\mathbf{r}'_{ij} = \mathbf{r}_i - \mathbf{r}'_j = (x_i - x_j, y_i - y_j, z_i + z_j)$ is the vector pointing from the image of dipole j to the (real) dipole i. The vector $\mathbf{n} = (n_x, n_y, 0)$, with $n_x, n_y \in \mathbb{Z}$, runs over all periodic images of the cell and the replication vector is defined as $\mathbf{r}_{\mathrm{rep}} = (n_x L_x, n_y L_y, 0)$. The prime on the summation indicates that $j \neq i$ when $\mathbf{n} = (0, 0, 0)$.

The slow convergence of the series in eqn (5.5) can be addressed by a standard Ewald summation. In view of the more rapid convergence of this summation in three dimensions than in two dimensions, it is convenient to periodically replicate the system in the z direction after adding a so-called "vacuum layer" above $z = L_z$. This makes it possible to apply the standard three-dimensional (3D) dipolar Ewald summation. Artifacts resulting from the additional periodicity are then suppressed via a so-called slab correction[250]. To accommodate

the image dipoles, we first extend the system to $-L_z \leq z \leq L_z$ and then expand the volume by a factor m, i.e., we add $m - 1$ $(m > 1)$ vacuum layers to obtain a total system volume $V = 2mL_xL_yL_z$. In practice, we choose $m = 3$.

Thus, the total dipolar energy can be written as

$$U_{\text{dip}} = U_{\text{S}} + U_{\text{L}} - U_{\text{self}} + U_{\text{cor}} . \tag{5.6}$$

The short-range contribution U_{S} consists of a sum over all dipole–dipole pairs as well as all dipole–image pairs (including the interaction of each dipole with its own image) whose distance is within the real-space cutoff r_{c},

$$\begin{aligned}
U_{\text{S}} = \frac{1}{2\epsilon_{\text{m}}} \sum_{i=1}^{N} \Bigg\{ & \sideset{}{'}\sum_{j=1}^{N} \{ (\boldsymbol{\mu}_i \cdot \boldsymbol{\mu}_j) F(r_{ij}) - (\boldsymbol{\mu}_i \cdot \mathbf{r}_{ij})(\boldsymbol{\mu}_j \cdot \mathbf{r}_{ij}) G(r_{ij}) \} \\
& + \sum_{j=1}^{N} \{ (\boldsymbol{\mu}_i \cdot \boldsymbol{\mu}'_j) F(r'_{ij}) - (\boldsymbol{\mu}_i \cdot \mathbf{r}'_{ij})(\boldsymbol{\mu}'_j \cdot \mathbf{r}'_{ij}) G(r'_{ij}) \} \Bigg\} ,
\end{aligned} \tag{5.7}$$

where $r_{ij} = |\mathbf{r}_{ij}| < r_{\text{c}}$, $r'_{ij} = |\mathbf{r}'_{ij}| < r_{\text{c}}$, and we require $r_{\text{c}} \leq L_{x,y}/2$. The functions $F(r)$ and $G(r)$ are defined as

$$F(r) = \frac{\text{erfc}(\sqrt{\alpha}r)}{r^3} + 2\sqrt{\frac{\alpha}{\pi}} \frac{\exp(-\alpha r^2)}{r^2} , \tag{5.8}$$

$$G(r) = 3\frac{\text{erfc}(\sqrt{\alpha}r)}{r^5} + 2\sqrt{\frac{\alpha}{\pi}} \left(2\alpha + \frac{3}{r^2} \right) \frac{\exp(-\alpha r^2)}{r^2} . \tag{5.9}$$

The parameter α determines the decay of the short-range potentials. Note that interactions between image dipoles do not contribute to the energy.

The long-range contribution U_L is computed in Fourier space summing all the wave vectors whose magnitude is within the k-space cutoff k_c,

$$U_\mathrm{L} = \frac{2\pi}{\epsilon_\mathrm{m} V} \sum_{\substack{\mathbf{k}\neq 0}}^{|\mathbf{k}|\leq k_\mathrm{c}} \frac{1}{k^2} e^{-k^2/4\alpha}$$

$$\times \left\{ A(\mathbf{k})^2 + B(\mathbf{k})^2 + A(\mathbf{k})C(\mathbf{k}) + B(\mathbf{k})D(\mathbf{k}) \right\} \ , \tag{5.10}$$

with

$$A(\mathbf{k}) = \sum_{i=1}^{N} \boldsymbol{\mu}_i \cdot \mathbf{k} \cos(\mathbf{k}\cdot\mathbf{r}_i) \ , \tag{5.11}$$

$$B(\mathbf{k}) = -\sum_{i=1}^{N} \boldsymbol{\mu}_i \cdot \mathbf{k} \sin(\mathbf{k}\cdot\mathbf{r}_i) \ , \tag{5.12}$$

$$C(\mathbf{k}) = \sum_{i=1}^{N} \boldsymbol{\mu}_i' \cdot \mathbf{k} \cos(\mathbf{k}\cdot\mathbf{r}_i') \ , \tag{5.13}$$

$$D(\mathbf{k}) = -\sum_{i=1}^{N} \boldsymbol{\mu}_i' \cdot \mathbf{k} \sin(\mathbf{k}\cdot\mathbf{r}_i') \ . \tag{5.14}$$

Note that he combined choice of α, r_c, and k_c determines the accuracy and efficiency of the computation. In this study the Ewald accuracy reaches 10^{-5}.

To correct for spurious self-interactions (which occur for the real dipoles only), we subtract the self energy U_self,

$$U_\mathrm{self} = \frac{2\pi}{3\epsilon_\mathrm{m}} \left(\frac{\alpha}{\pi}\right)^{3/2} \sum_{i=1}^{N} \mu_i^2 = \frac{2\pi}{3\epsilon_\mathrm{m}} \left(\frac{\alpha}{\pi}\right)^{3/2} N\mu^2 \ . \tag{5.15}$$

Lastly, the slab correction term is

$$
\begin{aligned}
U_{\text{cor}} &= \frac{2\pi}{3\epsilon_{\text{m}}} \left[\left(\sum_{i=1}^{N} \mu_{i,z} \right)^2 + \left(\sum_{i=1}^{N} \mu'_{i,z} \right)^2 \right] \\
&= \frac{2\pi}{\epsilon_{\text{m}} V} (1 - \gamma) \left(\sum_{i=1}^{N} \mu_{i,z} \right)^2 .
\end{aligned}
\tag{5.16}
$$

Having thus obtained the dipolar interaction energy including the effect of the dielectric interface, we can write the total system energy as

$$
U = U_{\text{dip}} + \frac{1}{2} \sum_{i=1}^{N} \sum_{\substack{j=1 \\ j \neq i}}^{N} u_{\text{HS}}(r_{ij}) + \sum_{i=1}^{N} u_{\text{wall}}(z_i) .
\tag{5.17}
$$

5.3.3. Simulation methods

We perform MC simulations in the canonical ensemble for a system of lateral dimensions $L_x = L_y = 10\sigma$ and height $L_z = 10\sigma$. Each simulation runs for 5×10^6 MC cycles for equilibration followed by another 5×10^6 cycles for production, where a cycle consists of N MC moves. In each MC move, a dipole is selected at random and a translation or rotation trial move is attempted with equal probability. For a translational move, the maximum displacement is determined during the equilibration process, adjusting it after every 1000 MC cycles to achieve an acceptance rate of 10%. A rotational trial move is generated by adding a randomly oriented vector with magnitude δ_{r} to the original unit vector of the dipole moment. In practice we choose $\delta_{\text{r}} = 0.4$. After each attempted move, the change of the total energy is computed to employ Metropolis algorithm. Note that it is unnecessary to recompute the whole energy at each time and only the energy change associated with

the particle being moved is computed. The initial configuration of the system consists of randomly oriented dipoles placed on a simple cubic lattice.

To explore the behavior of this dipolar fluid, we vary both the coupling constant $\lambda = \mu^2/(\epsilon_{\mathrm{m}}\sigma^3 k_{\mathrm{B}}T)$ and the reduced number density $\rho = N\sigma^3/(L_x L_y L_z)$. We systematically tune ρ from 0.05 to 0.9 and λ from 1 to 8, respectively. To examine the role of substrate permittivity, we choose three different cases: $\epsilon_{\mathrm{s}} = 100\epsilon_{\mathrm{m}}$ (high-permittivity or "conducting"), $\epsilon_{\mathrm{s}} = \epsilon_{\mathrm{m}}$ (equal-permittivity), and $\epsilon_{\mathrm{s}} = 0.01\epsilon_{\mathrm{m}}$ (low-permittivity).

To quantify the global orientational order, we introduce the order parameters P_1 and P_2 measuring the degree of global polarization and alignment, respectively[251]. For an instantaneous configuration, P_2 is the largest eigenvalue of the ordering matrix $\mathbf{Q} = \frac{1}{2N}\sum_{i=1}^{N}(3\hat{\boldsymbol{\mu}}_i\hat{\boldsymbol{\mu}}_i - \mathbf{I})$, where $\hat{\boldsymbol{\mu}}_i$ is the unit vector associated with $\boldsymbol{\mu}_i$ and $\mathbf{I}$ the identity matrix. The corresponding normalized eigenvector is the global director $\hat{\mathbf{d}}$ from which the instantaneous value of P_1 follows as $P_1 = \frac{1}{N}|\sum_{i=1}^{N}\hat{\boldsymbol{\mu}}_i \cdot \hat{\mathbf{d}}|$. Whereas P_2 merely characterizes global *alignment* of the dipolar particles, P_1 is a measure of the global *polarization*. The degree of the uniaxial alignment along the z-direction can be quantified by $Q_{zz} = \langle\frac{1}{2N}\sum_{i=1}^{N}(3\hat{\mu}_{i,z}^2 - 1)\rangle$, where Q_{zz} is zero in orientationally isotropic states, whereas $Q_{zz} = -0.5$ and $Q_{zz} = 1$ reflect configurations of perfectly in-plane or out-of-plane dipoles, respectively.

5.4. Results and Discussion

5.4.1. Ferroelectric transition and global orientational order

The orientational order of dipolar fluids has been the subject of considerable attention. The existence of ferroelectric orientational order in strongly interacting dipolar soft- and hard-sphere fluids at high density was first shown in computer simulations[226,252–254], demonstrating that dipolar forces alone can create an orientationally ordered *liquid* phase. The observation

(a)

(b)

Figure 5.2. Order parameter P_1 as a function of (a) number density ρ at coupling constant $\lambda = 7$; (b) λ at $\rho = 0.7$ for conducting (blue squares), equal-permittivity (green circles), and low-permittivity (yellow triangles) substrates.

of this spontaneous polarization not only answered a long-standing question in the liquid-crystal literature[255], but also provided guidance for constructing ferroelectric nematic liquid crystals in the laboratory.

Spatial confinement, such as the presence of an interface, reduces the orientational entropy and thereby promotes the formation of ferroelectric arrangements[243]. To investigate whether the dielectric properties of the substrate further influence the isotropic–ferroelectric

transition of the system, we study the global polarization order parameter P_1 for conducting, equal-permittivity (i.e., no dielectric mismatch between solvent and substrate), and low-permittivity interfaces. As found previously[226,243,252–254], the spontaneous polarization, where dipoles point in the same direction (along the global director $\hat{\mathbf{d}}$), is induced when either the number density ρ (Fig. 5.2a) or the dipolar coupling strength λ (Fig. 5.2b) is increased. Substrate permittivity ϵ_s does not qualitatively affect the global polarization, except that for a high-permittivity surface the polarization is slightly suppressed. This small shift of the global polarization curve can be understood from inspecting the orientational preference at different wall boundary conditions, as demonstrated below.

For dipolar system confined by two walls without dielectric contrast at the interfaces, the presence of the confining walls constrains the dipole orientations parallel to the walls in both isotropic and ferroelectric phases[243]. The origin of this preferred in-plane orientation of the confined dipoles is that (i) the head-to-tail chainlike configuration is energetically favorable and will be formed at large λ[243,254]; (ii) with the existence of the confining walls, long chains can only be formed parallel to the walls such that the out-of-plane orientations are largely suppressed. When the dielectric contrast at the interface is considered, the attractive (repulsive) surface polarization induced by high- (low-) permittivity plate can alter the orientational structure in different ways.

To explore the global orientational preference, i.e., uniaxial alignment given the reduced symmetry, for different substrates, we calculate the order parameter Q_{zz} as a function of ρ (at $\lambda = 7$) and λ (at $\rho = 0.7$) in Fig. 5.3a,b, respectively. Q_{zz} is always negative, suggesting that the global orientation is always more in-plane than out-of-plane regardless of ϵ_s. Combining this with the transition curves in Fig. 5.2, we find the isotropic–ferroelectric transition is shown to accompany with the transformation from nearly orientationally isotropic state
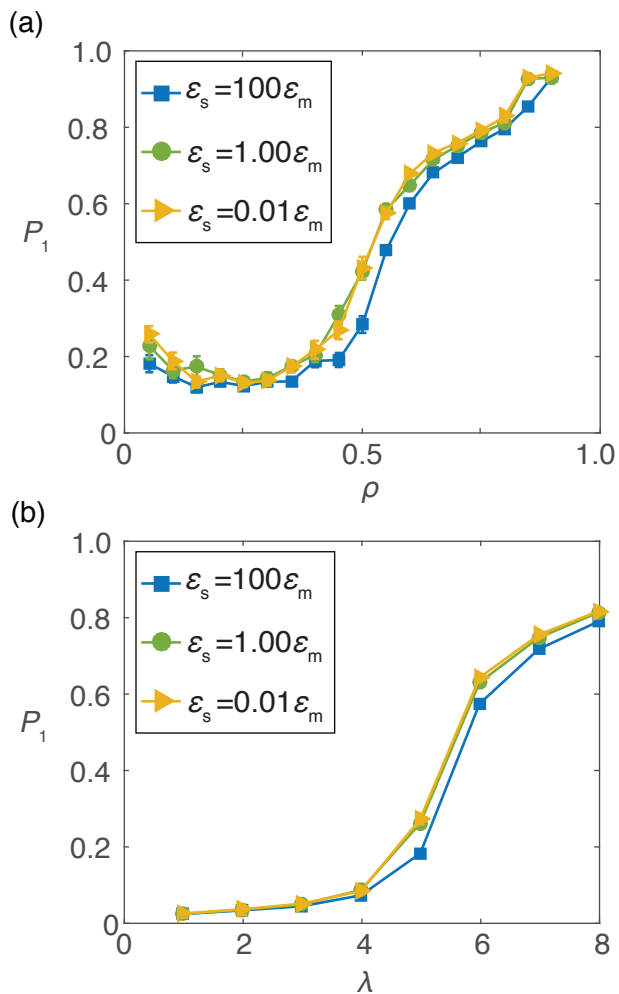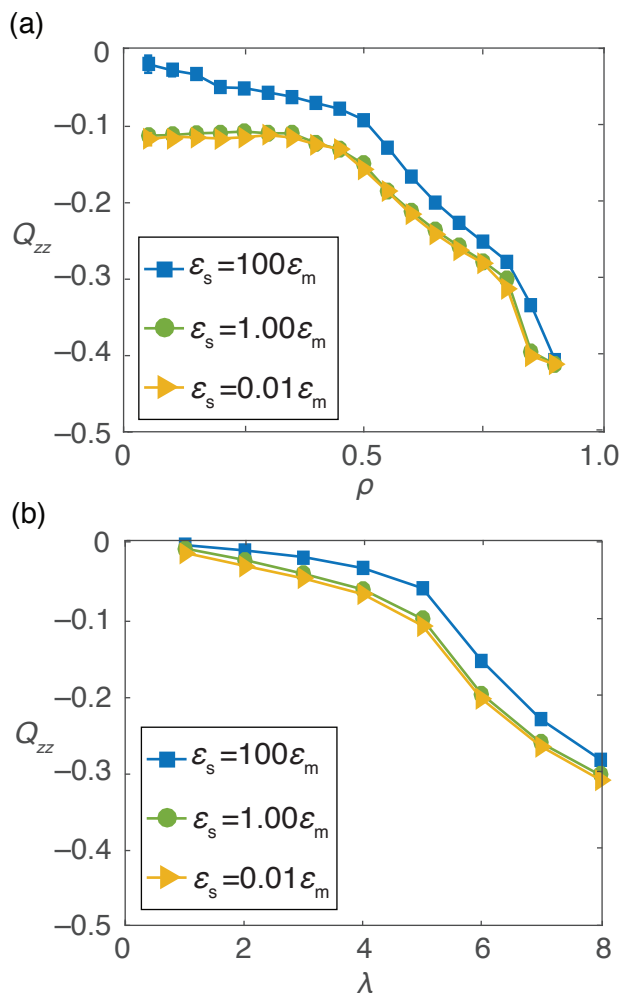
Figure 5.3. Order parameter Q_{zz} as a function of (a) number density ρ at coupling constant $\lambda = 7$; (b) λ at $\rho = 0.7$ for conducting (blue square), equal-permittivity (green circle), and low-permittivity (yellow triangle) lower slabs.

($Q_{zz} \approx 0$) to in-plane state ($Q_{zz} \approx -0.5$), consistent with the previous work[243]. However, there is a clear disparate behavior of the conducting wall (blue squares in Fig. 5.3), where the in-plane orientation is less preferred at $\epsilon_\text{s} = 100\epsilon_\text{m}$ than the other two cases. This difference is more pronounced at the low-density regimes (Fig. 5.3a), where the dipoles are almost orientationally isotropic at $\rho = 0.05$ with "conducting slab," while they clearly favor in-plane arrangement for equal- and low-permittivity slabs.
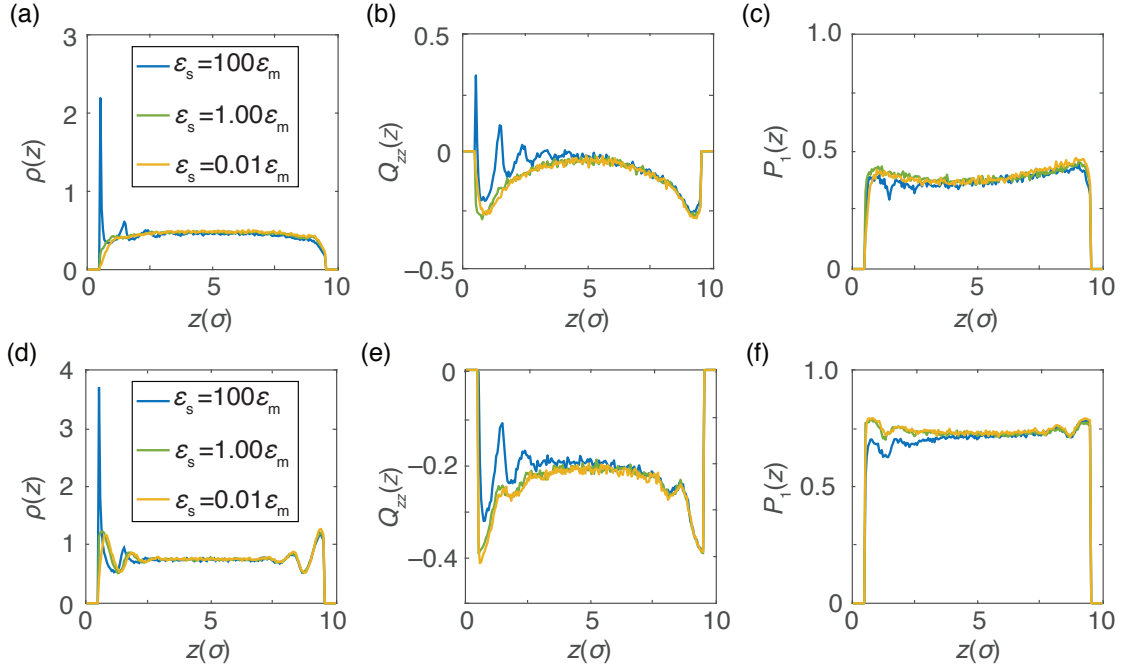
Figure 5.4. Local structural properties for dipolar fluids at coupling constant $\lambda = 7$ and reduced global number density $\rho = 0.4$ (panels a–c, isotropic phase) and $\rho = 0.7$ (panels d–f, ferroelectric phase). (a,d) Local number density $\rho(z)$. (b,e) Uniaxial alignment $Q_{zz}(z)$. (c,f) Polarization $P_1(z)$. Blue curve: conducting substrate; green curve: no dielectric mismatch between dipolar medium and substrate; yellow curve: low-permittivity substrate.

5.4.2. Local structural properties: density, polarization, and uniaxial alignment

Whereas dielectric properties of the substrate have only a minor effect on the global polarization and orientational order when averaged over the entire system, it turns out that the *local* structure of the dipolar fluid varies significantly depending on the dielectric mismatch at the fluid–solid interface. We demonstrate this by examining various structural properties as a function of distance z to the interface. As representative examples of the isotropic and ferroelectric phases, we consider systems with global number density $\rho = 0.4$ and $\rho = 0.7$, respectively. In both cases, we set the coupling constant to $\lambda = 7$.

Figure 5.4a,d illustrates (for $\rho = 0.4$ and $\rho = 0.7$, respectively) the reduced local number density $\rho(z) = \langle N(z)\sigma^3/(L_x L_y \Delta z)\rangle$, where $\Delta z = 0.05\sigma$ is the bin width and $N(z)$ is the number of particles i with $z \leq z_i < z + \Delta z$. For conducting substrates, we observe a strong condensation near the interface owing to the induced attractive polarization. In the isotropic phase, this condensation also leads to a layered structure near the interface (blue curve in Fig. 5.4a), unlike the structureless $\rho(z)$ observed in the absence of a dielectric mismatch (green curve) or for a low-permittivity substrate (yellow curve). In the latter case, the dipoles are noticeably depleted from the interfacial region due to the repulsive polarization.

The local orientational order as a function of distance to the interface is characterized via $Q_{zz}(z) = \langle \frac{1}{2N(z)} \sum_z (3\hat{\mu}_{i,z}^2 - 1)\rangle$, where the sum runs over all dipoles within layers of thickness $\Delta z = 0.05\sigma$ (Fig. 5.4b,e). Just as for the density, the degree of uniaxial alignment is strongest for a conducting substrate. There, in the isotropic phase (Fig. 5.4b), $Q_{zz}(z)$ displays positive peaks, indicating that the dipoles are oriented more perpendicular than parallel to the interface (blue curve), in particular for layers close to the interface. For substrates with permittivity equal to (green curve) or less than (yellow curve) that of the fluid medium, $Q_{zz}(z)$ is negative throughout the entire region. Even in the ferroelectric phase (Fig. 5.4e), where $Q_{zz}(z)$ is strongly negative in the equal- and low-permittivity cases due to the long-range polarization parallel to the interface, the orientational order near the conducting substrate shows significantly smaller in-plane preference. Note that the oscillatory behavior of the $Q_{zz}(z)$ curves near the interface originates from the (moderate) stratification of the fluid within that region.

Lastly, the profile of polarization along the global director $\hat{\mathbf{d}}$ is calculated as $P_1(z) = \langle \frac{1}{N(z)} | \sum_z \hat{\boldsymbol{\mu}}_i \cdot \hat{\mathbf{d}} | \rangle$ and shown in Fig. 5.4c,f, for the isotropic and ferroelectric phases, respectively. When the reduced number density ρ is raised from 0.4 to 0.7, $P_1(z)$ displays

(a) Ideally conducting surface ($\varepsilon_s/\varepsilon_m \to +\infty$)

U^*_{dip} $-\lambda < -\lambda/2$ $(-3+\sqrt{2}/8)\lambda = (-3+\sqrt{2}/8)\lambda$

(b) Equal-permittivity surface ($\varepsilon_s/\varepsilon_m = 1$)

U^*_{dip} $0 = 0$ $-2\lambda < -\lambda$

(c) Zero-permittivity surface ($\varepsilon_s/\varepsilon_m \to 0$)

U^*_{dip} $-\lambda < -\lambda/2$ $(-1-\sqrt{2}/8)\lambda < (1-\sqrt{2}/8)\lambda$
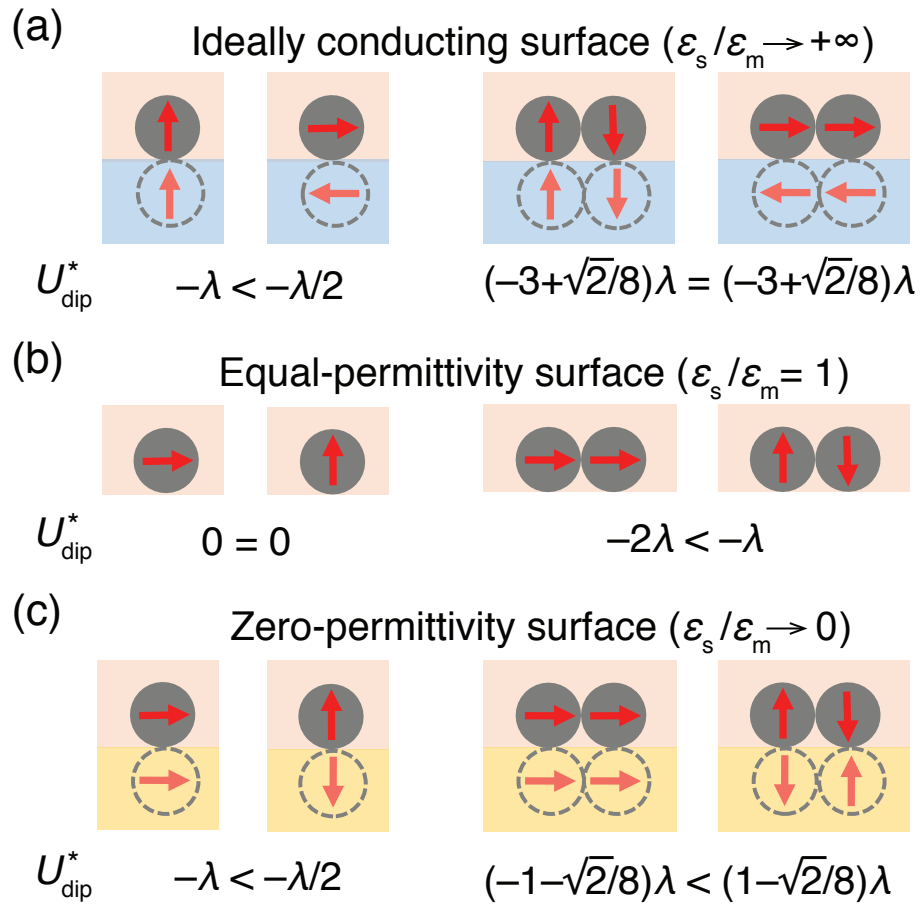
Figure 5.5. Typical one-particle (left) and two-particle (right) configurations near an (a) ideally conducting, (b) equal-permittivity ($\epsilon_s = \epsilon_m$), and (c) zero-permittivity slab. The dimensionless dipolar energy $U^*_{dip} = U_{dip}/k_B T$ consisting of both dipole–dipole and dipole–image interactions is shown for each arrangement. The induced image dipoles in panels (a) and (c) are indicated by dashed gray circles.

an increase for all distances to the interface, as anticipated based upon the growth with ρ in Fig. 5.2a. Near a conducting substrate, $P_1(z)$ is smaller than for the other two types of boundaries, as the dipoles have a lower tendency to orient parallel to the interface (cf. Fig. 5.4b,e) and are therefore less polarized along $\hat{\mathbf{d}}$ which is parallel to the wall.

5.4.3. Mechanistic understanding of dielectric effects on orientational structure

In Sec. 5.4.1 and 5.4.2, we found a weak dependence of global polarization on interfacial dielectric mismatch, but a qualitative variation of orientational order in the surface layer. To understand the origin of the orientational preference induced by the substrate permittivity, we start by comparing the dipolar energy U_{dip} of typical one- and two-particle configurations for different boundary conditions. This energy follows directly from eqns (5.4) and (5.5) if the sum over periodic images is omitted, $\mathbf{n} = (0, 0, 0)$.

We first consider the parallel and perpendicular arrangements of a single dipole near a perfectly conducting ($\epsilon_{\mathrm{s}} = +\infty$), equal-permittivity ($\epsilon_{\mathrm{s}} = \epsilon_{\mathrm{m}}$), and zero-permittivity ($\epsilon_{\mathrm{s}} = 0$) substrate, cf. left-hand side of Fig. 5.5a,b,c, respectively. Note that for $\epsilon_{\mathrm{s}} = +\infty$ and $\epsilon_{\mathrm{s}} = 0$ the *magnitude* of the dipole moment of the induced image dipoles equals that of the real dipoles. Yet, the two cases have opposite orientational preference: for the conducting substrate, U_{dip} is minimized by the perpendicular state, whereas the parallel orientation is favored by the zero-permittivity wall.

Addition of a second dipole near the interface, neighboring the first one, introduces dipole–dipole and additional dipole–image interactions, which leads to a qualitative change. For this two-particle configuration, both equal- and zero-permittivity surfaces prefer the in-plane head-to-tail configuration. However, as a result of the competition between dipole–dipole and dipole–image interactions, the ideally conducting plane *equally* favors out-of-plane and in-plane arrangements. For a two-particle configuration near a *nonideal* high-permittivity substrate, i.e., $\epsilon_{\mathrm{m}} < \epsilon_{\mathrm{s}} < +\infty$, in-plane alignment will be weakly favored over the perpendicular arrangement These observations explain why the contact layer near a high-permittivity surface has a much weaker in-plane orientation that the other two cases.
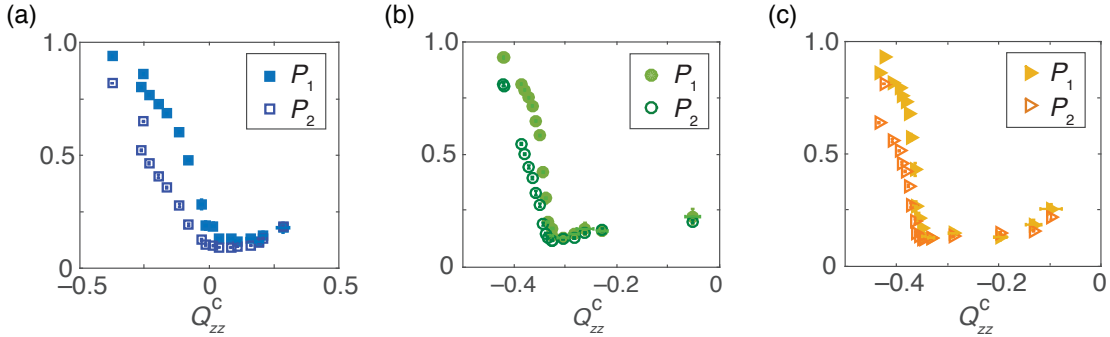
Figure 5.6. Scatter plot of the global order parameters P_1 (solid symbols) and P_2 (open symbols) versus the degree of uniaxial alignment of the contact layer, Q_{zz}^{c}, for (a) conducting ($\epsilon_{s} = 100\epsilon_{m}$), (b) equal-permittivity ($\epsilon_{s} = \epsilon_{m}$), and (c) low-permittivity ($\epsilon_{s} = 0.01\epsilon_{m}$) substrates. Different data points are obtained at different number densities ρ ranging from 0.05 to 0.9. The dipolar coupling is fixed at $\lambda = 7$.

In particular when the density is low, where the system exhibits an isotropic phase already for all substrates, the dipole–dipole interaction is reduced and the interaction between a dipole and its own image becomes dominant. This leads to the strong tendency toward out-of-plane orientations near a conducting surface in the isotropic phase, reflected by the positive peaks of $Q_{zz}(z)$ in Fig. 5.4b.

5.4.4. Correlation between global polarization and local orientational order

Given the different degrees to which global polarization and local orientational order depend on dielectric mismatch, it is instructive to examine their correlation for different boundary conditions. We quantify the degree of uniaxial alignment in the contact layer only via the order parameter $Q_{zz}^{c} = \langle \frac{1}{2N_c} \sum_{z_i < z^c} (3\hat{\mu}_{i,z}^{2} - 1) \rangle$, summing over all dipoles contacting the interface, i.e., those particles i with $z_i < z^{c}$, where z^{c} is the location of the first minimum after the first peak in $\rho(z)$. We examine this property for systems with fixed coupling $\lambda = 7$, varying the density from 0.05 to 0.9. The correlation between Q_{zz}^{c} and the global order parameters P_1 and P_2 (cf. Sec. 5.3.3) is illustrated in the scatter plots Fig. 5.6a–c, for the
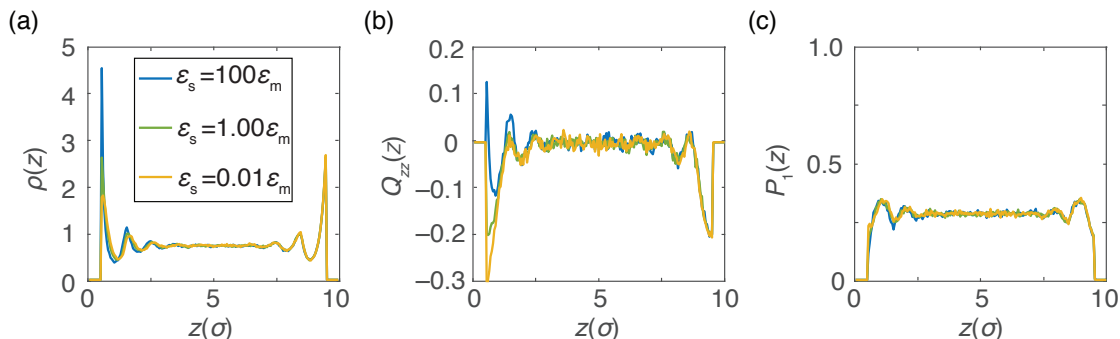
Figure 5.7. Structural properties of the system residing in the isotropic phase ($\lambda = 3$, $\rho = 0.7$) for which we study dipolar dynamics. (a) Local number density $\rho(z)$, (b) uniaxial alignment $Q_{zz}(z)$, and (c) polarization order parameter $P_1(z)$ for conducting (blue curve), equal-permittivity (green curve), and low-permittivity (yellow curve) substrates.

three choices of interfacial dielectric mismatch. The three cases share a similar trend: ferroelectric polarization occurs as Q_{zz}^c decreases towards -0.5, corresponding to the increasing in-plane orientational ordering of the contact layer. However, the onset of the ferroelectric ordering occurs at different threshold values of Q_{zz}^c. In particular, for the conducting interface this phase transition takes place when $Q_{zz}^c \approx 0$ (Fig. 5.6a), indicating that the local orientational structure *near the surface* is still isotropic and does not promote the global isotropic–ferroelectric transition. Conversely, if the substrate has a permittivity equal or lower than the medium spontaneous polarization happens when the dipolar orientation near the interface already has a strong in-plane order, $Q_{zz}^c \approx -0.35$ (Fig. 5.6b,c).

5.4.5. Rotational dynamics

Since our MC simulations employ only local translational and rotational moves, their evolution can be interpreted as reflecting the dynamics of the system. In the absence of dielectric effects, the rotational dynamics of a dipolar fluid in a slit-like geometry was shown to be
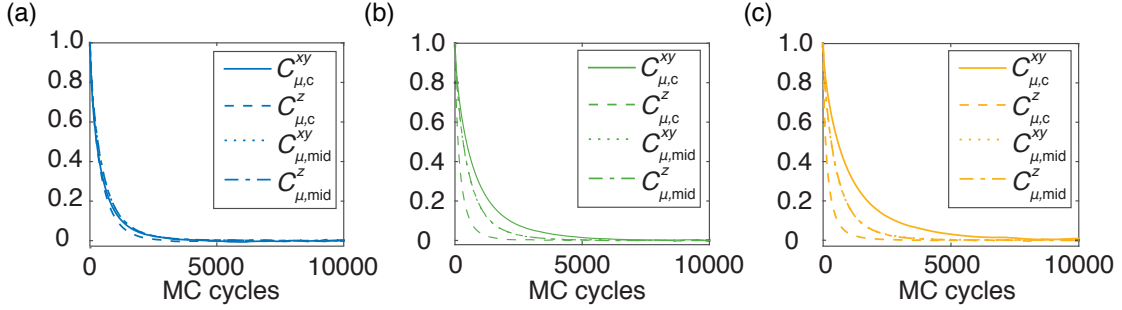
Figure 5.8. Normalized dipole–dipole autocorrelation functions $C_{\mu,c}^{xy}(t)$ (solid line) and $C_{\mu,c}^{z}(t)$ (dashed line) in the contact layer, $C_{\mu,\mathrm{mid}}^{xy}(t)$ (dotted line) and $C_{\mu,\mathrm{mid}}^{z}(t)$ (dash-dotted line) in the middle region for (a) conducting, (b) equal-permittivity, and (c) low-permittivity walls at $\lambda = 3$ and $\rho = 0.7$. Note that since $C_{\mu,\mathrm{mid}}^{xy}(t) \approx C_{\mu,\mathrm{mid}}^{z}(t)$ in the middle layers, the two curves (dotted and dash-dotted) overlap with each other.

anisotropic[246]. Here, we examine the role of interfacial dielectric effects on dipolar dynamics, focusing on the *globally isotropic* phase, selecting the parameters ($\lambda = 3$, $\rho = 0.7$) as a representative example. For reference, the structural properties $\rho(z)$, $Q_{zz}(z)$, and $P_1(z)$ at these conditions are shown in Fig. 5.7a–c.

We characterize the single-particle rotational dynamics via the dipole–dipole autocorrelation functions[246],

$$C_{\mu}^{\alpha}(t) = \left\langle \frac{1}{N} \sum_{i=1}^{N} \mu_{i,\alpha}(t_0)\mu_{i,\alpha}(t_0 + t) \right\rangle_{t_0} , \qquad (5.18)$$

where $\mu_{i,\alpha}$ is the α-component ($\alpha = x, y, z$) of dipole moment $\boldsymbol{\mu}_i$. The corresponding relaxation time of $C_{\mu}^{\alpha}(t)$ is defined as

$$\tau_{\mu}^{\alpha} = \frac{1}{C_{\mu}^{\alpha}(0)} \int_0^{\infty} C_{\mu}^{\alpha}(t)dt , \qquad (5.19)$$

which is in unit of MC cycle. To identify the effects of the dielectric mismatch on the single-particle dynamics, we calculate the in-plane and out-of-plane functions, $C_{\mu}^{xy}(t) = (C_{\mu}^{x}(t) + C_{\mu}^{y}(t))/2$ and $C_{\mu}^{z}(t)$, as well as their relaxation times for the contact layer and

the central bulk-like region separately at different boundary conditions (Fig. 5.8). Here the contact layer consists of dipoles located at $z < z^{\mathrm{c}}$ (as in Sec. 5.4.4), while the central region extends over $3\sigma < z < 7\sigma$. For the central region, regardless of boundary conditions, two correlation functions $C_{\mu,\mathrm{mid}}^{xy}$ and $C_{\mu,\mathrm{mid}}^{z}$ are indistinguishable. On the other hand, in the contact layer the dynamics are anisotropic for equal- and low-permittivity substrates, with the out-of-plane correlation decaying much more rapidly than the in-plane correlation. This is clearly manifested by their distinct relaxation times: $\tau_{\mu,\mathrm{c}}^{xy} = 884$ as opposed $\tau_{\mu,\mathrm{c}}^{z} = 273$ for the equal-permittivity case and $\tau_{\mu,\mathrm{c}}^{xy} = 1138$ as opposed $\tau_{\mu,\mathrm{c}}^{z} = 256$ for the low-permittivity case. This anisotropy of rotational dynamics is attributed to the predominantly parallel orientations near the surface (Fig. 5.7b). For the same reason, dipoles near the conducting surface whose in-plane character is very much weakened by the dipole–image interaction possess almost isotropic dynamics and behave similarly with the middle-region dipoles.

5.5. Conclusion

We have performed extensive simulations of dipolar hard-sphere fluids confined by a dielectric interface. These simulations are made possible by a formulation of the 3D dipolar Ewald summation supplemented by a so-called slab correction and extended to incorporate image dipoles. We have used this method to systematically study the effects of interfacial dielectric mismatch on the orientational structure and dynamics of the dipolar fluid. Unlike previous studies[187,256] where a soft repulsive fluid–wall potential was applied that suppressed polarization effects, we employed a hard fluid–wall potential and modeled the fluid as dipolar hard spheres. This does not only highlight the role of polarization effects, but also is more appropriate for dipolar colloidal particles, where the structural or hydration forces are extremely short-ranged compared with the particle size.

We find that the presence of a conducting surface shifts the global isotropic–ferroelectric transition only slightly toward a higher density and coupling strength, but that dielectric effects in general have a significant influence on the orientational structure of the contact layer. Specifically, low-permittivity interfaces enhance the in-plane orientation of the dipolar particles, whereas a conducting or high-permittivity surface suppresses the in-plane character and can even promote out-of-plane dipolar orientation when the particle density is low.

The induced orientational structure in turn affects the dynamical properties of the system, especially close to the interface. In the absence of surface polarization or for low-permittivity interfaces, the contact layer exhibits highly anisotropic single-particle dynamics, where the out-of-plane dipole moment decorrelates much more rapidly than the in-plane components. For conducting substrates, this anisotropy disappears, as the in-plane character of the induced dipole moment is significantly weakened near such interfaces.

Our findings not only clarify the effects of substrate permittivity on confined dipolar fluids, instrumental for the fundamental understanding of a variety of experimental systems, but also have implications for the design of tunable dipolar material by exploiting dielectric effects.

CHAPTER 6

Dielectric Modulation of Two-dimensional Dipolar Materials

The content of this chapter is based on the following publication:

- Z. Wang and E. Luijten, "Dielectric modulation of two-dimensional dipolar materials," Phys. Rev. Lett. **123**, 096101 (2019)

6.1. Abstract

Spontaneous pattern formation plays an important role in a wide variety of natural phenomena and materials systems. A key ingredient for the occurrence of modulated phases is the presence of competing interactions, generally of different physical origins. We demonstrate that in dipolar films, a prototypical system for pattern formation, patterns can be induced by dielectric effects alone. A rich phase diagram arises, where striped and circular morphologies emerge with geometric properties that can be controlled through variation of particle shape and substrate permittivity or permeability. These effects are particularly enhanced by metamaterial substrates.

6.2. Introduction

Spontaneous pattern formation and modulation of phases in two dimensions occur in a diverse set of physical, chemical, and biological systems[257,258]. The domains can exhibit a variety of patterns—notably stripes, islands, and circular droplets—that are often characterized by spatial periodicity. Examples include the orientational patterns in ferromagnetic thin films[236,259,260], the domain structure of dipolar Langmuir monolayers[261,262], and microphase

separation in block copolymer melts[263,264]. These phenomena have significant potential for technological applications, such as nanofabrication[265,266] and nanomagnetism[267].

One of the central common, and in fact necessary, factors underlying pattern formation in thermodynamic equilibrium is the presence of competing interactions[257,258]. Dipolar interactions, so ubiquitous in nature, have emerged as the most basic and widely studied starting point. Yet, a second potential is required for modulated patterns to appear, such as the short-range exchange interaction[260,268,269], interfacial energy[261,262], geometric constraints[7,270,271], or an external field[272,273]. No modulated phases have been reported in systems with solely dipolar interactions.

Two-dimensional (2D) dipolar systems exhibit a rich phase diagram[244,274–277], with an isotropic–polymeric phase transition at low surface densities[275,277] and more complicated structures as well as orientational ordering at high densities[244,274]. Although these systems have received widespread attention, a parameter that has been mostly ignored (with dipolar particles confined between metallic plates as a notable exception[187,256]) is the dielectric mismatch between the substrate and the medium containing the dipolar particles. This omission is noteworthy, given the demonstrated effect of substrate permittivity on properties of a wide range of electromagnetic systems, from plasmonics[36] to ion mobilities in electrolytes[37]. Moreover, with the emergence of electromagnetic metamaterials[278,279], in which the electric permittivity and/or magnetic permeability are negative, the magnitude of polarization effects can be greatly enhanced[280,281].

Here, we demonstrate that variation of dielectric mismatch can qualitatively alter the orientational phases of (quasi-)2D dipolar systems. Remarkably, even *modulated* phases can be induced in purely dipolar systems, without the need for external fields or other interactions. We elucidate the origin of the different phases and map the corresponding phase diagram.

In addition, we illustrate how even within an individual phase the characteristic length scale can be accurately controlled. Throughout this work, we employ electric dipoles, yet all our findings are directly applicable to magnetic dipolar systems as well[282]. There, tuning of the interfacial dielectric contrast must be replaced by variation of the permeability of the substrate. Experimental realizations of the model studied here include charged Janus colloids[283] and ferromagnetic particles. Various aspects of this work pertain to metamaterial substrates with negative *static* permittivity or permeability. Whereas the former can be realized in a wide range of materials (e.g., metals[284,285], quasi-2D crystals[286], and nanoparticle[287,288] and polymeric systems[289]), the latter can be realized by including active components in artificial metamaterials[290].

6.3. Model and Simulation Methods

We examine monolayers of $N = N_x \times N_y$ spheres of diameter d that each carry a point dipole $\boldsymbol{\mu}$. To minimize the influence of the underlying lattice[269], the particles are placed on a hexagonal lattice with lattice constant a and dimensions $L_x = N_x a$, $L_y = \sqrt{3}N_y a/2$, periodically replicated in the x and y directions. All particles have fixed z-coordinate $d/2$ and are embedded in a medium with uniform permittivity ϵ_{m}. The substrate has permittivity ϵ_{s}, so that there is a dielectric mismatch at $z = 0$. We study this system via Monte Carlo simulations in the canonical ensemble where only 3D rotations of the dipoles are permitted. Owing to the piecewise uniform permittivity, the electric dipoles induce surface polarization charge at the substrate interface. Mathematically, the influence of this polarization is most conveniently phrased in terms of "image" dipoles, centered at $z = -d/2$ and with dipole moment $\boldsymbol{\mu}'$ (Fig. 6.1).
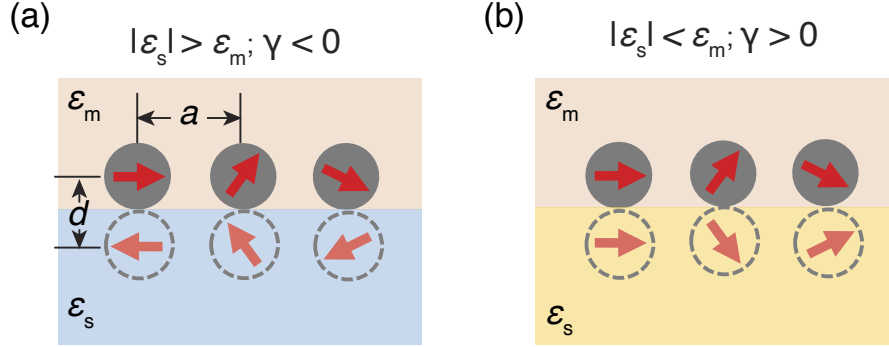
Figure 6.1. Schematic depiction of a system of 2D hexagonally packed dipolar spheres immersed in a uniform dielectric medium with permittivity ϵ_{m} above of a dielectric substrate with permittivity ϵ_{s}. To account for the polarization charges induced at the interface, we employ "image" dipoles (dashed circles). (a) For high-permittivity substrates (as well as for metamaterials with sufficiently negative permittivity), the in-plane component of these induced dipoles is anti-parallel to their counterpart above the surface, whereas the perpendicular component is parallel. (b) For substrate materials with small absolute permittivity, the situation is reversed. In both cases, nonintuitive collective behavior can emerge, since the images are induced by individual dipoles, but interact with all other dipoles above the substrates.

The Hamiltonian of the system is characterized by two energy scales, the interaction between neighboring dipoles $\lambda_{\mathrm{dd}} = \mu^2/(\epsilon_{\mathrm{m}}a^3 k_{\mathrm{B}}T)$ and the dipole–image coupling $\lambda_{\mathrm{di}} = \gamma\mu^2/(\epsilon_{\mathrm{m}}d^3 k_{\mathrm{B}}T) = \gamma\lambda_{\mathrm{dd}}/\alpha^3$, where $\gamma = (\epsilon_{\mathrm{m}} - \epsilon_{\mathrm{s}})/(\epsilon_{\mathrm{m}} + \epsilon_{\mathrm{s}})$ is the dielectric mismatch, $\alpha = d/a$ is reduced by the lattice constant a, $\mu = |\boldsymbol{\mu}|$, k_{B} is Boltzmann's constant, and T the temperature. We choose a as the unit length and use a tilde to denote reduced lengths. The Hamiltonian reads

$$\frac{\mathcal{H}}{k_{\mathrm{B}}T} = \frac{1}{2}\sum_{i=1}^{N}\sum_{\mathbf{n}}^{\infty}\left\{\lambda_{\mathrm{dd}}\sum_{j=1}^{N}{}'\frac{\hat{\boldsymbol{\mu}}_i\cdot\hat{\boldsymbol{\mu}}_j - 3(\hat{\boldsymbol{\mu}}_i\cdot\hat{\mathbf{r}}_{ij}^{\mathrm{rep}})(\hat{\boldsymbol{\mu}}_j\cdot\hat{\mathbf{r}}_{ij}^{\mathrm{rep}})}{|\tilde{\mathbf{r}}_{ij}^{\mathrm{rep}}|^3}\right.$$
$$\left. +\lambda_{\mathrm{di}}\sum_{j=1}^{N}\frac{\hat{\boldsymbol{\mu}}_i\cdot\hat{\boldsymbol{\mu}}_j' - 3(\hat{\boldsymbol{\mu}}_i\cdot\hat{\mathbf{r}}_{ij}'^{\mathrm{rep}})(\hat{\boldsymbol{\mu}}_j'\cdot\hat{\mathbf{r}}_{ij}'^{\mathrm{rep}})}{\left|1 + |\tilde{\mathbf{r}}_{ij}^{\mathrm{rep}}/\alpha|^2\right|^{3/2}}\right\},$$

where $\hat{\boldsymbol{\mu}}_i = \boldsymbol{\mu}_i/\mu$ and $\hat{\boldsymbol{\mu}}_i' = (\mu_{i,x}, \mu_{i,y}, -\mu_{i,z})/\mu$. The periodicity of the lattice is accounted for via summation over $\mathbf{n} = (n_x, n_y, 0)$ $(n_x, n_y \in \mathbb{Z})$, where the prime indicates that $i \neq j$ for

$\mathbf{n} = \mathbf{0}$. The vector $\tilde{\mathbf{r}}_{ij}^{\mathrm{rep}} = (\tilde{r}_{j,x} - \tilde{r}_{i,x} + n_x \tilde{L}_x, \tilde{r}_{j,y} - \tilde{r}_{i,y} + n_y \tilde{L}_y, 0)$ points from dipole i to (a replica of) dipole j, with corresponding unit vector $\hat{\mathbf{r}}_{ij}^{\mathrm{rep}}$, and $\tilde{\mathbf{r}}_{ij}^{\prime\mathrm{rep}} = (\tilde{r}_{j,x} - \tilde{r}_{i,x} + n_x \tilde{L}_x, \tilde{r}_{j,y} - \tilde{r}_{i,y} + n_y \tilde{L}_y, -\alpha)$ points from dipole i to (a replica of) image dipole j, with corresponding unit vector $\hat{\mathbf{r}}_{ij}^{\prime\mathrm{rep}}$. Whereas λ_{dd} and λ_{di} control the total contributions of the dipole–dipole (D–D) and dipole–image (D–I) interactions to the system energy, respectively, the geometric factor α determines the ratio between the second-order (and higher) contributions to the D–I interaction (i.e., between dipoles and images of other dipoles) and the first-order D–I interaction (between dipoles and their own images), which only depends on λ_{di} (which we regard as independent of α as it can be controlled via γ). The observation that α can serve as an independent control parameter has profound consequences for the tunability of patterns that arise for different choices of the coupling strength and dielectric mismatch, as we will explore below.

In practice, we compute the energy via 3D dipolar Ewald summation (relative precision 10^{-5}) modified to include image charges and supplemented with a slab correction[188]. For each parameter choice, we employ 5×10^5 Monte Carlo cycles of N rotational moves.

To quantify the global orientational order, we introduce the parameters P_1 and P_2[251]. For an instantaneous configuration, P_2 is the largest eigenvalue of the ordering matrix $Q = \frac{1}{2N} \sum_{i=1}^{N} (3\hat{\boldsymbol{\mu}}_i \hat{\boldsymbol{\mu}}_i - I)$, where I is the identity matrix. The corresponding normalized eigenvector is the global director $\hat{\boldsymbol{d}}$ from which the instantaneous value of P_1 follows as $P_1 = \frac{1}{N} |\sum_{i=1}^{N} \hat{\boldsymbol{\mu}}_i \cdot \hat{\boldsymbol{d}}|$. Whereas P_2 merely characterizes global alignment (nematic order) of the dipolar particles, P_1 is a measure of the global polarization. The degree of *uniaxial* alignment (along the z axis) is quantified by $Q_{zz} = \langle \frac{1}{2N} \sum_{i=1}^{N} (3\hat{\mu}_{i,z}^2 - 1) \rangle$, where Q_{zz} vanishes in orientationally isotropic states, whereas $Q_{zz} = -0.5$ and $Q_{zz} = 1$ reflect configurations of perfectly in-plane or out-of-plane dipoles, respectively.

6.4. Results and Discussion

To establish a baseline, we examine a system of dense-packed spheres ($\alpha = 1$) in the absence of dielectric contrast at the interface ($\gamma = 0$). In this case, the energy is minimized by head-to-tail chains, yielding an in-plane ferroelectric (IF) state at strong couplings (Fig. 6.2a)[274,275]. Note that this is indeed a *global*, long-range ferroelectric order, unlike the vortex-like structure observed for quasi-2D dipolar spheres with positions that are not constrained to a lattice structure[275]. This tendency of dipolar interactions to favor arrangements with in-plane orientation is enhanced in the presence of low-permittivity substrates ($\gamma > 0$), since the interaction energy of dipoles with the induced surface charge is also minimized for such configurations. More interesting is the situation of substrates with a higher permittivity than the medium ($\gamma < 0$), where this energy is minimized for *perpendicular* dipoles. The resulting competition between the dipole–dipole interactions favoring in-plane ferroelectric ordering and the dipole–polarization interaction favoring out-of-plane configurations raises the possibility of a dielectrically induced structural transition.

The magnitude of polarization effects, especially the first-order D–I interaction, is controlled by λ_{di}. This corresponds to the surface anisotropy in magnetic films[270], which promotes the out-of-plane orientation of dipoles. λ_{di} can be varied by either the dielectric mismatch at the interface γ or the geometric ratio α. Decreasing the latter from $\alpha = 1$ to $\alpha = \frac{2}{3}$ while keeping $\lambda_{\mathrm{dd}} = 5$ leads to $\lambda_{\mathrm{di}} = -16.875$ for a perfectly conducting substrate ($\gamma = -1$). As shown in Fig. 6.2b, this indeed transforms the IF state into a state with out-of-plane orientation. Owing to the strong interaction of the dipoles with their own images, they are predominantly aligned with the z-axis, so that P_2 and Q_{zz} are close to 1. Simultaneously, the nearest-neighbor dipolar interaction is minimized by an antiparallel arrangement, i.e.,
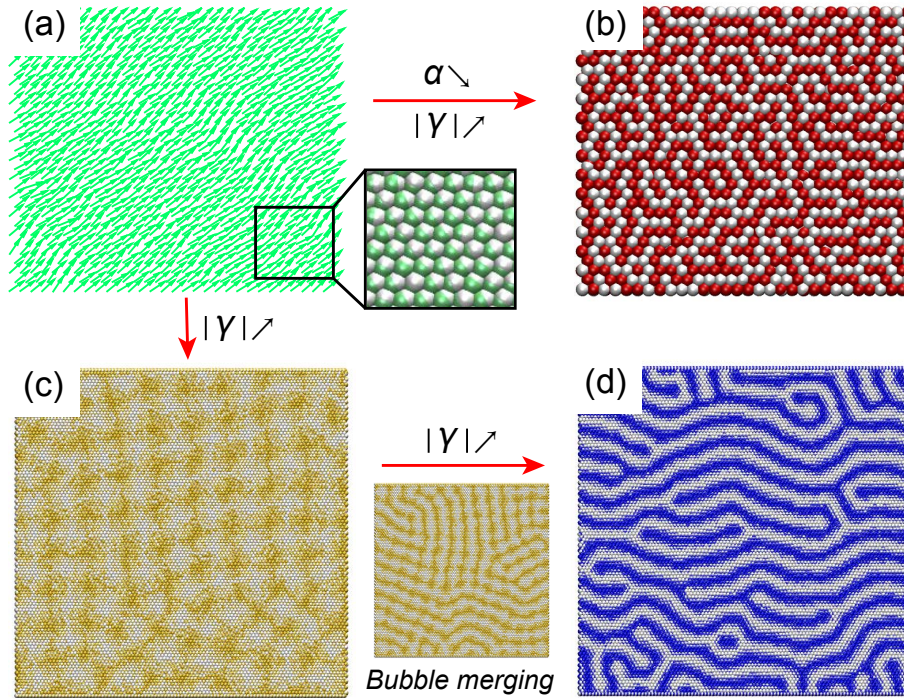
Figure 6.2. Typical structures formed by $N = 100 \times 114$ dipolar spheres placed on a 2D hexagonal lattice at dipolar coupling $\lambda_{\mathrm{dd}} = 5$. (a) Representative partial (30×30) configuration in the absence of dielectric contrast ($\epsilon_{\mathrm{s}} = \epsilon_{\mathrm{m}}$, so $\gamma = 0$ and $\lambda_{\mathrm{di}} = 0$) and at packing $\alpha = 1$, showing an IF phase with $P_1 = 0.88$, $P_2 = 0.68$, $Q_{zz} = -0.43$. (b) Same subsample on a perfectly conducting substrate ($\epsilon_{\mathrm{s}} = +\infty$, $\gamma = -1$) with geometric ratio $\alpha = \frac{2}{3}$, so that the dipole–image coupling is raised to $\lambda_{\mathrm{di}} = -16.875$. This results in an OAF phase with $P_1 = 0.01$, $P_2 = 0.79$, $Q_{zz} = 0.78$. (c) Snapshot of the full dense-packed ($\alpha = 1$) system on a metamaterial substrate with $\gamma = -1.6$, exhibiting a bubble phase with $P_1 = 0.01$, $P_2 = 0.23$, $Q_{zz} = -0.12$. (d) As the dielectric contrast is increased further to $\gamma = -3$, the bubble phase transforms to a stripe-like phase with $P_1 = 0.01$, $P_2 = 0.34$, $Q_{zz} = 0.12$. Between the bubble and stripe phases, the bubbles gradually merge into stripes, see snapshot between panels (c) and (d), for $\gamma = -2$. Colors characterize the different phases: IF phase – green; OAF phase – red; bubble phase – yellow; stripe phase – blue.

an out-of-plane anti-ferroelectric (OAF) state with $P_1 \approx 0$. This structure is confirmed by the orientational pair correlation function (not shown). Experimentally, α can be reduced by increasing the lattice constant either through variation of the particle shape or by employing a patterned substrate to control the lattice structure[291]. Alternatively, polarization

effects can be enhanced (at fixed λ_{dd}) by increasing the magnitude of dielectric mismatch γ. Although $|\gamma|$ is bounded by 1 for conventional materials (i.e., the magnitude of an image dipole cannot exceed the real dipole), this constraint is lifted for a negative-permittivity material (or negative-permeability material for magnetic dipoles) [280,281]. Specifically, $\gamma < -1$ when $\epsilon_s < -\epsilon_m$. Remarkably, this additional control parameter gives rise to new modulated phases. At fixed $\alpha = 1$ and $\lambda_{dd} = 5$, increasing the dielectric contrast to $\gamma = -1.6$ ($\lambda_{di} = -8$) yields the "bubble" phase (Fig. 6.2c), followed by the "stripe" phase (Fig. 6.2d) at $\gamma = -3$ ($\lambda_{di} = -15$). The bubble and stripe phases both consist of alternating 'up' and 'down' domains with a continuous variation of the dipolar orientation, and only differ in the shape of the domains. Neither of these phases has a global polarization ($P_1 \to 0$ in the thermodynamic limit), but due to their geometric difference they have either slight global in-plane (bubble, $Q_{zz} < 0$) or out-of-plane (stripe, $Q_{zz} > 0$) characteristics.

We construct the phase diagram of this system as λ_{dd}–λ_{di} sections for different fixed α (Fig. 6.3; see the Appendix 6.6 and Fig. 6.5 for an alternative representation of the phase diagram). In addition to the four ordered phases identified above (IF, OAF, bubble, stripe) we find a disordered phase at low λ_{dd}, $|\lambda_{di}|$. When dipolar couplings dominate, we observe the IF phase, which transitions to either the OAF phase or the stripe phase upon increase of $|\lambda_{di}|$, when polarization interactions become dominant. For larger geometric ratio α (Fig. 6.3a) the IF phase transitions to the stripe phase via a narrow region exhibiting the bubble phase. This intermediate phase can be interpreted by noting that as $|\lambda_{di}|$ increases, the stripe phase forms via merging of circular domains (Fig. 6.2, between panels c and d), thereby reducing the area of the boundaries between oppositely oriented bubbles and thus the fraction of in-plane dipoles. As α is increased further, the stripe region grows at the expense of the IF and bubble regions (Fig. 6.3b). Conversely, for small α (Fig. 6.3c,d) the IF and disordered
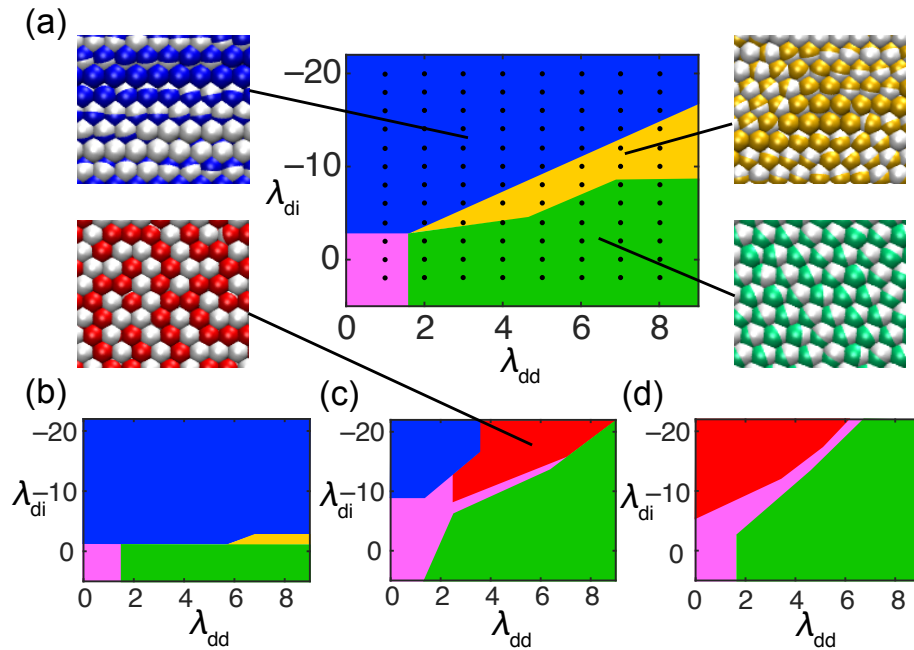
Figure 6.3. Phase diagrams parametrized by λ_{dd} and λ_{di}, at different values of the geometric factor α: (a) $\alpha = 1$; (b) $\alpha = 3$; (c) $\alpha = \frac{2}{3}$; (d) $\alpha = \frac{1}{3}$. Colors characterize the different phases: IF phase – green; OAF phase – red; bubble phase – yellow; stripe phase – blue; disordered phase – pink. Phase boundaries are drawn based on discrete simulation data points with positions indicated by black dots in (a).

phases occupy larger regions of the phase diagram, and the OAF phase replaces the stripe phase. Interestingly, when the competing parameters λ_{dd} and $|\lambda_{di}|$ become large enough to overwhelm entropic effects, at fixed α only their ratio determines the phase of the system (cf. diagonal phase boundaries in Fig. 6.3a,c,d).

What is then the role of the geometric factor α in the phase diagram of Fig. 6.3? We focus on conditions with strong polarization effects (large $|\lambda_{di}|$), where the dipoles are predominantly oriented out-of-plane. In addition to the first-order D–D and D–I interactions characterized by λ_{dd} and λ_{di}, respectively, dipoles interact with the surface polarization induced by *other* dipoles. The second-order D–I interaction (between a dipole and its nearest-neighbor images) is controlled by $\lambda_{di}^{(2)} = \lambda_{di}[\alpha^2/(1 + \alpha^2)]^{3/2}$ and grows in magnitude with

Figure 6.4. (a) Role of geometric factor α in the effect of polarization charge on the (anti-)parallel alignment of neighboring dipolar particles. The schematic shows the electric field generated by a central dipole above a substrate (blue s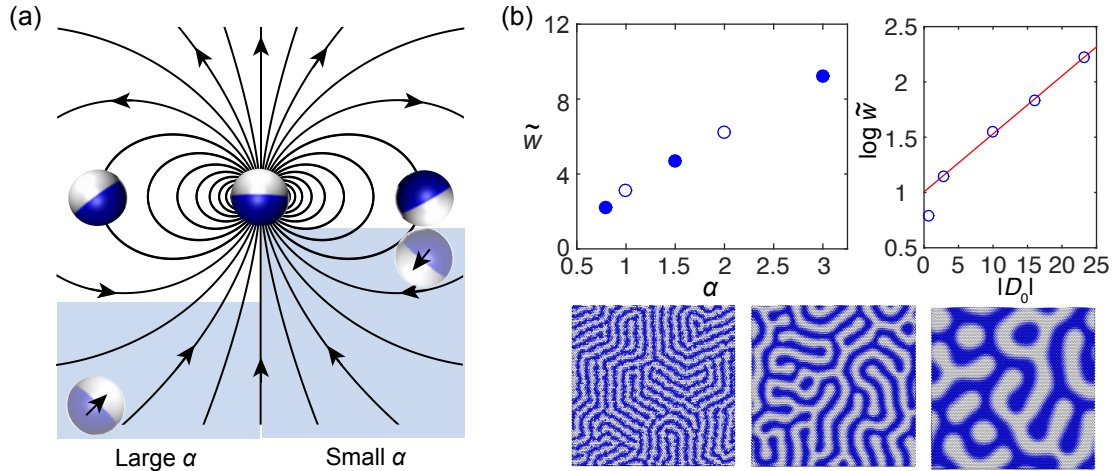haded region). The interaction with the "image" of a neighboring dipole (also shown) is characterized by the parameter $\lambda_{\mathrm{di}}^{(2)}$. At small geometric factor α (right) the field will promote anti-parallel alignment of the neighboring image dipole and hence also of the real dipole, in accordance with the direct dipole–dipole interaction. However, for large α (left), the polarization will promote parallel alignment of two neighboring dipoles, opposing the direct dipolar interaction. (b) Control of stripe width via the geometric factor. Reduced stripe width $\tilde{w}$ is shown as a function of α for fixed $\lambda_{\mathrm{dd}} = 5$ and $\lambda_{\mathrm{di}} = -16$ (upper left panel). The width exhibits an exponential dependence on the exchange parameter D_0 (upper right panel), confirming theoretical predictions. Representative equilibrium configurations of a 100×114 system are shown for $\alpha = 0.8$, 1.5, and 3 (lower panel).

increasing α, at fixed λ_{di}. For large α, its contribution to the total energy becomes comparable to the first-order (direct) D–I interaction. Interestingly, precisely in this situation of large α, the secondary images promote the parallel alignment of neighboring dipoles (cf. dipolar field in Fig. 6.4a, left-hand side), opposing (and overwhelming) the influence of the direct D–D interaction between nearest neighbors. Thus, the second-order D–I interaction acts as an 'exchange parameter' with magnitude $|D_0| = |\frac{2\alpha^2-1}{\alpha^2+1}\lambda_{\mathrm{di}}^{(2)}|$ that promotes short-range ferroelectric order (see Appendix 6.7 for derivation). However, at larger distances the dipolar coupling dominates and favors anti-ferroelectric order, resulting in modulated

(i.e., stripe and bubble) phases. By contrast, at small α the 'exchange parameter' D_0 is not only smaller in magnitude, but owing to the geometry of the dipolar field it also favors the same anti-parallel alignment as imposed by the D–D interactions (Fig. 6.4a, right-hand side, see Appendix 6.7 for details). This explains why different values of α result in modulated (stripe) or nonmodulated (OAF) equilibrium phases at large $|\lambda_{\mathrm{di}}|$.

The stripe phase, in particular, has been the subject of considerable attention[264,268,269,292], notably its formation mechanism in different systems and the degree to which it can be controlled. Remarkably, the dielectric modulation mechanism identified here allows fine control over the stripe width $\tilde{w}$ via the geometric factor α. The reduced stripe width is defined as $\tilde{w} = \langle N/N_{\mathrm{p}} \rangle$, where $N_{\mathrm{p}} = \sum_{\langle jk \rangle} H(-\mu_{j,z}\mu_{k,z})$ is the number of dipole pairs at stripe interfaces selected by the Heaviside function $H(x) = [1 + \mathrm{sgn}(x)]/2$. For fixed dipolar coupling λ_{dd} and dielectric coupling λ_{di}, the width of stripes can be manipulated accurately through variation of the geometric factor, as illustrated in Fig. 6.4b via $\tilde{w}$ as a function of α and D_0, as well as accompanying representative snapshots. The stripe width accurately reflects an exponential dependence on D_0 for sufficiently large $\tilde{w}$ (Fig. 6.4b), in accordance with predictions based upon the asymptotic expression for the ground-state energy of a 2D Ising dipole system[268]. Moreover, the domain-wall thickness t, which is determined by the balance between the exchange interaction D_0 and the surface anisotropy λ_{di}, increases with α. This is consistent with the theoretical prediction[293] that t scales as the square root of the ratio between the exchange enery and surface anisotropy.

6.5. Conclusion

In conclusion, we have demonstrated that dielectric effects can induce modulated phases in quasi-2D dipolar systems, without the presence of an additional competing interaction.

Notably, the so-called striped and bubble patterns can be realized in dipolar films on a substrate with negative static permittivity and/or permeability. Accurate control of the properties of these modulated phases is possible via a geometric factor, related to particle shape and separation, which can be interpreted in terms of an effective 'exchange parameter' promoting local ferroelectricity. Besides elucidating the pattern-modulation mechanism, our findings may also provide guidance to future applications of such metamaterials.

6.6. Appendix A: Reformulation of the Hamiltonian and phase diagram

We discuss an alternate representation of the Hamiltonian as well as the phase diagram constructed under this representation. The Hamiltonian presented in the main text can be written as

$$
\frac{\mathcal{H}}{k_{\mathrm{B}}T} = \frac{1}{2} \sum_{i=1}^{N} \sum_{\mathbf{n}}^{\infty} \left\{ \lambda_{\mathrm{dd}} \sum_{j=1}^{N}{}' \frac{\hat{\boldsymbol{\mu}}_i \cdot \hat{\boldsymbol{\mu}}_j - 3(\hat{\boldsymbol{\mu}}_i \cdot \hat{\mathbf{r}}_{ij}^{\mathrm{rep}})(\hat{\boldsymbol{\mu}}_j \cdot \hat{\mathbf{r}}_{ij}^{\mathrm{rep}})}{|\tilde{\mathbf{r}}_{ij}^{\mathrm{rep}}|^3} \right.
$$
$$
\left. + \gamma \lambda_{\mathrm{dd}} \sum_{j=1}^{N} \frac{\hat{\boldsymbol{\mu}}_i \cdot \hat{\boldsymbol{\mu}}_j' - 3(\hat{\boldsymbol{\mu}}_i \cdot \hat{\mathbf{r}}_{ij}'^{\mathrm{rep}})(\hat{\boldsymbol{\mu}}_j' \cdot \hat{\mathbf{r}}_{ij}'^{\mathrm{rep}})}{\left|\alpha^2 + |\tilde{\mathbf{r}}_{ij}^{\mathrm{rep}}|^2\right|^{3/2}} \right\},
$$

in which all variables have been introduced in the main text. In this formulation, we choose the dielectric mismatch γ as an independent variable rather than λ_{di}. There are two motivations for adopting this representation. First, γ is more directly related to materials properties, thus facilitating the connection to experiments. Second, in the long-range limit ($|\tilde{\mathbf{r}}_{ij}^{\mathrm{rep}}| \gg \alpha$) the total dipole–image energy scales as $\gamma \lambda_{\mathrm{dd}}$ compared to the dipole–dipole energy, which scales as λ_{dd}. Therefore, γ measures the anisotropy of the effective long-range interaction. However, we remark that γ only determines the *magnitude* of the dipole–image energy relative to the total long-range energy. Whether this contribution will reinforce or
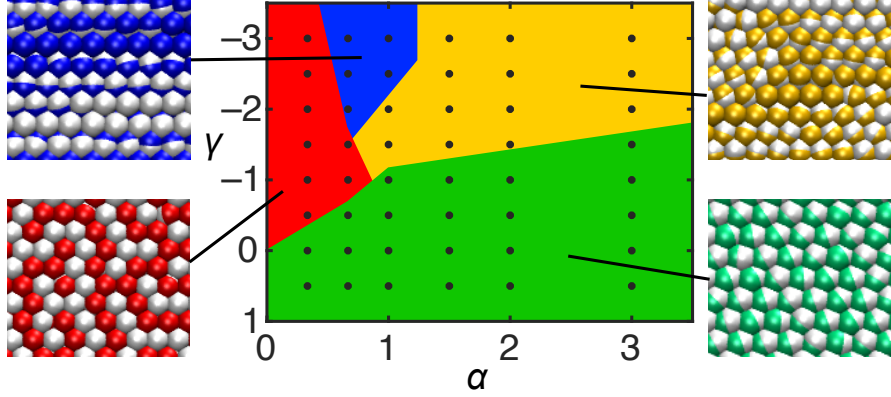
Figure 6.5. Phase diagram parametrized by α and γ at $\lambda_{dd} = 5$. Phase boundaries are drawn based on discrete simulation data points with positions indicated by the black dots.

counteract the dipole–dipole energy is different for dipoles with in-plane and out-of-plane orientation.

In addition to λ_{dd}, which serves as a global energy scale (or inverse temperature), and γ, we choose α as the third independent parameter. α determines the magnitude of the surface anisotropy (i.e., the first-order dipole–image interaction), characterized by $\gamma\lambda_{dd}/\alpha^3$. Figure 6.5 shows a $\lambda_{dd} = 5$ section of the phase diagram in the α–γ plane .

6.7. Appendix B: Energy analysis of the modulated phases

We (i) derive the effective pairwise potential between two dipoles placed on a dielectric substrate and (ii) demonstrate how this potential affects the resultant modulated phases. As a representative example, we focus on the stripe phase ($\lambda_{di} < 0$, $\gamma < 0$) and assume that the dipole moments of the particles are oriented perpendicular to the substrate owing to the attraction by their own images (cf. Fig. 4a, main text). Thus, the dipole moment $\boldsymbol{\mu}_i$ of particle i is given by $\boldsymbol{\mu}_i = \mu\boldsymbol{\sigma}_i$, where $\boldsymbol{\sigma}_i = (0, 0, \sigma_{i,z}) = (0, 0, \pm 1)$. The induced image dipole is $\boldsymbol{\mu}_i' = -\gamma\mu\boldsymbol{\sigma}_i$ (with γ as defined in the main text).

The electric field at the position $\mathbf{r}_j$ of dipole j, generated by dipole i located at $\mathbf{r}_i$ and its image located at $\mathbf{r}'_i = \mathbf{r}_i - (0, 0, d)$ (we recall that all dipoles are located at a distance $d/2$ above the surface) is

$$\mathbf{E}(\boldsymbol{\sigma}_i, r_{ij}) = \mathbf{E}^{\mathrm{dd}}(\boldsymbol{\sigma}_i, r_{ij}) + \mathbf{E}^{\mathrm{di}}(\boldsymbol{\sigma}_i, r_{ij}) , \tag{6.1}$$

where $r_{ij} = |\mathbf{r}_{ij}| = |\mathbf{r}_j - \mathbf{r}_i|$. Here the contributions $\mathbf{E}^{\mathrm{dd}}$ of the real dipole and $\mathbf{E}^{\mathrm{di}}$ of the image dipole are expressed as

$$\mathbf{E}^{\mathrm{dd}}(\boldsymbol{\sigma}_i, r_{ij}) = -\frac{\mu \boldsymbol{\sigma}_i}{\epsilon_m r_{ij}^3} , \tag{6.2}$$

$$\mathbf{E}^{\mathrm{di}}(\boldsymbol{\sigma}_i, r_{ij}) = \frac{\gamma \mu}{\epsilon_{\mathrm{m}}} \left(\frac{\boldsymbol{\sigma}_i}{(r_{ij}^2 + d^2)^{3/2}} - \frac{3d\sigma_{i,z} \mathbf{r}'_{ij}}{(r_{ij}^2 + d^2)^{5/2}} \right) , \tag{6.3}$$

where $\mathbf{r}'_{ij} = \mathbf{r}_j - \mathbf{r}'_i = \mathbf{r}_{ij} + (0, 0, d)$. Thus, the total pairwise electrostatic energy between dipole i and j is

$$U_{\mathrm{p}}^{\mathrm{tot}}(\boldsymbol{\sigma}_i, \boldsymbol{\sigma}_j, r_{ij}) = -\boldsymbol{\mu}_j \cdot \mathbf{E}(\boldsymbol{\sigma}_i, r_{ij}) = U_{\mathrm{p}}^{\mathrm{dd}} + U_{\mathrm{p}}^{\mathrm{di}} , \tag{6.4}$$

where the dipole–dipole and dipole–image (i.e., interaction of a dipole with the polarization induced by the *other* dipole) contributions, $U_{\mathrm{p}}^{\mathrm{dd}}$ and $U_{\mathrm{p}}^{\mathrm{di}}$, are given by

$$\frac{U_{\mathrm{p}}^{\mathrm{dd}}(\boldsymbol{\sigma}_i, \boldsymbol{\sigma}_j, \tilde{r}_{ij})}{k_{\mathrm{B}} T} = \lambda_{\mathrm{dd}} \frac{\sigma_{i,z} \sigma_{j,z}}{\tilde{r}_{ij}^3} , \tag{6.5}$$

$$\frac{U_{\mathrm{p}}^{\mathrm{di}}(\boldsymbol{\sigma}_i, \boldsymbol{\sigma}_j, \tilde{r}_{ij})}{k_{\mathrm{B}} T} = \lambda_{\mathrm{di}} \left(\frac{2\alpha^2 - \tilde{r}_{ij}^2}{\alpha^2 + \tilde{r}_{ij}^2} \right) \frac{\sigma_{i,z} \sigma_{j,z}}{(1 + \tilde{r}_{ij}^2/\alpha^2)^{3/2}} . \tag{6.6}$$

As in the main text, we choose the lattice constant a as the unit length and use a tilde to denote reduced lengths.

From the energy expressions Eqs. (6.5) and (6.6) it is evident that the magnitudes of both $U_{\mathrm{p}}^{\mathrm{dd}}$ and $U_{\mathrm{p}}^{\mathrm{di}}$ decay asymptotically with the center-to-center distance $\tilde{r}$ as $1/\tilde{r}^3$. However,
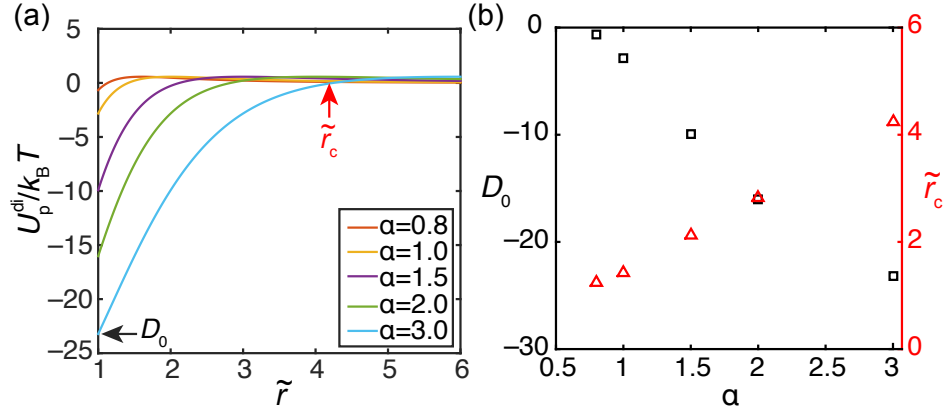
Figure 6.6. Illustration of the effective pairwise interaction between two dipoles placed on a dielectric substrate and oriented parallel to the z-axis. As in Fig. 4 in the main text, we set $\lambda_{dd} = 5$ and $\lambda_{di} = -16$, corresponding to the stripe phase. (a) Dipole–image component of the pairwise interaction, U_p^{di}, as a function of the center-to-center distance $\tilde{r}$ at different values of the geometric factor α. The depth D_0 of the energy well and the critical separation $\tilde{r}_c$ at which U_p^{di} switches sign are marked by arrows. (b) Dependence of the two characteristic parameters D_0 (left-hand axis) and $\tilde{r}_c$ (right-hand axis) as functions of α. Both quantities grow in magnitude with increasing α.

what truly matters is how these interactions depend, at different length scales, on the relative dipolar orientations $\{\sigma_{i,z}, \sigma_{j,z}\}$. The direct interaction U_p^{dd} decays monotonically, favoring anti-parallel orientational arrangements (with $\sigma_{i,z}\sigma_{j,z} = -1$) at all length scales. However, at sufficiently short $\tilde{r}$ this is overwhelmed by the deep energy well of the dipole–image interaction U_p^{di} with $\sigma_{i,z}\sigma_{j,z} = 1$ (Fig. 6.6a), favoring parallel arrangements. At $\tilde{r}_c = \sqrt{2}\alpha$, the dipole–image contribution changes sign, so that a nonmonotonic trend results, where ferroelectric order is preferred at short distances and anti-parallel arrangements become favorable at larger $\tilde{r}$. Thus, as illustrated in the main text, the dipole–image component of the pairwise interaction acts as an effective 'exchange interaction' to promote short-range ferroelectricity. Here the depth of the energy well $D_0 = \lambda_{di}^{(2)} \frac{2\alpha^2 - 1}{\alpha^2 + 1}$ (in reduced units) and the critical distance $\tilde{r}_c$ at which U_p^{di} switches sign characterize the strength and range of this exchange interaction, both of which grow in magnitude with α (Fig. 6.6b).

Interestingly, even though the interaction range extends beyond the nearest neighbors (especially at large α), we observe that the exponential dependence of the stripe width on the exchange parameter, as found for the 2D dipolar Ising system[268] (with nearest-neighbor exchange interaction only), accurately describes our system as well (see Fig. 6.4b).

Finally, it is noteworthy that while the observed orientational phases can be realized in magnetic films by exploiting the quantum exchange interaction, they cannot be sustained in systems with larger length scales (e.g., in colloidal systems). By contrast, in the approach proposed here the many-body dielectric force acts effectively as an exchange interaction in which both strength and range can be tuned independently by varying λ_{di} and α. This provides new ways to realize and control orientationally modulated patterns beyond the atomic scale, with potential applications in optical devices and the possibility to serve as a starting point for other studies on controlling orientational structure in materials.

CHAPTER 7

Comparison of the Efficient Hybrid Method and the Boundary Element Method

This chapter presents a close comparison between the hybrid method and the boundary-element method in terms of the accuracy and efficiency. The content of this chapter is based on the following publication:

- Z. Gan[1], Z. Wang[1], S. Jiang, Z. Xu and E. Luijten, "Efficient dynamic simulations of charged dielectric colloids through a novel hybrid method," J. Chem. Phys. **151**, 024112 (2019)

7.1. Abstract

Modern particle-based simulations increasingly incorporate polarization charges arising from spatially nonuniform permittivity. For complex dielectric geometries, calculation of these induced many-body effects typically requires numerical solvers based upon boundary-element methods, which very significantly increase the required computational effort. For the special case of dielectric spheres, such as colloids or nanoparticles, a semi-analytical spectrally accurate hybrid method has been proposed recently that combines the Method of Moments, the Image-Charge Method, and the Fast Multipole Method. The hybrid method is efficient and accurate even when dielectric spheres are closely packed. Here, we apply this hybrid method to both static configurations and molecular dynamics simulations. The

---

[1]These authors contributed equally to the work

choice of the relevant numerical parameters for molecular dynamics simulations is discussed in detail, as well as comparisons to the boundary-element method. As a concrete example, we examine the challenging case of binary crystal structures composed of close-packed dielectric colloidal spheres.

7.2. Introduction

Electrostatic interactions are ubiquitous in nature and arise in many areas of science and engineering[22,28,114]. Whereas the long-range nature of these interactions makes their computational treatment already costly, the problem is compounded in systems with spatially nonuniform permittivity. Materials that differ in dielectric constant respond differently to electric fields, a property that—for systems with piecewise uniform permittivity—can be described in terms of an induced surface charge density distributed on the dielectric interfaces. This *polarization charge* contributes to the electric field, and hence must be solved self-consistently[143,145]. Due to the computational effort involved this contribution is often ignored, but various studies have demonstrated that this approximation can have profound consequences, as polarization can influence protein folding[35], ion transport through pores[170] and nanochannels[37], and nanoparticle aggregation and self-assembly[12,164]. As these many-body effects are often analytically intractable, computational methods constitute an important tool toward greater physical understanding of the underlying phenomena.

The practical computational challenge associated with investigating polarization effects arises from the difficulty in efficiently obtaining an accurate estimate for the polarization charge. Note that even if the polarization contribution can be accurately resolved, the calculation usually becomes very demanding in the context of molecular dynamics (MD) or Monte Carlo (MC) simulations. The internal energy or forces need to be evaluated at

each time step, and typically millions of time steps are required to obtain sufficient data for accurate ensemble averages, even after reaching thermodynamic equilibrium.

To overcome this computational challenge, various numerical methods have been proposed[46–50,129,130,163,249,294–301]. Electrostatic solvers using finite-difference and finite-element methods[114,296] are less efficient for practical MD/MC simulations since (i) they require discretizing the entire three-dimensional (3D) space and (ii) special treatment is needed to accurately model sharp dielectric interfaces and point charges. In the latter case, boundary element methods (BEMs)[46–50,129,163,294,300,301] offer an alternative. The BEM reduces the 3D electrostatic Poisson equation to a boundary integral equation, thus only requiring the discretization of two-dimensional dielectric interfaces. The first MD simulation for *mobile* dielectric objects was carried out using this approach, studying a system of 100 dielectric spheres[164]. Yet, the BEM remains highly time consuming, in particular for dielectric interfaces that are closely spaced. This situation typically arises in self-assembly processes of densely packed structures, where a large amount of boundary elements is required to resolve the numerical singularity due to nearly touching interfaces.

Instead of considering dielectric interfaces with arbitrary shape, the numerical difficulties can be reduced if we start with models that are comprised of simple geometric shapes yet still capture the essential physics. Naturally, the simplest case is based on the primitive model, i.e., an ensemble of dielectric spheres with central charges, immersed in a solvent modeled implicitly as a dielectric continuum. For such systems of charged dielectric spheres, alternative approaches can be employed to solve the electrostatic potential, e.g., the Method of Moments (MoM)[41–45], the Image Charge Method (ICM)[38–40], and the perturbative many-body expansion method[51,52]. These methods are developed by taking advantage of the spherical geometry and based on analytical forms, thus avoiding the need to discretize the dielectric

boundaries into elements. The MoM scales as $\mathcal{O}(N)$ if accelerated using the Fast Multipole Method (FMM)[123,302,303], where N is the total number of spheres. However, it suffers from slow convergence if spheres are close. The ICM is both accurate and efficient if there are only one or two spheres, but as the number of spheres grows, the ICM computational cost increases as a power law (typically $\mathcal{O}(N^3)$, see Ref. 200) due to the repeated image reflection between spheres. Finally, the perturbative many-body expansion method is also an analytical method tailored for charged dielectric sphere systems, again with computational complexity that scales as $\mathcal{O}(N^m)$ if the expansion is truncated at the level of m-body interactions. As the expansion converges more slowly if spheres get closer, this approach (just like the ICM) becomes costly for systems of closely spaced objects. An alternative method in this category is the hybrid method developed in Ref. 53 by Gan et al., an efficient and spectrally accurate semi-analytical approach for solving the electrostatics in systems of multiple dielectric spheres. In this approach, the ICM was first extended to analytically account for the effect of multipoles in the 3D dielectric case. Then the MoM, the ICM, and the FMM were combined to obtain an accurate and well-conditioned numerical method that requires a nearly optimal number of unknowns with optimal $\mathcal{O}(N)$ computational complexity. It is worth noting that the hybrid method works well even for compact configurations of spheres, since the most singular part of the problem is removed by the ICM.

In this chapter, we present numerical tests to determine the dependence of the accuracy and efficiency of the hybrid method on various numerical parameters, and perform a comparison of the hybrid method with the BEM. By matter of illustration, we carry out efficient MD simulations using the hybrid method for a representative binary mixture of dielectric spheres. We conclude with a discussion of the possible extensions of the hybrid method to other systems, periodic boundary conditions, and MC simulations.

7.3. Results and Discussion

7.3.1. Overview of the hybrid method

The basic idea of this hybrid method is as follows (see Fig. 7.1). If the dielectric spheres are well separated (with center-to-center distance larger than the cutoff η), the MoM is coupled with the FMM and an iterative solver to take advantage of the spherical geometry and achieve optimal complexity. If the spheres are close to each other (with center-to-center distance smaller than η), images are generated only for nearly touching pairs of spheres and the ICM is applied. The accuracy of the hybrid method is solely determined by the truncation order p for the spherical harmonics and the cutoff distance η which controls the number of image charges. The computational cost for both the MoM and the ICM parts is linear to N, specifically scaling as $\mathcal{O}(Np^3)$ and $\mathcal{O}(N\eta^3)$, respectively[203]. This method has been incorporated in a MD simulation and demonstrates simultaneously linear scaling behavior and high accuracy[203]. The key issues for the implementation and extension of the hybrid method, including a detailed derivation of the expressions for the electrostatic energy, surface charge density, and forces on individual dielectric spheres, have been detailed in Ref. 203. In the rest of Section 7.3, we provide a systematical comparison between the hybrid method and the GMRES-accelerated BEM in terms of accuracy and efficiency at different parameter settings.

7.3.2. Numerical tests: static configurations

To illustrate the accuracy and efficiency of the hybrid method, we apply it to representative close-packed crystal structures formed by a binary mixture of size-asymmetric and oppositely charged dielectric spheres. We examine two crystal structures, namely a NaCl and a wurtzite
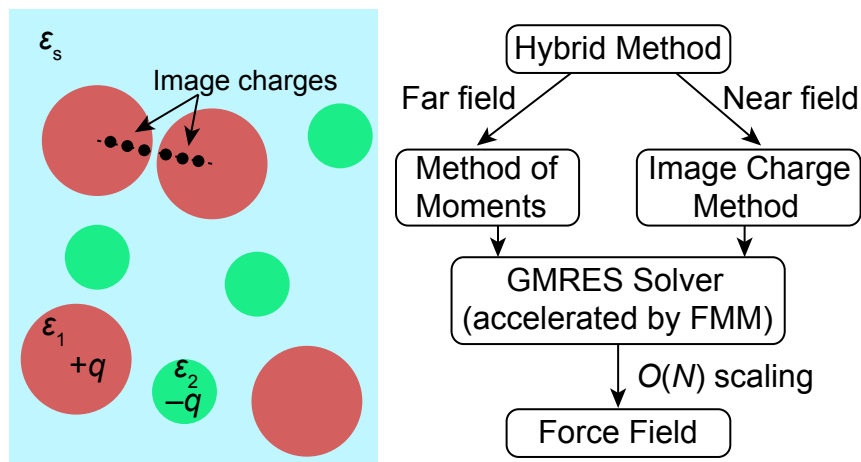
Figure 7.1. Schematic showing the system and workflow of the hybrid method.

structure, illustrated in Fig. 7.2. Such densely packed structures with closely spaced dielectric interfaces are generally challenging for most numerical methods. Disordered configurations occurring in dynamic simulations tend to have fewer of the particle arrangements that yield the largest numerical errors, and are typically also less costly to evaluate as the number of image charges needed is generally smaller. The large and small spheres have diameters d_{L} and d_{s}, respectively, and a size ratio $d_{\mathrm{L}}/d_{\mathrm{s}} = 8$. To avoid divergences due to the overlap of two dielectric interfaces, we place the dielectric surface of each large sphere at $r = 3.5d_{\mathrm{s}}$, i.e., $0.5d_{\mathrm{s}}$ below the sphere surface. The large spheres each carry a charge $+q$ and the small spheres each a charge $-q$. The two species are present in a 1:1 number ratio, so that charge neutrality is satisfied. We select interaction parameters similar to those chosen in Ref. 164, where the dielectric constant of the solvent is rescaled to $\varepsilon_{\mathrm{s}} = 1.0$ and the small spheres have the same dielectric constant as the solvent. For the NaCl structure, we set the dielectric constant of the large spheres to $\varepsilon_{\mathrm{L}} = 0.01$, whereas for the wurtzite structure we choose the inverse mismatch, with $\varepsilon_{\mathrm{L}} = 100$. In both cases, the magnitude of the charge q is chosen

such that the dimensionless coupling strength $\lambda = q^2/[0.5\varepsilon_s(d_L + d_s)k_BT] = 100$, where k_BT is the thermal energy (with k_B Boltzmann's constant and T the absolute temperature).
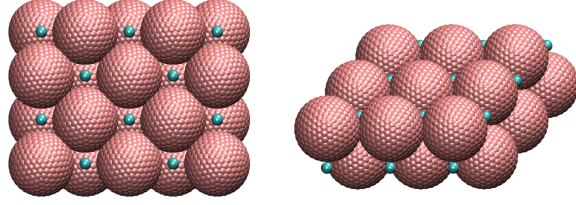

Figure 7.2. Two crystal structures formed by binary size-asymmetric dielectric spheres, used for testing the hybrid method. (left) NaCl crystal structure with lattice constant $\sqrt{2}d_L$ formed by 20 large spheres and 20 small spheres; (right) wurtzite crystal structure with lattice constants $a = b = d_L$, $c = 2\sqrt{2}d_L/\sqrt{3}$, formed by 18 large spheres and 18 small spheres. The lattice constants are chosen such that the large spheres are precisely touching. Since the dielectric interface is located $0.5d_s$ below the sphere surface, the dielectric surfaces of two touching spheres are separated by d_s.

To obtain reference values for these two static configurations, we first calculate the energy for both structures using the analytic MoM. The multipole expansion is truncated at a sufficiently high order (with the truncation order $p = 30$) to guarantee that the energies are correct to the first six digits, with values $-1028.49k_BT$ and $-2267.41k_BT$ for the NaCl and wurtzite configurations, respectively. To quantify the performance of the hybrid method, we compute both the total electrostatic energy of the configurations and the net electrostatic force exerted on each sphere. We examine the convergence of the hybrid method as a function of algorithm parameters by comparison to the corresponding reference values. To establish the efficiency of the hybrid method, we also compute the results via the BEM of Ref. 50.

In the hybrid method, we set the FMM accuracy to 9 digits, the GMRES tolerance to 10^{-6}, and use 3-point Gauss–Jacobi quadrature for discretizing the image line integrals. The accuracy of the hybrid method is then solely determined by the truncation order p for the

Table 7.1. Accuracy and efficiency of the hybrid method and the BEM for the electrostatic energy calculation of the NaCl and wurtzite configurations in Fig. 7.2. All CPU time results are obtained by averaging over 100 calculations of both the total energy and the force on each large dielectric spheres (the initialization time is not counted in both methods). For both methods, the corresponding numerical parameters are varied to show the convergence (as reference values we use the energies computed via the analytic MoM at $p = 30$, $-1028.49 k_\mathrm{B}T$ for the NaCl configuration and $-2267.41 k_\mathrm{B}T$ for the wurtzite configuration). p is the order at which the multipole expansion is truncated in the hybrid method and η is the cutoff that controls the total number of images N_im between close pairs. In the BEM, N_p is the number of the discretized patches on each large sphere. The results with $N_\mathrm{p} \to \infty$ are obtained by extrapolation, cf. Fig 7.3. Timing data for the BEM data with $N_\mathrm{p} = 14522$ are affected by memory constraints and therefore not reported.

			Hybrid method			Boundary element method		
	p	η	N_im	energy $(k_\mathrm{B}T)$	time (s)	N_p	energy $(k_\mathrm{B}T)$	time (s)
NaCl	3	3	480	-1009.20	0.014	372	-1098.86	1.116
crystal	3	4	1392	-1038.23	0.047	732	-1077.85	1.355
	4	4	1392	-1023.76	0.056	1472	-1062.54	2.284
	4	5	1614	-1023.73	0.069	3002	-1051.56	6.320
	5	5	1614	-1028.38	0.084	6072	-1043.88	21.341
	5	6	2688	-1028.43	0.140	14522	-1037.55	n/a
						∞	-1025.80	
Reference				-1028.49			-1028.49	
wurtzite	3	3	508	-2375.67	0.014	372	-2326.40	1.112
crystal	3	4	1194	-2382.37	0.037	732	-2310.07	1.335
	4	4	1194	-2284.24	0.044	1472	-2297.53	2.215
	4	5	1518	-2282.63	0.061	3002	-2288.63	5.812
	5	5	1518	-2272.37	0.074	6072	-2282.39	19.772
	5	6	2216	-2267.43	0.081	14522	-2277.17	n/a
						∞	-2267.90	
Reference				-2267.41			-2267.41	

spherical harmonics and the number of image charges (via the cutoff distance η). Table 7.1 lists the energies for both systems as a function of these two parameters.

As we systematically increase p and η, we observe a clear convergence of the energy for both the NaCl and wurtzite structures (left-hand side of Table 7.1). Specifically, in both cases the energy is accurate up to the fifth digit at $p = 5$ and $\eta = 6$, with a moderate

number of image charges ($\sim$130 image charges per sphere). As the computational cost of the hybrid method is proportional to both p^3 and η^3, we gradually increase both parameters simultaneously in Table 7.1 to keep both of them sufficiently small.
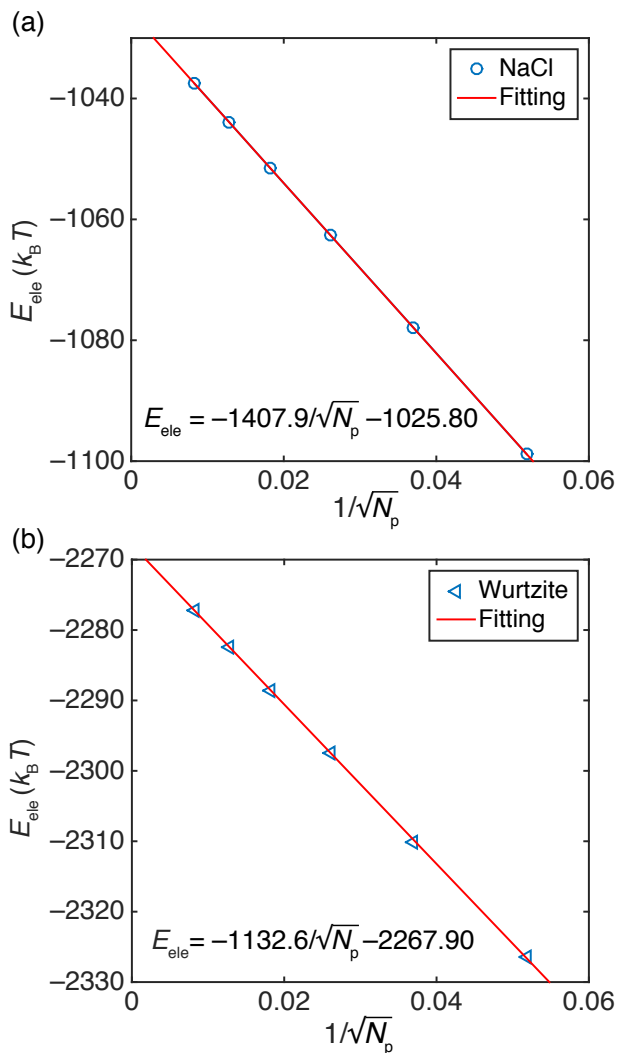
Figure 7.3. Extrapolation of the electrostatic energy E_{ele} in the BEM as a function of $1/\sqrt{N_p}$ (N_p the number of surface patches per sphere) for the (a) NaCl and (b) wurtzite crystal structures. The extrapolated values are in close agreement with the reference values obtained via the Method of Moments.

For the BEM, the accuracy is controlled by the accuracy of the particle–particle particle–mesh (PPPM) electrostatic solver, the GMRES tolerance, and the number of surface patches.

By testing different combinations of the PPPM and GMRES accuracies, we empirically determined that (at fixed number of patches) the energy converges to at least the fourth digit if both are set to 10^{-5}. We employ these tolerances for all BEM data shown and only vary the number of surface elements. It should be noted that the BEM calculations are performed for a system with periodic boundary conditions, so that the system size matters. We used a cube of linear size $L = 60d_s$ and confirmed (by comparison to $L = 100d_s$ and $L = 200d_s$) that this periodicity has an effect of less than 10^{-4} on the energy. We systematically vary the number of patches on each large sphere N_p from 372 to 14522 and compute the total electrostatic energy of both configurations (right-hand side of Table 7.1). The energy values show a quite strong dependence on N_p, but a plot of the energy as a function of $1/\sqrt{N_p}$ (which is proportional to the boundary element size), Fig. 7.3, illustrates convergence to -1025.80 for the NaCl structure and -2267.90 for the wurtzite structure as $N_p \to \infty$. These values are in quite good agreement with the reference values, deviating by 0.3% and 0.03%, respectively. The linear convergence with boundary-element size has been reported for other BEM approaches[304,305]. Whereas a fairly accurate estimate for the energy can be obtained in the BEM through extrapolation, this is not a particularly useful approach in a practical MD or MC simulation, where each run employs only a single number of surface patches. Without the extrapolation, the BEM shows deviations of $\sim 1\%$ even at the largest N_p (14522 patches per large sphere) tested here, owing to the closely separated dielectric interfaces.

Since MD simulations evolve via Newton's equations of motion, i.e., based upon forces rather than energies, we also compare the force exerted on each sphere in the hybrid method and the BEM. Since these forces are not extrapolated as a function of N_p in an actual (BEM-based) MD simulation, we directly compare the forces obtained in the BEM at $N_p = 14522$

with those obtained in the hybrid method at $p = 5$ and $\eta = 6$. The relative root-mean-square difference in the forces is defined as

$$\Delta_{\mathbf{F}} = \sqrt{\frac{\sum_{i=1}^{N} |\mathbf{F}_{HM}^i - \mathbf{F}_{BEM}^i|^2}{\sum_{i=1}^{N} |\mathbf{F}_{HM}^i|^2}} \, , \tag{7.1}$$

where the summation extends over all large spheres, and $\mathbf{F}_{HM}^i$ and $\mathbf{F}_{BEM}^i$ denote the electrostatic force exerted on sphere i computed via the hybrid method and the BEM, respectively. We find that the relative discrepancy $\Delta_{\mathbf{F}}$ is 0.6% and 2.6% for the NaCl and wurtzite crystal test cases, respectively.

The hybrid method needs far fewer image charges than the number of patches in the BEM to achieve a high accuracy. Since the electrostatic solver is the dominant factor in the computational cost of the induced energy and force calculation, the hybrid method accordingly outperforms the BEM (see CPU time comparison in Table. 7.1). At four-digit accuracy in the electrostatic energy, the hybrid method (with $p = 5$, $\eta = 6$) is more than a hundred times faster than the BEM for $N_{\mathrm{p}} = 6072$ (which yields significantly lower accuracy) for both test cases.

7.3.3. MD simulations: ensemble averages

Whereas numerical tests on static configurations provide information on accuracy and on the appropriate numerical parameter settings, it is also informative to apply the hybrid method to practical simulations of the aggregation of a binary mixture of dielectric spheres. We examine the performance of the method and also cross-check ensemble-averaged equilibrium properties with simulations performed using the BEM.

We employ the same parameter settings as the NaCl case tested in the previous section. In addition to the electrostatic interactions, we impose excluded-volume interactions modeled via a shift-truncated Lennard-Jones (LJ) potential,

$$u_{\mathrm{LJ}}(r) = 4k_{\mathrm{B}}T \left[\left(\frac{d_{\mathrm{s}}}{r - \Delta} \right)^{12} - \left(\frac{d_{\mathrm{s}}}{r - \Delta} \right)^{6} + \frac{1}{4} \right] , \tag{7.2}$$

for $\Delta < r \leq 2^{\frac{1}{6}} d_{\mathrm{s}} + \Delta$, with $\Delta = 0, 3.5 d_{\mathrm{s}}$, and $7 d_{\mathrm{s}}$ for small–small, small–large, and large–large interactions, respectively. This yields a large–small size ratio of 8. As before, we place the dielectric surface of each large sphere at $r = 3.5 d_{\mathrm{s}}$, where the purely repulsive LJ potential already diverges. The mass of all spheres, which affects the dynamical evolution of the system but not its thermodynamic properties, is set to m_0, yielding a time scale $t_0 = d_{\mathrm{s}} \sqrt{m_0 / k_{\mathrm{B}}T}$.

We perform MD simulations of a binary mixture containing 20 large and 20 small spheres. For the hybrid method, the system is confined in a spherical cell with cell radius $R_{\mathrm{shell}} = 30 d_{\mathrm{s}}$ and the algorithm parameters are set to $p = 5$ and $\eta = 6$. For the BEM, we employ a cubic cell of size $L = 60 d_{\mathrm{s}}$ and periodic boundary conditions. The number of patches per large sphere is set to $N_{\mathrm{p}} = 1472$, for reasons of computational feasibility. The tolerances are set as detailed in Sec. 7.3.2.

In each time step, the (direct and induced) electrostatic force on each particle is calculated and used to propagate the particles via the standard velocity-Verlet algorithm. A Langevin thermostat with damping time t_0 is used to control the temperature. Simulations are run for 5×10^5 steps for equilibration and another 5×10^5 steps to generate samples, with a timestep of $0.001 t_0$. The various contributions to the total energy as well as the radial distribution functions are sampled every 500 steps during the production phase.
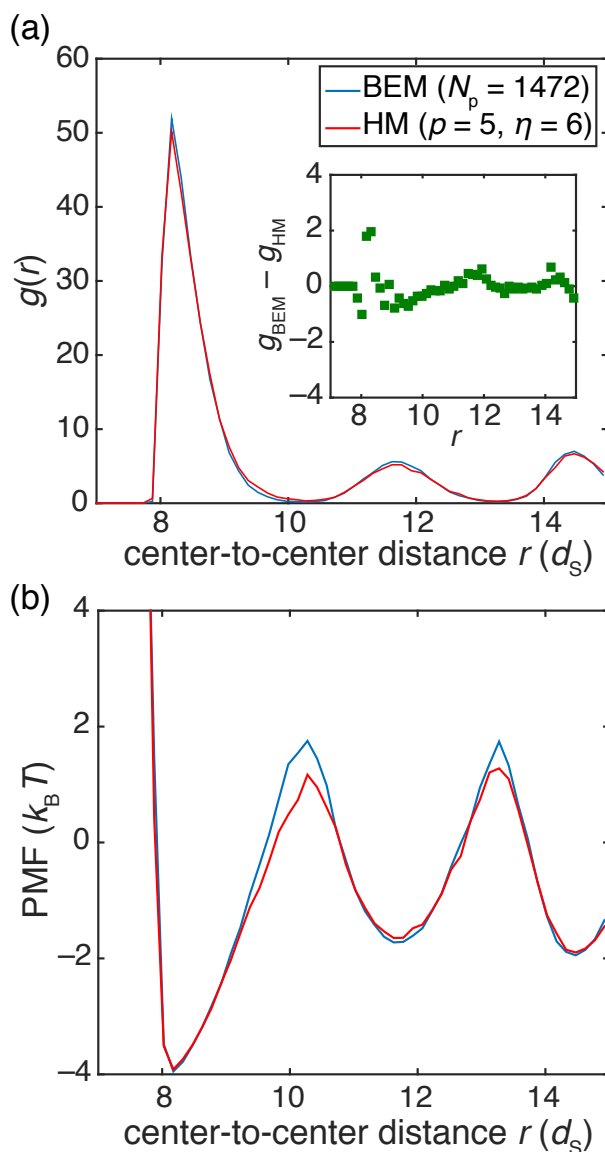
Figure 7.4. (a) Large–large particle radial distribution functions for the system described in Sec. 7.3.3, obtained using the BEM (blue curve) and the hybrid method (HM, red curve). Inset: difference between the two distribution functions. (b) Corresponding potential of mean force $-k_B T \ln g(r)$.

The equilibrated structure is predicted to be a NaCl crystal[164], which is confirmed visually

for both methods. Moreover, the radial distribution function for the large spheres (Fig. 7.4)

produced by the hybrid method is almost identical to that produced by the BEM-based

simulation. While the two dielectric solvers show excellent consistency in the self-assembled structure, the hybrid method achieves this at a rate of 0.140 seconds per time step, compared to 2.284 seconds per time step for the BEM (see Table 7.1). In addition, the static tests show that for the settings adopted, the hybrid method method yields an electrostatic energy that is virtually indistinguishable from the reference value, whereas the BEM yields an energy that deviates from this value by more than 3%. As this deviation refers to a truly dense-packed configuration, it is worthwhile to examine whether the ensemble-averaged energy shows a similar deviation. Table 7.2 shows the ensemble-averaged energies for MD simulations employing either the hybrid method or the BEM, with different parameter settings. Even though the hybrid and BEM simulations with the most precise parameter choices produced very similar self-assembled structures, the average electrostatic energies differ by approximately 4%, comparable to the difference in Table 7.1 for the same parameters.

Table 7.2. Ensemble averaged electrostatic and LJ energies obtained through MD simulations using the hybrid method and BEM.

hybrid method		
numerical parameters	E_{ele}	E_{LJ}
$p = 4, \eta = 4$	-954.0 ± 0.5	3.58 ± 0.07
$p = 4, \eta = 5$	-941.4 ± 0.6	2.69 ± 0.06
$p = 5, \eta = 6$	-943.9 ± 0.6	2.69 ± 0.05
boundary element method		
$N_{\mathrm{p}} = 372$	-1019.3 ± 0.8	2.98 ± 0.06
$N_{\mathrm{p}} = 732$	-997.5 ± 0.9	2.86 ± 0.06
$N_{\mathrm{p}} = 1472$	-984.5 ± 0.8	3.00 ± 0.06

7.4. Conclusion

We have provided a concise overview of the hybrid method, systematically explored the effect of various parameters on efficiency, convergence, and accuracy, and illustrated

application of the method in a practical case that is challenging for competing approaches. Unlike boundary-element approaches, which suffer from significant inaccuracies in situations with closely spaced dielectric interfaces (such as in densely packed structures), and other analytical approaches, which require an effort that increases rapidly (at least cubic power-law dependence) with the number of dielectric spheres, the hybrid solver simultaneously offers linear scaling behavior and high accuracy. We demonstrated that, for densely packed configurations of relatively small numbers of dielectric spheres, the hybrid method computes the electrostatic energy with a deviation of less than 0.01% at a rate that is more than two orders of magnitude faster than the BEM can achieve for deviations of 3%.

This approach is generally applicable to multicomponent systems of charged dielectric spheres. In principle, extension of our method to continuously variable, radially symmetric permittivities $\epsilon(r)$ is feasible by using a harmonic interpolation, which results in a spherical harmonic series than can be transformed into an image-charge method. Lastly, although the current algorithm is restricted to finite systems, it can be further extended to situations with periodic boundary conditions.

CHAPTER 8

Anisotropic self-assembly of polarizable colloidal mixtures

The content of this chapter is based on the following publication:

- Z. Wang, Z. Gan, S. Jiang, Z. Xu and E. Luijten, "Anisotropic self-assembly of polarizable colloidal mixtures," To be published (2020)

8.1. Abstract

Particles with directional interactions are often realized through anisotropic shape or surface patches. We demonstrate that dielectric many-body effects can impart effective directionality to isotropic building blocks, which permits robust self-assembly of binary mixtures of oppositely charged colloids into anisotropic superstructures. Using a high-precision simulation strategy, we show that both local coordination number and fractal dimension can be accurately controlled through variation of particle size ratio and relative permittivity. This mechanism offers a potential avenue to designing materials with controllable structural properties.

8.2. Introduction

Self-assembly of nano- and micron-sized colloidal particles has long been a powerful means for creating materials with tailored mechanical, optical, and electronic properties in applications ranging from electro-mechanical systems to photonics and biomedical devices[307–309]. Thus, uncovering new design rules which lead to structures with precisely controlled local and global properties is highly desirable. While isotropic inter-particle interactions often

lead to close-packed ordered structures[310,311] (with a few exceptions that exploit the presence of multiple length scales[292,312]), far richer phase diagrams can be achieved by introducing anisotropic (directional) interactions[313], which can arise from, e.g., shape[21], surface patchiness[314], external fields[5,315], or grafted polymers[316,317].

Ubiquitous versatile, electrostatic forces have shown their great power in mediating and directing self-assembly of colloidal particles, including colloidal aggregation[29,30], clustering[31], and formation of nanostructured materials[32–34]. However, a parameter that, owing to its complicated many-body nature, has often been neglected or oversimplified in both experiment and computation, is the dielectric mismatch between particles and the surrounding medium, which gives rise to polarization charge at all interfaces. This omission is noteworthy, given the demonstrated effects of polarization on protein folding[35], plasmonics[36], pattern formation[318], and ion transport[37]. The first molecular dynamics (MD) simulations studying dielectric effects in colloidal aggregation were performed using the boundary element method (BEM)[164], and demonstrated that polarization interactions can indeed qualitatively alter the resultant structures of charged colloids. Yet, this conceptual study was carried out for a specific parameter choice, as the BEM-based approach is computationally very costly, in particular for closely spaced dielectric interfaces that typically arise in self-assembly processes. This problem is exacerbated by the subtle energy differences between distinct structures[319], which makes high precision imperative for predictive modeling of self-assembly. As a result, no systematic exploration exists that elucidates how dielectric effects influence the properties of self-assembled structures and the associated design rules are unknown.

Here, we set out to establish how polarization phenomena can be exploited to control self-assembly of binary colloidal mixtures. We take advantage of a newly developed efficient

"hybrid method"[53,203] that reduces systematic errors by three orders of magnitude and simultaneously accelerates calculations by one or two orders of magnitude compared to the BEM. This powerful improvement, in particular for densely packed dielectric interfaces, allows reliable exploration of the full phase space. We demonstrate that the many-body nature of the dielectric effects imparts effective directionality to the inter-particle interactions and thereby dictates the geometry of the resultant self-assembled structures. Moreover, we formulate design rules in which the local coordination number and fractal dimension can be controlled through variation of the particle size ratio and the mismatch in relative permittivity.

8.3. Model and Simulation Methods

As a model system, we choose a prototypical binary mixture of oppositely charged size-asymmetric spherical colloids[29–33,164,320]. This mixture consists of N_L large colloids (positive charge $+q_L$, permittivity ϵ_L, radius r_L) and N_S small colloids (negative charge $-q_S$, permittivity ϵ_S, radius r_S) suspended in an implicit solvent (permittivity ϵ_m). Charge neutrality is imposed by requiring $N_L q_L = N_S q_S$. Owing to the piecewise uniform permittivity, surface polarization charge is induced at all particle–solvent interfaces. We choose a salt-free system to isolate the role of dielectric effects, but our findings also apply to colloidal systems at low salt concentration as well as macroscopic systems, especially granular particles[321].

We study this system via large-scale MD simulations in the canonical ensemble under spherical confinement. This choice is dictated by the hybrid method that is essential to high-fidelity predictions. The number of large colloids is fixed at $N_L = 100$ (except in the calculation of fractal dimensions), which is sufficient to reveal large-scale structures. The box volume is chosen such that the large colloids have a volume fraction of 2.5%.

This ensures that boundary effects are negligible, yet is high enough to stabilize the crystalline phase. We fix the size of the large sphere to be $r_{\mathrm{L}} = 4\sigma$ and systematically vary the size ratio $\alpha = r_{\mathrm{L}}/r_{\mathrm{S}}$ from 1.5 to 8.0. The excluded-volume interactions between colloids are modeled via a purely repulsive shifted-truncated Lennard-Jones (LJ) potential, $4k_{\mathrm{B}}T\left\{[\sigma/(r-\Delta)]^{12} - [\sigma/(r-\Delta)]^6 + 1/4\right\}$ for $\Delta < r < 2^{1/6}\sigma + \Delta$, with hard-core diameter $\Delta = 2r_{\mathrm{S}} - \sigma$, $r_{\mathrm{S}} + r_{\mathrm{L}} - \sigma$, and $2r_{\mathrm{L}} - \sigma$ for small–small, small–large, and large–large interactions, respectively. The electrostatic energy and forces are computed using the hybrid method with relative accuracy 10^{-3}; by comparison, an efficient BEM-based approach with tenfold larger computational expenditures leads to errors of 5% in the internal energy. To avoid divergences due to the overlap of dielectric interfaces, the dielectric surface of each colloid is placed at $r = \Delta/2$. Temperature is controlled via a Langevin thermostat and the characteristic coupling strength $\lambda = U_{\mathrm{Coul}}/(k_{\mathrm{B}}T)$ is set to be 100, where $U_{\mathrm{Coul}} = q_{\mathrm{L}}q_{\mathrm{S}}/[4\pi\epsilon_0\epsilon_{\mathrm{m}}(r_{\mathrm{L}} + r_{\mathrm{S}})]$ is the magnitude of the direct Coulombic interaction of a large and a small colloid at contact. All particles have mass m, yielding a time scale $t_0 = \sigma\sqrt{m/k_{\mathrm{B}}T}$; the timestep used is $0.005t_0$. A typical simulation run consists of 10^6 steps for aggregation and equilibration, followed by 20 annealing cycles to prevent the system getting kinetically trapped. Each cycle contains 2.5×10^4 steps at temperature T and another 2.5×10^4 steps at a higher temperature $2.5T$. Finally, we run another 10^6 steps (at temperature T), sampling structural properties each 10^3 steps.

8.4. Results and Discussion

We first explore how size ratio α and permittivity combinations $(\epsilon_{\mathrm{L}}, \epsilon_{\mathrm{S}})$ affect the total electrostatic energy U_{elec} of two oppositely charged polarizable spheres at contact. For equisized spheres, polarizability modifies the contact energy by only a few percent (Fig. 8.1a).
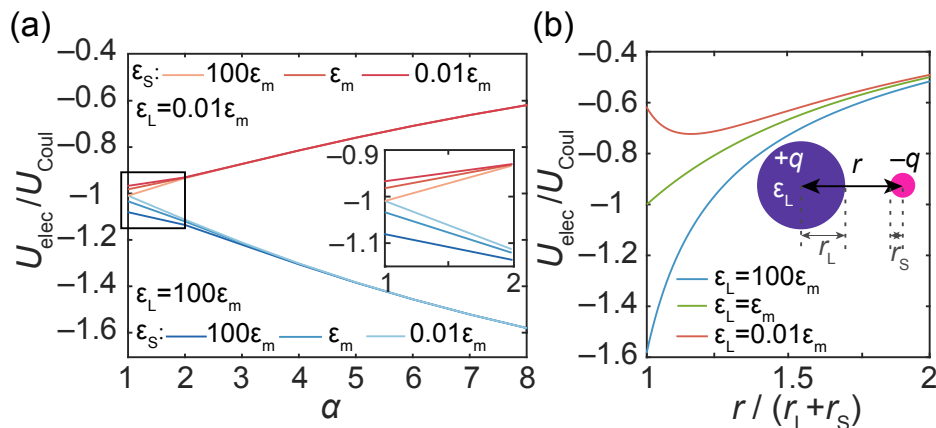
Figure 8.1. Pairwise electrostatic energy U_{elec} between two oppositely charged $(q_{\text{L}} = q_{\text{S}} = q)$ *polarizable* spheres. (a) U_{elec} (normalized by the magnitude of the direct Coulombic contact energy $U_{\text{Coul}} = q^2/[4\pi\epsilon_0\epsilon_{\text{m}}(r_{\text{L}} + r_{\text{S}})]$) between two touching spheres with fixed center-to-center distance $r = r_{\text{L}} + r_{\text{S}}$, as a function of size ratio α. Different combinations of the particle permittivities (ϵ_{L}, ϵ_{S}) are shown. Curves for the same ϵ_{L} but different ϵ_{S} coincide everywhere except for small α (inset). In the absence of dielectric mismatch (i.e., $\epsilon_{\text{L}} = \epsilon_{\text{S}} = \epsilon_{\text{m}}$), $U_{\text{elec}}/U_{\text{Coul}}$ would have been -1 for all α. (b) U_{elec} (normalized by U_{Coul}) between two spheres with size ratio $\alpha = 8$ and $\epsilon_{\text{S}} = \epsilon_{\text{m}}$ as a function of their center-to-center distance r, for different values of ϵ_{L}.

However, as the size asymmetry increases, this effect (shown as deviation from -1 in the figure) is greatly amplified. For $\epsilon_{\text{L}} > \epsilon_{\text{m}}$, such as metallic colloids, the (attractive) contact energy increases with size asymmetry, and is already enhanced by 60% for $\alpha = 8$. Conversely, for low-permittivity colloids with $\epsilon_{\text{L}} < \epsilon_{\text{m}}$ polarization effects diminish the Coulombic attraction by 40% at the same size ratio. The permittivity of the smaller species plays only a secondary role (Fig. 8.1a, inset) and is negligible for $\alpha \gtrsim 2$, so that in subsequent large-scale simulations of colloidal aggregation we ignore this parameter and assume no dielectric mismatch between small spheres and the solvent ($\epsilon_{\text{S}} = \epsilon_{\text{m}}$).

Next, we review how dielectric effects modulate the pairwise electrostatic energy as a function of separation between the two spheres. For a size-asymmetric pair, the charge on the smaller particle induces an attractive surface polarization if $\epsilon_{\text{L}} > \epsilon_{\text{m}}$, resulting in a strong

amplification of the attractive potential (Fig. 8.1b, blue curve; to be compared to the pure Coulombic attraction, green curve). On the other hand, if $\epsilon_L < \epsilon_m$, a repulsive polarization is induced. As an interesting consequence, the pairwise interaction now has a minimum away from contact (Fig. 8.1b, red curve).

The two control parameters determining the shape of the potential then are size ratio α and the dielectric mismatch between large spheres and the medium, $\gamma = (\epsilon_m - \epsilon_L)/(\epsilon_m + \epsilon_L)$. The two limiting cases $\gamma = \{-1, 1\}$ correspond to conducting colloids (with attractive dielectric effects) and low-permittivity colloids (with repulsive dielectric effects), respectively. Computationally, we approximate these two extremes by $\epsilon_L = 100\epsilon_m$ and $\epsilon_L = 0.01\epsilon_m$, respectively.

Whereas pairwise configurations can be understood from straightforward considerations, the situation changes once many-body effects come into play. Indeed, since the pairwise energies demonstrate enhanced binding of large and small spheres for $\gamma < 0$, yet weakened and looser binding for $\gamma > 0$, it appears intuitive that large-scale assembly yields compact structures for the former condition and more open aggregates for the latter. However, this expectation is refuted by the phase diagram of a binary mixture with 1:1 number ratio obtained from large-scale simulations (Fig. 8.2a). At small α, where dielectric effects are minimal, we consistently observe FCC crystal structures, independent of γ. The situation changes at large size ratio, where the assembled structures strongly depend on γ (cf. configurations in Fig. 8.2a). For $\gamma \gg 0$ we observe FCC crystal structures, followed by the Wurtzite crystal (at $\alpha = 3.5, 5.0$) and hexagonal monolayer shell (at $\alpha = 7.0, 8.0$, cf. green box in Fig. 8.2a) for $\gamma \approx 0$. Lastly, for $\gamma < 0$ we find anisotropic open aggregates, including two-dimensional sheets and one-dimensional single and dual chains. The Wurtzite structure is consistent with prior predictions in the absence of dielectric effects[320], and the chain-like
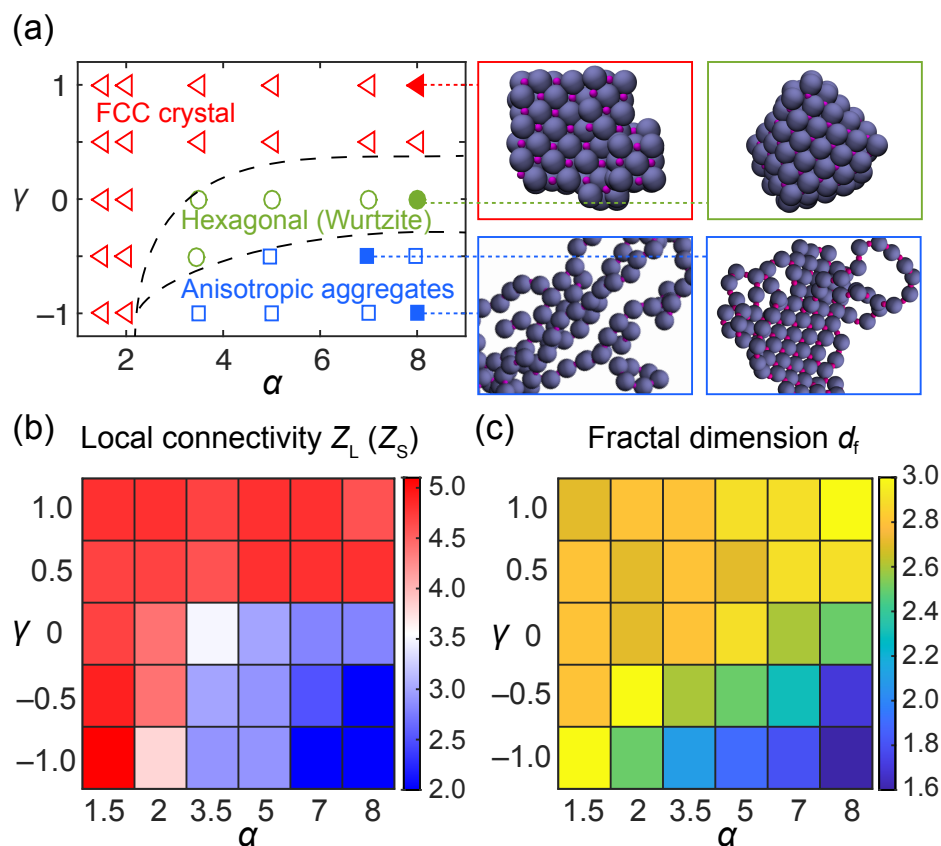
Figure 8.2. Large-scale aggregation of a 1:1 mixture of polarizable particles, parametrized by size ratio α and dielectric mismatch γ: (a) phase diagram; (b) local connectivity Z_L (or Z_S); (c) fractal dimension d_f. Representative structures are shown on the right of panel (a), with parameters (α, γ) marked by solid symbols in the phase diagram.

conformations have been observed experimentally for nanoparticles in organic solvent[322] and computationally for size-asymmetric mixtures of metallic colloids[164]. However, the counter-intuitive trend of *decreasing* compactness with *increasingly* attractive polarization effects has neither been explored systematically nor been explained even qualitatively.

To make this classification more precise, we compute the local connectivity as well as the (correlated) fractal dimension as a function of the control parameters α and γ (Fig. 8.2b,c). The local connectivity is quantified via the coordination number Z_L (Z_S), i.e., the number of
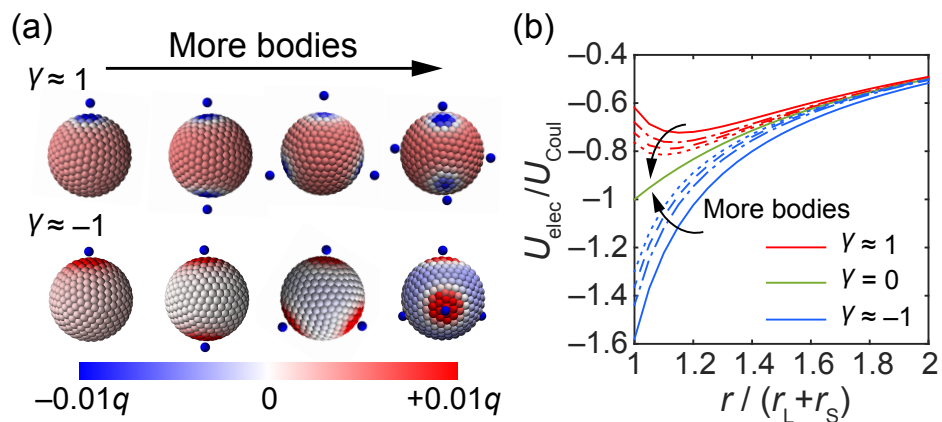
Figure 8.3. Influence of dielectric many-body effects on coordination number, illustrated for size ratio $\alpha = 8$. (a) Surface polarization charge (shading on large sphere, which carries a total charge $+q$) for increasing number of small satellite particles (each carrying total charge $-q$). Top row: $\gamma \approx 1$; bottom row: $\gamma \approx -1$. The small particles are placed at symmetric positions with respect to the center of the large particle. (b) Pair energy (normalized as in Fig. 8.1) $U_{\text{elec}}/U_{\text{Coul}}$ between the large sphere and a single small particle as a function of their center-to-center distance with increasing number of satellite particles (progressing from solid line to dotted line, as indicated by arrows) for $\gamma \approx 1$ (red), $\gamma = 0$ (green), and $\gamma \approx -1$ (blue).

large–small contacts around a large (small) sphere[323], where a cutoff distance corresponding to the first minimum in the large–small radial distribution function is imposed to identify contacts. The fractal dimension d_{f} is estimated from the scaling law $N_{\text{c}} \sim R_{\text{g}}^{d_{\text{f}}}$, with N_{c} the number of large particles in the cluster and R_{g} the associated radius of gyration. We use five different system sizes with $N_{\text{L}} = 25$, 50, 75, 100, and 200 large spheres (constant volume fraction) and obtain clear power-law relationships. Owing to the limited range in R_{g}, the uncertainty in d_{f} is around 0.4, yet this is still sufficiently accurate to exhibit clear trends (Fig. 8.2c).

The key to understanding these observations lies in the many-body nature of the dielectric effects, which impart anisotropy to the inter-particle interactions. Moreover, the consequences of this anisotropy are distinctly different for high-permittivity ($\gamma < 0$) and low-permittivity ($\gamma > 0$) particles. In the latter case, the polarization charge distribution

induced by a (negative) small particle bound to a larger sphere not only weakens its own attraction, but simultaneously renders the remaining surface of the large particle more positive and thereby makes it more attractive to other small particles (Fig. 8.3a, top panel). Conversely, for $\gamma \approx -1$, the binding of a small particle is enhanced by the (positive) polarization charge around the contact point, but away from this location the surface of the large sphere becomes less positively (or even negatively) charged, making it less attractive or even repulsive to additional small spheres (Fig. 8.3a, bottom panel). This is quantified systematically in Fig. 8.3b. In the absence of dielectric mismatch, the pairwise interaction between a large and a small particle is independent of the local coordination number (green curve, $\gamma = 0$). However, for positive (negative) γ the individual binding strength becomes stronger (weaker) with increasing number of large–small contacts. As a result, dielectric effects that are traditionally classified as "repulsive" in fact promote higher coordination numbers, and vice versa. Full predictive capabilities for α- and γ-dependent self-assembled structures rely on the subtle competition between these electrostatic interactions, steric constraints, and— at higher temperatures–entropic contributions to the free energy. All these are captured in the MD simulations and give rise to compact structures with high Z_L and d_f for spheres with $\epsilon_L < \epsilon_m$ and elongated and anisotropic structures with small Z_L and d_f for $\epsilon_L > \epsilon_m$. Interestingly, the directionality of the inter-particle interactions in the latter case is reminiscent of the many-body nature of self-assembly of polymer-grafted nanoparticles/colloids[316,324].

The control afforded by polarization effects extends to colloidal clusters as well. For asymmetric number ratio, e.g., $N_L/N_S = 3$ (and thus, by virtue of charge neutrality, $q_L/q_S = 1/3$), under dilute conditions at $\gamma = 0$ the particles assemble into flower-like clusters, with a small sphere at the center and three large spheres (size ratio $\alpha = 5$) as "petals." However, these arrangements are generally unstable, because the positively charged large spheres at the
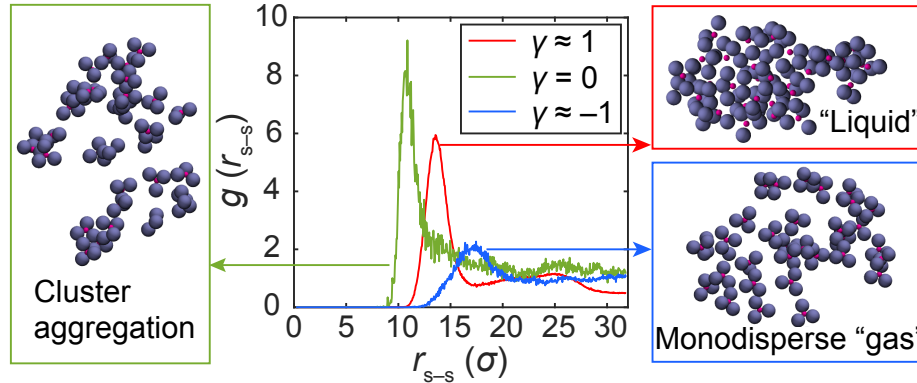
Figure 8.4. Stabilization of colloidal clusters comprised of a central small particle and three larger "petals" (size ratio $\alpha = 5$). In the absence of dielectric effects ($\gamma = 0$), the clusters aggregate (snapshot on the left, small–small radial distribution functions $g(r_{S-S})$ in green). For low-permittivity spheres ($\gamma \approx 1$), the aggregation is so strong that the clusters disassemble and a liquid phase results (snapshot top right, red curve). For negative mismatch (metallic large particles, $\gamma \approx -1$), a "gas" of isolated clusters emerges (snapshot bottom right, blue curve), reflecting the tendency of high permittivity to lower the coordination number. To eliminate artifacts due to the finite boundary condition in the simulations, we computed $g(r_{S-S})$ by only counting the number of neighbors of particles that are at least a distance $r_c = 32\sigma$ from the boundary of the simulation cell.

outside of each cluster remain attractive to small particles inside other clusters, resulting in cluster–cluster aggregation (Fig. 8.4, snapshot in green box and small–small pair correlation function in green). Remarkably, stabilization of the individual clusters can be achieved by introducing negative dielectric mismatch ($\gamma \approx -1$), which reduces the coordination of the large spheres by rendering their exposed parts less attractive. As a result, we observe a gas phase of monodisperse flower-like clusters (Fig. 8.4, snapshot in blue box), as also confirmed by the right-ward shift of the first peak of the pair correlation function (blue line). Conversely, a positive permittivity mismatch ($\gamma \approx 1$) causes disappearance of the clusters and the formation of a liquid mixture of large and small spheres (Fig. 8.4, snapshot in red box). These observations are further supported by direct sampling of the number of large–small contacts around a small sphere, for which we find $Z_S = 3.5 \pm 0.1$ at $\gamma = 0$ (cluster

aggregation), $Z_{\rm S} = 5.6 \pm 0.1$ at $\gamma \approx 1$ (liquid state), and lastly $Z_{\rm S} = 3.0$ (no fluctuation), i.e., perfect flower structures at $\gamma \approx -1$. These observations also hold, mutatis mutandis, for other number ratios, with the caveat that as the number of "petals" increases, the clusters become more stable already at $\gamma = 0$. Controlled aggregation of colloids into small clusters has been the subject of considerable attention[31,315,325]. The mechanism uncovered here provides an additional protocol to generate stable, monodisperse suspensions of multi-component clusters.

8.5. Conclusion

In summary, by adopting a newly developed dielectric solver that combines high accuracy and efficiency, we have been able to systematically explore the role of dielectric effects in the self-assembly of binary colloidal mixtures. We have demonstrated that the many-body nature of polarization imparts directionality to the interaction between isotropic and uniformly charged spherical particles, making the phase diagram dependent on dielectric mismatch. As an illustrative example, we found that the FCC phase in size-asymmetric mixtures is stabilized by polarizability. The tunability of the assembly process extends beyond controlling fractal dimension of large-scale aggregates to the stabilization of well-defined small clusters, providing an avenue for producing building blocks for novel structures and materials[313]. As an outlook, we note that the integration of the hybrid dielectric solver with molecular dynamics simulations also opens the possibility to explore the kinetics of dielectric aggregation processes.

CHAPTER 9

Conclusion

Self-assembly of nano and micro-scale colloidal particles has been a powerful approach to synthesize novel structures with emergent optical, electrical, and mechanical properties in various applications. The assembled structure usually results from an intricate competition between different mechanisms, including various physical interactions, thermal fluctuations, and external fields. Therefore, understanding, predicting, and controlling the self-assembly process is of both fundamental interests and technical relevance. By performing particle-based simulations and collaborating with experimental groups, I focus on understanding how shape anisotropy (Part 1) and electrostatic polarization effects (Part 2) play a role in the self-assembly process. Here I present a summary of the main findings and future outlook for each chapter.

Part 1 (Chapter 2 to Chapter 3) is concerned with crystallization process of anisotropic nanoparticles, driven by various nanoscale forces (e.g., van der Waals interaction, electro-statics, and shape entropy). The content of this part is closely interwoven with experimental imaging which is made possible by low-dose liquid-phase transmission electron microscopy (TEM). Chapter 2 focuses on the system of triangular nanoprisms which crystallize into a novel hierarchical hexagonal lattice. To properly capture the nanoscale interactions, which later prove essential to reproduce the experimental observation, I derive analytical functional forms of pairwise potential from the detailed coarse-grained model of nanoprism which allow efficient large-scale simulations. Monte Carlo simulations not only reveal the microscopic

details of the assembled superlattice which is composed of columns of randomly stacked prisms, but also demonstrate that positional ordering of the lattice indeed emerges from orientational disorder. By further exploring the phase space, I propose the design rule that different phases can be realized through varying the morphology of columns which is controlled by the ionic strength and the cell height. These findings are generalizable to other systems of plate-like nanoparticles, which could provide guidance to future experimental design of functional nano-materials. This experimental–computational study, combining direct imaging of particle motion at single-particle level and detailed modeling of nanoscale interactions, offers a general workflow which can be translated to future research on other artificial and biological nanoscopic entities. Particularly, great efforts are spent on developing the analytical model of nanoprism which captures the practical nanoscale interactions in great details but at the same time stays efficient enough to allow large-scale simulations. The modeling approach here can also be applied to other anisotropic nanoparticles.

While Chapter 2 emphasizes on understanding and controlling the assembled structures, Chapter 3 focuses on the crystal growth kinetics at the nanoscale. By examining the crystallization process of a diversity of nanoparticles under liquid-phase TEM, our collaborators discover a prevalent layer-by-layer growth mode, in contrast to the roughened growth of micron-sized colloids reported previously. Coarse-grained modeling and molecular dynamic simulations are applied to map the energy landscape involving key diffusive barriers of the nanoparticle system, which explains the thermodynamic and kinetic driving forces of the observed growth mode. By further coupling analysis of experimental imaging and kinetic Monte Carlo simulations, we show that building block size governs the crystal growth process by simultaneously controlling the ratio of surface diffusion rate to incoming flux and the interaction range. Our combined experimental–computational work fills the knowledge gap

of the crystal growth law at this intermediate nanoscale. Such understanding can greatly enrich the design rules and quantitative prediction for engineering ensemble order and surface morphology in nanoparticle superlattices or other forms of nanoscale assemblies.

Part 2 (Chapter 4 to Chapter 8) is devoted to exploring the electrostatic polarization effects in self-assembly of colloidal particles. A general literature review is presented in Chapter 4, which provides comparison between different methods for solving polarization in simulations and highlights key physical phenomena which are induced by the dielectric effects at the nano- and microscale.

I start with systems with dielectric interfaces of slab geometry, which can be treated by incorporating the Image Charge Method into the Ewald summation. In Chapter 5, I examine the confined dipolar hard-sphere fluids near a dielectric interface. Simulation results show that the presence of a conducting surface shifts the global isotropic-ferroelectric transition only slightly toward a higher density and coupling strength, but that dielectric effects have a significant influence on the orientational structure of the contact layer. Specifically, low-permittivity interface enhances the in-plane orientation of the dipolar spheres, whereas a conducting surface promotes out-of-plane dipolar orientations. The findings here not only clarify the effects of substrate permittivity on confined dipolar fluids, e.g., magnetic colloids or charged janus particles, which is instrumental for the fundamental understanding of a variety of experimental systems, but also have implications for the design of tunable dipolar materials by exploiting dielectric effects.

Inspired by the above findings, I take a closer look at a two-dimensional dipolar film supported by a dielectric substrate and investigate how dielectric effects can be utilized achieve modulated patterns (Chapter 6). Specifically, a rich phase diagram arises induced by polarization across the substrate, where striped and circular morphologies emerge with

geometric properties that can be controlled through variation of particle shape and permittivity mismatch. These effects are particularly enhanced by metameterial substrates. Besides elucidating the pattern-modulation mechanism, our findings may also provide guidance to future applications of such metamaterials.

To explore system with spherical dielectric interfaces, which is able to represent a wide range of biological and synthetic systems, more complicated approach needs to be applied to solve the polarization. Chapter 7 presents a detailed comparison between the recently proposed hybrid method, which combines the Method of Moments, the Image Charge Method, and the Fast Multipole Method, and the iterative Boundary Element Method. By exploring the effects of various parameters on efficiency, convergence, and accuracy, we demonstrate that for close-packed crystal structures of dielectric spheres, the hybrid method computes the electrostatic energy with a deviation of less than 0.01% at a rate that is more than two orders of magnitude faster than the Boundary Element Method can achieve for deviations of 3%.

By further applying this efficient hybrid method in simulations, I study the self-assembly of binary suspensions of oppositely charged polarizable colloids (Chapter 8). I show that a variety of anisotropic superstructures can be assembled, resulting from the many-body dielectric effects which impart effective directionality to interactions. Both local coordination number and fractal dimension can be well controlled by varying particle size ratio and relative permittivity. The findings here can provide a new mechanism for designing materials with controllable structural properties. As an outlook, we note that the integration of the hybrid dielectric solver with molecular dynamics simulations also opens the possibility to explore the kinetics of dielectric aggregation processes.

References

[1] G. M. Whitesides and B. Grzybowski, "Self-assembly at all scales," Science **295**, 2418–21 (2002).

[2] X. Ye, J. Chen, M. Eric Irrgang, M. Engel, A. Dong, S. C. Glotzer and C. B. Murray, "Quasicrystalline nanocrystal superlattice with partial matching rules," Nature Mater. **16**, 214–219 (2017).

[3] Y. Xia, T. D. Nguyen, M. Yang, B. Lee, A. Santos, P. Podsiadlo, Z. Tang, S. C. Glotzer and N. a. Kotov, "Self-assembly of self-limiting monodisperse supraparticles from polydisperse nanoparticles," Nature Nanotech. **6**, 580–587 (2011).

[4] H. Lin, S. Lee, L. Sun, M. Spellings, M. Engel, S. C. Glotzer and C. A. Mirkin, "Clathrate colloidal crystals," Science **355**, 931–935 (2017).

[5] A. Yethiraj and A. van Blaaderen, "A colloidal model system with an interaction tunable from hard sphere to soft and dipolar," Nature **421**, 513–517 (2003).

[6] J. J. Crassous, A. M. Mihut, E. Wernersson, P. Pfleiderer, J. Vermant, P. Linse and P. Schurtenberger, "Field-induced assembly of colloidal ellipsoids into well-defined microtubules," Nature Comm. **5**, 5516 (2014).

[7] N. Osterman, D. Babič, I. Poberaj, J. Dobnikar and P. Ziherl, "Observation of condensed phases of quasiplanar core-softened colloids," Phys. Rev. Lett. **99**, 248301 (2007).

[8] A. F. Nieves, *Fluids, Colloids and Soft Materials: An Introduction to Soft Matter Physics* (John Wiley & Sons, Inc, Hoboken, NJ, USA, 2016).

[9] K. J. M. Bishop, C. E. Wilmer, S. Soh and B. A. Grzybowski, "Nanoscale forces and their uses in self-assembly," Small **5**, 1600–1630 (2009).

[10] G. van Anders, D. Klotsa, N. K. Ahmed, M. Engel and S. C. Glotzer, "Understanding shape entropy through local dense packing," Proc. Natl. Acad. Sci. U.S.A. **111**, E4812–E4821 (2014).

[11] M. Grzelczak, J. Vermant, E. M. Furst and L. M. Liz-Marzán, "Directed self-assembly of nanoparticles," ACS Nano **4**, 3591–3605 (2010).

[12] C. A. Silvera Batista, R. G. Larson and N. A. Kotov, "Nonadditivity of nanoparticle interactions," Science **350**, 1242477–1242477 (2015).

[13] F. M. Ross, "Opportunities and challenges in liquid cell electron microscopy," Science **350**, aaa9886 (2015).

[14] J. Kim, M. R. Jones, Z. Ou and Q. Chen, "In situ electron microscopy imaging and quantitative structural modulation of nanoparticle superlattices," ACS Nano **10**, 9801–9808 (2016).

[15] B. Luo, J. W. Smith, Z. Ou and Q. Chen, "Quantifying the self-assembly behavior of anisotropic nanoparticles using liquid-phase transmission electron microscopy," Acc. Chem. Res. **50**, 1125–1133 (2017).

[16] M. A. Boles, M. Engel and D. V. Talapin, "Self-assembly of colloidal nanocrystals: From intricate structures to functional materials," Chem. Rev. **116**, 11220–11289 (2016).

[17] R. J. Macfarlane, B. Lee, H. D. Hill, A. J. Senesi, S. Seifert and C. A. Mirkin, "Assembly and organization processes in DNA-directed colloidal crystallization," Proc. Natl.

Acad. Sci. U.S.A. **106**, 10493–10498 (2009).

[18] K. L. Young, M. R. Jones, J. Zhang, R. J. Macfarlane, R. Esquivel-Sirvent, R. J. Nap, J. Wu, G. C. Schatz, B. Lee and C. A. Mirkin, "Assembly of reconfigurable one-dimensional colloidal superlattices due to a synergy of fundamental nanoscale forces," Proc. Natl. Acad. Sci. U.S.A. **109**, 2240–2245 (2012).

[19] A. Haji-Akbari, M. Engel, A. S. Keys, X. Zheng, R. G. Petschek, P. Palffy-Muhoray and S. C. Glotzer, "Disordered, quasicrystalline and crystalline phases of densely packed tetrahedra," Nature **462**, 773–777 (2009).

[20] J. Henzie, M. Grünwald, A. Widmer-Cooper, P. L. Geissler and P. Yang, "Self-assembly of uniform polyhedral silver nanocrystals into densest packings and exotic superlattices," Nature Mater. **11**, 131–137 (2011).

[21] P. F. Damasceno, M. Engel and S. C. Glotzer, "Predictive self-assembly of polyhedra into complex structures," Science **337**, 453–457 (2012).

[22] R. H. French, V. A. Parsegian, R. Podgornik, R. F. Rajter, A. Jagota, J. Luo, D. Asthagiri, M. K. Chaudhury, Y.-m. Chiang, S. Granick, S. Kalinin, M. Kardar, R. Kjellander, D. C. Langreth, J. Lewis, S. Lustig, D. Wesolowski, J. S. Wettlaufer, W.-Y. Ching, M. Finnis, F. Houlihan, O. A. von Lilienfeld, C. J. van Oss and T. Zemb, "Long range interactions in nanoscale science," Rev. Mod. Phys. **82**, 1887–1944 (2010).

[23] D. G. A. L. Aarts, M. Schmidt and H. N. W. Lekkerkerker, "Direct visual observation of thermal capillary waves," Science **304**, 847–850 (2004).

[24] R. Xie and X.-Y. Liu, "Controllable epitaxial crystallization and reversible oriented patterning of two-dimensional colloidal crystals," J. Am. Chem. Soc. **131**, 4976–4982 (2009).

[25] L. Rossi, S. Sacanna, W. T. M. Irvine, P. M. Chaikin, D. J. Pine and A. P. Philipse, "Cubic crystals from cubic colloids," Soft Matter **7**, 4139-4142 (2011).

[26] E. Auyeung, T. I. N. G. Li, A. J. Senesi, A. L. Schmucker, B. C. Pals, M. O. de la Cruz and C. A. Mirkin, "DNA-mediated nanoparticle crystallization into wulff polyhedra," Nature **505**, 73–77 (2014).

[27] S. E. Seo, M. Girard, M. Olvera de la Cruz and C. A. Mirkin, "Non-equilibrium anisotropic colloidal single crystal growth with DNA," Nature Comm. **9**, 4558 (2018).

[28] D. A. Walker, B. Kowalczyk, M. Olvera de la Cruz and B. A. Grzybowski, "Electrostatics at the nanoscale," Nanoscale **3**, 1316–1344 (2011).

[29] P. Linse and V. Lobaskin, "Electrostatic attraction and phase separation in solutions of like-charged colloidal particles," Phys. Rev. Lett. **83**, 4208–4211 (1999).

[30] M. E. Leunissen, C. G. Christova, A.-P. Hynninen, C. P. Royall, A. I. Campbell, A. Imhof, M. Dijkstra, R. van Roij and A. van Blaaderen, "Ionic colloidal crystals of oppositely charged particles," Nature **437**, 235–240 (2005).

[31] A. F. Demirörs, J. C. P. Stiefelhagen, T. Vissers, F. Smallenburg, M. Dijkstra, A. Imhof and A. van Blaaderen, "Long-ranged oppositely charged interactions for designing new types of colloidal clusters," Phys. Rev. X **5**, 021012 (2015).

[32] E. V. Shevchenko, D. V. Talapin, N. A. Kotov, S. O'Brien and C. B. Murray, "Structural diversity in binary nanoparticle superlattices," Nature **439**, 55–59 (2006).

[33] A. M. Kalsin, M. Fialkowski, M. Paszewski, S. K. Smoukov, K. J. M. Bishop and B. A. Grzybowski, "Electrostatic self-assembly of binary nanoparticle crystals with a diamond-like lattice," Science **312**, 420–424 (2006).

[34] D. A. Walker, K. P. Browne, B. Kowalczyk and B. A. Grzybowski, "Self-assembly of nanotriangle superlattices facilitated by repulsive electrostatic interactions," Angew.

Chem. Int. Ed. **49**, 6760–6763 (2010).

[35] A. van der Vaart, B. D. Bursulaya, C. L. Brooks, III and K. M. Merz, "Are many-body effects important in protein folding?," J. Phys. Chem. B **104**, 9554–9563 (2000).

[36] M. W. Knight, Y. Wu, J. B. Lassiter, P. Nordlander and N. J. Halas, "Substrates matter: Influence of an adjacent dielectric on an individual plasmonic nanoparticle," Nano Letters **9**, 2188–2192 (2009).

[37] H. S. Antila and E. Luijten, "Dielectric modulation of ion transport near interfaces," Phys. Rev. Lett. **120**, 135501 (2018).

[38] W. Thomson, "Extrait d'une Lettre de M. William Thomson à M. Liouville," Journal de mathématiques pures et appliquées **10**, 364–367 (1845).

[39] W. Thomson, "Geometrical investigations with reference to the distribution of electricity on spherical conductors," Camb. Dublin Math. J. **3**, 141–148 (1848).

[40] C. Neumann, *Hydrodynamische Untersuchungen, nebst einem Anhange über die Probleme der Elektrostatik und der magnetischen Induction* (B. G. Teubner, Leipzig, 1883).

[41] D. R. McKenzie, R. C. McPhedran and G. H. Derrick, "The conductivity of lattices of spheres. II. The body centred and face centred cubic lattices," Proc. R. Soc. London, Ser. A **362**, 211–232 (1978).

[42] R. C. McPhedran and D. R. McKenzie, "The conductivity of lattices of spheres. I. The simple cubic lattice," Proc. R. Soc. London, Ser. A **359**, 45–63 (1978).

[43] A. S. Sangani and A. Acrivos, "The effective conductivity of a periodic array of spheres," Proc. R. Soc. London, Ser. A **386**, 263–275 (1983).

[44] K. Hinsen and B. U. Felderhof, "Dielectric constant of a suspension of uniform spheres," Phys. Rev. B **46**, 12955–12963 (1992).

[45] L. Greengard and M. Moura, "On the numerical evaluation of electrostatic fields in composite materials," Acta Numer. **3**, 379–410 (1994).

[46] D. G. Levitt, "Electrostatic calculations for an ion channel. I. Energy and potential profiles and interactions between ions," Biophys. J. **22**, 209–219 (1978).

[47] R. J. Zauhar and R. S. Morgan, "A new method for computing the macromolecular electric potential," J. Mol. Biol. **186**, 815–820 (1985).

[48] D. Boda, D. Gillespie, W. Nonner, D. Henderson and B. Eisenberg, "Computing induced charges in inhomogeneous dielectric media: Application in a Monte Carlo simulation of complex ionic systems," Phys. Rev. E **69**, 046702 (2004).

[49] S. Tyagi, M. Süzen, M. Sega, M. Barbosa, S. S. Kantorovich and C. Holm, "An iterative, fast, linear-scaling method for computing induced charges on arbitrary dielectric boundaries," J. Chem. Phys. **132**, 154112 (2010).

[50] K. Barros, D. Sinkovits and E. Luijten, "Efficient and accurate simulation of dynamic dielectric objects," J. Chem. Phys. **140**, 064903 (2014).

[51] K. F. Freed, "Perturbative many-body expansion for electrostatic energy and field for system of polarizable charged spherical ions in a dielectric medium," J. Chem. Phys. **141**, 034115 (2014).

[52] J. Qin, J. J. de Pablo and K. F. Freed, "Image method for induced surface charge from many-body system of dielectric spheres," J. Chem. Phys. **145**, 124903 (2016).

[53] Z. Gan, S. Jiang, E. Luijten and Z. Xu, "A hybrid method for systems of closely spaced dielectric spheres and ions," SIAM J. Sci. Comp. **38**, B375–B395 (2016).

[54] J. J. De Yoreo, P. U. P. A. Gilbert, N. A. J. M. Sommerdijk, R. L. Penn, S. Whitelam, D. Joester, H. Zhang, J. D. Rimer, A. Navrotsky, J. F. Banfield, A. F. Wallace, F. M. Michel, F. C. Meldrum, H. Colfen and P. M. Dove, "Crystallization by particle

attachment in synthetic, biogenic, and geologic environments," Science **349**, aaa6760–aaa6760 (2015).

[55] B. Li, D. Zhou and Y. Han, "Assembly and phase transitions of colloidal crystals," Nat. Rev. Mater. **1**, 15011 (2016).

[56] N. D. Loh, S. Sen, M. Bosman, S. F. Tan, J. Zhong, C. A. Nijhuis, P. Král, P. Matsudaira and U. Mirsaidov, "Multistep nucleation of nanocrystals in aqueous solution," Nature Chem. **9**, 77–82 (2017).

[57] K. Henzler, E. O. Fetisov, M. Galib, M. D. Baer, B. A. Legg, C. Borca, J. M. Xto, S. Pin, J. L. Fulton, G. K. Schenter, N. Govind, J. I. Siepmann, C. J. Mundy, T. Huthwelker and J. J. De Yoreo, "Supersaturated calcium carbonate solutions are classical," Sci. Adv. **4**, eaao6283 (2018).

[58] J. Chen, B. Sarma, J. M. B. Evans and A. S. Myerson, "Pharmaceutical crystallization," Cryst. Growth Des. **11**, 887–895 (2011).

[59] S. John, "Strong localization of photons in certain disordered dielectric superlattices," Phys. Rev. Lett. **58**, 2486–2489 (1987).

[60] J.-H. Choi, H. Wang, S. J. Oh, T. Paik, P. Sung, J. Sung, X. Ye, T. Zhao, B. T. Diroll, C. B. Murray and C. R. Kagan, "Exploiting the colloidal nanocrystal library to construct electronic devices," Science **352**, 205–208 (2016).

[61] W. L. Noorduin, A. Grinthal, L. Mahadevan and J. Aizenberg, "Rationally designed complex, hierarchical microarchitectures," Science **340**, 832–837 (2013).

[62] P. R. Ten Wolde and D. Frenkel, "Enhancement of protein crystal nucleation by critical density fluctuations," Science **277**, 1975–1978 (1997).

[63] É. Ducrot, M. He, G.-r. Yi and D. J. Pine, "Colloidal alloys with preassembled clusters and spheres," Nature Mater. **16**, 652–657 (2017).

[64] T. H. Zhang and X. Y. Liu, "How does a transient amorphous precursor template crystallization," J. Am. Chem. Soc. **129**, 13520–13526 (2007).

[65] P. Tan, N. Xu and L. Xu, "Visualizing kinetic pathways homogeneous nucleation in colloidal crystallization," Nature Phys. **10**, 1–18 (2013).

[66] K. G. Libbrecht, "The physics of snow crystals," Rep. Prog. Phys. **68**, 855–895 (2005).

[67] J. J. De Yoreo and S. N. A. J. M., "Investigating materials formation with liquid-phase and cryogenic tem," Nat. Rev. Mater. **1**, 16035 (2016).

[68] J. R. Savage, D. W. Blair, a. J. Levine, R. a. Guyer and a. D. Dinsmore, "Imaging the sublimation dynamics of colloidal crystallites," Science **314**, 795–798 (2006).

[69] J. Park, H. Elmlund, P. Ercius, J. M. Yuk, D. T. Limmer, Q. Chen, K. Kim, S. H. Han, D. A. Weitz, A. Zettl and A. P. Alivisatos, "3d structure of individual nanocrystals in solution by electron microscopy," Science **349**, 290–295 (2015).

[70] H.-G. Liao, L. Cui, S. Whitelam and H. Zheng, "Real-time imaging of pt3fe nanorod growth in solution," Science **336**, 1011–1014 (2012).

[71] E. Sutter, P. Sutter, A. V. Tkachenko, R. Krahne, J. de Graaf, M. Arciniegas and L. Manna, "In situ microscopy of the self-assembly of branched nanocrystals in solution," Nature Comm. **7**, 11213 (2016).

[72] N. M. Schneider, M. M. Norton, B. J. Mendel, J. M. Grogan, M. Frances and H. H. Bau, "Electron - water interactions and implications for liquid cell electron microscopy supporting information," J. Phys. Chem. C **118**, 22373–22382 (2014).

[73] J. Kim, Z. Ou, M. R. Jones, X. Song and Q. Chen, "Imaging the polymerization of multivalent nanoparticles in solution," Nature Comm. **8**, 761 (2017).

[74] U. Agarwal and F. A. Escobedo, "Mesophase behaviour of polyhedral particles," Nature Mater. **10**, 230–235 (2011).

[75] M. R. Jones, R. J. Macfarlane, B. Lee, J. Zhang, K. L. Young, A. J. Senesi and C. A. Mirkin, "DNA-nanoparticle superlattices formed from anisotropic building blocks," Nature Mater. **9**, 913–917 (2010).

[76] D. P. Fraser, M. J. Zuckermann and O. G. Mouritsen, "Simulation technique for hard-disk models in two dimensions," Phys. Rev. A **42**, 3186–3195 (1990).

[77] W. Liu, M. Tagawa, H. L. Xin, T. Wang, H. Emamy, H. Li, K. G. Yager, F. W. Starr, A. V. Tkachenko and O. Gang, "Diamond family of nanoparticle superlattices," Science **351**, 582–586 (2016).

[78] A. Sauter, F. Roosen-Runge, F. Zhang, G. Lotze, A. Feoktystov, R. M. J. Jacobs and F. Schreiber, "On the question of two-step nucleation in protein crystallization," Faraday Disc. **179**, 41-58 (2015).

[79] J. F. Lutsko and G. Nicolis, "Theoretical evidence for a dense fluid precursor to crystallization," Phys. Rev. Lett. **96**, 046102 (2006).

[80] S. Auer and D. Frenkel, "Prediction of absolute crystal-nucleation rate in hard-sphere colloids," Nature **409**, 1020–1023 (2001).

[81] A. Donev, J. Burton, F. H. Stillinger and S. Torquato, "Tetratic order in the phase behavior of a hard-rectangle system," Phys. Rev. B **73**, 054109 (2006).

[82] J. Timmermans, "Plastic crystals: A historical review," J. Phys. Chem. Solids **18**, 1–8 (1961).

[83] B. Liu, T. H. Besseling, M. Hermes, A. F. Demirörs, A. Imhof and A. van Blaaderen, "Switching plastic crystals of colloidal rods with electric fields," Nature Comm. **5**, 3092 (2014).

[84] M. Gruebele, K. Dave and S. Sukenik, "Globular protein folding in vitro and in vivo," Annu. Rev. Biophys. **45**, 233-251 (2016).

[85] V. A. Parsegian, *Van der Waals Forces: a Handbook for Biologists, Chemists, Engineers, and Physicists* (Cambridge Univ Press, Cambridge, U.K., 2005).

[86] A. A. Lee, C. S. Perez-Martinez, A. M. Smith and S. Perkin, "Scaling analysis of the screening length in concentrated electrolytes," Phys. Rev. Lett. **119**, 026002 (2017).

[87] Y. Li, M. Girard, M. Shen, J. A. Millan and M. Olvera de la Cruz, "Strong attractions and repulsions mediated by monovalent salts," Proc. Natl. Acad. Sci. U.S.A. **114**, 11838–11843 (2017).

[88] S. W. Chee, Z. Baraissov, N. D. Loh, P. T. Matsudaira and U. Mirsaidov, "Desorption-mediated motion of nanoparticles at the liquid–solid interface," J. Phys. Chem. C **120**, 20462–20470 (2016).

[89] E. C. Mbamala and H. H. von Grünberg, "Charged colloids and proteins at an air-water interface: The effect of dielectric substrates on interaction and phase behavior," Phys. Rev. E **67**, 031608 (2003).

[90] T. Möller and B. Trumbore, "Fast, minimum storage ray-triangle intersection," J. Graphics Tools **2**, 21–28 (1997).

[91] R. Eppenga and D. Frenkel, "Monte carlo study of the isotropic and nematic phases of infinitely thin hard platelets," Mol. Phys. **52**, 1303-1334 (1984).

[92] V. V. Voronkov, *Growth of Crystals: Volume 10* (Springer US, Boston, 1976).

[93] Z. Zhang and M. G. Lagally, "Atomistic processes in the early stages of thin-film growth," Science **276**, 377–383 (1997).

[94] R. Ganapathy, M. R. Buckley, S. J. Gerbode and I. Cohen, "Direct measurements of island growth and step-edge barriers in colloidal epitaxy," Science **327**, 445–448 (2010).

[95] T. L. Einstein and T. J. Stasevich, "Epitaxial growth writ large," Science **327**, 423–424 (2010).

[96] G. Ju, D. Xu, M. J. Highland, C. Thompson, H. Zhou, J. A. Eastman, P. H. Fuoss, P. Zapol, H. Kim and G. B. Stephenson, "Coherent x-ray spectroscopy reveals the persistence of island arrangements during layer-by-layer growth," Nature Phys. **15**, 589–594 (2019).

[97] J. V. Barth, G. Costantini and K. Kern, "Engineering atomic and molecular nanostructures at surfaces," Nature **437**, 671–679 (2005).

[98] Y. Liu, X. Wang and C. B. Ching, "Toward further understanding of lysozyme crystallization: Phase diagram, proteinprotein interaction, nucleation kinetics, and growth kinetics," Cryst. Growth Des. **10**, 548–558 (2010).

[99] N. Kleppmann, F. Schreiber and S. H. L. Klapp, "Limits of size scalability of diffusion and growth: Atoms versus molecules versus colloids," Phys. Rev. E **95**, 020801 (2017).

[100] H. Brune, "Microscopic view of epitaxial metal growth: nucleation and aggregation," Surface Science Reports **31**, 125 - 229 (1998).

[101] Z. Ou, Z. Wang, B. Luo, E. Luijten and Q. Chen, "Kinetic pathways of crystallization at the nanoscale," Nature Mater. **19**, 450–455 (2020).

[102] Y. Nagaoka, H. Zhu, D. Eggert and O. Chen, "Single-component quasicrystalline nanocrystal superlattices through flexible polygon tiling rule," Science **362**, 1396–1400 (2018).

[103] P. J. Santos, Z. Cao, J. Zhang, A. Alexander-Katz and R. J. Macfarlane, "Dictating nanoparticle assembly via systems-level control of molecular multivalency," J. Am. Chem. Soc. **141**, 14624–14632 (2019).

[104] J. Zhang, M. R. Langille, M. L. Personick, K. Zhang, S. Li and C. A. Mirkin, "Concave cubic gold nanocrystals with high-index facets," Journal of the American Chemical Society **132**, 14012–14014 (2010).

[105] G. Ehrlich and F. G. Hudda, "Atomic view of surface self-diffusion: Tungsten on tungsten," J. Chem. Phys. **44**, 1039-1049 (1966).

[106] R. L. Schwoebel and E. J. Shipsey, "Step motion on crystal surfaces," J. Appl. Phys. **37**, 3682-3686 (1966).

[107] H. Hwang, D. A. Weitz and F. Spaepen, "Direct observation of crystallization and melting with colloids," Proc. Natl. Acad. Sci. U.S.A. **116**, 1180–1184 (2019).

[108] Z. Zhang, J. Detch and H. Metiu, "Surface roughness in thin-film growth: The effect of mass transport between layers," Phys. Rev. B **48**, 4972–4975 (1993).

[109] F. Lu, K. G. Yager, Y. Zhang, H. Xin and O. Gang, "Superlattices assembled through shape-induced directional binding," Nature Comm. **6**, 6912 (2015).

[110] M. Rubinstein and R. H. Colby, *Polymer Physics* (Oxford University Press, Oxford, 2003).

[111] J. N. Israelachvili, *Intermolecular and Surface Forces*, 3rd ed. (Academic, San Diego, 2011).

[112] A. Slepoy, A. P. Thompson and S. J. Plimpton, "A constant-time kinetic monte carlo algorithm for simulation of large biochemical reaction networks," J. Chem. Phys. **128**, 205101 (2008).

[113] S. Clarke and D. D. Vvedensky, "Growth kinetics and step density in reflection high-energy electron diffraction during molecular-beam epitaxy," J. Appl. Phys. **63**, 2272-2283 (1988).

[114] B. Honig and A. Nicholls, "Classical electrostatics in biology and chemistry," Science **268**, 1144–1149 (1995).

[115] Y. Levin, "Strange electrostatics in physics, chemistry, and biology," Physica A **352**, 43–52 (2005).

[116] R. Messina, "Electrostatics in soft matter," J. Phys.: Condens. Matter **21**, 113102 (2009).

[117] A. M. Kalsin, M. Fialkowski, M. Paszewski, S. K. Smoukov, K. J. M. Bishop and B. A. Grzybowski, "Electrostatic self-assembly of binary nanoparticle crystals with a diamond-like lattice," Science **312**, 420–424 (2006).

[118] H.-X. Zhou and X. Pang, "Electrostatic interactions in protein structure, folding, binding, and condensation," Chem. Rev. **118**, 1691–1741 (2018).

[119] D. Frenkel and B. Smit, *Understanding Molecular Simulation*, 2nd ed. (Academic, San Diego, 2002).

[120] A. Arnold and C. Holm, in *Advanced Computer Simulation Approaches for Soft Matter Sciences II*, edited by C. Holm and K. Kremer (Springer Berlin Heidelberg, Berlin, Heidelberg, 2005), pp. 59–109.

[121] P. P. Ewald, "Die Berechnung optischer und elektrostatischer Gitterpotentiale," Ann. Phys. (Leipzig) **369**, 253–287 (1921).

[122] T. Darden, D. York and L. Pedersen, "Particle mesh Ewald: An $N \cdot \log(N)$ method for Ewald sums in large systems," J. Chem. Phys. **98**, 10089–10092 (1993).

[123] L. Greengard and V. Rokhlin, "A fast algorithm for particle simulations," J. Comp. Phys. **73**, 325–348 (1987).

[124] M. Shen, H. Li and M. Olvera de la Cruz, "Surface polarization effects on ion-containing emulsions," Phys. Rev. Lett. **119**, 138002 (2017).

[125] M. E. Leunissen, A. van Blaaderen, A. D. Hollingsworth, M. T. Sullivan and P. M. Chaikin, "Electrostatics at the oil–water interface, stability, and order in emulsions and colloids," Proc. Natl. Acad. Sci. U.S.A. **104**, 2585–2590 (2007).

[126] K. Breitsprecher, C. Holm and S. Kondrat, "Charge me slowly, i am in a hurry: Optimizing chargedischarge cycles in nanoporous supercapacitors," ACS Nano **12**, 9733–9741 (2018).

[127] B. W. Kwaadgras, R. van Roij and M. Dijkstra, "Self-consistent electric field-induced dipole interaction of colloidal spheres, cubes, rods, and dumbbells," J. Chem. Phys. **140**, 154901 (2014).

[128] Z. M. Sherman, D. Ghosh and J. W. Swan, "Field-directed self-assembly of mutually polarizable nanoparticles," Langmuir **34**, 7117-7134 (2018).

[129] R. Allen, J.-P. Hansen and S. Melchionna, "Electrostatic potential inside ionic solutions confined by dielectrics: a variational approach," Phys. Chem. Chem. Phys. **3**, 4177–4186 (2001).

[130] V. Jadhao, F. J. Solis and M. Olvera de la Cruz, "Simulation of charged systems in heterogeneous dielectric media via a true energy functional," Phys. Rev. Lett. **109**, 223905 (2012).

[131] V. Jadhao, F. J. Solis and M. Olvera de la Cruz, "A variational formulation of electrostatics in a medium with spatially varying dielectric permittivity," J. Chem. Phys. **138**, 054119 (2013).

[132] L. Vrbka, M. Mucha, B. Minofar, P. Jungwirth, E. C. Brown and D. J. Tobias, "Propensity of soft ions for the air/water interface," Curr. Opin. Colloid Interface Sci. **9**, 67–73 (2004).

[133] P. Cieplak, F.-Y. Dupradeau, Y. Duan and J. Wang, "Polarization effects in molecular mechanical force fields," J. Phys.: Condens. Matter **21**, 333102 (2009).

[134] P. E. M. Lopes, B. Roux and A. D. MacKerell, "Molecular modeling and dynamics studies with explicit inclusion of electronic polarizability: theory and applications,"

Theor. Chem. Acc. **124**, 11–28 (2009).

[135] J. A. Lemkul, J. Huang, B. Roux and A. D. MacKerell, "An empirical polarizable force field based on the classical drude oscillator model: Development history and recent applications," Chem. Rev. **116**, 4983–5013 (2016).

[136] Z. Jing, C. Liu, S. Y. Cheng, R. Qi, B. D. Walker, J.-P. Piquemal and P. Ren, "Polarizable force fields for biomolecular simulations: Recent advances and applications," Annu. Rev. Biophys. **48**, 371–394 (2019).

[137] D. Bedrov, J.-P. Piquemal, O. Borodin, A. D. MacKerell, B. Roux and C. Schröder, "Molecular dynamics simulations of ionic liquids and electrolytes using polarizable force fields," Chem. Rev. **119**, 7940–7995 (2019).

[138] M. M. Hatlo and L. Lue, "The role of image charges in the interactions between colloidal particles," Soft Matt. **4**, 1582–1596 (2008).

[139] A. Arnold, K. Breitsprecher, F. Fahrenberger, S. Kesselheim, O. Lenz and C. Holm, "Efficient algorithms for electrostatic interactions including dielectric contrasts," Entropy **15**, 4569–4588 (2013).

[140] J. Zhou and F. Schmid, "Computer simulations of single particles in external electric fields," Soft Matt. **11**, 6728–6739 (2015).

[141] E. B. Lindgren, H.-K. Chan, A. J. Stace and E. Besley, "Progress in the theory of electrostatic interactions between charged particles," Phys. Chem. Chem. Phys. **18**, 5883–5895 (2016).

[142] J. Qin, "Charge polarization near dielectric interfaces and the multiple-scattering formalism," Soft Matt. **15**, 2125–2134 (2019).

[143] J. D. Jackson, *Classical Electrodynamics*, 3rd ed. (Wiley, New York, 1999).

[144] L. D. Landau, E. M. Lifshitz and L. P. Pitaevskii, *Electrodynamics of Continuous Media*, Vol. 8 of *Course of Theoretical Physics*, 2nd ed. (Elsevier Butterworth Heinemann, Oxford, 1993).

[145] A. Zangwill, *Modern Electrodynamics* (Cambridge University Press, Cambridge, U.K., 2013).

[146] A.-P. Hynninen and M. Dijkstra, "Phase diagram of dipolar hard and soft spheres: Manipulation of colloidal crystal structures by an external field," Phys. Rev. Lett. **94**, 138303 (2005).

[147] A.-P. Hynninen and M. Dijkstra, "Phase behavior of dipolar hard and soft spheres," Phys. Rev. E **72**, 051402 (2005).

[148] M. Rotunno, T. Bellini, Y. Lansac and M. A. Glaser, "Phase behavior of polarizable spherocylinders in external fields," J. Chem. Phys. **121**, 5541-5549 (2004).

[149] T. Troppenz, L. Filion, R. van Roij and M. Dijkstra, "Phase behaviour of polarizable colloidal hard rods in an external electric field: A simulation study," J. Chem. Phys. **141**, 154903 (2014).

[150] A. Kuijk, T. Troppenz, L. Filion, A. Imhof, R. van Roij, M. Dijkstra and A. van Blaaderen, "Effect of external electric fields on the phase behavior of colloidal silica rods," Soft Matt. **10**, 6249-6255 (2014).

[151] A. Azari, J. J. Crassous, A. M. Mihut, E. Bialik, P. Schurtenberger, J. Stenhammar and P. Linse, "Directed self-assembly of polarizable ellipsoids in an external electric field," Langmuir **33**, 13834-13840 (2017).

[152] M. Renne and B. Nijboer, "Microscopic derivation of macroscopic van der waals forces," Chem. Phys. Lett. **1**, 317 - 320 (1967).

[153] B. Nijboer and M. Renne, "Microscopic derivation of macroscopic van der waals forces. ii," Chem. Phys. Lett. **2**, 35 - 38 (1968).

[154] B. W. Kwaadgras, M. Verdult, M. Dijkstra and R. van Roij, "Polarizability and alignment of dielectric nanoparticles in an external electric field: Bowls, dumbbells, and cuboids," J. Chem. Phys. **135**, 134105 (2011).

[155] B. W. Kwaadgras, M. Dijkstra and R. van Roij, "Communication: Bulkiness versus anisotropy: The optimal shape of polarizable brownian nanoparticles for alignment in electric fields," J. Chem. Phys. **136**, 131102 (2012).

[156] H.-Y. Kim, J. O. Sofo, D. Velegol, M. W. Cole and G. Mukhopadhyay, "Static polarizabilities of dielectric nanoclusters," Phys. Rev. A **72**, 053201 (2005).

[157] B. W. Kwaadgras, T. H. Besseling, T. J. Coopmans, A. Kuijk, A. Imhof, A. v. Blaaderen, M. Dijkstra and R. v. Roij, "Orientation of a dielectric rod near a planar electrode," Phys. Chem. Chem. Phys. **16**, 22575-22582 (2014).

[158] R. J. Zauhar and R. S. Morgan, "Computing the electric potential of biomolecules: Application of a new method of molecular surface triangulation," J. Comput. Chem. **11**, 603–622 (1990).

[159] M. E. Davis and J. A. McCammon, "Electrostatics in biomolecular structure and dynamics," Chem. Rev. **90**, 509–521 (1990).

[160] J. Tomasi and M. Persico, "Molecular interactions in solution: An overview of methods based on continuous distributions of the solvent," Chem. Rev. **94**, 2027–2094 (1994).

[161] R. Bharadwaj, A. Windemuth, S. Sridharan, B. Honig and A. Nicholls, "The fast multipole boundary element method for molecular electrostatics: An optimal approach for large systems," J. Comput. Chem. **16**, 898–913 (1995).

[162] X. Jiang, J. Li, X. Zhao, J. Qin, D. Karpeev, J. Hernandez-Ortiz, J. J. de Pablo and O. Heinonen, "An $O(N)$ and parallel approach to integral problems by a kernel-independent fast multipole method: Application to polarization and magnetization of interacting particles," J. Chem. Phys. **145**, 064307 (2016).

[163] H. Hoshi, M. Sakurai, Y. Inoue and R. Chûjô, "Medium effects on the molecular electronic structure. I. The formulation of a theory for the estimation of a molecular electronic structure surrounded by an anisotropic medium," J. Chem. Phys. **87**, 1107–1115 (1987).

[164] K. Barros and E. Luijten, "Dielectric effects in the self-assembly of binary colloidal aggregates," Phys. Rev. Lett. **113**, 017801 (2014).

[165] M. Han, H. Wu and E. Luijten, "Electric double layer of anisotropic dielectric colloids under electric fields," Eur. Phys. J. Special Topics **225**, 685–698 (2016).

[166] H. Wu, M. Han and E. Luijten, "Dielectric effects on the ion distribution near a Janus colloid," Soft Matt. **12**, 9575–9584 (2016).

[167] H. Wu, H. Li, F. J. Solis, M. Olvera de la Cruz and E. Luijten, "Asymmetric electrolytes near structured dielectric interfaces," J. Chem. Phys. **149**, 164701 (2018).

[168] T. D. Nguyen, H. Li, D. Bagchi, F. J. Solis and M. Olvera de la Cruz, "Incorporating surface polarization effects into large-scale coarse-grained molecular dynamics simulation," Comput. Phys. Commun. **241**, 80–91 (2019).

[169] R. A. Marcus, "On the theory of oxidation-reduction reactions involving electron transfer. I," J. Chem. Phys. **24**, 966–978 (1956).

[170] R. Allen, S. Melchionna and J.-P. Hansen, "Intermittent permeation of cylindrical nanopores by water," Phys. Rev. Lett. **89**, 175502 (2002).

[171] R. Allen and J.-P. Hansen, "Density functional approach to the effective interaction between charges within dielectric cavities," J. Phys.: Condens. Matter **14**, 11981–11997 (2002).

[172] R. Allen, S. Melchionna and J.-P. Hansen, "Permeation of nanopores by water: the effects of channel polarization," J. Phys.: Condens. Matter **15**, S297–S302 (2002).

[173] R. Allen and J.-P. Hansen, "Electrostatic interactions of charges and dipoles near a polarizable membrane," Mol. Phys. **101**, 1575-1585 (2003).

[174] R. Allen, J.-P. Hansen and S. Melchionna, "Molecular dynamics investigation of water permeation through nanopores," J. Chem. Phys. **119**, 3905-3919 (2003).

[175] E. S. Reiner and C. J. Radke, "Variational approach to the electrostatic free energy in charged colloidal suspensions: general theory for open systems," J. Chem. Soc., Faraday Trans. **86**, 3901-3912 (1990).

[176] D. M. York and M. Karplus, "A smooth solvation potential based on the conductor-like screening model," J. Phys. Chem. A **103**, 11060-11079 (1999).

[177] P. Attard, "Variational formulation for the electrostatic potential in dielectric continua," J. Chem. Phys. **119**, 1365-1372 (2003).

[178] B. U. Felderhof, "Fluctuations of polarization and magnetization in dielectric and magnetic media," J. Chem. Phys. **67**, 493–500 (1977).

[179] M. Marchi, D. Borgis, N. Levy and P. Ballone, "A dielectric continuum molecular dynamics method," J. Chem. Phys. **114**, 4377–4385 (2001).

[180] A. C. Maggs, "Auxiliary field Monte Carlo for charged particles," J. Chem. Phys. **120**, 3108–3118 (2004).

[181] A. C. Maggs and R. Everaers, "Simulating nanoscale dielectric response," Phys. Rev. Lett. **96**, 230603 (2006).

[182] F. Lipparini, G. Scalmani, B. Mennucci, E. Cancs, M. Caricato and M. J. Frisch, "A variational formulation of the polarizable continuum model," J. Chem. Phys. **133**, 014106 (2010).

[183] S. Buyukdagli, M. Manghi and J. Palmeri, "Ionic exclusion phase transition in neutral and weakly charged cylindrical nanopores," J. Chem. Phys. **134**, 074706 (2011).

[184] O. I. Obolensky, T. P. Doerr, R. Ray and Y.-K. Yu, "Rigorous treatment of electrostatics for spatially varying dielectrics based on energy minimization," Phys. Rev. E **79**, 041907 (2009).

[185] R. Car and M. Parrinello, "Unified approach for molecular dynamics and density-functional theory," Phys. Rev. Lett. **55**, 2471–2474 (1985).

[186] A. P. dos Santos and Y. Levin, "Electrolytes between dielectric charged surfaces: Simulations and theory," J. Chem. Phys. **142**, 194104 (2015).

[187] S. H. L. Klapp, "Monte-Carlo simulations of strongly interacting dipolar fluids between two conducting walls," Mol. Simul. **32**, 609–621 (2006).

[188] Z. Wang and E. Luijten, "Structural and dynamical properties of dipolar fluids near a dielectric interface," To be published (2019).

[189] A. P. dos Santos, M. Girotto and Y. Levin, "Simulations of polyelectrolyte adsorption to a dielectric like-charged surface," J. Phys. Chem. B **120**, 10387–10393 (2016).

[190] Z.-Y. Wang, "Charge reversal at a planar boundary between two dielectrics," Phys. Rev. E **93**, 012605 (2016).

[191] J. Yuan, H. S. Antila and E. Luijten, "Dielectric effects on ion transport in polyelectrolyte brushes," ACS Macro Lett. **8**, 183–187 (2019).

[192] Z. Wang and E. Luijten, "Dielectric modulation of two-dimensional dipolar materials," Phys. Rev. Lett. **123**, 096101 (2019).

[193] H. L. Friedman, "Image approximation to the reaction field," Mol. Phys. **29**, 1533-1543 (1975).

[194] P. Linse, "Image charge effects in spherical symmetry with applications to micellar systems," J. Phys. C **90**, 6821–6828 (1986).

[195] R. Abagyan and M. Totrov, "Biased probability monte carlo conformational searches and electrostatic calculations for peptides and proteins," J. Mol. Biol. **235**, 983 - 1002 (1994).

[196] Z. Xu and W. Cai, "Fast analytical methods for macroscopic electrostatic models in biomolecular simulations," SIAM Rev. **53**, 683-720 (2011).

[197] F. Olyslager and I. V. Lindell, "Closed form solutions of Maxwell's equations in the computer age," Radio Science Bull. **2003**, 30–37 (2003).

[198] Z. Xu, "A fast algorithm for treating dielectric discontinuities in charged spherical colloids," Interdiscip. Sci. Comput. Life Sci. **4**, 19–26 (2012).

[199] Z. Xu, "Electrostatic interaction in the presence of dielectric interfaces and polarization-induced like-charge attraction," Phys. Rev. E **87**, 013307 (2013).

[200] Z. Gan, H. Wu, K. Barros, Z. Xu and E. Luijten, "Comparison of efficient techniques for the simulation of dielectric objects in electrolytes," J. Comp. Phys. **291**, 317–333 (2015).

[201] J. Qin, J. Li, V. Lee, H. Jaeger, J. J. de Pablo and K. F. Freed, "A theory of interactions between polarizable dielectric spheres," J. Colloid Interface Sci. **469**, 237–241 (2016).

[202] K. S. Gustafson, G. Xu, K. F. Freed and J. Qin, "Image method for electrostatic energy of polarizable dipolar spheres," J. Chem. Phys. **147**, 064908 (2017).

[203] Z. Gan, Z. Wang, S. Jiang, Z. Xu and E. Luijten, "Efficient dynamic simulations of charged dielectric colloids through a novel hybrid method," J. Chem. Phys. **151**,

024112 (2019).

[204] H. Cheng and L. Greengard, "A method of images for the evaluation of electrostatic fields in systems of closely spaced conducting cylinders," SIAM J. Appl. Math. **58**, 122-141 (1998).

[205] S. T. Cui, "Electrostatic potential in cylindrical dielectric media using the image charge method," Mol. Phys. **104**, 2993–3001 (2006).

[206] Z. Xu, W. Cai and X. Cheng, "Image charge method for reaction fields in a hybrid ion-channel model," Commun. Comp. Phys. **9**, 1056–1070 (2011).

[207] Q. Zhao, P. Liu and Z. Xu, "A fast method for evaluating green's function in irregular domains with application to charge interaction in a nanopore," Commun. Comp. Phys. **24**, 1241–1258 (2018).

[208] E. B. Lindgren, I. N. Derbenev, A. Khachatourian, H.-K. Chan, A. J. Stace and E. Besley, "Electrostatic self-assembly: Understanding the significance of the solvent," J. Chem. Theory Comput. **14**, 905-915 (2018).

[209] E. B. Lindgren, B. Stamm, Y. Maday, E. Besley and A. J. Stace, "Dynamic simulations of many-body electrostatic self-assembly," Philosophical Transactions of the Royal Society A: Mathematical, Physical and Engineering Sciences **376**, 20170143 (2018).

[210] S. Kesselheim, M. Sega and C. Holm, "Applying icc to dna translocation: Effect of dielectric boundaries," Comput. Phys. Commun. **182**, 33 - 35 (2011), computer Physics Communications Special Edition for Conference on Computational Physics Kaohsiung, Taiwan, Dec 15-19, 2009.

[211] S. Kesselheim, M. Sega and C. Holm, "Effects of dielectric mismatch and chain flexibility on the translocation barriers of charged macromolecules through solid state nanopores," Soft Matt. **8**, 9480-9486 (2012).

[212] S. Howorka and Z. Siwy, "Nanopore analytics: sensing of single molecules," Chem. Soc. Rev. **38**, 2360-2384 (2009).

[213] K. Breitsprecher, K. Szuttor and C. Holm, "Electrode models for ionic liquid-based capacitors," J. Phys. Chem. C **119**, 22445-22451 (2015).

[214] K. Breitsprecher, M. Abele, S. Kondrat and C. Holm, "The effect of finite pore length on ion structure and charging," J. Chem. Phys. **147**, 104708 (2017).

[215] L. Li, Q. Cao and C. Zuo, "Effect of counterion valence on conformational behavior of spherical polyelectrolyte brushes confined between two parallel walls," Polymers **10**, 363 (2018).

[216] J. Rottler and A. C. Maggs, "A continuum, o(n) monte carlo algorithm for charged particles," J. Chem. Phys. **120**, 3119-3129 (2004).

[217] F. Fahrenberger and C. Holm, "Computing the Coulomb interaction in inhomogeneous dielectric media via a local electrostatics lattice algorithm," Phys. Rev. E **90**, 063304 (2014).

[218] F. Fahrenberger, Z. Xu and C. Holm, "Simulation of electric double layers around charged colloids in aqueous solution of variable permittivity," J. Chem. Phys. **141**, 064902 (2014).

[219] F. Fahrenberger, O. A. Hickey, J. Smiatek and C. Holm, "Importance of varying permittivity on the conductivity of polyelectrolyte solutions," Phys. Rev. Lett. **115**, 118301 (2015).

[220] A. T. Skjeltorp and G. Helgesen, "Condensation and ordering of colloidal spheres dispersed in a ferrofluid," Physica A **176**, 37–53 (1991).

[221] R. E. Rosensweig, ""Negative viscosity" in a magnetic fluid," Science **271**, 614–615 (1996).

[222] A. Mertelj, D. Lisjak, M. Drofenik and M. Čopič, "Ferromagnetism in suspensions of magnetic platelets in liquid crystal," Nature **504**, 237–241 (2013).

[223] T. C. Halsey, "Electrorheological fluids," Science **258**, 761–766 (1992).

[224] P. I. C. Teixeira, J. M. Tavares and M. M. T. da Gama, "The effect of dipolar forces on the structure and thermodynamics of classical fluids," J. Phys.: Condens. Matter **12**, R411–R434 (2000).

[225] P. K. Jog, S. G. Sauer, J. Blaesing and W. G. Chapman, "Application of dipolar chain theory to the phase behavior of polar fluids and mixtures," Ind. Eng. Chem. Res. **40**, 4641–4648 (2001).

[226] J. J. Weis, D. Levesque and G. J. Zarragoicoechea, "Orientational order in simple dipolar liquid-crystal models," Phys. Rev. Lett. **69**, 913–916 (1992).

[227] E. Lomba, F. Lado and J. J. Weis, "Structure and thermodynamics of a ferrofluid monolayer," Phys. Rev. E **61**, 3838–3849 (2000).

[228] L. Rovigatti, J. Russo and F. Sciortino, "Structural properties of the dipolar hard-sphere fluid at low temperatures and densities," Soft Matt. **8**, 6310 (2012).

[229] J. Winkelmann, "Perturbation theory of dipolar hard spheres: The vapour–liquid equilibrium of strongly polar substances," Fluid Phase Equilibria **7**, 207–217 (1981).

[230] S. C. McGrother and G. Jackson, "Island of vapor-liquid coexistence in dipolar hard-core systems," Phys. Rev. Lett. **76**, 4183–4186 (1996).

[231] P. J. Camp, J. C. Shelley and G. N. Patey, "Isotropic fluid phases of dipolar hard spheres," Phys. Rev. Lett. **84**, 115–118 (2000).

[232] T. Tlusty and S. A. Safran, "Defect-induced phase separation in dipolar fluids," Science **290**, 1328–1331 (2000).

[233] R. Blaak, M. A. Miller and J.-P. Hansen, "Reversible gelation and dynamical arrest of dipolar colloids," Europhys. Lett. **78**, 26002 (2007).

[234] M. A. Miller, R. Blaak, C. N. Lumb and J.-P. Hansen, "Dynamical arrest in low density dipolar colloidal gels," J. Chem. Phys. **130**, 114507 (2009).

[235] J. Klein and E. Kumacheva, "Confinement-induced phase transitions in simple liquids," Science **269**, 816–819 (1995).

[236] K. De'Bell, A. B. MacIsaac and J. P. Whitehead, "Dipolar effects in magnetic thin films and quasi-two-dimensional systems," Rev. Mod. Phys. **72**, 225–257 (2000).

[237] N.-T. Nguyen, K. M. Ng and X. Huang, "Manipulation of ferrofluid droplets using planar coils," Appl. Phys. Lett. **89**, 052509 (2006).

[238] M. Klokkenburg, B. H. Erné, J. D. Meeldijk, A. Wiedenmann, A. V. Petukhov, R. P. A. Dullens and A. P. Philipse, "In situ imaging of field-induced hexagonal columns in magnetite ferrofluids," Phys. Rev. Lett. **97**, 185702 (2006).

[239] M. E. Sadat, R. Patel, J. Sookoor, S. L. Bud'Ko, R. C. Ewing, J. Zhang, H. Xu, Y. Wang, G. M. Pauletti, D. B. Mast and D. Shi, "Effect of spatial confinement on magnetic hyperthermia via dipolar interactions in fe3o4 nanoparticles for biomedical applications," Mater. Sci. Eng. C **42**, 52–63 (2014).

[240] S. H. Lee, J. C. Rasaiah and J. B. Hubbard, "Molecular dynamics study of a dipolar fluid between charged plates," J. Chem. Phys. **85**, 5232–5237 (1986).

[241] S. Senapati and A. Chandra, "Molecular relaxation in simple dipolar liquids confined between two solid surfaces," Chem. Phys. **231**, 65–80 (1998).

[242] S. Senapati and A. Chandra, "Molecular dynamics simulations of simple dipolar liquids in spherical cavity: Effects of confinement on structural, dielectric, and dynamical properties," J. Chem. Phys. **111**, 1223–1230 (1999).

[243] S. H. L. Klapp and M. Schoen, "Spontaneous orientational order in confined dipolar fluid films," J. Chem. Phys. **117**, 8050–8062 (2002).

[244] J.-J. Weis, "Simulation of quasi-two-dimensional dipolar systems," J. Phys.: Condens. Matter **15**, S1471–S1495 (2003).

[245] V. Ballenegger and J.-P. Hansen, "Dielectric permittivity profiles of confined polar fluids," J. Chem. Phys. **122**, 114711 (2005).

[246] V. A. Froltsov and S. H. L. Klapp, "Anisotropic dynamics of dipolar liquids in narrow slit pores," J. Chem. Phys. **124**, 134701 (2006).

[247] V. A. Froltsov and S. H. L. Klapp, "Dielectric response of polar liquids in narrow slit pores," J. Chem. Phys. **126**, 114703 (2007).

[248] J. Jordanovic and S. H. L. Klapp, "Field-induced layer formation in dipolar nanofilms," Phys. Rev. Lett. **101**, 038302 (2008).

[249] H. Wu and E. Luijten, "Accurate and efficient numerical simulation of dielectrically anisotropic particles," J. Chem. Phys. **149**, 134105 (2018).

[250] I.-C. Yeh and M. L. Berkowitz, "Ewald summation for systems with slab geometry," J. Chem. Phys. **111**, 3155–3162 (1999).

[251] M. P. Allen and D. J. Tildesley, *Computer Simulation of Liquids* (Clarendon, Oxford, 1987).

[252] D. Wei and G. N. Patey, "Orientational order in simple dipolar liquids: Computer simulation of a ferroelectric nematic phase," Phys. Rev. Lett. **68**, 2043–2045 (1992).

[253] D. Wei and G. N. Patey, "Ferroelectric liquid-crystal and solid phases formed by strongly interacting dipolar soft spheres," Phys. Rev. A **46**, 7783–7792 (1992).

[254] J. J. Weis and D. Levesque, "Ferroelectric phases of dipolar hard spheres," Phys. Rev. E **48**, 3728–3740 (1993).

[255] G. R. Luckhurst, *The Molecular Physics of Liquid Crystals* (Academic, London, 1979).

[256] K. Takae and A. Onuki, "Applying electric field to charged and polar particles between metallic plates: Extension of the Ewald method," J. Chem. Phys. **139**, 124108 (2013).

[257] M. Seul and D. Andelman, "Domain shapes and patterns: The phenomenology of modulated phases," Science **267**, 476–483 (1995).

[258] D. Andelman and R. E. Rosensweig, "Modulated phases: Review and recent results," J. Phys. Chem. B **113**, 3785–3798 (2009).

[259] R. Allenspach, M. Stampanoni and A. Bischof, "Magnetic domains in thin epitaxial Co/Au(111) films," Phys. Rev. Lett. **65**, 3344–3347 (1990).

[260] I. Booth, A. B. MacIsaac, J. P. Whitehead and K. De'Bell, "Domain structures in ultrathin magnetic films," Phys. Rev. Lett. **75**, 950–953 (1995).

[261] H. Möhwald, "Direct characterization of monolayers at the air–water interface," Thin Solid Films **159**, 1–15 (1988).

[262] D. Andelman, F. Broçhard and J.-F. Joanny, "Phase transitions in Langmuir monolayers of polar molecules," J. Chem. Phys. **86**, 3673–3681 (1987).

[263] L. Leibler, "Theory of microphase separation in block copolymers," Macromolecules **13**, 1602–1617 (1980).

[264] M. P. Stoykovich, M. Müller, S. O. Kim, H. H. Solak, E. W. Edwards, J. J. de Pablo and P. F. Nealey, "Directed assembly of block copolymer blends into nonregular device-oriented structures," Science **308**, 1442–1446 (2005).

[265] Y. A. Vlasov, X.-Z. Bo, J. C. Sturm and D. J. Norris, "On-chip natural assembly of silicon photonic bandgap crystals," Nature **414**, 289–293 (2001).

[266] E. F. Borra, A. M. Ritcey, R. Bergamasco, P. Laird, J. Gingras, M. Dallaire, L. Da Silva and H. Yockell-Lelievre, "Nanoengineered astronomical optics," Astron. Astrophys.

419, 777–782 (2004).

[267] C. L. Dennis, R. P. Borges, L. D. Buda, U. Ebels, J. F. Gregg, M. Hehn, E. Jouguelet, K. Ounadjela, I. Petej, I. L. Prejbeanu and M. J. Thornton, "The defining length scales of mesomagnetism: a review," J. Phys.: Condens. Matter **14**, R1175–R1262 (2002).

[268] A. B. MacIsaac, J. P. Whitehead, M. C. Robinson and K. De'Bell, "Striped phases in two-dimensional dipolar ferromagnets," Phys. Rev. B **51**, 16033–16045 (1995).

[269] A. D. Stoycheva and S. J. Singer, "Stripe melting in a two-dimensional system with competing interactions," Phys. Rev. Lett. **84**, 4657–4660 (2000).

[270] A. B. MacIsaac, J. P. Whitehead, K. De'Bell and P. H. Poole, "Phase diagram for a magnetic thin film with dipolar interactions and magnetic surface anisotropy," Phys. Rev. Lett. **77**, 739–742 (1996).

[271] K. D. Usadel and A. Hucht, "Anisotropy of ultrathin ferromagnetic films and the spin reorientation transition," Phys. Rev. B **66**, 024419 (2002).

[272] T. Garel and S. Doniach, "Phase transitions with spontaneous modulation – the dipolar Ising ferromagnet," Phys. Rev. B **26**, 325–329 (1982).

[273] J. Dobnikar, A. Snezhko and A. Yethiraj, "Emergent colloidal dynamics in electromagnetic fields," Soft Matt. **9**, 3693–3704 (2013).

[274] V. Russier, "Calculated magnetic properties of two-dimensional arrays of nanoparticles at vanishing temperature," J. Appl. Phys. **89**, 1287–1294 (2001).

[275] J. J. Weis, J. M. Tavares and M. M. Telo da Gama, "Structural and conformational properties of a quasi-two-dimensional dipolar fluid," J. Phys.: Condens. Matter **14**, 9171–9186 (2002).

[276] P. D. Duncan and P. J. Camp, "Structure and dynamics in a monolayer of dipolar spheres," J. Chem. Phys. **121**, 11322–11331 (2004).

[277] H. Schmidle, C. K. Hall, O. D. Velev and S. H. L. Klapp, "Phase diagram of two-dimensional systems of dipole-like colloids," Soft Matt. **8**, 1521–1531 (2012).

[278] V. G. Veselago, "The electrodynamics of substances with simultaneously negative values of ϵ and μ," Sov. Phys. Usp. **10**, 509–514 (1968).

[279] D. R. Smith, J. B. Pendry and M. C. Wiltshire, "Metamaterials and negative refractive index," Science **305**, 788–792 (2004).

[280] Y. Urzhumov, W. Chen, C. Bingham, W. Padilla and D. R. Smith, "Magnetic levitation of metamaterial bodies enhanced with magnetostatic surface resonances," Phys. Rev. B **85**, 054430 (2012).

[281] M. W. Coffey, "Magnetic levitation from negative permeability materials," Phys. Lett. A **376**, 2739–2742 (2012).

[282] P. Hammond, "Electric and magnetic images," Proc. IEE - Part C **107**, 306–313 (1960).

[283] L. Hong, A. Cacciuto, E. Luijten and S. Granick, "Clusters of charged Janus spheres," Nano Letters **6**, 2510–2514 (2006).

[284] O. Dolgov, D. Kirzhnits and V. Losyakov, "On the admissible values of the static magnetic permeability," Solid State Commun. **46**, 147–149 (1983).

[285] J. Kana Kana, G. Vignaud, A. Gibaud and M. Maaza, "Thermally driven sign switch of static dielectric constant of vo2 thin film," Opt. Mater. (Amst). **54**, 165–169 (2016).

[286] V. U. Nazarov, "Negative static permittivity and violation of Kramers-Kronig relations in quasi-two-dimensional crystals," Phys. Rev. B **92**, 161402(R) (2015).

[287] C. W. Chu, F. Chen, J. Shulman, S. Tsui, Y. Y. Xue, W. Wen and P. Sheng, "A negative dielectric constant in nano-particle materials under an electric field at very low frequencies," Strongly Correl. Electron Mater. Phys. Nanoeng. **5932**, 59320X (2006).

[288] J. Shulman, S. Tsui, F. Chen, Y. Y. Xue and C. W. Chu, "Plasmalike negative capacitance in nanocolloids," Appl. Phys. Lett. **90**, 8–11 (2007).

[289] H. Yan, C. Zhao, K. Wang, L. Deng, M. Ma and G. Xu, "Negative dielectric constant manifested by static electricity," Appl. Phys. Lett. **102**, 062904 (2013).

[290] R. Mach-Batlle, A. Parra, J. Prat-Camps, S. Laut, C. Navau and A. Sanchez, "Negative permeability in magnetostatics and its experimental demonstration," Phys. Rev. B **96**, 094422 (2017).

[291] A. van Blaaderen, R. Ruel and P. Wiltzius, "Template-directed colloidal crystallization," Nature **385**, 321–324 (1997).

[292] G. Malescio and G. Pellicane, "Stripe phases from isotropic repulsive interactions," Nature Mater. **2**, 97–100 (2003).

[293] R. C. O'Handley, *Modern Magnetic Materials: Principles and Applications* (Wiley, New York, 1999).

[294] A. H. Juffer, E. F. F. Botta, B. A. M. van Keulen, A. van der Ploeg and H. J. C. Berendsen, "The electric potential of a macromolecule in a solvent: A fundamental approach," J. Comp. Phys. **97**, 144–171 (1991).

[295] A. Nicholls and B. Honig, "A rapid finite difference algorithm, utilizing successive over-relaxation to solve the Poisson–Boltzmann equation," J. Comput. Chem. **12**, 435–445 (1991).

[296] N. A. Baker, D. Sept, S. Joseph, M. J. Holst and J. A. McCammon, "Electrostatics of nanosystems: Application to microtubules and the ribosome," Proc. Natl. Acad. Sci. U.S.A. **98**, 10037–10041 (2001).

[297] A. C. Maggs and V. Rossetto, "Local simulation algorithms for Coulomb interactions," Phys. Rev. Lett. **88**, 196402 (2002).

[298] J. Rottler and A. C. Maggs, "Local molecular dynamics with Coulombic interactions," Phys. Rev. Lett. **93**, 170201 (2004).

[299] I. Pasichnyk and B. Dünweg, "Coulomb interactions via local dynamics: a molecular-dynamics algorithm," J. Phys.: Condens. Matter **16**, S3999–S4020 (2004).

[300] P.-G. Martinsson, "Fast evaluation of electro-static interactions in multi-phase dielectric media," J. Comp. Phys. **211**, 289–299 (2006).

[301] R. Yokota, J. P. Bardhan, M. G. Knepley, L. A. Barba and T. Hamada, "Biomolecular electrostatics using a fast multipole BEM on up to 512 GPUs and a billion unknowns," Comput. Phys. Commun. **182**, 1272–1283 (2011).

[302] H. Cheng, L. Greengard and V. Rokhlin, "A fast adaptive multipole algorithm in three dimensions," J. Comp. Phys. **155**, 468–498 (1999).

[303] L. Ying, G. Biros and D. Zorin, "A kernel-independent adaptive fast multipole algorithm in two and three dimensions," J. Comp. Phys. **196**, 591–626 (2004).

[304] B. Lu, X. Cheng and J. A. McCammon, ""New-version-fast-multipole-method" accelerated electrostatic calculations in biomolecular systems," J. Comp. Phys. **226**, 1348–1366 (2007).

[305] W. Geng and R. Krasny, "A treecode-accelerated boundary integral Poisson–Boltzmann solver for electrostatics of solvated biomolecules," J. Comp. Phys. **247**, 62–78 (2013).

[306] Z. Wang, Z. Gan, S. Jiang, Z. Xu and E. Luijten, "Anisotropic self-assembly of polarizable colloidal mixtures," To be published (2020).

[307] A. D. Dinsmore, J. C. Crocker and A. G. Yodh, "Self-assembly of colloidal crystals," Curr. Opin. Colloid Interface Sci. **3**, 5–11 (1998).

[308] A. D. Dinsmore, M. F. Hsu, M. G. Nikolaides, M. Marquez, A. R. Bausch and D. A. Weitz, "Colloidosomes: Selectively permeable capsules composed of colloidal particles," Science **298**, 1006–1009 (2002).

[309] S.-H. Kim, S. Y. Lee, S.-M. Yang and G.-R. Yi, "Self-assembled colloidal structures for photonics," NPG Asia Mater. **3**, 25–33 (2011).

[310] K. Kremer, M. O. Robbins and G. S. Grest, "Phase diagram of Yukawa systems: Model for charge-stabilized colloids," Phys. Rev. Lett. **57**, 2694–2697 (1986).

[311] P. G. Bolhuis, D. Frenkel, S.-C. Mau and D. A. Huse, "Entropy difference between crystal phases," Nature **388**, 235–236 (1997).

[312] A. Jain, J. R. Errington and T. M. Truskett, "Dimensionality and design of isotropic interactions that stabilize honeycomb, square, simple cubic, and diamond lattices," Phys. Rev. X **4**, 031049 (2014).

[313] S. C. Glotzer and M. J. Solomon, "Anisotropy of building blocks and their assembly into complex structures," Nature Mater. **6**, 557–562 (2007).

[314] Q. Chen, J. K. Whitmer, S. Jiang, S. C. Bae, E. Luijten and S. Granick, "Supracolloidal reaction kinetics of Janus spheres," Science **331**, 199–202 (2011).

[315] D. Zerrouki, J. Baudry, D. Pine, P. Chaikin and J. Bibette, "Chiral colloidal clusters," Nature **455**, 380–382 (2008).

[316] P. Akcora, H. Liu, S. K. Kumar, J. Moll, Y. Li, B. C. Benicewicz, L. S. Schadler, D. Acehan, A. Z. Panagiotopoulos, V. Pryamitsyn, V. Ganesan, J. Ilavsky, P. Thiyagarajan, R. H. Colby and J. F. Douglas, "Anisotropic self-assembly of spherical polymer-grafted nanoparticles," Nature Mater. **8**, 354–359 (2009).

[317] H. Lin, S. Lee, L. Sun, M. Spellings, M. Engel, S. C. Glotzer and C. A. Mirkin, "Clathrate colloidal crystals," Science **355**, 931–935 (2017).

[318] Z. Wang and E. Luijten, "Dielectric modulation of two-dimensional dipolar materials," Phys. Rev. Lett. **123**, 096101 (2019).

[319] J. P. K. Doye, M. A. Miller and D. J. Wales, "The double-funnel energy landscape of the 38-atom Lennard-Jones cluster," J. Chem. Phys. **110**, 6896–6906 (1999).

[320] A. P. Hynninen, C. G. Christova, R. van Roij, A. van Blaaderen and M. Dijkstra, "Prediction and observation of crystal structures of oppositely charged colloids," Phys. Rev. Lett. **96**, 138308 (2006).

[321] V. Lee, S. R. Waitukaitis, M. Z. Miskin and H. M. Jaeger, "Direct observation of particle interactions and clustering in charged granular streams," Nature Phys. **11**, 733–737 (2015).

[322] Z. Tang, N. A. Kotov and M. Giersig, "Spontaneous organization of single CdTe nanoparticles into luminescent nanowires," Science **297**, 237–240 (2002).

[323] J. A. Dodds, "The porosity and contact points in multicomponent random sphere packings calculated by a simple statistical geometric model," J. Colloid Interface Sci. **77**, 317–327 (1980).

[324] C. H. J. Evers, J. A. Luiken, P. G. Bolhuis and W. K. Kegel, "Self-assembly of microcapsules via colloidal bond hybridization and anisotropy," Nature **534**, 364–368 (2016).

[325] V. N. Manoharan, M. T. Elsesser and D. J. Pine, "Dense packing and symmetry in small clusters of microspheres," Science **301**, 483–487 (2003).